

Aerodynamic Perspectives on Wind Energy Efficiency

De Oliveira Andrade, Gael

DOI

[10.4233/uuid:0981a422-4927-4d07-9e40-a99b7e93779b](https://doi.org/10.4233/uuid:0981a422-4927-4d07-9e40-a99b7e93779b)

Publication date

2019

Document Version

Final published version

Citation (APA)

De Oliveira Andrade, G. (2019). *Aerodynamic Perspectives on Wind Energy Efficiency*. [Dissertation (TU Delft), Delft University of Technology]. <https://doi.org/10.4233/uuid:0981a422-4927-4d07-9e40-a99b7e93779b>

Important note

To cite this publication, please use the final published version (if applicable). Please check the document version above.

Copyright

Other than for strictly personal use, it is not permitted to download, forward or distribute the text or part of it, without the consent of the author(s) and/or copyright holder(s), unless the work is under an open content license such as Creative Commons.

Takedown policy

Please contact us and provide details if you believe this document breaches copyrights. We will remove access to the work immediately and investigate your claim.

**WIND IS
SURPASSING ALL
EXPECTATIONS
TO DECARBONIZE
ENERGY
PRODUCTION.**

**HOW FAR CAN
IT GO?**

This thesis investigates the efficiency of wind energy conversion from three aerodynamic perspectives. The first, purely theoretical, considers steady inviscid flow conditions to identify multi-rotor setups that can extract more power per unit area than isolated rotors. The second, practical perspective, assesses the extent to which site-tailored airfoils could reduce the cost of wind energy. The third, data-driven perspective, considers opportunities to better predict airfoil and vortex-generator flows relevant to wind turbine load calculations.

Oliveira

aerodynamic perspectives on WIND ENERGY EFFICIENCY

aerodynamic

perspectives on

WIND ENERGY

EFFICIENCY

**Gaël
de Oliveira**

ISBN 978-94-6384-036-1
9 789463 840361

AERODYNAMIC PERSPECTIVES ON WIND ENERGY EFFICIENCY

AERODYNAMIC PERSPECTIVES ON WIND ENERGY EFFICIENCY

Dissertation

for the purpose of obtaining the degree of doctor
at Delft University of Technology
by the authority of the Rector Magnificus, Prof. dr. ir. T.H.J.J. van der Hagen,
chair of the Board for Doctorates
to be defended publicly on
Monday 6 May 2019 at 12:30 o'clock

by

Gaël Ludovic DE OLIVEIRA ANDRADE

Master of Science in Aerospace Engineering,
Delft University of Technology
born in Chateauroux, Frankrijk.

This dissertation has been approved by the promotor.

Composition of the doctoral committee:

Rector Magnificus, chairperson
Prof. dr. ir. G.J.W. van Bussel
promotor
Dr. ir. B.W. van Oudheusden
promotor

Independent members:

Prof. dr. ir. G.A.M. van Kuik
Delft University of Technology
Prof. dr. ir. J. Meyers Catholic University of Leuven, Belgium
Prof. dr. V.L. Okulov Technical University of Denmark, Denmark
Prof. dr. A. Seifert Tel Aviv University, Israel
Prof. dr. Fulvio Scarano Delft University of Technology, reserve member

Other members:

Ir. W.A. Timmer Delft University of Technology



Keywords: Aerodynamics, Wind Energy, Betz limit

Printed by: Duplicaprint

Front & Back: Convection, by the author

Copyright © 2019 by G. de Oliveira

ISBN 978-94-6384-036-1

An electronic version of this dissertation is available at
<http://repository.tudelft.nl/>.

CONTENTS

Summary	11
Samenvatting	13
Acknowledgements	15
I Introduction	17
1.1 Wind energy research trends	20
1.2 Thesis research question	20
1.3 Definitions of efficiency	21
1.4 Research strategy	22
1.5 Thesis structure	23
II Maximum power coefficient	27
2 Exploiting wake interactions in ideal flow	35
2.1 Matched-actuator setup	36
2.2 Infinite distance between actuators	38
2.3 Finite distance between actuators	49
2.4 Findings and implications	53
3 Exploiting body interactions in ideal flow	57
3.1 Exact model of de Vries	58
3.2 Power coefficient trends	63
3.3 Actuator-body coupling	68
3.4 Findings and implications	70
4 Towards a general power coefficient limit	75
4.1 Infinitesimal streamtube formulation	76
4.2 Formal description of actuation surface.	79
4.3 Application to actuator-disk problem	81
4.4 New findings and implications	87
5 Exploiting wake interactions in non-conservative flows	91
5.1 Matched-actuator setup with enthalpy losses	92
5.2 Alternative reference area.	97
5.3 Estimating inter-actuator enthalpy losses.	100
5.4 Main findings	110

III	Efficiency of wind turbine airfoils	119
6	Effect of inflow perturbations	125
6.1	Angle of attack perturbations	126
6.2	Perturbation probability distribution	130
6.3	Expected wind turbine airfoil loads	132
7	Tailoring airfoils to inflow conditions	137
7.1	Multi-objective airfoil optimization	138
7.2	Maximizing glide-ratio across inflow perturbations	139
7.3	Compromise between glide-ratio and lift overshoot	143
7.4	Findings and Implications	145
8	Impact of tailored airfoils on cost of energy	149
8.1	Rotor planform optimization approach	150
8.2	Effect of airfoils on rotor feasibility frontier	153
8.3	Linearized model for cost of energy	155
8.4	Selection of optimal design	157
IV	Minimization of flow simulation uncertainties	165
9	Machine-learning of turbulent closure relations	173
9.1	Boundary layer treatment in Rfoil	174
9.2	Supervised learning of closure relations	177
9.3	Results and discussion	179
9.4	Findings and future perspectives	184
10	Machine-learning of similarity in vortex generator flows	187
10.1	Asymptotic development	189
10.2	Reconstruction of flow structures	195
10.3	Validation against PIV measurements	199
10.4	Universal features of forced-mixing	203
10.5	Findings and future perspectives	206
V	Conclusion	213
	Appendix	223
A	Matched Actuator Setups	225
A.1	Dimensions, sets and smoothness	225
A.2	Asymptotic configuration	226
A.3	Complementary configuration	228
A.4	Total Enthalpy and Energy Conservation	229
B	Infinitesimal streamtube lemmas	233
B.1	Conservation of Mass	233
B.2	Conservation of Momentum	234
B.3	Conservation of Energy	235
B.4	Crossing of Actuation Surface	236

<i>CONTENTS</i>	9
B.5 Consistency with macroscopic models	240
C Discretization of vortex-mixing equation	243
References	245
List of Publications	267
Authorship Notice	269
Curriculum Vitae	271

SUMMARY

The wind industry is consolidating after decades of growth. Added value shifts from turbine manufacturers to service providers while windpower prices approach grid parity. These results pay tribute to industry-wide efficiency gains obtained through technical and institutional innovation. But how far can wind go? Wind turbines already converged to a common aerodynamic paradigm: upwind rotors with three pitch-controlled blades. The aerodynamic power coefficient of individual turbines is no longer growing, and it might seem that future performance gains will be restricted to multidisciplinary design refinements. Is aerodynamic progress still relevant to wind energy? The present thesis seeks to answer this question from three different perspectives formulated as questions.

What is the maximum power coefficient of wind energy conversion? The performance of isolated wind turbines is bounded by a universal threshold: the Betz-Joukowski limit. This limit was defined by studying an isolated actuator disk in inviscid incompressible flow but there could be other arrangements that lead to higher power extraction per unit area. Passive flow augmentation, for example, is the well-known mechanism behind shrouded wind turbines. It consists in increasing mass flow over the energy extraction surface by deforming the static pressure field with stationary bodies. Active flow augmentation is a new mechanism identified in this thesis. It consists in exploiting interactions between the wakes of multiple actuator disks to increase the amount of flow from which energy is extracted. These observations lead to the proposal of a formal approach for deriving power coefficient limits for complex flow configurations. Finally, the relevance of active flow augmentation mechanisms in non-conservative flow conditions is also briefly assessed.

To which extent can improved airfoils reduce the cost of wind energy? Performance of wind energy converters depends on a combination of subsystems whose design spans multiple scales. These linkages are illustrated with a case-study about airfoils. First, the environment in which blade sections operate is characterized using a semi-analytical probability distribution for angle-of-attack perturbations. The procedure highlights that average blade section loads differ from static loads in average flow conditions. Implications for airfoil design are assessed with multi-objective optimization techniques. The result is a collection of Pareto fronts that illustrate the effect of inflow variations on the compromise between clean and soiled airfoil performance. Optimized airfoils are then used to quantify the impact of airfoil choice on rotor efficiency. Again, efficiency is interpreted from a multi-objective perspective: improvements correspond to shifts in the compromise between power coefficient maximization and blade load minimization. Finally, cost indifference curves are drawn over the Pareto fronts to identify optimal designs. The main conclusion is that tailoring wind turbine airfoils to local site conditions reduces the cost of energy in modest but relevant ways. The industry should seize this opportunity.

How can machine-learning improve the accuracy of flow predictions? Prediction un-

certainties limit the adoption of improved wind turbine airfoils because good baseline designs exist and the margin for potential gain is relatively small. A major challenge concerns the prediction of turbulent phenomena characteristic of very high Reynolds wind energy flows. Two data-driven approaches for tackling that challenge are explored. First, regression techniques are used to learn boundary-layer closure relations that lead to improved airfoil polar predictions. Second, synergies between asymptotic expansion and dimensionality reduction techniques are exploited to model the effect of vortex generators on turbulent boundary layers. Both problems are relevant to wind energy and show how data can breathe new life into structural interpretations of turbulent phenomena.

Discussions about the aerodynamic efficiency of wind energy conversion do not fit in three questions. Yet, the issues raised in this thesis show that aerodynamic developments remain determinant to the progress of wind energy.

SAMENVATTING

De windindustrie consolideert na tientallen jaren van groei. Toegevoegde waardeverschuivingen van turbinefabrikanten naar serviceproviders, terwijl windkrachtprijzen netpariteit benaderen. Deze resultaten zijn een eerbetoon aan de efficiëntie van de gehele industrie die door technische en institutionele innovatie is verkregen. Maar hoe ver kan wind gaan? Windturbines zijn al geconvergeerd naar een gemeenschappelijk aërodynamisch paradigma: opwaartse rotoren met drie pitch-controlled bladen. De aerodynamische vermogenscoëfficiënt van individuele turbines groeit niet langer en het lijkt erop dat toekomstige prestatiewinsten beperkt blijven tot multidisciplinaire ontwerpverfijningen. Is aerodynamische vooruitgang nog steeds relevant voor windenergie? Het huidige proefschrift tracht deze vraag vanuit drie verschillende perspectieven te beantwoorden.

Wat is de maximale vermogenscoëfficiënt van windenergieconversie? De prestaties van geïsoleerde windturbines worden begrensd door een universele drempel: de limiet van Betz-Joukowsky. Deze limiet werd gedefinieerd door het bestuderen van een geïsoleerde actuatorschijf in een niet-visceuze niet-samendrukbare stroom, maar er zouden andere regelingen kunnen zijn die leiden tot een hogere vermogensextractie per oppervlakte-eenheid. Passieve stromingsvergroting is bijvoorbeeld het bekende mechanisme achter verholde windturbines. Het bestaat uit het vergroten van de massastroom over het oppervlak van de energie-extractie door het statische drukveld te vervormen met stationaire lichamen. Actieve stroomvergroting is een nieuw mechanisme dat in dit proefschrift wordt geïdentificeerd. Het bestaat uit het benutten van interacties tussen de wakes van meerdere actuatorschijven om de hoeveelheid stroom waaruit energie wordt geëxtraheerd te vergroten. Deze waarnemingen leiden tot het voorstellen van een formele benadering voor het afleiden van vermogenscoëfficiëntlimieten voor complexe stroomconfiguraties. Ten slotte wordt ook de relevantie van actieve stroomvergrotingsmechanismen in niet-conservatieve stroomomstandigheden kort beoordeeld.

In welke mate kunnen verbeterde draagvlakken de kosten van windenergie verlagen? De prestaties van windenergieconvertors zijn afhankelijk van een combinatie van subsystemen waarvan het ontwerp meerdere schalen omvat. Deze koppelingen worden geïllustreerd met een case-study over draagvlakken. Ten eerste wordt de omgeving waarin bladsecties werken gekenmerkt door een semi-analytische kansverdeling voor verstoringshoeken. De procedure benadrukt dat de gemiddelde laddersegmentbelastingen verschillen van statische belastingen in gemiddelde stroomomstandigheden. Implicaties voor aerodynamische ontwerp worden beoordeeld met multi-objectieve optimalisatie technieken. Het resultaat is een verzameling Pareto-fronten die het effect van instroomvariëaties op het compromis tussen schone en vervuilde aerodynamische prestaties illustreren. Geoptimaliseerde schoepen worden vervolgens gebruikt voor het kwantificeren van de impact van keuze van het schoepenprofiel op rotorefficiëntie. Nogmaals, efficiëntie wordt geïnterpreteerd vanuit een multi-objectief perspectief: verbe-

teringen komen overeen met verschuivingen in het compromis tussen maximalisatie van de vermogenscoëfficiënt en minimalisatie van de bladbelasting. Ten slotte worden kostenonafhankelijkheidscurven over de Pareto-fronten getekend om optimale ontwerpen te identificeren. De belangrijkste conclusie is dat tailoring windturbinevleugels naar plaatselijke omstandigheden de energiekosten op bescheiden maar relevante manieren verlagen. De industrie zou van deze gelegenheid gebruik moeten maken.

Hoe kan machine-learning de nauwkeurigheid van flowvoorspellingen verbeteren? Voorspellingsonzekerheden beperken de acceptatie van verbeterde windturbinedraagvlakken omdat er goede baselineontwerpen bestaan en de marge voor potentiële winst relatief klein is. Een grote uitdaging betreft de voorspelling van turbulente fenomenen die kenmerkend zijn voor zeer hoge Reynolds windenergiestromen. Twee data-gestuurde benaderingen voor het aanpakken van die uitdaging worden verkend. Ten eerste worden regressietechnieken gebruikt om grenslaagrelaties te leren die leiden tot verbeterde voorspellingen van de vleugelprofielen. Ten tweede worden synergieën tussen asymptotische expansie en dimensionaliteitsreductietechnieken benut om het effect van vortexgeneratoren op turbulente grenslagen te modelleren. Beide problemen zijn relevant voor windenergie en laten zien hoe data een nieuw leven kunnen blazen in structurele interpretaties van turbulente fenomenen.

Discussies over de aerodynamische efficiëntie van windenergieconversie passen niet in drie vragen. Toch tonen de kwesties die in dit proefschrift aan de orde komen aan dat aërodynamische uitdagingen bepalend blijven voor de voortgang van windenergieerendement.

ACKNOWLEDGEMENTS

Doctoral regulations state that a thesis must be the work of its author. While that is the case, it is equally true that this work results from a collective effort to challenge pre-conceived ideas in wind energy aerodynamics.

Gerard van Bussel, my promotor, made it possible by offering unparalleled academic freedom. Your elegant guidance through the subtleties of academic life was also deeply appreciated. It taught me the ability to defend positions in firm yet empathetic ways. Bas van Oudheusden, also my promotor, provided a welcome sense of perspective at several key moments of the present research. Nando Timmer, who acted as daily advisor for this thesis and supervised my master thesis, shared his aerodynamic intuition to help create bridges between seemingly disjoint research approaches.

Ricardo Pereira was central to the successful completion of this thesis. It is now several weeks, if not months, since I have been searching for the right words to thank you. And yet, I still hesitate as to whether I should emphasize your exceptional scientific skills, your immensely supportive attitude as a friend, or your impeccable work ethics. The challenge is about not sounding too superlative. All I can I say, is that I would not have made it to the end of this thesis, nor stood so firmly by its findings, had you not been there as a friend and a scientist.

Together with Ricardo, Daniele Ragni was also very important to this thesis. Your (plural) courage, open attitude, and sense of justice strengthened my faith in humanity when faced to painfully unusual situations. Both of you are great assets to our department because you manage the rare feat of combining scientific excellence with a courageous human attitude that promotes collaboration. Your generosity in connecting me to other researchers is one amongst many examples.

These connections sparked wonderful collaborations with Marios Kotsonis, Francesco Avallone, Vinit Dighe, Erik Quagebeur and Fernando Lau. Francesco and Vinit, I truly enjoyed working with you and want to thank you for getting me on-board whenever a ducted rotor was around. You were always supportive and focused, and I feel indebted for your comprehension about delays in delivering updates to the steady-state vortex code. Marios, I wanted to thank for providing advice and sharing your wisdom on both scientific and human matters. Finally, I would also like to thank Erik Quagebeur for our good humored collaboration on probabilistic design, and Fernando Lau for hosting me at IST (Lisbon) for a few months in early 2016.

The list is already long, but there are yet other people that must be thanked for our joint work. Paul Thedens got me on board for a great collaboration about airfoil design for airborne wind energy applications. Roland Schmehl was also part of the fun and I thank him for nice discussions on the topic. Airborne wind energy cannot be mentioned without thanking Uwe Fechner for introducing me to the field, and for our collaboration at Aenarete. Also, our long evening conversations about the promotion of a more sustainable and peaceful world were both enjoyable and stimulating.

Acknowledgements would not be complete without thanking the wind energy section as whole. In random order: Wei Yu, Ashim Giyanani, Rene Bos, Marten Holtslag, Zi Wang, Lorenzo Lignarolo, Edoardo Grande, Damiano Casalino, Tom Berdowski, Wim Bierbooms, Julia Steiner, Axelle Viré, Simon Watson, Michiel van Zaaijer and Ruud van Rooij. Exhaustive acknowledgements . That being said, it is my duty to thank Sylvia Willems for her generosity, professionalism and effectiveness at keeping everyone's administration on track. And Jaco Brandsen for being a great officemate.

Finally, I would like to wholeheartedly thank my family and friends. While this is not the venue for a detailed mention of your constant contribution to my life, there are a few persons that must be explicitly thanked here. First, I want to thank my mother for her constant support throughout this thesis. But that is, obviously, only the tip of the iceberg. The sense of curiosity that animated this research is the product of her ambition to educate new generations that would contribute to build a more sustainable, peaceful, solidary and creative world. Both of my parents should be thanked for promoting a can-do attitude in all things of life. Also, my aunt and uncle should be thanked for their good humour and for traveling to the defence. Family friends are also important, so I would like to thank Cristina Lourenço and her family as well as Assunção Seïça. Last but not least, I want to thank my girlfriend, Simona Marcu, for sticking around with me throughout this thesis. My prolonged absences for focusing on this work gave her many sorrows. I will try to make up for it.

I

INTRODUCTION

Introduction

How to make sense of such an ill-posed question as the efficiency of wind energy?

Wind energy is Europe's second source of electricity generation capacity. European windpower capacity tripled in less than a decade, reaching 169GW by the end of 2017 compared to 57GW in 2007 (WindEurope, 2018; ewe, 2010). During that period, the average capacity factor of wind progressed from 21% to 28% (IRENA, 2017). These achievements create unprecedented opportunities for decarbonising the energy sector (OECD et al., 2017) and result from continued innovation (EWEA, 2009; Gonzalez and Lacal-Arantegui, 2016).

New wind turbines employ higher towers and longer blades to operate more frequently at nominal power. In the early 2000s, a typical 2MW machine had a rotor of about 80m diameter. Today's 2MW machines can reach diameters as large as 122m for low-wind sites (e.g. AS, 2017; Gamesa, 2018). The maximum power of individual wind turbines is also growing: machines installed in Denmark in 2017 had an average rating of 3.4MW compared to 2.1MW in 2010 (IRENA, 2017; WindEurope, 2018).

Offshore wind turbines grew even bigger because of harsh operating conditions. It is cheaper to maintain a small fleet of large machines than a large fleet of small machines. Even so, wind turbines correspond to a relatively small share of capital expenditure in offshore installations: 32% compared to 71% in onshore environments (Mone et al., 2014).

The levelised cost of wind energy is decreasing faster than expected for both onshore and offshore environments (IRENA, 2017). New wind turbines produce more power instead even if they are generally more expensive (IRENA, 2017). Until about 2012-2014, reductions in the cost of energy resulted primarily from technological innovations – introduction of roughness insensitive airfoils, pitch control, low induction rotors and better foundation design (IEA, 2012). Since then, costs decreased mostly thanks to economies of scale, improved reliability, and refined operation strategies.

A recent report by the International Renewable Energy Agency (IRENA) contends that the levelised cost of wind energy (LCOE) follows an inverse exponential trendline to installed capacity (IRENA 2017). If that trend persists, costs will decrease at a slower rate in the future unless new capacity is added at an ever-increasing rate. That could happen in offshore environments if floating wind turbines reach maturity fast enough. It seems unlikely for onshore installations, however, as good onshore locations are becoming increasingly scarce (Petersen, 2017).

1.1. WIND ENERGY RESEARCH TRENDS

Is onshore wind already converging to an optimum? Wind turbines already converged to a common aerodynamic concept. The “Danish” machine that dominates commercial installations consists of a 3-bladed upwind rotor with pitch-control. Manufacturers differ primarily in their choice of airfoils, placement of vortex generators, and usage of tip or hub devices. Commercial machines display more diversity in powertrain design. Generators can be of the permanent magnet or induction type, and about 25% of current wind turbines use a direct drive [Polinder and Abrahamsen \(2017\)](#). Hydraulic drives are also under consideration.

Recent roadmaps for the development of wind energy give little attention to wind turbine aerodynamics. The research agenda of the European Technology and Innovation Platform (ETIP) on Wind Energy insists on challenges related to industrialisation, grid integration and offshore installation ([ETIP, 2016](#)). Of its seventy pages, a mere half page is dedicated to rotor aerodynamics. The technology roadmap of the International Energy Agency (IEA) [IEA \(2013\)](#) follows the same direction. It puts even more emphasis on financial and institutional questions.

The IRENA offshore wind innovation outlook shows more enthusiasm for long-term technological advances ([IRENA, 2016](#)). It postulates that decarbonised electricity production requires widespread penetration of wind energy across the globe. That would hinge on disruptive technological advancements like floating platforms, two-bladed downwind rotors ([Madsen et al., 2013](#)), multi-rotor arrangements ([Jamieson and Branney, 2012](#)), or airborne wind energy systems ([Ahrens et al., 2013](#); [ECORYS, 2018](#)).

The research agenda of the European Academy of Wind Energy (EAWWE) goes even further. It argues that wind energy is still a young field of human endeavour and calls for investment in basic science to disrupt its advancement. The importance of immediate practical challenges is acknowledged, but there is a definite conviction that progress in wind energy could take unexpected and yet unimagined paths. Hence the need for curiosity-driven research.

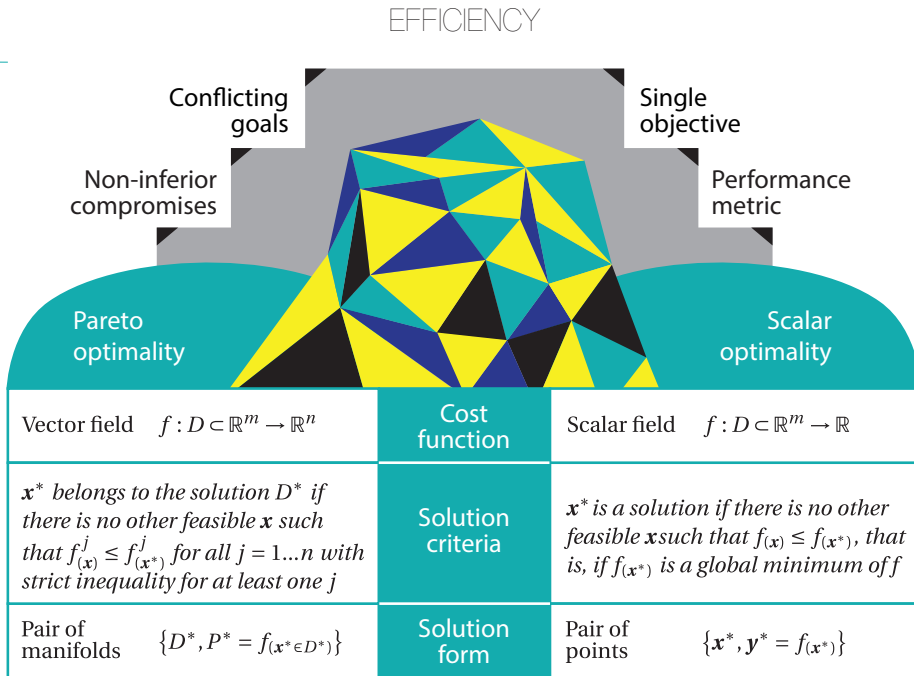
1.2. THESIS RESEARCH QUESTION

This thesis echoes to the EAWWE call. It stems from the author’s desire to address a deliberately vast, and curiosity-driven, question:

Can aerodynamic progress still lead to substantial increases in the efficiency of wind energy conversion?

It would be ill-advised to promise an exhaustive answer to such a vast question. Think of a wind farm and all it takes to maximise its energy output. Wind turbines must sit at the right location, rotors must be oriented into the wind, and blades must operate at the right pitch and rotational speed. Blades must have suitable planforms and employ airfoils that provide high lift and low drag irrespective of soiling conditions. The list of requirements is an endless fractal.

Even so, the question of efficiency is even broader. Most people regard efficiency as a desirable feature, but different people have different understandings of what makes a system efficient or optimal. Should wind energy systems seek to maximise power pro-



duction, minimise market cost or environmental impact? There are no clear-cut answers to these ethical questions.

The choice of goals and the multiscale nature of physical processes are not the only challenges to the study of wind energy efficiency. The formal definition of efficiency is subject to different views. Should an efficient system maximise a single goal? Or should it compromise optimally between conflicting goals?

1.3. DEFINITIONS OF EFFICIENCY

Physicists often describe efficiency as a ratio between desired outputs and available inputs. The efficiency of a gearbox, for example, corresponds to the ratio between output and input shaft powers. The power coefficient of wind energy conversion is the ratio between extracted power and available power across the system’s swept area in unperturbed inflow. Both examples see efficiency as a scalar whose maximisation leads to optimality.

Economic doxa adopts a different perspective (Blaug, 2007). It seeks to maximise aggregate utility – a proxy for human welfare – by combining multiple stages of efficient resource allocation (Feldman and Serrano, 2006). Consumption efficiency, for example, is attained when produced goods are allocated across consumers such that no alternative distribution can raise the utility of one consumer without reducing the utility of

another consumer. In this example, efficiency describes optimal compromises between goals but the ultimate goal still corresponds to the maximisation of a scalar variable (aggregate utility).

1.4. RESEARCH STRATEGY

The thesis dissects the aerodynamic efficiency of wind energy conversion from both single and multi-objective perspectives. It does so by focusing on three subquestions. The first one explores the macroscopic scales of wind energy conversion from a scalar optimality perspective :

Thesis subquestion 1	<i>Are disruptive increases in the power coefficient of wind energy conversion physically possible?</i>
-----------------------------	---

It responds to the EAWE call for curiosity-driven research and relates with challenge 3-3 of its research agenda:

EAWE challenge 3-3	<i>To achieve a fundamental understanding of the aerodynamics of wakes and interacting wakes behind wind turbines</i>
--------------------	---

The second question deals with intermediate physical scales, at the blade and airfoil level, and adopts a multi-objective perspective on efficiency:

Thesis subquestion 2	<i>What is the remaining scope for improving the aerodynamic efficiency of horizontal-axis wind-turbine airfoils?</i>
-----------------------------	---

It seeks to promote medium-term gains in wind energy efficiency and relates with challenge 7-1 of the EAWE research agenda:

EAWE challenge 7-1	<i>To develop holistic automated and comprehensive design methods for wind turbines and wind power plants for exploring the available design space and identify optimal compromises</i>
--------------------	---

The third question focuses on even smaller physical scales, at the boundary layer level, and seeks to lift barriers to the numerical optimisation of aerodynamic designs:

Thesis subquestion 3	<i>How can machine-learning improve flow simulations used for the design of wind energy systems ?</i>
-----------------------------	---

It relates to long-standing challenges in turbulence modelling and to challenge 7-2 of the EAWE research agenda:

EAWE challenge 7-1 (abridged)	<i>To develop a full range of validated models of varying fidelity and complexity that can support all phases of the design of wind turbine and power plants with sufficient fidelity at reasonable computation cost</i>
-------------------------------	--

Answers to these questions do not provide exhaustive coverage of the question of wind energy efficiency. Important questions concerning the detailed design of wind turbines or wind farms were left aside. The author hopes, however, that the questions addressed in this thesis help identify new aerodynamic opportunities for advancing the efficiency of wind energy conversion.

1.5. THESIS STRUCTURE

The thesis addresses each research question in a dedicated part. Parts comprise several chapters, start with an opening note, and end with a closing note. Part I corresponds to this introduction.

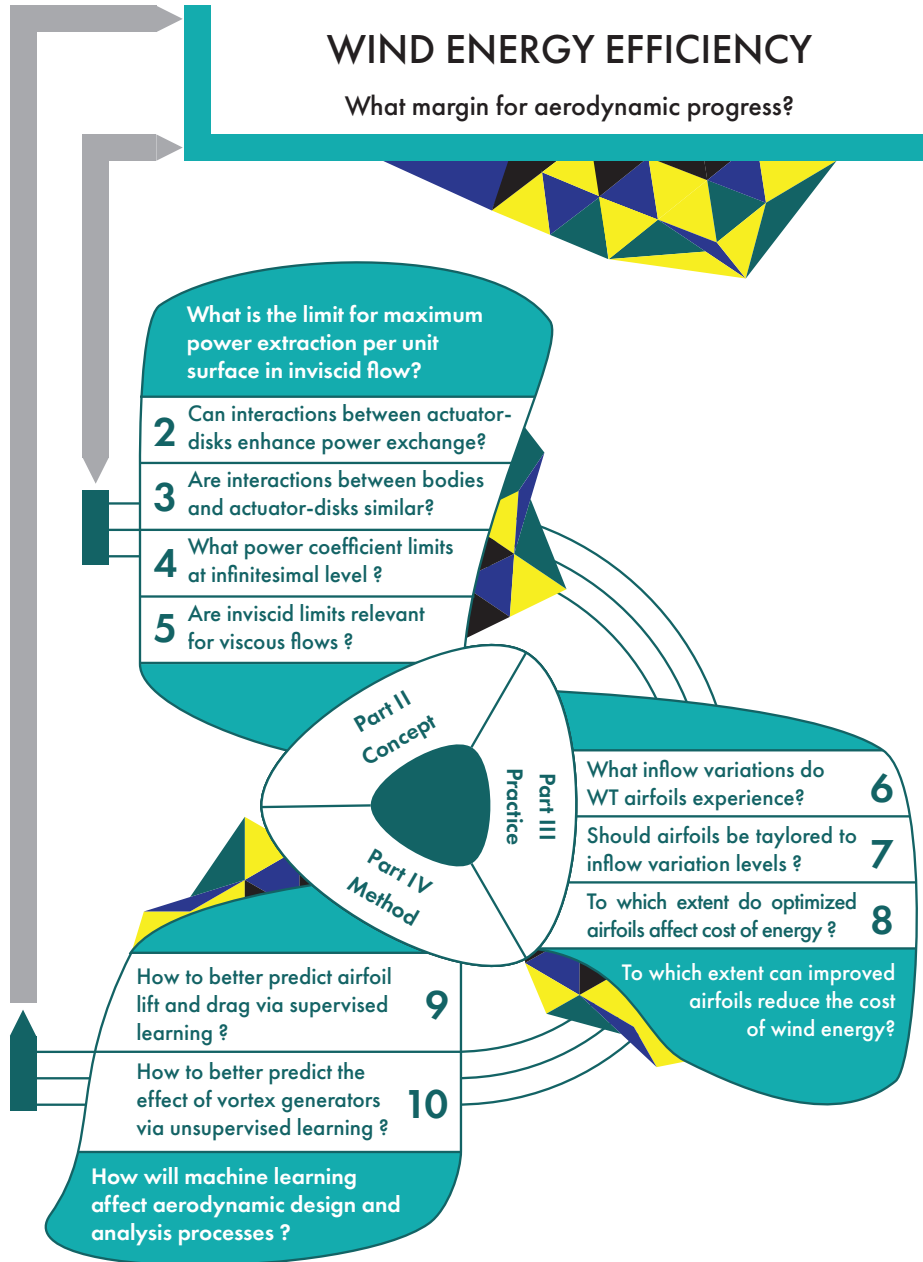
Part II adopts a macroscopic perspective on the physical processes of wind energy conversion. It focuses on scalar optimality and seeks to determine a theoretical upper bound for the power coefficient of wind energy conversion. Chapter 2 questions the applicability of the Betz-Joukowsky limit to abstract setups where flow crosses more than one energy extraction surface. The inquiry is mostly analytical, but it is relevant because wind farms consist of several wind turbines that may operate in each other's wake. It points to opportunities for augmenting flow across energy extraction surfaces by exploiting interactions between rotor wakes. Chapter 3 moves on to study the flow augmentation effect of wind turbine shrouds. The investigation builds on established analytical approaches but challenges previous design guidelines about the selection of optimal thrust coefficients. Chapters 2 and 3 highlight shortcomings in the Betz-Joukowsky framework of power coefficient limits. So chapter 4 attempts to tackle these issues with a new analytical treatment. The part concludes by telling whether disruptive increases in the surface density of wind energy conversion may be physically possible.

Part III focuses on intermediate flow scales and targets the design of wind turbine airfoils and blade planforms. It adopts a multi-objective interpretation of efficiency to connect airfoil design with rotor design. Chapter 6 characterizes the environment in which wind turbine airfoils operate by deriving a semi-analytical probability distribution for angle-of-attack perturbations. Doing so highlights that static loads in average

flow conditions differ from average blade section loads. Chapter 7 assesses the implications of this observation on airfoil design with multi-objective optimization techniques. Airfoil designs are ranked according to their efficiency: the ability to strike non-inferior compromises between conflicting design goals. Compromises between glide ratio in clean and soiled conditions are assessed for different levels of inflow fluctuations, and aerodynamic damping demands are also considered. Chapter 8 uses airfoils designed in chapter 7 to quantify the impact of airfoil choice on rotor efficiency. Efficiency is interpreted in a multi-objective sense again: improvements appear as shifts in the compromise between rotor loads and power coefficient. Finally, approximate cost indifference curves are drawn over Pareto fronts of non-inferior rotor designs to identify optimal compromises. The part concludes by discussing the margin for reducing the cost of wind energy through airfoil and rotor planform optimization.

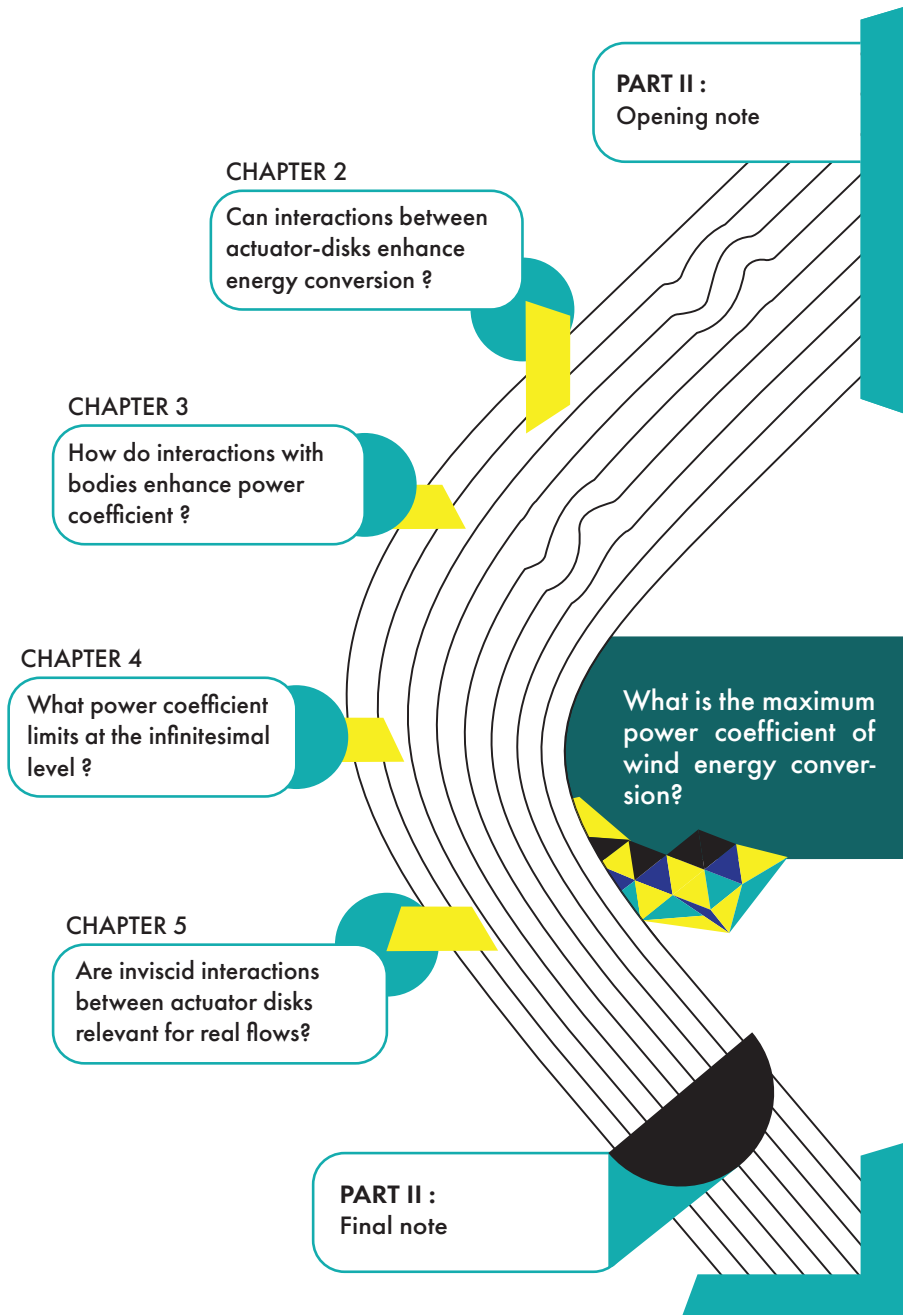
Part IV zooms into finer flow scales to discuss the prediction of turbulent phenomena. Imperfect turbulence models hinder the design of optimal aerodynamic designs by limiting the accuracy of flow predictions. We contend that machine-learning offers new opportunities for addressing these issues. Chapter 9 uses supervised learning to infer new closure relations for turbulent boundary layers. The goal is to improve the prediction of airfoil polar curves to facilitate the design of optimized airfoils. Chapter 10 combines asymptotic expansions with unsupervised learning to better predict the effect of vortex generators. Vortex generators are ubiquitous on wind turbine blades but their effect on airfoil loads remains hard to predict. Better prediction of forced-mixing by vortex generators is expected to lead to better designs. As a whole, part IV of this thesis helps clarify how machine learning might enhance turbulence models, and thereby enhance the efficiency of aerodynamic design procedures used in wind energy.

Part V discusses the main findings of the thesis and discusses their for industry and society as a whole. Recommendations for future research are also provided.



II

MAXIMUM POWER COEFFICIENT



OPENING NOTE

Maximum power coefficient in inviscid flow

Aerodynamicists often think about the efficiency of wind energy in terms of power coefficient: the ratio between extracted power and the flux of energy across the system surface in an unperturbed flow. This scalar quantity is meaningful because it confronts the useful output of rotors (power) with a representation of efforts put into their construction (via size). The representation is imperfect, however, because rotors of the same size can originate different loads and manufacturing costs.

Design of wind energy systems considers several goals and power coefficient is only one of them. Considerations about material use, system robustness and ease of maintenance go a long way in reducing annualized cost of wind energy. Modern wind turbines, for example, are designed to strike sensible compromises between rotor power and bending loads instead of maximizing power coefficient. Even so, insight about the maximum achievable power coefficient is important because it forges the collective imaginary. It serves as a compass for what wind energy can potentially achieve.

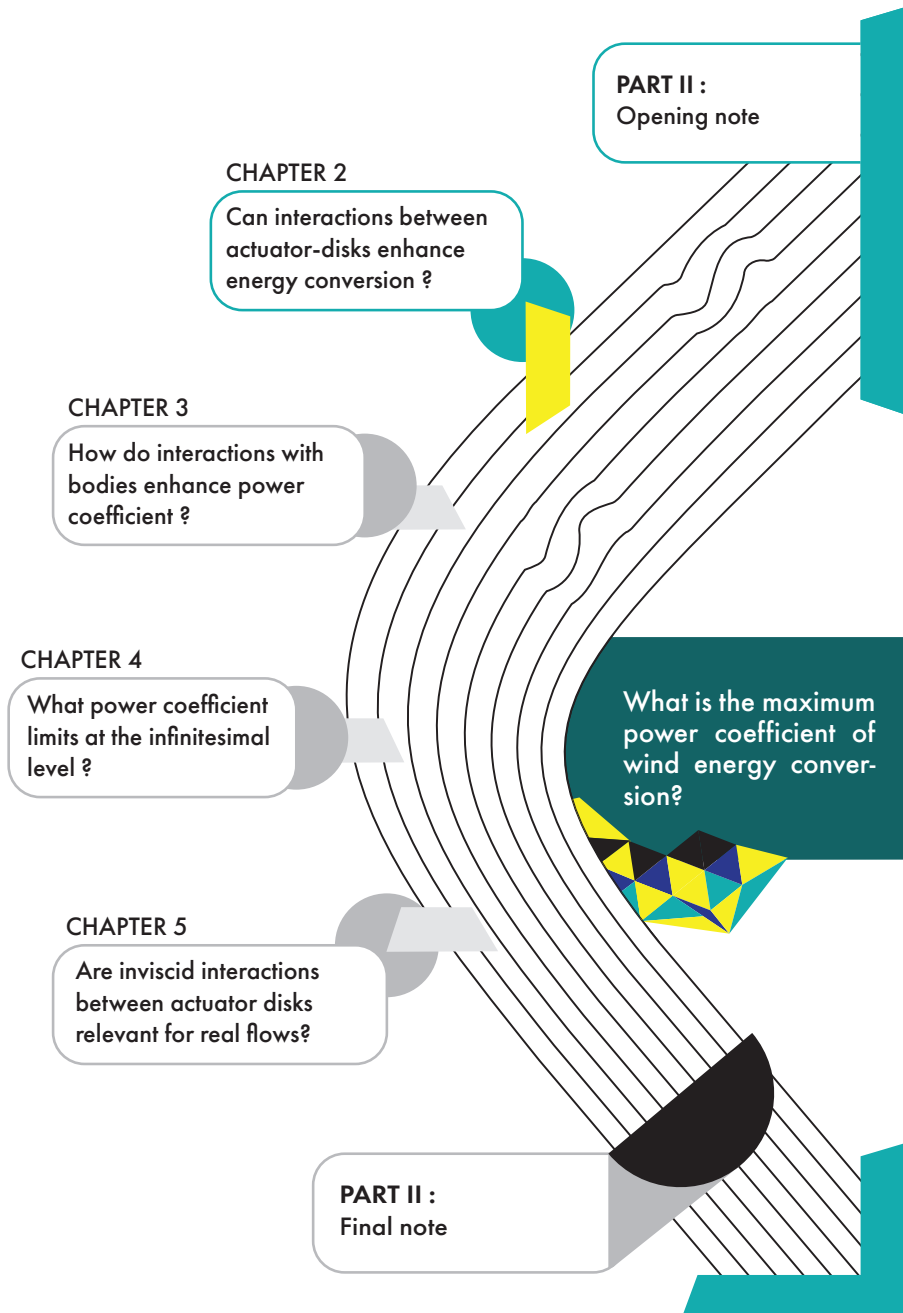
Consensus on the maximum power coefficient of isolated rotors is about a hundred years old. Betz and Joukowski used actuator disk analogies to determine the maximum power coefficient of a constant loading actuator disk operated in inviscid flow. They found a maximum power coefficient of $16/27$, for an optimal thrust coefficient of $8/9$, by searching for the extremes of an exact power coefficient law.

Two schools of thought co-existed since the Betz-Joukowski limit became widely publicized. One approach attempted to explain disparities between the performance of actual wind turbines and actuator disk predictions. It focused on non-idealities and originated important developments like blade-element-momentum (BEM) theory, detailed vortex models and actuator-disk corrections. The other, sought alternative configurations that would lead to enhanced power conversion. It originated several innovations that did not materialize into commercially viable systems yet – like vertical axis (VAWT)

and diffuser augmented (DAWT) wind turbines. Betz himself contributed to both approaches (Betz, 1919, 1929b).

Through which mechanisms can higher power coefficients be achieved? This part of the thesis seeks to address these questions with actuator-disk analogies. Most recent analytical work about actuator-disks includes the effect of wake rotation (Van Kuik et al., 2014; Sorensen, 2016; Jamieson et al., 2018) but this thesis took a different path: the entire study is restricted to pure axial-loading scenarios. It was hoped that the simplicity of axial-loading systems might permit bolder steps while maintaining a level of formal exactitude compatible with the requirements of mathematical proof.

Part II of this thesis consists in four chapters. Chapter 2 exploits interactions between actuator-disks in ideal flow conditions to identify an active flow augmentation mechanism. Chapter 5 contrasts that mechanism with the passive flow augmentation mechanism of shrouding bodies. Chapter 5 introduces three formal lemmas that help in establishing power coefficient limits for complex flow configurations. Chapter 5 discusses the feasibility of active flow augmentation and outlines strategies for applying ideal flow insight to non-conservative flows. The main findings are summarized in a closing note that also discusses possible design opportunities.



2

EXPLOITING WAKE INTERACTIONS IN IDEAL FLOW

*Interactions between rotor wakes are generally perceived as an hindrance to wind energy conversion. Is this perception legitimate? Can it be reversed?*¹

INTRODUCTION

What happens when a wind turbine operates behind a fan? The question may sound absurd because aerodynamic theories of wind energy focused on isolated machines for more than a century. [Betz \(1920\)](#) and [Joukowsky \(1920\)](#) defined the optimal wind turbine as an isolated actuator-disk operating in inviscid incompressible flow ([Okulov and Van Kuik, 2012](#)). Subsequent discussions about achievable power coefficient seemed forever limited to tip-speed ratio paradoxes ([Mikkelsen et al., 2014](#); [Wood, 2015](#); [Van Kuik, 2017](#)) and interactions with bodies ([De Vries, 1979](#); [Van Bussel, 2007](#); [Bontempo and Manna, 2016](#)). Research about rotor-aerodynamics therefore focused on the nonidealities of practical rotors ([Wilson and Lissaman, 1974](#); [Snel and Van Holten, 1995](#); [Burton et al., 2002](#); [Sorensen, 2016](#)): finite number of blades ([Goldstein, 1929](#); [Theodorsen, 1948](#)), inhomogeneous loading ([Betz, 1919](#); [Glauert, 1935](#); [Coleman et al., 1945](#)), and misaligned ([Glauert, 1926b, 1948](#)) or dynamic ([Van Bussel, 1992](#); [Sorensen and Myken, 1992](#)) inflow.

¹*Parts of this chapter are being submitted to the Proceedings of the Royal Society A: Physical Sciences with co-authors G. de Oliveira, R.B. Pereira, W.A. Timmer and G. van Bussel under the title "Role of wake interactions in optimal conversion of wind energy".*

Interactions between rotors appeared as a supplementary departure from ideality during the construction of the first wind farms (Lissaman, 1979; Jensen, 1983). Wind turbines operating behind each other face irregular inflow (Madsen et al., 2005; Meyers and Meneveau, 2013; Astolfi et al., 2018), increased transient loads (Volund, 1992; Thomsen and Sorensen, 1999; Astolfi et al., 2018) and reduced power output (Mosetti et al., 1994; Machielse et al., 2007). Several approaches are being developed to mitigate rotor shadow effects. A first approach seeks to determine wind farm layouts that minimise rotor-wake interactions (Rethore et al., 2013; Stanley et al., 2017) while maintaining acceptable grid connection costs (Marden et al., 2012; Wu and Porte-Agel, 2013). A second approach intervenes on wake generation and development processes: by deflecting trajectories (Vollmer et al., 2016; Bastankhah and Porte-Agel, 2017; Quick et al., 2017), enhancing mixing (Tobin and Chamorro, 2017; Lee et al., 2018), or weakening initial strength (Corten and Schaak, 2003; Corten et al., 2004). These approaches are not contradictory and it is increasingly stressed that wind turbine siting and control strategies should be determined together (Goit and Meyers, 2015; Gebraad et al., 2016).

The quest for aerodynamic optimality is shifting from the wind turbine to the array level (Acero et al., 2014; Stanley et al., 2017; Padron et al., 2018). Optimization algorithms are increasingly used to maximise the efficiency of wind turbine arrays (Rethore et al., 2013; Quick et al., 2016; King et al., 2017) but conceptual insight about system optimality remains sparse (Gebraad et al., 2016; Quick et al., 2017; van den Boz and Sande, 2017). One of the strongest conceptual results was presented by Meyers and Meneveau (2012): they considered the effect of atmospheric boundary layer (ABL) turbulence on the optimal spacing of an infinite row of wind turbines. This result was powerful because it described the maximum aerodynamic efficiency of multi-rotor setups in terms of viscous and turbulent flow phenomena. Can similar criteria be established within the ideal flow framework? How should multiple actuator-disks be trimmed to maximise extraction of energy from steady flows of inviscid fluids?

We answer these questions by studying a conceptual setup that comprises two actuator-disks and a free-stream. Actuators are placed behind each other and sized to share the same streamtube while the distance between them is varied. The study is mostly analytical and setup details are described in section 2.1. Section 2.2 focuses on the asymptotic case in which the two actuator-disks are infinitely far apart. The main result is an analytical description of the power coefficient. Section 2.3 studies matched-actuator setups whose actuators are separated by a finite distance. This serves as a consistency check for the results of section 2.2, and a way to better understand the implications of the present work. Conclusions regarding the optimality of energy exchanges in ideal flow are presented in section 2.4.

2.1. MATCHED-ACTUATOR SETUP

This article focuses on a peculiar setup consisting of two actuator-disks that operate behind each other in a steady and homogeneous free-stream. Actuator disks are an idealized representation of rotors: we treat them as flat surfaces that exert forces on the flow in a direction normal to the actuation surface. Furthermore, actuators can have different loadings but actuation forces per unit area (f_1, f_2) are chosen to be constant over each disk. The peculiarity of the setup lies in the choice of actuator sizes: the size

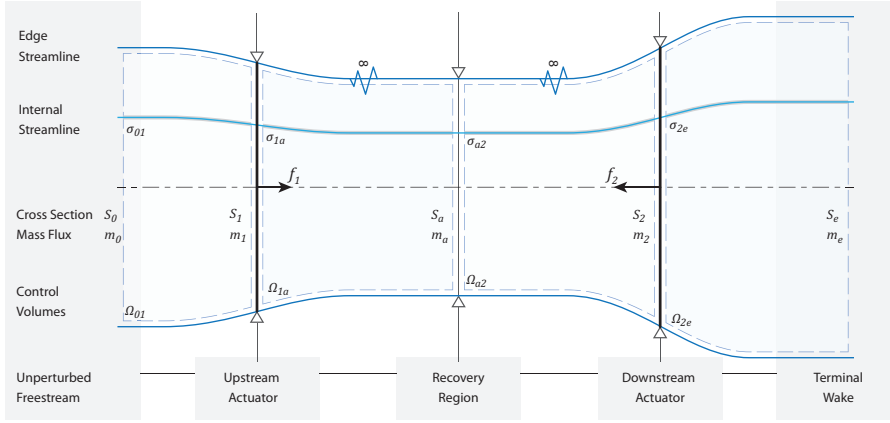


Figure 2.1: Matched-actuator setup with notation.

of the upstream actuator is always chosen such that its slipstream covers exactly all the downstream actuator.

The two actuators always span the same streamtube, and that is why the arrangement is designated as a matched-actuator setup. A comparable setup was also proposed independently and around the same time by [Overbeek \(2015\)](#). Figure 2.1 illustrates the construction, sketched for the particular case of an upstream actuator that injects energy (fan mode) and a downstream actuator that extracts energy (wind turbine mode). It should be noted, however, that all analytical manipulations presented in this chapter apply to arbitrary loading combinations in planar ($n = 2$) and axisymmetric ($n = 3$) spaces.

2.1.1. FLOW ANALYSIS FRAMEWORK

The flow is studied from the perspective of inviscid incompressible fluids that move along time-invariant paths. Mass and momentum conservation are then completely described by the steady variant of the incompressible Euler equations ([Euler, 1757](#); [Batchelor, 1967](#)):

$$(\mathbf{U}\nabla)\mathbf{U} = -\frac{1}{\rho}\nabla p + \frac{1}{\rho}\mathbf{f} \quad , \quad \rho\nabla\cdot\mathbf{U} = 0 \quad (2.1)$$

Energy conservation is implicit in equation 2.1 and the total-enthalpy equation makes it explicit through the theorem of Crocco [Greitzer et al. \(2004\)](#).

$$\nabla h^t - \mathbf{U} \times \boldsymbol{\omega} = \frac{1}{\rho}\mathbf{f} \quad , \quad \begin{cases} \boldsymbol{\omega} = \nabla \times \mathbf{U} \\ h^t = h + \frac{1}{2}(\mathbf{U} \cdot \mathbf{U}) \\ h = \varepsilon + \frac{p}{\rho} \end{cases} \quad (2.2)$$

Specific internal energy (ε) and density (ρ) are considered constant, in which case static pressure (p) and enthalpy (h) are linearly correlated. Static enthalpy is associated with

potential energy, whereas total enthalpy (h^t) represents total energy content per unit mass (Greitzer et al., 2004). Mass, momentum and energy conservation statements will be obtained by integrating the above equations over suitable sets.

2.1.2. MATCHED MASS-FLUX

The main design choice of matched-actuator setups consists in demanding that the two actuator-disks span the same streamtube. This is equivalent to requiring that they share the same mass-flux, which translates into a formal statement by integrating the continuity equation over a suitable control volume:

$$0 = \int \rho \nabla \cdot \mathbf{U} d(\Omega_{1a} \cup \Omega_{a2}) \quad \Leftrightarrow \quad \dot{m}_1 - \dot{m}_2 = 0 \quad (2.3)$$

$$\begin{aligned} \dot{m}_1 &= \rho U_1 S_1 & S_1 &= \int d\phi_1 & U_1 &= \frac{1}{S_1} \int \mathbf{U} \cdot \mathbf{n} d\phi_1 \\ \dot{m}_2 &= \rho U_2 S_2 & S_2 &= \int d\phi_2 & U_2 &= \frac{1}{S_2} \int \mathbf{U} \cdot \mathbf{n} d\phi_2 \end{aligned}$$

Sets Ω_{1a} and Ω_{a2} are depicted on figure 2.1 and defined formally in appendix A.1, which also clarifies smoothness assumptions. Expression 2.3 can be reworked to relate actuator-disk areas (S_1, S_2) with averaged normal flow velocities (U_1, U_2) across their surfaces (ϕ_1, ϕ_2):

$$\dot{m} = \rho S_1 U_1 = \rho S_2 U_2 \quad \Rightarrow \quad \frac{S_1}{S_2} = \frac{U_2}{U_1} \quad (2.4)$$

Similar relations hold for the area of streamtube cross-sections in the unperturbed free-stream (S_0), recovery region (S_a) and terminal wake (S_e).

$$\left. \begin{aligned} \int \rho \nabla \cdot \mathbf{U} d\Omega_{a2} &= \dot{m}_a - \dot{m}_2 = 0 \\ \int \rho \nabla \cdot \mathbf{U} d\Omega_{2e} &= \dot{m}_2 - \dot{m}_e = 0 \end{aligned} \right\} \Rightarrow \rho S_a U_a = \rho S_2 U_2 = \rho S_e U_e$$

$$\left. \begin{aligned} \int \rho \nabla \cdot \mathbf{U} d\Omega_{01} &= \dot{m}_0 - \dot{m}_1 = 0 \\ \int \rho \nabla \cdot \mathbf{U} d\Omega_{1a} &= \dot{m}_1 - \dot{m}_0 = 0 \end{aligned} \right\} \Rightarrow \rho S_0 U_0 = \rho S_1 U_1 = \rho S_a U_a$$

2.2. INFINITE DISTANCE BETWEEN ACTUATORS

Matched actuator setups with asymptotically distant actuator-disks can be studied with simple tools comparable to those of the Betz (1920), Froude (1889) and Rankine (1865) deductions. Let us then denote the separation between actuator-disks as D_x and focus on the asymptotic limit:

$$D_x \rightarrow \infty$$

This configuration is analytically tractable because wakes cannot sustain static pressure differences across themselves. It follows that, in the absence of swirl and unsteady phenomena, wakes develop into configurations that induce no static enthalpy perturbations of the far-field. The static enthalpy of the recovery region must therefore approach free-stream values when the distance between actuators tends to zero. This occurs because the wake of the upstream actuator can develop completely before it reaches the downstream actuator.

$$D_x \rightarrow \infty \quad \Rightarrow \quad \left\{ \begin{array}{l} p_a \rightarrow p_0 \\ p_e \rightarrow p_0 \end{array} \right. \quad \Rightarrow \quad \left\{ \begin{array}{l} h_a \rightarrow h_0 \\ h_e \rightarrow h_0 \end{array} \right. \quad (2.5)$$

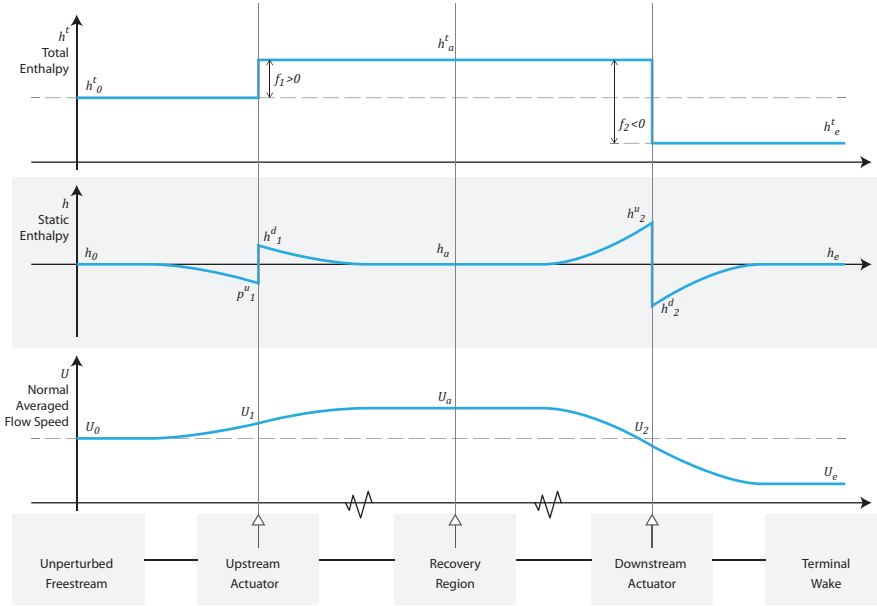


Figure 2.2: Stylised enthalpy paths across matched-actuator setup with asymptotically distant actuators. Actuator loadings ($f_1 > 0, f_2 < 0$) are compatible with the depiction of figure 2.1 in qualitative terms.

The static enthalpy of final wake tends to free-stream independently of the distance between actuators as long as swirl and unsteady breakdown are absent. Figure 2.2 sketches a qualitative overview of total and static enthalpy paths for the case in which D_x tends to infinity.

2.2.1. DIMENSIONAL MODEL

A closed algebraic model for the performance of asymptotic matched-actuator setups is now deduced. The procedure is relatively simple and starts by integrating momentum (2.1) and energy (2.2) conservation statements separately for each actuator. Streamlines and control volumes are then connected to obtain exact expressions for the power exchange of the entire setup.

DOWNSTREAM ACTUATOR

Momentum conservation across the downstream actuator is expressed by integrating the Euler equations (2.1) over the union of two control volumes $\Omega_{ae} = (\Omega_{a2} \cup \Omega_{2e})$:

$$\int \rho (\mathbf{U}\nabla) \mathbf{U} d\Omega_{ae} = - \int \rho \nabla h d\Omega_{ae} + \int \mathbf{f} d\Omega_{ae} \tag{2.6}$$

In the absence of external bodies and conservative-force interactions, the action-reaction principle imposes that the static enthalpy integral vanishes **de Oliveira et al. (2016)**.

$$\left. \begin{array}{l} h_a \rightarrow h_0 \\ h_e \rightarrow h_0 \end{array} \right\} \Rightarrow h_a \rightarrow h_e \Rightarrow \int \nabla h d\Omega_{ae} = 0$$

Reworking the integrals of equation 2.6 then leads to a closed expression for the total force of the downstream actuator, denoted as $F_2^{(q)}$.

$$\Leftrightarrow F_2^{(q)} = f_2 S_2 = \rho S_2 U_2 (U_e - U_a) \quad (2.7)$$

On the other hand, the downstream actuator loading (f_2) is proportional to the enthalpy jump that it imposes on the flow. Formally, this is shown by integrating Crocco's equation (2.2) along a streamline $\sigma_{ae} = (\sigma_{a2} \cup \sigma_{2e})$:

$$\Leftrightarrow \begin{array}{l} \int_{\sigma_{ae}} \mathbf{f} \cdot \mathbf{r} d\sigma_{ae} = \rho \int (\nabla h^t - \mathbf{U} \times \boldsymbol{\omega}) \cdot \mathbf{r} d\sigma_{ae} \\ f_2 = \rho (h_e^t - h_a^t) \end{array} \quad (2.8)$$

The force of the downstream actuator $F_2^{(h)}$ can therefore be written anew by multiplying equation 2.8 with the actuator area, expanding total enthalpies — into dynamic and static components — and inserting the limit of expression 2.5.

$$\Leftrightarrow F_2^{(h)} = f_2 S_2 = \rho S_2 \left(\frac{U_a + U_e}{2} \right) (U_e - U_a) \quad (2.9)$$

Simultaneous enforcement of momentum and energy conservation requires consistency between the two descriptions of actuator force ($F_2^{(q)}$ and $F_2^{(h)}$). Expressions 2.7 and 2.9 are therefore matched:

$$\Leftrightarrow \begin{array}{l} F_2^{(q)} \equiv F_2^{(h)} \\ \rho S_2 U_2 (U_e - U_a) = \rho S_2 \left(\frac{U_a + U_e}{2} \right) (U_e - U_a) \end{array} \quad (2.10)$$

Reworking expression 2.10 shows that the mean normal speed over the downstream actuator corresponds to the average of inlet and outlet mean normal velocities:

$$\Leftrightarrow U_2 = \frac{U_a + U_e}{2} \quad (2.11)$$

Finally, the rate of energy exchange across the downstream actuator corresponds to the balance of total-enthalpy fluxes. It is written from the flow perspective:

$$\begin{array}{l} P_2 = \dot{m}_2 (h_e^t - h_a^t) \\ = \frac{1}{2} \rho S_2 U_2 (U_e^2 - U_a^2) + \rho S_2 U_2 (h_e - h_a) \end{array}$$

Applying the limit of expression 2.5 and inserting expression 2.11 leads to a compact statement for the power of the downstream actuator:

$$P_2 = \frac{1}{4} \rho S_2 (U_a + U_e) (U_e^2 - U_a^2) \quad (2.12)$$

UPSTREAM ACTUATOR

Momentum conservation across the upstream actuator is stated by integrating the Euler equations (2.1) over a control volume ($\Omega_{0a} = \Omega_{01} \cup \Omega_{1a}$), just like for the downstream actuator. Again, the static enthalpy term can be neglected thanks to the absence of conservative-force interactions (per expression 2.5). The result is an algebraic expression for the total force of the upstream actuator $F_1^{(q)}$.

$$\Leftrightarrow \quad \begin{aligned} \int \mathbf{f} \, d\Omega_{0a} &= \int \rho (\mathbf{U}\nabla) \mathbf{U} \, d\Omega_{0a} + \int \rho \nabla h \, d\Omega_{0a} \\ F_1^{(q)} = f_1 S_1 &= \rho S_1 U_1 (U_a - U_0) \end{aligned} \quad (2.13)$$

The energy balance is obtained by integrating Crocco's equation along a streamline segment $\sigma_{0a} = \sigma_{01} \cup \sigma_{1a}$, multiplying the result with the actuator area, and simplifying everything with the asymptotic limit of expression 2.5:

$$\begin{aligned} F_1^{(h)} = f_1 S_1 &= \frac{1}{2} \rho S_1 (U_a^2 - U_0^2) \\ &= \rho S_1 \left(\frac{U_a + U_0}{2} \right) (U_a - U_0) \end{aligned} \quad (2.14)$$

Momentum and energy conservation are made consistent by matching expression 2.13 with expression 2.14, and that determines the average normal speed over the upstream actuator :

$$F_1^{(q)} \equiv F_1^{(h)} \quad \Leftrightarrow \quad U_1 = \frac{U_a + U_0}{2} \quad (2.15)$$

Power exchange between the flow and the upstream actuator is written in terms of total-enthalpy fluxes, and simplified using the limit of expression 2.5:

$$\begin{aligned} P_1 &= \dot{m}_1 (h_a^t - h_0^t) \\ &= \frac{1}{2} \dot{m}_1 (U_a^2 - U_0^2) \end{aligned}$$

The mass-flux of the upstream actuator is then matched with that of the downstream actuator to prepare the treatment of the combined system:

$$\dot{m}_1 = \dot{m}_2 \quad \Rightarrow \quad P_1 = \frac{1}{2} \dot{m}_2 (U_a^2 - U_0^2) \quad (2.16)$$

Inserting expression (2.11) into (2.16) leads to a statement for the power of the upstream actuator:

$$\begin{aligned} P_1 &= \frac{1}{2} \rho U_2 S_2 (U_a^2 - U_0^2) \\ &= \frac{1}{4} \rho S_2 (U_a + U_e) (U_a^2 - U_0^2) \end{aligned} \quad (2.17)$$

COMPLETE SETUP

The net power of the complete asymptotic setup is stated by summing the contributions of each actuator:

$$\begin{aligned} P &= P_1 + P_2 \\ &= \frac{1}{4} \rho S_2 \underbrace{(U_a + U_e) (U_a^2 - U_0^2)}_{\text{Upstream}} + \frac{1}{4} \rho S_2 \underbrace{(U_a + U_e) (U_e^2 - U_a^2)}_{\text{Downstream}} \end{aligned} \quad (2.18)$$

2.2.2. NON-DIMENSIONAL MODEL

Raw power exchange does not tell much about system performance. Deeper insight requires that equations 2.7-2.18 be restated in terms of non-dimensional parameters to enable the definition of a meaningful power coefficient for matched-actuator setups.

NON-DIMENSIONAL PARAMETERS

The design space of matched-actuator setups with asymptotically distant actuators can be represented with diverse pairs of non-dimensional groups. We chose to use the relative induction factor (a_2) and intermediate speed ratio (b) defined below:

- a_2 describes the loading of the downstream actuator:

$$a_2 : U_2 = (1 - a_2) U_a \quad \Rightarrow \quad \frac{U_2}{U_a} = (1 - a_2) \quad \Leftrightarrow \quad a_2 = 1 - \frac{U_2}{U_a} \quad (2.19)$$

- b relates the mean flow speed in the recovery region with the free-stream:

$$b = \frac{U_a}{U_0} \quad \Rightarrow \quad U_a = b U_0 \quad (2.20)$$

Steady flow assumptions are incompatible with flow reversal and that restricts model validity to a certain range of non-dimensional parameters. Restrictions on the relative induction factor (a_2) are identical to those of classical induction factors (Betz, 1920; Glauert, 1948; Sorensen, 2016):

$$\frac{1}{2} > \begin{cases} a_2 > 0 & \text{downstream actuator extracts energy (decelerate flow)} \\ a_2 = 0 & \text{no downstream actuator} \\ a_2 < 0 & \text{downstream actuator injects energy (accelerate flow)} \end{cases} \quad (2.21)$$

The intermediate speed ratio (b), however, must be strictly positive. It sets the type and strength of the upstream actuation module:

$$0 < \begin{cases} b < 1 & \text{upstream actuator extracts energy (decelerate flow)} \\ b = 1 & \text{no upstream actuator} \\ b > 1 & \text{upstream actuator injects energy (accelerate flow)} \end{cases} \quad (2.22)$$

Mean normal velocities over the actuators and wake can be rewritten in terms of the non-dimensional parameters (a_2, b) and the free-stream :

$$\frac{U_1}{U_0} = \frac{1}{2}(b+1) \quad , \quad \frac{U_2}{U_0} = b(1 - a_2) \quad , \quad \frac{U_e}{U_0} = b(1 - 2a_2) \quad (2.23)$$

All dimensional expressions applicable to matched-actuator setups with infinitely distant actuators, (2.6) to (2.18), can be reworked into equivalent non-dimensional forms using expressions (2.19) to (2.23). Appendix B.1 reports intermediate steps and presents expressions for non-dimensional actuator loadings.

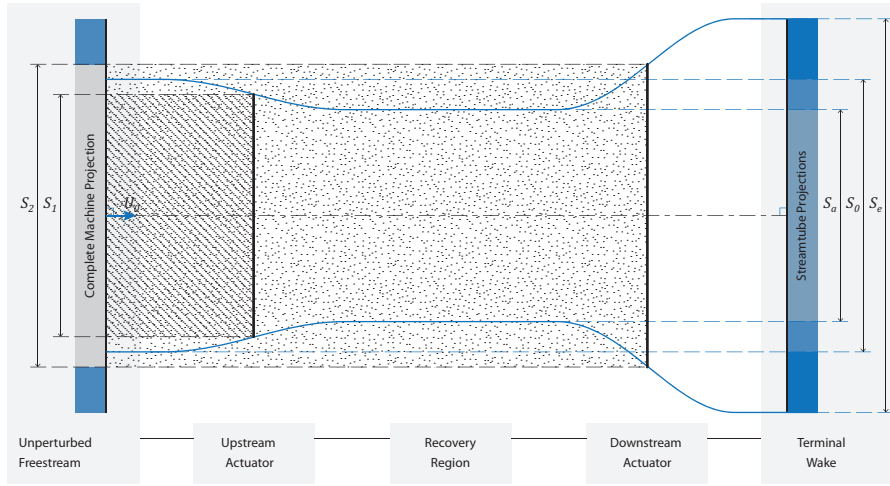


Figure 2.3: Surface projections onto the free-stream normal plane.

REFERENCE AREA

The formulation of a meaningful power coefficient depends on the selection of a consensual reference area (S_{ref}). The area of the setup projection onto a plane normal to the unperturbed free-stream is an unambiguous choice. It corresponds to the area of the largest actuator, as shown on figure 2.3:

$$S_{ref} = \max\{S_1, S_2\} \quad \Rightarrow \quad S_{ref} = \begin{cases} S_1 & S_1 > S_2 \\ S_2 & S_1 \leq S_2 \end{cases}$$

The actuators share a common mass flow and span the same streamtube. The ratio between their areas is therefore fixed by expression 2.4, which can be rewritten in non-dimensional terms through expression 2.23:

$$\frac{S_1}{S_2} = \frac{U_2}{U_1} = \frac{b(1-a_2)}{\frac{1}{2}(b+1)} \quad (2.24)$$

Transforming expression 2.24 into an inequality 2.25 shows what it takes for the upstream actuator (S_2) to be smaller than the downstream (S_1) actuator:

$$\begin{aligned} S_1 < S_2 &\Leftrightarrow b(1-a_2) < \frac{1}{2}(b+1) \\ \Leftrightarrow 2b(1-a_2) - b < 1 &\Leftrightarrow b(1-2a_2) < 1 \end{aligned} \quad (2.25)$$

Reworking inequality 2.25 with expression 2.23 makes it clear that the upstream actuator is smaller than the downstream actuator when the final wake flows slower than the free-stream.

$$S_1 < S_2 \quad \Leftrightarrow \quad \frac{U_e}{U_0} < 1 \quad \Rightarrow \quad S_{ref} = S_2 \quad (2.26)$$

Condition 2.26 is fulfilled whenever the setup extracts a net amount of energy from the flow. The area of the downstream actuator (S_2) is a suitable reference (S_{ref}) for the

power coefficient of wind energy extraction with matched-actuator setups. The opposite choice ($S_{ref} = S_1$) would be appropriate for propulsion or ventilation applications.

2.2.3. POWER COEFFICIENT

The power coefficient relates the flux of kinetic energy crossing the reference area in an unperturbed free-stream with the rate of energy exchange between the matched actuator setup and the flow. It is a ratio:

$$C_P = \frac{P}{\frac{1}{2}\rho S_{ref} U_0^3} = \frac{P_1 + P_2}{\frac{1}{2}\rho S_2 U_0^3} \quad (2.27)$$

The contribution of the upstream actuator to power exchange is restated by inserting expressions 2.20 and 2.23 into expression 2.17:

$$\frac{P_1}{\frac{1}{2}\rho S_2 U_0^3} = \left(\frac{U_2}{U_0}\right) \left(\left(\frac{U_a}{U_0}\right)^2 - 1\right) = b(1 - a_2)(b^2 - 1) \quad (2.28)$$

For the downstream actuator, non-dimensionalized power is stated by reworking expression 2.12 with expressions 2.20 and 2.23:

$$\frac{P_2}{\frac{1}{2}\rho S_2 U_0^3} = 2 \left(\frac{U_2}{U_0}\right)^2 \left(\frac{U_e}{U_0} - \frac{U_a}{U_0}\right) = -b^3(4a_2)(1 - a_2)^2 \quad (2.29)$$

The contributions of each actuator, expressions 2.28 and 2.29, are inserted into expression 2.27 to write the power coefficient of the complete setup:

$$C_P = b(1 - a_2)(b^2 - 1) - b^3(4a_2)(1 - a_2)^2 \quad (2.30)$$

Negative power coefficients correspond to energy extraction because energy exchanges were stated from the flow perspective. Figure 2.4 illustrates the dependency of the power coefficient on relative induction factor a_2 and intermediate speed ratio b .

RELATION WITH BETZ LIMIT

The power coefficient law of expression 2.30 challenges aerodynamic common sense. It states that matched-actuator setups with asymptotically distant actuators can exceed the Betz-Joukowsky limit:

$$\exists a_2 < \frac{1}{2} \quad : \quad (-C_P) > (-C_P^{Betz}) = \frac{16}{27} \quad \forall b > 1$$

For that to happen, the upstream actuator must spend energy ($b > 1$) to accelerate the flow while the downstream actuator extracts energy ($a_2 > 0$) from a greater amount of fluid. Energy is transferred from the upstream to the downstream actuator without losses. This is possible because ideal flows are implicitly isentropic and (only) permit reversible energy exchanges Greitzer et al. (2004).

Expression 2.30 is an extension of previous work on single actuator machines and does not contradict established literature. If the upstream actuator exerts no forces

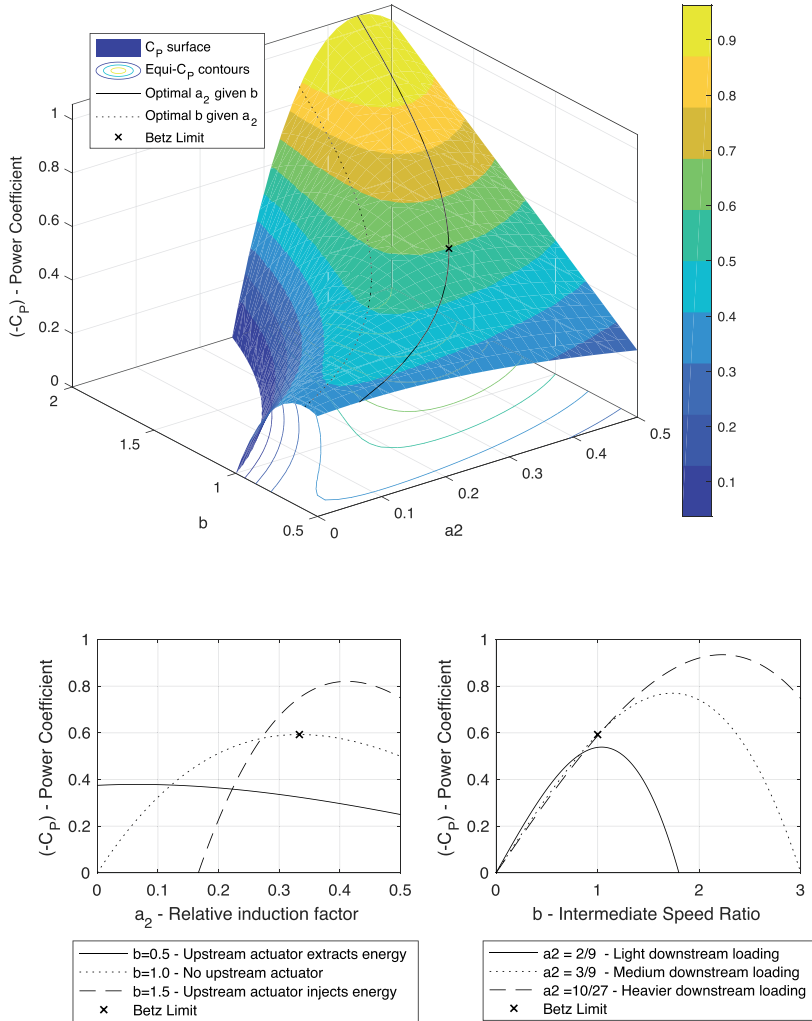


Figure 2.4: Power coefficient of matched-actuator setup with infinitely distant actuators illustrated as a surface (a) and as constant speed-ratio (b) or relative induction factor (c) cuts.

($b > 1$), expression (2.30) collapses into the usual power coefficient law of isolated actuators:

$$C_p|_{b=1} = -4a_2(1 - a_2)^2$$

Expression 2.30 is also consistent with isolated actuator models when the downstream actuator exerts no force, in which case the relative induction factor (a_2) is null. This is shown in appendix A.2.2, and compliance with conservation of energy is further verified in appendix A.2.3.

VALIDITY OF STEADY FLOW SOLUTIONS

If they occurred in the physical world, flows of inviscid incompressible fluids would be governed by the unsteady Euler equations. They would occasionally display chaotic behavior (Beale et al., 1984; Birkhoff, 1960) but expression 2.30 only applies to flows that obey steady solutions. It results from integration of the steady Euler equations (2.1) over a steady flow topology. Static boundary conditions are not sufficient to guarantee the absence of unsteadiness (Birkhoff, 1960), even if several flows with static boundary conditions are steady (Batchelor, 1967).

Heavily loaded rotors, for example, have conceptually static boundary conditions but shed chaotic wakes — the streamtube then ceases to be well defined and equations 2.3 to 2.30 loose validity. The phenomena was first identified by Glauert in the context of isolated rotors. He used the experimental data of Lock (Lock et al., 1926) to identify the thrust coefficient at which chaotic phenomena begin to dominate the wake (Glauert, 1926a; Lock, 1947), and described it as an upper threshold (a_{turb}) for the induction factor (a) of isolated rotors.

$$a < a_{turb} \approx 0.4 \quad \text{with} \quad a = 1 - \frac{U_{rotor}}{U_0} \quad (2.31)$$

Mechanistic arguments suggest that inequality 2.31 can be transposed to matched-actuator setups by matching the velocity discontinuity across wake edges (Rosenhead, 1931). This corresponds to imposing that wake velocities stay above the relative speed at which the wakes of isolated rotors change topology:

$$U_a > (1 - a_{turb})U_0 \quad , \quad U_e > (1 - a_{turb})U_0 \quad (2.32)$$

The inequalities of expression 2.32 can then be restated in terms of non-dimensional parameters using expression 2.23:

$$\begin{aligned} b &> (1 - 2a^{turb}) \\ b(1 - 2a_2) &> (1 - 2a^{turb}) \end{aligned} \quad (2.33)$$

Condition 2.33 is necessary, but probably insufficient, to ensure the stability of wakes of matched-actuator setups. These inequalities form approximate bounds for the validity of expression 2.33 and the underlying deduction. Even for isolated actuators, the value of the wake breakdown threshold (a_{turb}) is still debated (Buhl, 2005; Burton et al., 2002). Stability of flows across matched-actuators is an immensely complex matter that would require dedicated studies in its own right. The rest of this article focuses on matched-actuator setups that operate in steady flows.

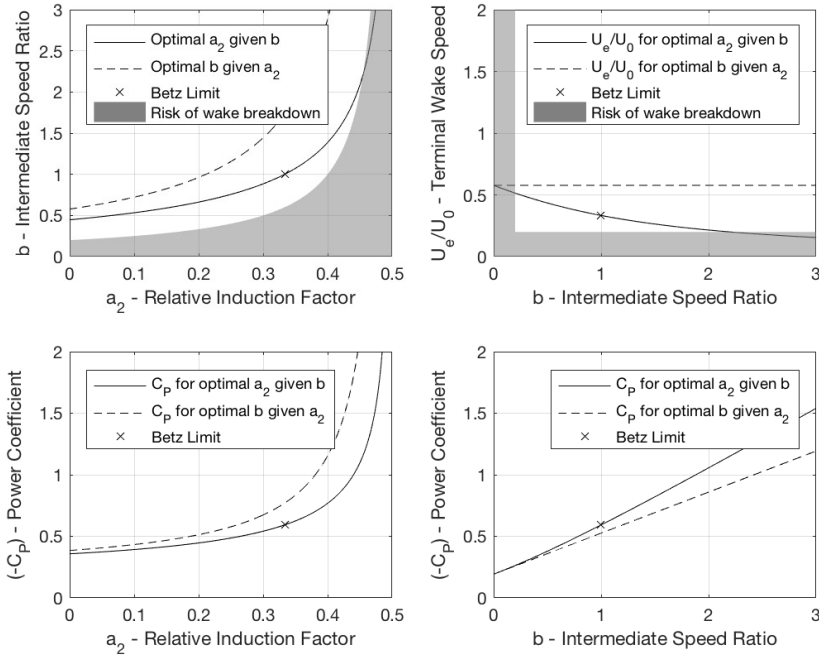


Figure 2.5: Optimal operation regimes of matched-actuator wind energy converters with infinitely distant actuators. Top: optimal trims (a) and corresponding final wake speed (b). Bottom: effect of relative induction factor (c) and intermediate speed ratio (d) on optimal power coefficient.

2.2.4. PERFORMANCE TRENDS

The power coefficient of matched-actuator setups with asymptotically distant actuators corresponds to a bivariate function a described by expression 2.30.

$$C_P : (a_2, b) \in D \rightarrow \mathbb{R}$$

Its inputs, relative induction factor (a_2) and intermediate speed ratio (b), belong to a domain $D \subset \mathbb{R}^2$ delineated by inequalities. Flow reversal must be avoided (2.21, 2.22), global loading should remain within reasonable limits (2.33) and the terminal wake should flow slower than than the free-stream (2.26).

$$D = \left\{ (a_2, b) \in \mathbb{R}^2 : \begin{array}{ll} a_2 < \frac{1}{2} & \wedge \quad 0 < (1 - 2a^{turb}) < b \\ b(1 - 2a_2) < 1 & \wedge \quad 0 < (1 - 2a^{turb}) < b(1 - 2a_2) \end{array} \right\} \quad (2.34)$$

Negative power coefficients correspond to removal of energy from the flow because expression 2.30 was defined from the flow perspective. Energy extraction is therefore maximised by minimising the power coefficient:

$$\min_{(a_2, b) \in D} C_P$$

As will soon become apparent, the power coefficient function is unbounded. It has no well defined minimum over its domain. Even so, constrained optima can be explored by prescribing a non-dimensional parameter, either b or a_2 , and optimising the other one accordingly.

OPTIMAL a_2 , GIVEN \tilde{b}

Let us prescribe an intermediate speed-ratio \tilde{b} , and look for the relative induction factor $a_2^{(\tilde{b})}$ that leads to optimal energy exchange under this constraint. The partial derivative of the power coefficient to the relative induction factor (a_2) is a quadratic polynomial:

$$\frac{\partial C_P}{\partial a_2} = -b(b^2 - 1) - 4b^3 \left(a_2 - \frac{1}{3} \right) (a_2 - 1)$$

It has two roots, but only one belongs to the design space ($D \subset R^2$) and corresponds to the optimal relative induction factor given \tilde{b} . It is denoted as $a_2^{(\tilde{b})}$:

$$a_2^{(\tilde{b})} : \frac{\partial C_P}{\partial a_2} = 0 \quad \Rightarrow \quad a_2^{(\tilde{b})} = \frac{2}{3} - \frac{1}{3} \sqrt{4 - 3 \left(\frac{5\tilde{b}^2 - 1}{4\tilde{b}^2} \right)}$$

When \tilde{b} is prescribed, the optimal loading of the downstream actuator increases when the upstream actuator injects more energy into the flow. The increase is so strong that the mean speed of the terminal wake decreases as \tilde{b} grows:

$$\left(\frac{U_e}{U_0} \right)^{(\tilde{b})} = \tilde{b} \left(1 - 2a_2^{(\tilde{b})} \right) = -\frac{1}{3} \left(\tilde{b} - \sqrt{\tilde{b}^2 + 3} \right)$$

There is a threshold beyond which optima cease to belong to the function domain, as illustrated on figure 2.5b).

$$\tilde{b} < \left((3(1 - 2a_{turb}) + 1)^2 - 1 \right)^{-\frac{1}{2}} \sqrt{3}$$

The power coefficient law of expression 2.30 is no longer valid for such high loading, so the interest of the above optimality regime is rather limited.

OPTIMAL b , GIVEN \tilde{a}_2

Let us instead prescribe a relative induction factor \tilde{a}_2 to look for the corresponding optimal speed-ratio $b^{(\tilde{a}_2)}$. The partial derivative of the power coefficient to the intermediate speed-ratio (b) is a quadratic polynomial in b :

$$\frac{\partial C_P}{\partial b} = (1 - a_2) (3(1 - 2a_2)^2 b^2 - 1)$$

It has a single positive root that corresponds to the optimal intermediate speedup ratio $b^{(\tilde{a}_2)}$ for a prescribed relative induction factor (\tilde{a}_2):

$$b^{(\tilde{a}_2)} : \frac{\partial C_P}{\partial b} = 0 \quad \Rightarrow \quad b^{(\tilde{a}_2)} = \frac{\sqrt{3}}{3(1 - 2\tilde{a}_2)} \quad (2.35)$$

The terminal wake speed (U_e/U_0) does not vary with the prescribed relative induction factor \tilde{a}_2 when b is set to the corresponding optima $b^{(\tilde{a}_2)}$.

$$\left(\frac{U_e}{U_0}\right)^{(\tilde{a}_2)} = b^{(\tilde{a}_2)} (1 - 2\tilde{a}_2) = \frac{\sqrt{3}}{3}, \quad \forall \tilde{a}_2 < \frac{1}{2}$$

Wake instabilities are therefore unlikely in this operation regime. Feeding the optimality condition (2.35) into the power coefficient expression (2.30) leads to surprising results:

$$C_P^{(\tilde{a}_2)} = -\frac{2\sqrt{3}}{9} \frac{(1 - \tilde{a}_2)}{(1 - 2\tilde{a}_2)}, \quad \forall \tilde{a}_2 < \frac{1}{2}$$

The optimal power coefficient tends to infinity as the prescribed induction factor approaches its maximum permissible value:

$$\lim_{\tilde{a}_2 \rightarrow \frac{1}{2}} C_P^{(\tilde{a}_2)} = -\infty \quad (2.36)$$

Even in this extreme condition, wake velocity is maintained because the increase in optimal speedup ratio $b^{(\tilde{a}_2)}$ offsets the increased loading of the downstream actuator. Appendix 5 elaborates on that observation.

$$\left. \begin{array}{l} \lim_{\tilde{a}_2 \rightarrow \frac{1}{2}} f_1^{(\tilde{a}_2)} = +\infty \\ \lim_{\tilde{a}_2 \rightarrow \frac{1}{2}} f_2^{(\tilde{a}_2)} = -\infty \end{array} \right\} \quad \text{but} \quad f_1^{(\tilde{a}_2)} + f_2^{(\tilde{a}_2)} = \frac{1}{2} \rho U_0^2 \left(\left(\frac{U_e}{U_0} \right)^{(\tilde{a}_2)} - 1 \right) \perp \tilde{a}_2$$

Expression 2.36 states that matched actuator setups with finite cross-section and infinite length can extract unbounded amounts of energy from steady flows of inviscid incompressible fluids. In these conditions, extraction of power from the free-stream is only constrained by the ability to generate arbitrarily large forces across actuation surfaces.

Of course, it would be absurd to think that unbounded power coefficients might be feasible in real flows. Viscous phenomena would diffuse and dissipate the wake of the upstream actuator even in superfluid Helium-2 (Kapitza (1938); Pitaevskii and Stringari (2016)). Compressible phenomena would induce thermal exchanges between the slipstream and the free-stream, in which case and the third law of thermodynamics would probably introduce additional constraints similar to a Carnot cycle (Greitzer et al. (2004)). Furthermore, it is probable that the wake of the upstream actuator would break into chaotic behavior as soon as the existence of time would be considered (Rosenhead (1931); Birkhoff (1960); Beale et al. (1984)). Such considerations fall outside the scope of this chapter, however, which is meant to study the performance of matched-actuator setups in conditions identical to those in which the Betz limit was derived: steady flows of inviscid incompressible fluids.

2.3. FINITE DISTANCE BETWEEN ACTUATORS

Matched-actuator setups with infinite inter-actuator distance can exceed the Betz power coefficient threshold. But constructing systems of infinite length is impossible. Are power coefficient trends similar when the distance between actuators is finite? This section seeks to answer with both analytical and numerical approaches. Objections to the practical feasibility of matched-actuator setups will be discussed in chapter 5.

2.3.1. VANISHING INTER-ACTUATOR DISTANCE

Matched-actuator setups can be studied with simple analytical tools when the distance between their actuators vanishes. We call this the complementary limit:

$$D_x \rightarrow 0 \quad (2.37)$$

Study of this configuration depends on the enforcement of appropriate smoothness assumptions, detailed in appendix A.1. Continuity dictates that the mean speed over the upstream actuator tends to that of the downstream actuator when the distance between actuators vanishes:

$$D_x \rightarrow 0 \quad \Rightarrow \quad \bar{U} \equiv U_1 \rightarrow U_2$$

The areas of the actuators then tend to the same value because of the matched mass-flux design choice, which had been formalised in expression 2.4.

$$\lim_{D_x \rightarrow 0} \frac{S_1}{S_2} = \lim_{U_1 \rightarrow U_2} \frac{U_2}{U_1} = 1 \quad \Rightarrow \quad \bar{S} \equiv S_1 \rightarrow S_2$$

Momentum balance across the complete setup is stated in terms of the force exerted by the two actuators, denoted as \bar{F} .

$$\bar{F} = F_1 + F_2 = \rho \bar{S} \bar{U} (U_e - U_0) \quad (2.38)$$

The energy balance leads to another expression for the total force (\bar{F}) that the actuators exert on the flow.

$$\bar{F} = (f_1 + f_2) \bar{S} = \rho \bar{S} \left(\frac{U_e + U_0}{2} \right) (U_e - U_0) \quad (2.39)$$

Matching equation 2.38 with equation 2.39 determines the mean normal speed across both actuators:

$$\bar{U} = \frac{U_e + U_0}{2} \quad (2.40)$$

A common induction-factor, denoted as \bar{a} , is defined together with the total power exchange (\bar{P}) between the flow and the matched-actuator setup:

$$\bar{a} : \bar{U} = U_0 (1 - \bar{a}) \quad , \quad \bar{P} = \bar{U} \bar{F} \quad (2.41)$$

Reworking expressions 2.39 and 2.40 with 2.41 leads to the power coefficient of a matched-actuator setup with vanishing inter-actuator separation:

$$\bar{C}_p = \frac{\bar{P}}{\frac{1}{2} \rho U_0^3 \bar{S}} = -4 \bar{a} (1 - \bar{a})^2 \quad (2.42)$$

Expression 2.42 is identical to the power coefficient law of single actuator machines (Betz, 1920; Joukowski, 1929; Burton et al., 2002). It follows that matched-actuator setups are unable to exceed the Betz limit when the distance between their actuators tends to zero.

2.3.2. NON-VANISHING INTER-ACTUATOR DISTANCE

Matched-actuator setups with finite but non-vanishing distance between actuators are still misunderstood. Obtention of closed analytical solutions is challenging for these configurations, so we study them with a numerical experiment. It consists in simulating matched-actuator setups with different length but identical actuator loading densities (f_1, f_2).

FLOW SIMULATION METHOD

Simulations were conducted with a boundary element method that solves the planar version of the steady-state Euler equations in vorticity form. The vorticity field is discretised with straight segments of distributed vorticity that cover the edges of actuator wakes with variable density. No regularisation is conducted and the velocity field is reconstructed with a Green function approach (Speck, 2011) using exact induction functions (Katz and Plotkin, 2006). The method adopts a weak formulation by defining residuals for field consistency and vorticity conservation (Cottet and Koumoutsakos, 2000). Solutions for the vorticity field are obtained by minimising residuals with an under-relaxed iterative solver (Putti and Paniconi, 1995). A detailed description of the procedure can be found in de Oliveira et al. (2018a) and validation exercises have been conducted by Dighe et al. (2018a)(2018b) and (de Oliveira et al., 2016). The implementation shared some development with the method of Gamme et al. (2017) and is conceptually similar with methods by de Campos (1983) and ?.

All cases were computed in non-dimensional space. Spatial coordinates were scaled against the diameter of the first actuator (d_1), whereas speeds and forces were scaled to a unit free-stream ($U_0 = 1$) and density ($\rho = 1$). The size of the downstream actuator (d_2) is determined during the solution process and used to post-process results. Power coefficients are computed by integrating reconstructed velocity fields with a quadrature method that uses 10000 control points over each cross-section. Wakes were discretised to at least 300 diameters downstream of the second actuator with a variable density mesh of no less than 200 streamwise stances.

ACTUATOR LOADING

Actuator loading densities were specified in non-dimensional terms and written from the flow perspective (negative means against the flow). The following values were chosen:

$$\frac{f_1}{\frac{1}{2}\rho U_0^2} = \frac{5}{4} \quad \frac{f_2}{\frac{1}{2}\rho U_0^2} = -2 \quad (2.43)$$

For matched-actuator setups with infinitely distant actuators ($D_x \rightarrow \infty$), the loading densities of expression 2.43 correspond to a relative induction factor $a_2 = \frac{1}{3}$, an intermediate speed-ratio $b = \frac{3}{2}$, and a power coefficient $C_P = -\frac{3}{4}$. For setups whose actuators tend to each other ($D_x \rightarrow 0$), the same loadings correspond to a composite-induction factor $\bar{a} = \frac{1}{4}$ and a power coefficient $\bar{C}_P = -\frac{9}{16}$. Details about the correspondence between asymptotic and complementary configurations are clarified in appendix A.3.2. The total enthalpy jump ($\Delta h^t = \rho^{-1} f_1 + \rho^{-1} f_2$) is kept constant across all cases. It fixes the terminal wake speed and does not depend on the distance between actuators.

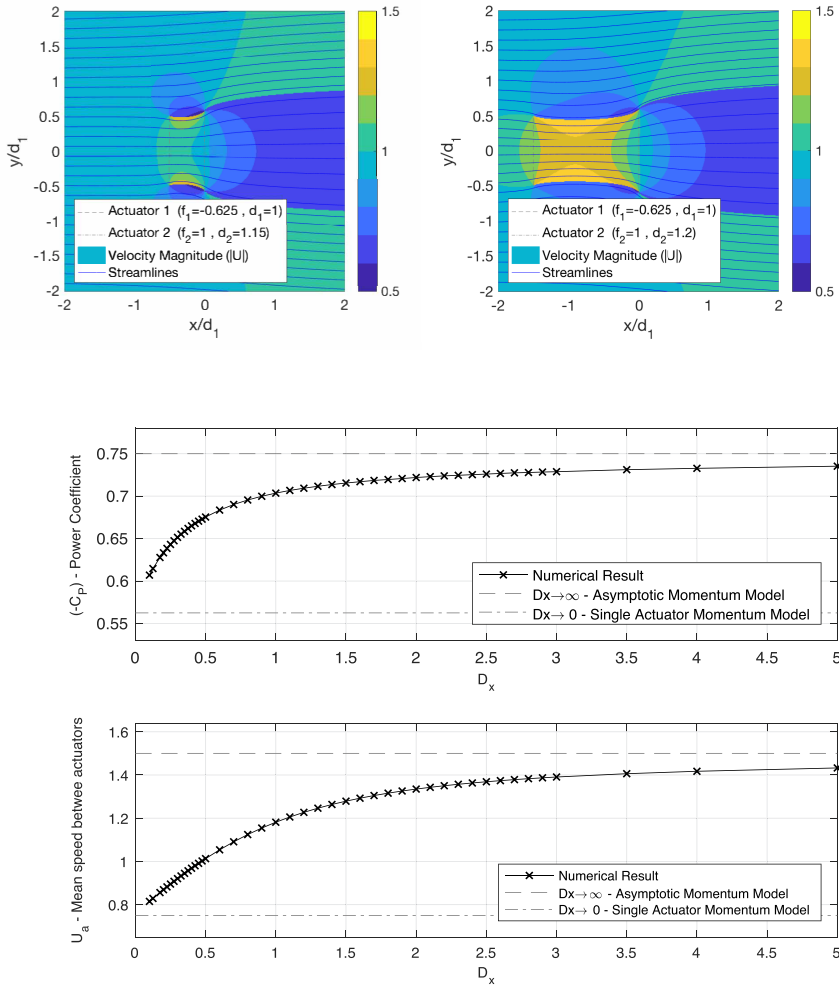


Figure 2.6: Effect of distance between actuators on flow across matched-actuator setup. Top: reconstructed velocity field for $D_x/d_1 = 1.5$ (a) and $D_x/d_1 = 0.5$ (b). Below: power coefficient (c) and mean flow velocity between actuators (midplane) (d) as a function of setup length (D_x). Actuator loading densities (f_1, f_2) and diameter of first actuator (d_1) remained constant.

EFFECT OF INTER-ACTUATOR DISTANCE

Results of the numerical experiment are presented on figure 2.6. Matched-actuator setups with finite inter-actuator spacing reach higher power coefficients than setups with vanishing inter-actuator distance, and lower than setups whose actuators are infinitely far apart. We contend that infinite inter-actuator separation scenarios ($D_x \rightarrow \infty$) set an upper bound for the performance of matched-actuator setups.

Actuator disks perturb static enthalpy and pressure fields. Perturbations vanish with distance but actuators operate in each other's influence region when they are separated by a finite distance. Downstream actuators with negative loading exerts forces against the flow that propagate upstream through the static enthalpy field. These forces hinder mass flow across the upstream actuator — and hence across the entire setup — and lead to reduced power extraction.

The enhanced performance of matched-actuator setups depends on the difference between the rate at which static and total enthalpy perturbations decay in space. In ideal flows, static enthalpy perturbations vanish with distance but total enthalpy changes remain indefinitely. Total enthalpy represents the total energy content of the flow and only changes across actuator disks. Static enthalpy represents the potential energy stored in the pressure field: it is exchanged with kinetic energy in the vicinity of actuation surfaces but, in the absence of swirl, returns to free-stream levels as wakes develop. Forces associated with the gradient of the static enthalpy field are said to be conservative, in contrast to non-conservative forces that cause total enthalpy changes (Van Kuik et al., 2014).

In a matched-actuator setup, actuators interact with each other through conservative and non-conservative forces if they are separated by a finite distance. When the distance is infinite, however, all interactions take place through non-conservative forces via the total enthalpy field.

2.4. FINDINGS AND IMPLICATIONS

The Betz-Joukowski limit places a firm upper bound on the power coefficient of isolated rotors. It withstood the test of time and applies independently of the qualities of specific rotors because it crystallises the opposition between the two mechanisms that dominate energy exchange. As Betz (1929a) elegantly stated, energy is extracted by exerting forces against the flow but these forces block the passage of flow across the actuation surface. On isolated rotors, mass-flux and total-enthalpy jump ($\Delta h^t = f/\rho$) are tied by a bijective relation that determines the maximum achievable power per unit area.

2.4.1. ACTIVE FLOW AUGMENTATION

Just like for isolated rotors, the power of a matched-actuator setup corresponds to the product of mass-flux with total-enthalpy jump. However, these quantities are no longer tied by a bijective relation. Mass flux can be influenced by varying the loading of each actuator while maintaining the total enthalpy jump ($\Delta h^t = \rho^{-1} f_1 + \rho^{-1} f_2$) constant. Compared with isolated actuators, smaller mass fluxes are obtained by operating matched-actuator setups with both actuators in wind turbine mode. Larger mass fluxes, which can lead to larger energy exchanges, are obtained by operating the upstream actuator in fan mode and the downstream actuator in wind turbine mode. Chapter ... will compare

that flow augmentation mechanism, which I call active, with the working principle of diffuser augmented wind turbines.

2.4.2. REVERSIBILITY OF ENERGY EXCHANGES

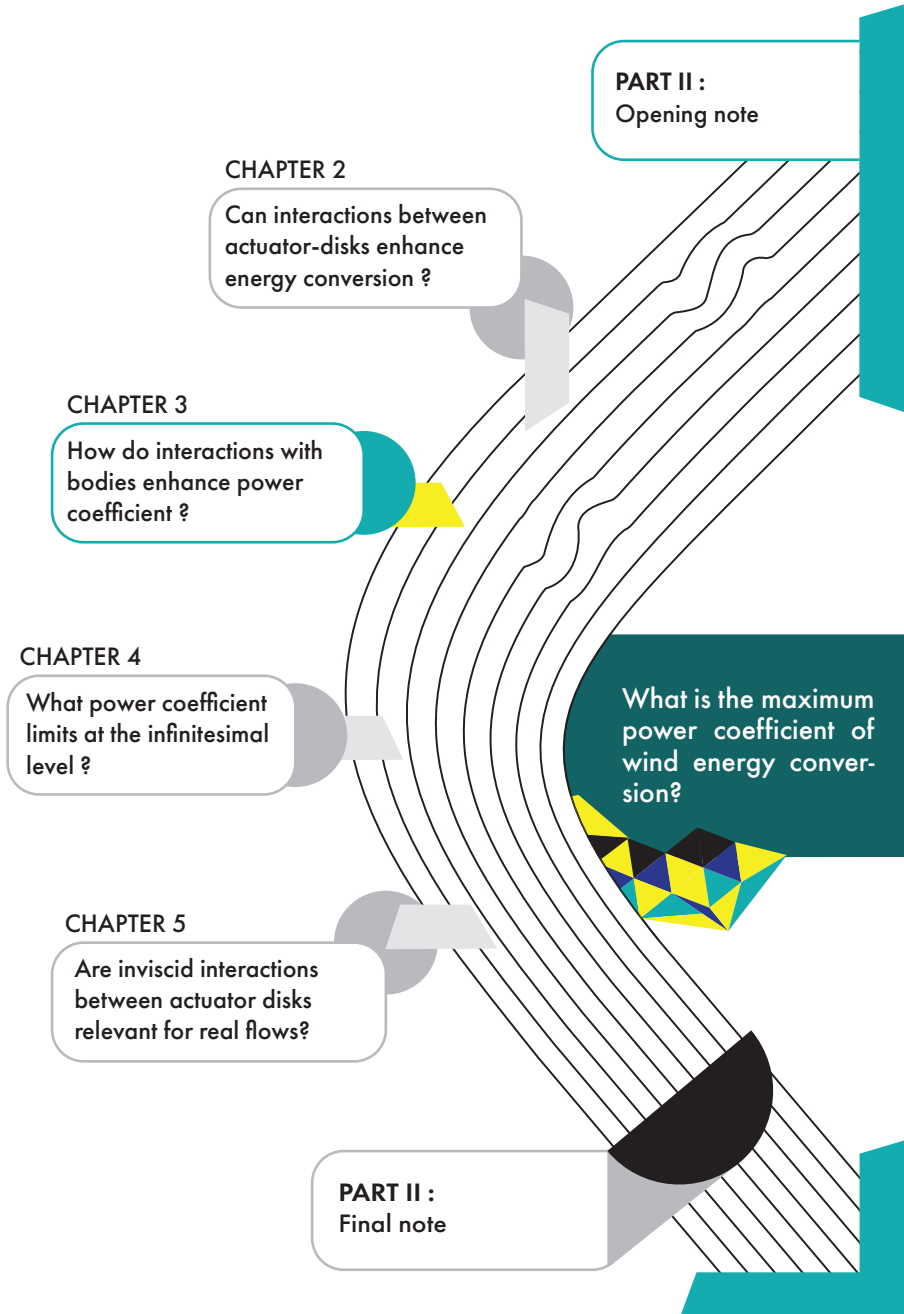
The efficacy of active augmentation mechanisms is subject to the reversibility of energy exchanges. In inviscid incompressible fluids, the downstream actuator of a matched-actuator setup recovers all the energy spent by the upstream actuator to increase mass flow. In viscous fluids however, wakes diffuse under the effect of shear and part of the energy injected by the upstream actuator is unrecoverable. Molecular viscosity, compressibility and thermal conductivity introduce irreversibilities that hinder the effectiveness of active concentration strategies. That is why matched-actuator setups seem unlikely to operate above the Betz limit in practice.

Imagine the extreme case of a matched-actuator setup with infinitely distant actuators attempting to extract energy from a viscous fluid. If the setup would operate with a speed-ratio above unity ($b > 1$) and a positive induction factor ($a_2 > 0$), the upstream actuator would inject energy into the flow but its wake would dissipate completely before reaching the downstream actuator. The downstream actuator would then fail to recover any of the energy injected by the upstream actuator. The power coefficient of the complete system would be inferior to that of a single actuator.

Yet, the dire scenery of the above paragraph does not completely invalidate the feasibility or relevance of active concentration mechanisms. There may exist a distance at which actuators are far enough for inter-actuator pressure interactions to be negligible but close enough for wakes to be sufficiently preserved. Chapter ... will investigate that possibility.

2.4.3. IMPLICATIONS FOR WIND ENERGY CONVERSION

Matched actuator setups contrast, but do not contradict, established practices in wind-farm design. The wind energy community has been mitigating the negative effects of wake interactions between rotors but rarely, if ever, attempted to use them for increasing power conversion. If they operated in inviscid flow, wind farms would be able to capture more energy by running some rotors in fan mode to channel flow onto other rotors that would operate in wind turbine mode. Obvious and immense practical obstacles oppose the successful materialization of such a strategy in real fluid flows. That being said, practical considerations left aside, curiosity could be a sufficient justification for continued research about active flow augmentation.



3

EXPLOITING BODY INTERACTIONS IN IDEAL FLOW

*Wakes are not the only means for tailoring mass-flow across actuator disks. Bodies, like diffusers or shrouds, can also alter the relation between actuator thrust and power. Are there parallels between the two mechanisms?*¹

INTRODUCTION

Questions about the interaction of actuator disks with nearby bodies arose at the dawn of rotor aerodynamics. Shrouded propellers were first considered in the pioneering works of [Coanda \(1910\)](#), [Stipa \(1933\)](#) and [Kort \(1936\)](#). Few concepts gained popularity in aeronautical applications ([Vuillet and Morelli, 1986](#); [Johnson and Turbe, 2006](#)) but shrouds are routinely used to improve the propulsive efficiency of maritime vessels ([Oosterveld, 1970](#); [Carlton, 2007](#)). Regarding wind energy, shrouds were first proposed by [Betz \(1929a\)](#) but detailed assessment of their effect had to wait for the studies of [Lilley and Rainbird \(1956\)](#). Their work reignited interest in ducted windmills and prompted further experimental ([Oman et al., 1975](#); [Igra, 1976](#)) and analytical ([De Vries, 1979](#)) inquiry into concentrator and diffuser systems ([Van Bussel, 1999](#)).

¹*Parts of this chapter have been published in [Journal of Physics Conference Series \(753\)](#) with co-authors [G. de Oliveira](#), [R. Pereira](#), [D. Ragni](#), [F. Avallone](#) and [G. van Bussel](#) under the title “How does the presence of a body affect the performance of an actuator disk” and in the [Proceedings of the 56th AIAA Aerospace Sciences meeting](#) with co-authors [V. Digne](#), [G. de Oliveira](#), [F. Avallone](#) and [G. van Bussel](#) under the title “On the shape of the duct for ducted wind turbines”.*

Literature about diffuser augmented wind turbines (De Vries, 1979; Van Bussel, 1999; Philips, 2003; Hansen et al., 2000; Van Bussel, 2007; Jamieson, 2008a,b; Werle and Presz, 2008; McLaren-Gow et al., 2013; Bontempo, 2014; Hjort and Larsen, 2015) promotes diverse and sometimes contradictory design recommendations (Van Bussel, 2007; Jamieson, 2008b; Werle and Presz, 2008; McLaren-Gow et al., 2013). The actuator-body problem remains a subject of controversy despite its canonic simplicity (Sorensen, 2016). Can a shrouded wind-turbine exceed the Betz limit if its power coefficient is written in terms of the system's projected area? Does the optimal thrust coefficient of an actuator-disk change with the presence of nearby bodies?

This chapter answers by exploring the implications of an exact power coefficient law proposed by De Vries (1979). Implications go beyond diffuser augmented wind turbines (DAWTs) because nearly all rotors operate in the presence of bodies. Conventional wind turbines stand at a finite distance from the ground and are frequently seek to take advantage of local terrain (Rokenes, 2009; Alfredsson and Segalini, 2017; Hyvarinnen and Segalini, 2017). These interactions are even more important for tidal turbines (Whelan et al., 2009), which stand closer to the seabed and employ bulkier supporting structures (Schluntz and Willden, 2015). Furthermore, it is interesting to compare the flow augmentation effect of bodies with active flow augmentation mechanisms discussed in the previous chapter.

Section 3.1 identifies interaction mechanisms between bodies and actuator-disks by (re)deducing the model of De Vries (1979). Section 3.2 explores the effect of body forces on actuator performance. Section 3.3 reverses the perspective to look at the effect of actuator loading on body forces. Implications for maximizing wind energy exchange are also confronted to previous literature. Section 3.4 summarizes new findings to close the chapter.

3.1. EXACT MODEL OF DE VRIES

The infinite diversity of possible body shapes limits analytical treatments of the actuator-body problem. Even so, a simple analytical approach pioneered by De Vries (1979) is sufficient to identify the fundamental interaction mechanisms between bodies and actuator-disks. This section departs from the steady variant of the Euler equations to replicate the De Vries (1979) deduction with added formalism:

$$(\mathbf{U}\nabla)\mathbf{U} = -\frac{1}{\rho}\nabla p + \frac{1}{\rho}\mathbf{f} \quad , \quad \rho\nabla\cdot\mathbf{U} = 0 \quad (3.1)$$

The study setup is represented on figure 3.1 and can be realized in both planar and axisymmetric spaces. It consists of a free-stream with an actuator disk and a symmetric collection of bodies. The actuator disk exerts homogeneously distributed forces while bodies can have arbitrary, and potentially disjoint, shapes. Each body lies inside or outside the actuator streamtube: continuity imposes that impermeable bodies cannot cross wake edges in steady inviscid flow.

Following De Vries (1979), we focus on actuator-disks that exert no azimuthal forces. This choice ensures the absence of swirl, so that static enthalpy (h) returns to free-stream values (h_0) as the distance to actuator (\mathbf{x}_a) and body (\mathbf{x}_b) locations grows (Sorensen,

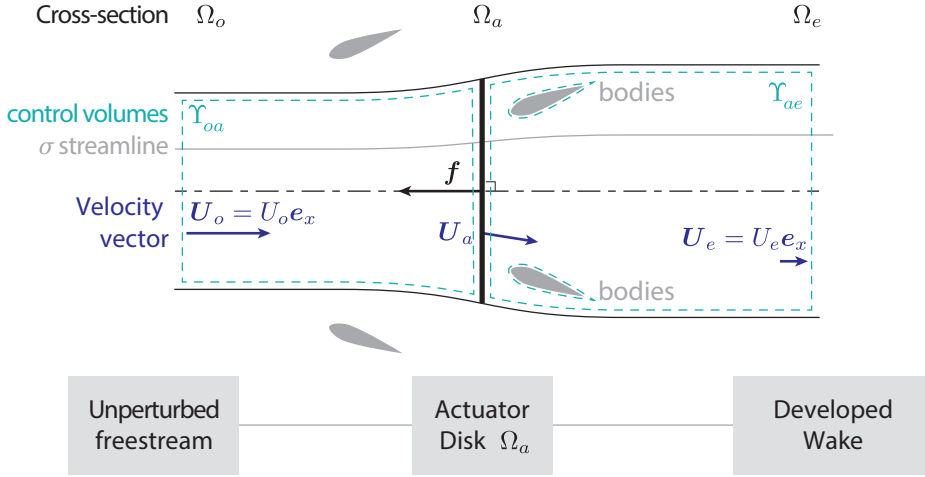


Figure 3.1: Setup and control volumes for deduction of the de Vries power coefficient law.

2016; Jamieson et al., 2018):

$$\lim_{d(x) \rightarrow \infty} h = h_0 \quad \Rightarrow \quad d_{(x)} = \min(|\mathbf{x} - \mathbf{x}_a|, |\mathbf{x} - \mathbf{x}_b|) \quad (3.2)$$

3.1.1. MASS, MOMENTUM AND ENERGY BALANCES

The deduction is rather standard and starts by integrating the continuity equation (3.1) to obtain a mass balance:

$$\left. \begin{aligned} \int \rho \nabla \cdot \mathbf{U} dY_{oa} = \dot{m}_o - \dot{m}_a = 0 \\ \int \rho \nabla \cdot \mathbf{U} dY_{ae} = \dot{m}_a - \dot{m}_e = 0 \end{aligned} \right\} \Rightarrow \rho S_o U_o = \rho S_a U_a = \rho S_e U_e$$

$$with \quad \begin{cases} S_o = \int d\Omega_o \\ S_a = \int d\Omega_a \\ S_e = \int d\Omega_e \end{cases} \quad (3.3)$$

Sets Y_{oa} and Y_{ae} are control volumes (n-manifolds) that partition the actuator streamtube. Cross-sections Ω_o , Ω_a and Ω_e belong to control volume boundaries and are used to define inlet (S_o), actuator (S_a) and outlet (S_e) areas.

The momentum balance is obtained by projecting the Euler equations (3.1) onto the free-stream direction (\mathbf{e}_x) and integrating the result over the $Y_{oe} = (Y_{oa} \cup Y_{ae})$ control volume :

$$\int (\rho (\mathbf{U} \nabla) \mathbf{U}) \cdot \mathbf{e}_x dY_{oe} = - \int (\rho \nabla h) \cdot \mathbf{e}_x dY_{oe} + \int (\mathbf{f}) \cdot \mathbf{e}_x dY_{oe} \quad (3.4)$$

The convective derivative term is easily integrated into an algebraic expression:

$$\int (\rho (\mathbf{U} \nabla) \mathbf{U}) \cdot \mathbf{e}_x d\Omega_{oe} = \rho S_e U_e^2 - \rho S_o U_o^2 = \rho S_2 U_2 (U_e - U_o) \quad (3.5)$$

The external forces term (\mathbf{f}) is integrated by denoting the actuator loading density per unit area as f_a :

$$\int \mathbf{f} \cdot \mathbf{e}_x d\Upsilon_{oe} = f_a S_a \quad (3.6)$$

The static enthalpy integral does not admit closed algebraic representations. We call it F_b and observe that it corresponds to a scalar value with the units of a force:

$$F_b = \int (\rho \nabla h) \cdot \mathbf{e}_x d\Upsilon_{oe} \quad (3.7)$$

Inserting expressions 3.5-3.7 into expression 3.4 transforms momentum conservation into a statement describing the total force (F_a) exerted by the actuator. The (q) superscript highlights its semantic origin.

$$F_a^{(q)} = f_a S_a = \rho S_a U_a (U_e - U_o) + F_b \quad (3.8)$$

Total actuator force can also be stated in terms of energy conservation, and denoted as F_a with a (h) superscript. This is done by integrating Crocco's equation along a streamline (σ) :

$$\Leftrightarrow \begin{aligned} \int \mathbf{f} \cdot \mathbf{r} d\sigma &= \rho \int (\nabla h^t - \mathbf{U} \times \boldsymbol{\omega}) \cdot \mathbf{r} d\sigma \\ f_a &= \rho (h_e^t - h_o^t) \end{aligned} \quad (3.9)$$

Expression 3.7 can be simplified by reworking total enthalpies and applying the limit of expression 3.2:

$$\Leftrightarrow \begin{aligned} F_a^{(h)} = f_a S_a &= \frac{1}{2} \rho S_a (U_e^2 - U_o^2) + \rho S_a (h_e - h_o) \\ &= \frac{1}{2} \rho S_a (U_e^2 - U_o^2) \end{aligned} \quad (3.10)$$

Expression 3.8 must be consistent with expression 3.10 for simultaneous enforcement of momentum and energy conservation. The match leads to an exact expression for average normal flow across the actuator:

$$U_a = \frac{1}{2} (U_e + U_o) - \frac{F_b}{\rho S_a (U_e - U_o)} \quad (3.11)$$

Expression (3.11) is exact for average flow velocities but does not rule out the possibility of normal velocity variations over the actuation surface. Furthermore, it shows that mass flow ($\dot{m} = S_a U_a$) depends simultaneously on the actuator loading (F_a) and static enthalpy (F_b) terms. This contrasts with wake velocities, which are uniquely determined by actuator loading and free-stream properties.

3.1.2. POWER COEFFICIENT

Actuator power exchange corresponds to the product of mass flow (\dot{m}) with total enthalpy jump ($h_e^t - h_o^t$). It is written from the flow perspective:

$$P = \dot{m} (h_e^t - h_o^t) = \frac{1}{2} \rho S_a U_a (U_e^2 - U_o^2) \quad (3.12)$$

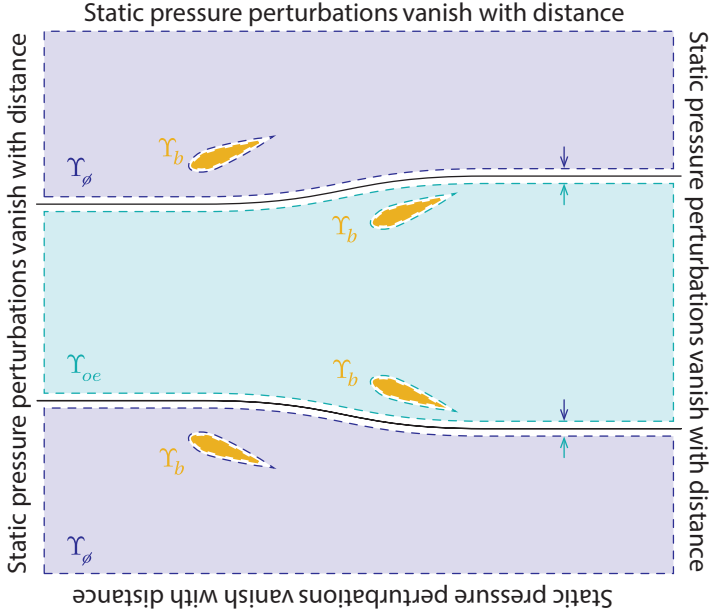


Figure 3.2: Partition of tri-dimensional space into three non-overlapping sets.

Before writing a power coefficient, it is convenient to recast expressions 3.3-3.11 into adimensional terms.

$$C_{F_a} = \frac{F_a}{\frac{1}{2}\rho S_a U_o^2} \quad , \quad C_{F_b} = \frac{F_b}{\frac{1}{2}\rho S_a U_o^2} \quad , \quad u_a = \frac{1}{2}(u_e + 1) - \frac{1}{2} \frac{1}{(u_e - 1)} C_{F_b} \quad (3.13)$$

The actuator area is used as a reference to avoid premature considerations about body shape. Power coefficient (C_P) is then stated as:

$$C_P = \frac{P}{\frac{1}{2}\rho S_a U_o^3} = u_a (u_e^2 - 1) = \frac{1}{2} (u_e + 1) ((u_e^2 - 1) - C_{F_b}) \quad (3.14)$$

Expression 3.14 is equivalent to the power coefficient law of De Vries (1979) and is consistent with isolated actuator disk models when C_{F_b} equals zero. Power coefficient trends will be discussed in section 3.2, once the meaning of the C_{F_b} term has been clarified.

3.1.3. BODY FORCE COEFFICIENT

The C_{F_b} coefficient arose from the integral of static enthalpies. Its meaning can be extracted from expression 3.7 with a few algebraic steps. First static enthalpies need to be recast into pressures. Then, the normal unit vector of the streamtube boundary is denoted as \mathbf{n} and used to apply the divergence theorem. The result is written below:

$$\begin{aligned}
F_b &= \int (\rho \nabla h) \cdot \mathbf{e}_x dY_{oe} = \int (\nabla p) \cdot \mathbf{e}_x dY_{oe} \\
&= \int (\mathbf{p}\mathbf{n}) \cdot \mathbf{e}_x d(\partial Y_{oe}) \\
&= \left(\int (\mathbf{p}\mathbf{n}) d(\partial Y_{oe}) \right) \cdot \mathbf{e}_x
\end{aligned} \tag{3.15}$$

Expression (3.15), which states that F_b corresponds to the streamwise component of the sum of all pressure forces ($\mathbf{p}\mathbf{n}$) that act on the boundary (∂Y_{oe}) of the streamtube control volume (Y_{oe}).

ORIGIN OF PRESSURE FORCES

The magnitude of the F_b term cannot be evaluated analytically but the origin of pressure forces can be traced through the action-reaction principle. The principle imposes that all forces be counter-acted. As such, the sum of all pressure forces that act on the flow must boil down to zero:

$$\int \nabla p d(\mathbb{R}^3) = 0 \tag{3.16}$$

Now, consider a partition of three-dimensional space into three non-overlapping sets:

- The first set (Y_b) is the compact support of all bodies in the flow
- The second set (Y_{oe}) is open ($Y_{oe} \cap \partial Y_{oe} = \emptyset$) and spans the actuator streamtube
- The third set (Y_\emptyset) corresponds to everything else ($Y_\emptyset = \mathbb{R}^3 \setminus \{Y_{oe}, Y_b\}$).

Inserting this partition into the integral of all pressure forces, expression 3.16, breaks it into three contributions:

$$\begin{aligned}
\mathbb{R}^3 &= Y_{oe} \cup Y_\emptyset \cup Y_b \quad \Rightarrow \\
0 &= \int \nabla p d(\mathbb{R}^3) = \int \nabla p d(Y_{oe}) + \int \nabla p d(Y_\emptyset) + \int \nabla p d(Y_b)
\end{aligned}$$

Expression 3.2 implies that the pressure integrand vanishes over all boundaries of Y_\emptyset that are not shared with the body or the streamtube:

$$\int \mathbf{p}\mathbf{n} d(\partial Y_\emptyset \setminus \{\partial Y_\emptyset \cap (Y_{oe} \cup Y_b)\}) = 0$$

It follows that all pressure forces exerted on the actuator streamtube (Y_{oe}) must stem from bodies (Y_b), even if forces can be transmitted over the Y_\emptyset set:

$$\int \nabla p d(Y_{oe}) + \int \nabla p d(Y_b) = 0$$

The F_b force therefore corresponds to the magnitude of streamwise forces exerted by bodies on the actuator streamtube, and that is why we call C_{F_b} the body force coefficient.

$$F_b \equiv \int \nabla p d(Y_{oe}) \cdot \mathbf{e}_x = - \left(\int \nabla p d(Y_b) \right) \cdot \mathbf{e}_x \tag{3.17}$$

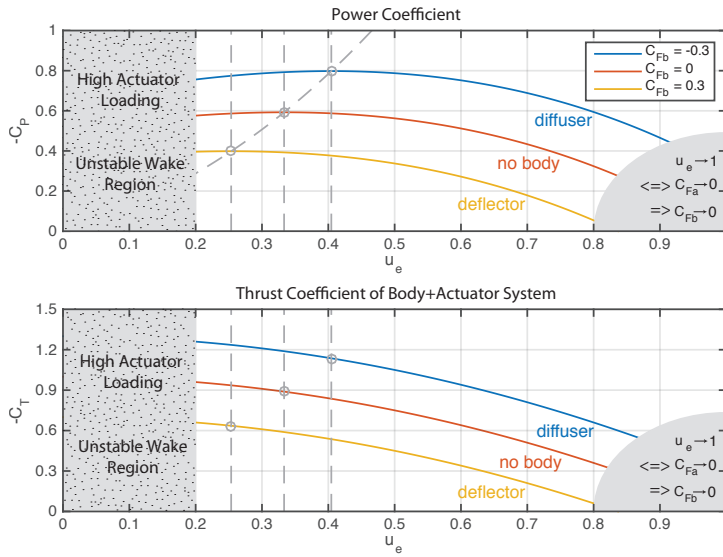


Figure 3.3: Thrust and Power Coefficient in Energy Extraction (Wind Turbine) Mode

3.1.4. PASSIVE FLOW AUGMENTATION

Equations 3.14 to 3.17 show that, in ideal flows, all interactions between bodies and actuator disks occur through the static enthalpy field. Bodies can exert streamwise pressure forces on the flow that crosses the actuator-disk, and thereby alter its mass flow and power exchange. But bodies do not exchange energy directly with the flow because they never shed wakes in steady symmetric flows of ideal fluids. In fact, and as stressed by d’Alembert’s paradox, bodies would not be able to exert streamwise forces on the flow if the actuator disk was absent:

$$\lim_{F_a \rightarrow 0} F_b = 0$$

The existence of non-zero net streamwise forces on bodies can be interpreted from a virtual work perspective. Actuator-body interactions depend entirely on conservative forces, but affect energy exchanges between the flow and the outside world despite the fact that all power extraction occurs on the actuator disk surface. That is why we call this flow augmentation mechanism passive.

3.2. POWER COEFFICIENT TRENDS

The power coefficient law of equation 3.14 describes a surface in the (u_e, C_{F_b}, C_p) space. Figure 3.3 presents three constant- C_{F_b} surface cuts. It treats the body force coefficient (C_{F_b}) as a free parameter, even if C_{F_b} must tend to zero when the actuator loading (C_{F_a}) vanishes.

$$\begin{aligned} C_{F_a} = 0 &\Leftrightarrow u_e = 1 \\ \Rightarrow C_{F_a} = 0 &\Rightarrow C_{F_b} = 0 \\ \Rightarrow C_{F_a} \neq 0 &\Rightarrow C_{F_b} \text{ is a design parameter} \end{aligned} \tag{3.18}$$

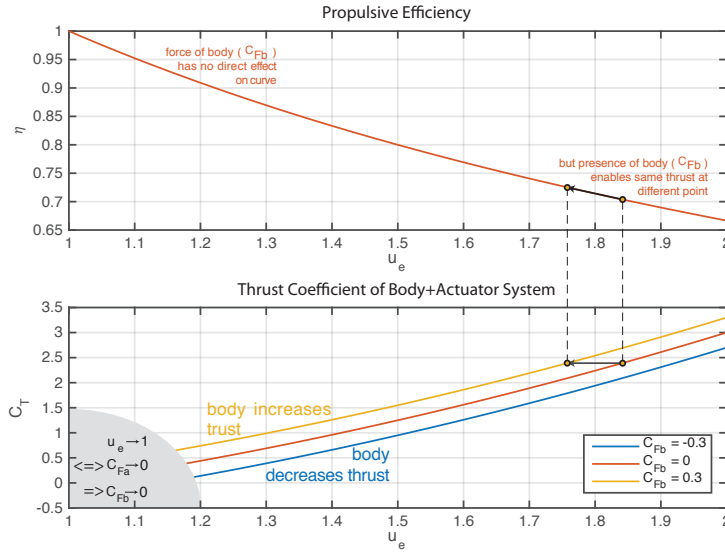


Figure 3.4: Thrust and Propulsive Efficiency for Actuator-Body System in Propeller Mode

The lower right corner of figure 3.3 is shaded to highlight that this region of the C_p curves is unreachable. The region of low terminal wake speeds ($u_e < 0.2$) is also shaded to stress that excessive flow deceleration cause wake instabilities that invalidate the present theory (Birkhoff, 1960).

3.2.1. EFFECT OF BODY SIZE

It is well known that the power coefficient of actuator-body setups can exceed $16/27$, the Betz limit value, when bodies surround the actuator and the area of the actuator is taken as a reference (Van Bussel, 1999, 2007; Jamieson, 2008a,b). It is also rather consensual that the power coefficient of an actuator-body system is enhanced whenever bodies exert a net accelerating force on the flow ($C_{F_b} < 0$) (Werle and Presz, 2008; Sorensen, 2016). What is more rarely discussed, however, is that bodies can also generate concentrating forces ($C_{F_b} < 0$) without surrounding the actuator. Does this mean that an actuator-body system can exceed the Betz limit when the power coefficient is defined using the largest cross-section of the system?

From the perspective of the power coefficient law (3.14) of De Vries (1979), which uses the actuator area as a reference, there is no difference between a body that lies inside or outside the actuator streamtube. What matters for power exchange, is the magnitude of streamwise forces exerted by all bodies in the flow. The size of bodies only affects the projected area of the entire system, which, in principle, should be used to define the power coefficient. It corresponds to the area of the actuator (S_a) when the bodies are smaller than the actuator.

There seem to be no theoretical obstacles for exceeding the Betz limit with actuator-body systems whose bodies fit inside the actuator-disk projection. Can this be observed

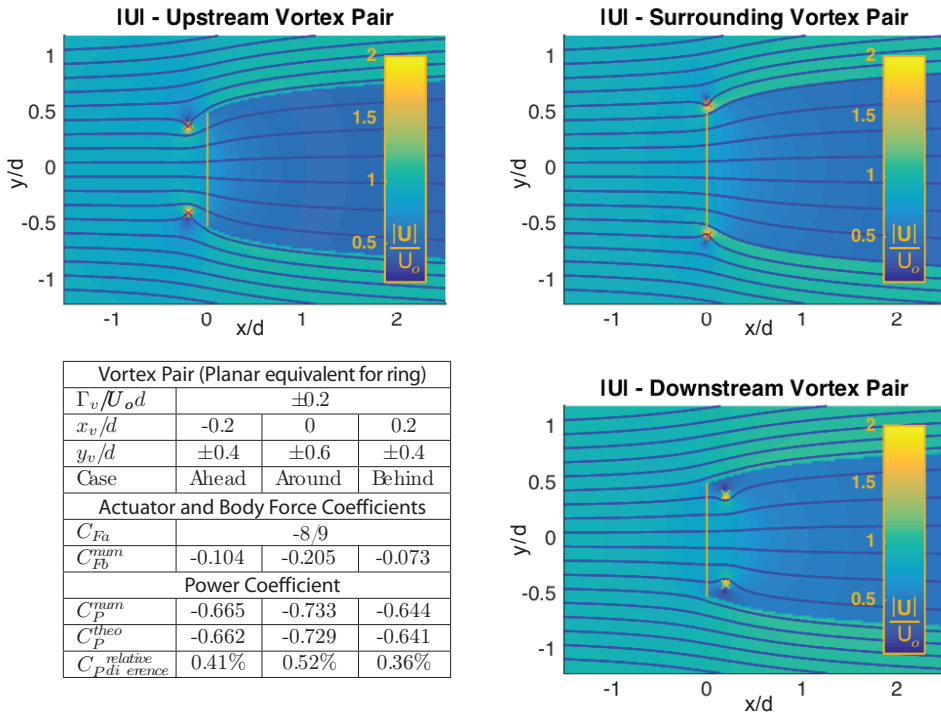


Figure 3.5: Numerical flow solution for three setups comprising a planar actuator (yellow line) and a pair of counter-rotating vortices (crosses) that is wider (top right) or narrower (top left and bottom right) than the actuator projected area.

in practice?

NUMERICAL EXPERIMENT

Figure 3.5 shows the results of three numerical experiments conducted with a numerical solver of the planar vorticity transport equation. This solver is closely related to the one used in chapter 2 and was validated by Dighe et al. (2018a) and Gamme et al. (2017). A flat actuator disk of width d and loading $C_{F_a} = -8/9$ was simulated together with a symmetric pair of counter-rotating vortices. The circulation Γ_v of the vortex pair was kept constant while its position $\mathbf{x}_v = (x_v, \pm y_v)$ changed across the three cases.

Numerical versions of the interaction $C_{F_b}^{num}$ and power C_P^{num} coefficient were obtained by postprocessing reconstructed velocity fields. Finally, the “numerical” body force coefficient $C_{F_b}^{num}$ was combined with the prescribed actuator loading coefficient C_{F_a} to compute the “theoretical” power coefficient C_P^{theo} with expression 3.14. The “numerical” and “theoretical” predictions match to within half a percent, irrespective of the presence and placement of bodies.

Changes in the placement of the vortex pair affect actuator mass flow, which scales linearly with power extraction because actuator loading is kept constant. The greatest power increase is obtained with the shrouding vortex pair, but smaller upstream and downstream vortices also lead to substantial increases in power extraction. The results of figure 3.5 suggest that actuator-body setups can exceed the Betz limit even when bodies are smaller than the actuator-disk. But the answer is not clear cut: the vortex rings used in this numerical experiment had rather strong circulation, and I was unable to create body geometries that would lead to similar outcomes. Does that point to a theory gap? The question remains open.

3.2.2. OPTIMAL ACTUATOR THRUST

The presence of bodies affects the terminal wake speed that maximizes wind energy extraction. If a body force coefficient (C_{F_b}) is prescribed, the optimal terminal wake speed u_e^{opt} is found by searching for extremes in the power coefficient law (3.14) :

$$u_e^{opt} \Big|_{C_{F_b}} : \frac{\partial}{\partial u_e} (C_P) \Big|_{C_{F_b}} = 0 \quad \Rightarrow \quad u_e^{opt} \Big|_{C_{F_b}} = -\frac{1}{3} \left(1 - \sqrt{4 - 3C_{F_b}} \right) \quad (3.19)$$

The bijection between u_e and C_{F_a} implies that the optimal actuator loading ($C_{F_a}^{opt}$) depends on the forces exerted by bodies (C_{F_b}). The dependency is clarified by expression 3.20, which is plotted in figure 3.6.

$$C_{F_a}^{opt} \Big|_{C_{F_b}} = \left(u_e^{opt} \Big|_{C_{F_b}} \right)^2 - 1 \quad , \quad C_T^{opt} = \left(u_e^{opt} \Big|_{C_{F_b}} \right)^2 - 1 + C_{F_b} \quad (3.20)$$

Expressions 3.19 and 3.20 contrast with previous knowledge. Earlier studies suggested that the presence of bodies did not affect the thrust coefficient at which actuator disks reach maximal energy extraction (Van Bussel, 2007; Jamieson, 2008a; Werle and Presz, 2008).

This is intriguing, since the approach of Werle and Presz (2008) shares several features with the present work. They proposed a power coefficient law that is formally

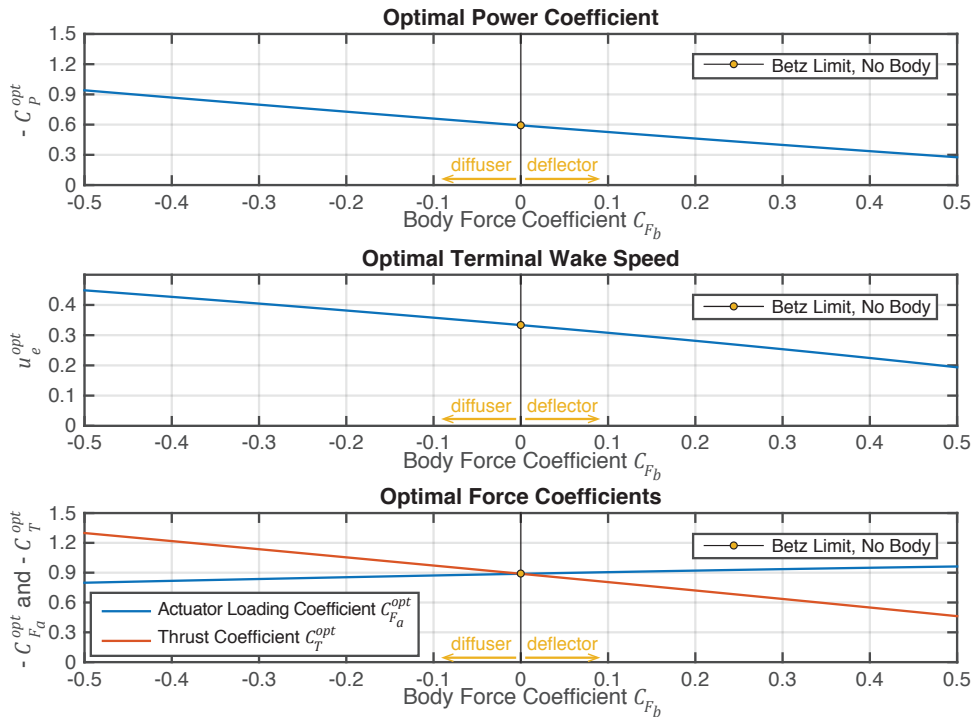


Figure 3.6: Optimal loading of actuator disk when surrounding bodies exert a constant force on the actuation streamtube.

equivalent to the expression of de Vries (3.14) but uses different variables to characterize actuator ($C_{F_a}^{wp}$) and body (C_s^{wp}) forces. It reads as follows:

$$C_P = -\frac{1}{2} (1 + C_s^{wp}) C_{F_a}^{wp} \left(1 + \sqrt{1 - C_{F_a}^{wp}} \right) \quad , \quad C_s^{wp} \equiv -\frac{C_{F_b}}{C_{F_a}} = \frac{F_b}{F_a} \quad \wedge \quad C_{F_a}^{wp} \equiv -C_{F_a}$$

The use of a different adimensional group for describing body forces leads to a different sets of constrained optima:

$$C_{F_a}^{opt} \Big|_{C_s^{wp}} : \frac{\partial}{\partial u_e} (C_P) \Big|_{C_s^{wp}} = 0 \quad \Rightarrow \quad C_{F_a}^{opt} \Big|_{C_s^{wp}} = \frac{8}{9} \quad \Rightarrow \quad u_e^{opt} \Big|_{C_s^{wp}} = \frac{1}{3} \quad (3.21)$$

The disparity between expressions 3.20 and 3.21 arises from the fact that searching for optima with fixed C_s^{wp} is equivalent to requiring that a linear relation exists between C_{F_a} and C_{F_b} . Only then does the optimal actuator loading coefficient correspond to $C_{F_a} = -8/9$ despite the presence of bodies. Similar arguments have been developed by Sorensen (Sorensen, 2016) and the assumption of a linear relation between C_{F_b} and C_{F_a} is unsupported.

3.3. ACTUATOR-BODY COUPLING

Werle and Presz (2008) do not seem to have realized that they were implicitly assuming a linear correlation when they searched for the optimal actuator loading (C_{F_a}). But understanding the nature of the $C_{F_b} \leftrightarrow C_{F_a}$ correlation is important:

1. If $C_{F_b} \propto C_{F_a}$ is true : optimal actuator loading will always have a value $C_{F_a} = 8/9$, independently of the presence of bodies in the flow
2. If $C_{F_b} \propto C_{F_a}$ is false : optimal actuator loading will depend on the presence of bodies in the flow

Which of the above options is right? This section answers in two steps. First, we assess possible trends by studying interactions between an actuator disk and a pair of stationary vortices. Stationary vortices are the simplest representation of lift generating bodies and all incompressible flows can be reconstructed by superposing singularities. Then, we move on to study interaction trends on the practical case of the DonQi wind turbine duct.

3.3.1. STATIONARY VORTEX PAIR

Figure 3.7 depicts a numerical study on the correlation between the body force coefficient C_{F_b} and the actuator force coefficient C_{F_a} . As in the numerical experiments of section 3.2.1, the setup consists of an actuator and a pair of counter rotating vortices in planar flow:

- Red lines depict the evolution of system parameters when the actuator loading C_{F_a} varies while the strength $\Gamma_v/(U_o d)$ of the stationary vortex pair (ring) stays constant. Comparable behaviors can be achieved in real flows with Magnus effect lifting devices like Flettner rotors.

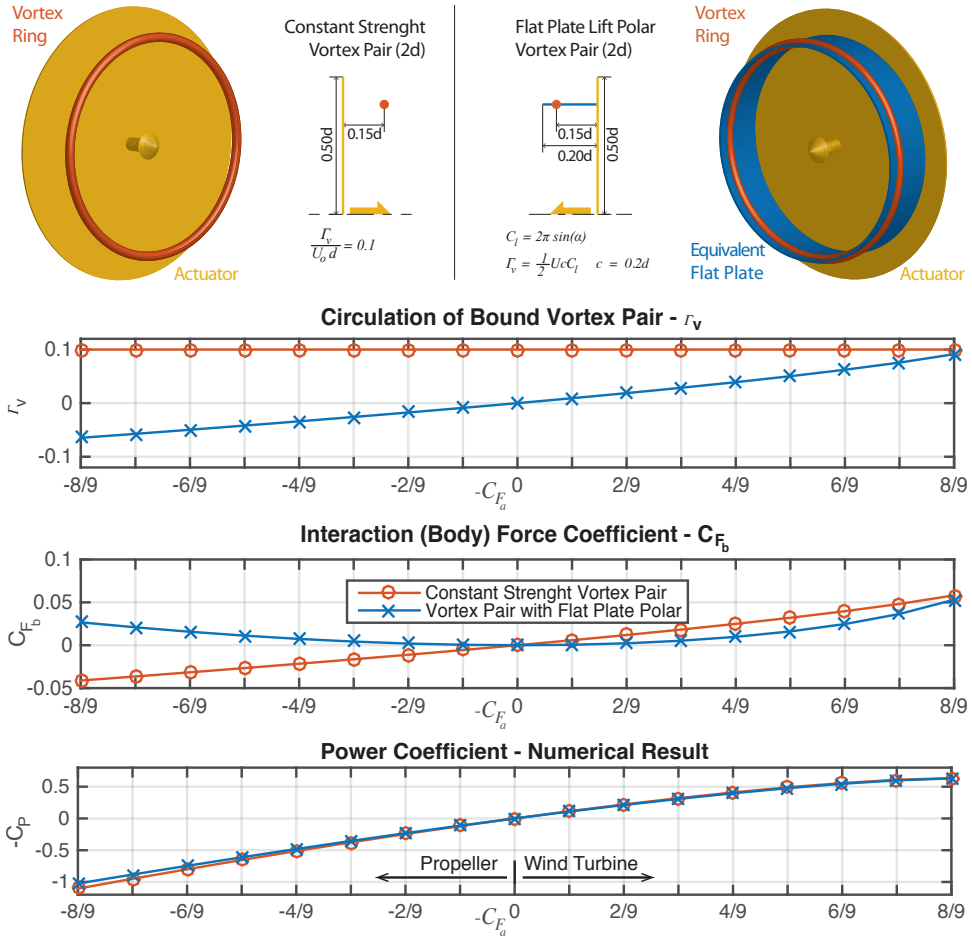


Figure 3.7: Effect of actuator loading on body force coefficient of a vortex pair: whose circulation remains constant (red), and whose circulation reacts to local flow conditions (blue).

- Blue lines show the effect of actuator loading C_{F_a} on system parameters when the strength of the stationary vortex pair is adjusted to mimic the polar of a flat plate with chord $c = 0.2d$ in straight flow. A real flat plate would exhibit a slightly different polar due to flow curvature effects but this effect is secondary (Migliore et al., 1980), specially for bodies low chord over diameter.

The relation between force coefficients (C_{F_a} and C_{F_b}) is nearly linear when the strength of the vortex pair is kept constant. Departures from linearity are subtle but noticeable for large actuator loading coefficients ($C_{F_a} > 6/9$). The correlation between the C_{F_b} and C_{F_a} force coefficients is primarily quadratic when the strength of the vortices grows with the angle of attack.

3.3.2. DONQI DUCT

Are actual relations between C_{F_a} and C_{F_b} non-linear for practical bodies? The geometry of the DonQi diffuser augmented wind turbine (DAWT) provides some answers. It is depicted on figure 3.8 and has been extensively studied (Dighe et al., 2018a,b,c).

NUMERICAL EXPERIMENT

Vinit Dighe, a colleague of the present author, studied the correlation between duct and actuator forces with two numerical methods. Several cases with identical geometry and different actuator force coefficient were considered, as described in (Dighe et al., 2018a). Results are summarized on figure 3.10: datapoints marked as *panel* were generated with the inviscid solver used in the previous sections, whereas those marked as *RANS* were computed with the Fluent CFD solver. Both simulations treated the flow as planar instead of axi-symmetric. Rotors and ducts are ultimately meant to be axisymmetric but planar setups have the same interaction mechanisms and permit the usage of faster, and potentially more accurate, numerical methods. Velocity fields are shown on figure 3.9.

FORCE COUPLING

The first graph of figure 3.10 shows the variation of duct force ($C_X = -C_{F_b}$) with actuator loading ($C_T = -C_{F_a}$). The offset between RANS and panel predictions results has multiple sources. The neglect of viscous and turbulent phenomena is significant, but the inviscid flow solver underpredicts the body force coefficient primarily because of truncation errors in the postprocessing of body pressures. Still, both flow solutions make it clear that duct force does not vary linearly with actuator loading. It is also clear that the optimal actuator loading is smaller than $C_T = 8/9$ when a realistic duct geometry is considered.

3.4. FINDINGS AND IMPLICATIONS

This chapter verified the exact nature of the power coefficient law proposed by de Vries (De Vries, 1979). By analyzing its extremes in rigorous ways, we pointed that naïve extremum analysis of the de Vries expression leads to erroneous design recommendations. It has often been suggested that external bodies do not affect optimal thrust coefficient (Werle and Presz, 2008; Jamieson, 2008b). This is not true. Optimal actuator loading depends on the resultant of streamwise pressure forces that act on the streamtube, which in turn depends on actuator loading.

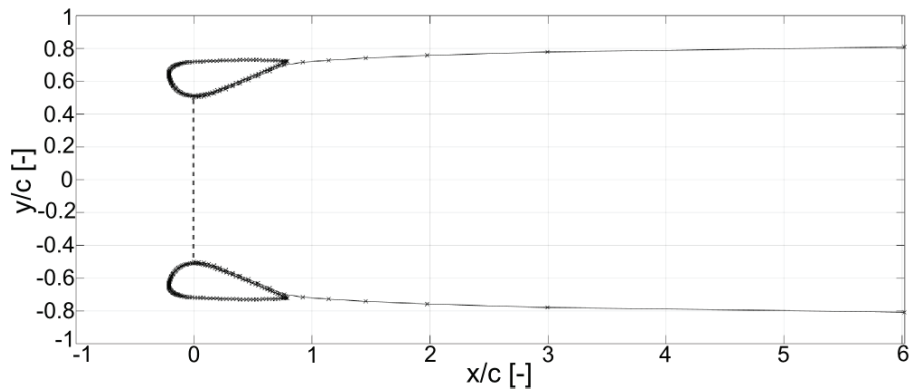


Figure 3.8: Inviscid solution of flow around the DonQi turbine (body and wake panels)

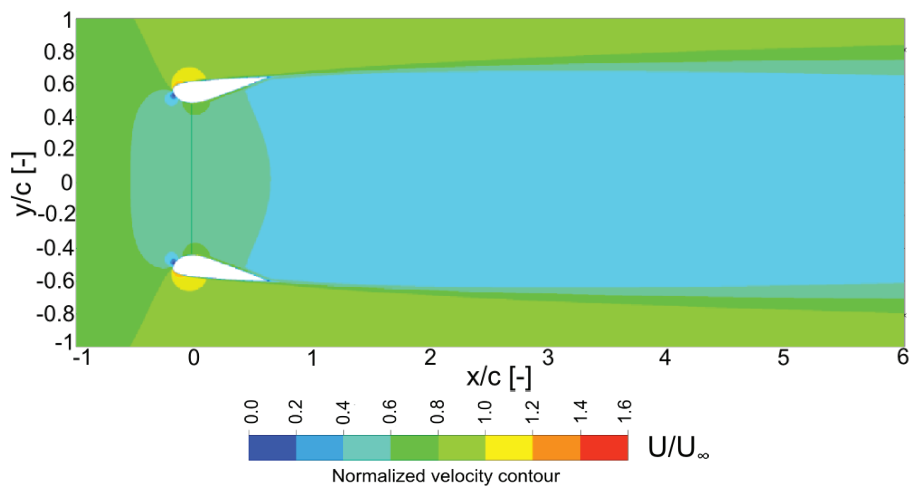


Figure 3.9: RANS solution of flow around the DonQi turbine (velocity magnitude)

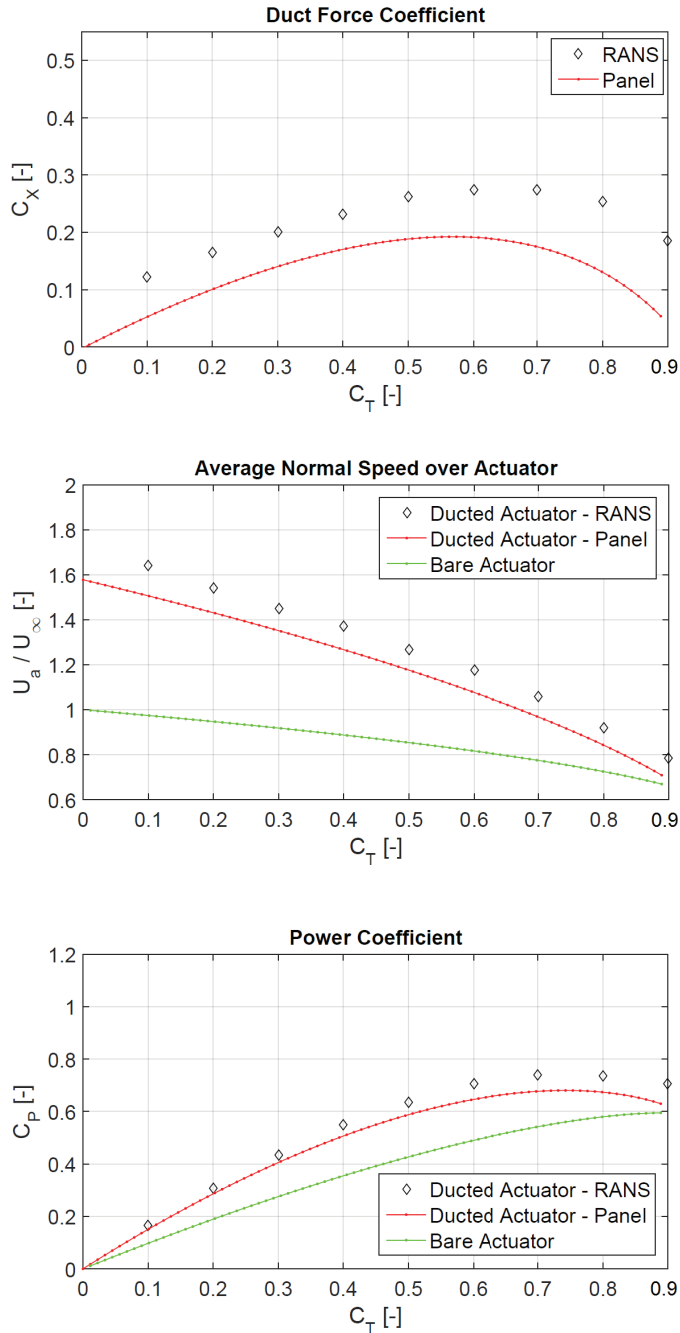


Figure 3.10: Effect of actuator thrust coefficient ($C_T = -C_{F_a}$) on: duct force (*top*, $C_X = -C_{F_b}$), average normal speed over actuator (*middle*, U_a) and power coefficient ($C_p = -C_p$) of actuator-disk surrounded by DonQi duct. ()

BETZ LIMIT EXCEEDANCE

No objections to the exercise of streamwise forces by bodies smaller than the actuator diameter were found. This suggests that wind energy conversion systems comprising a rotor and a small concentrating annular body, placed for example at the rotor mid-span, can in principle exceed the Betz limit in ideal flow conditions. While theoretical arguments in favor of such a possibility exist, no practical body shape leading to such increases could be identified. But we don't know why. Answering this question would go a long way in clarifying the

PASSIVE FLOW AUGMENTATION

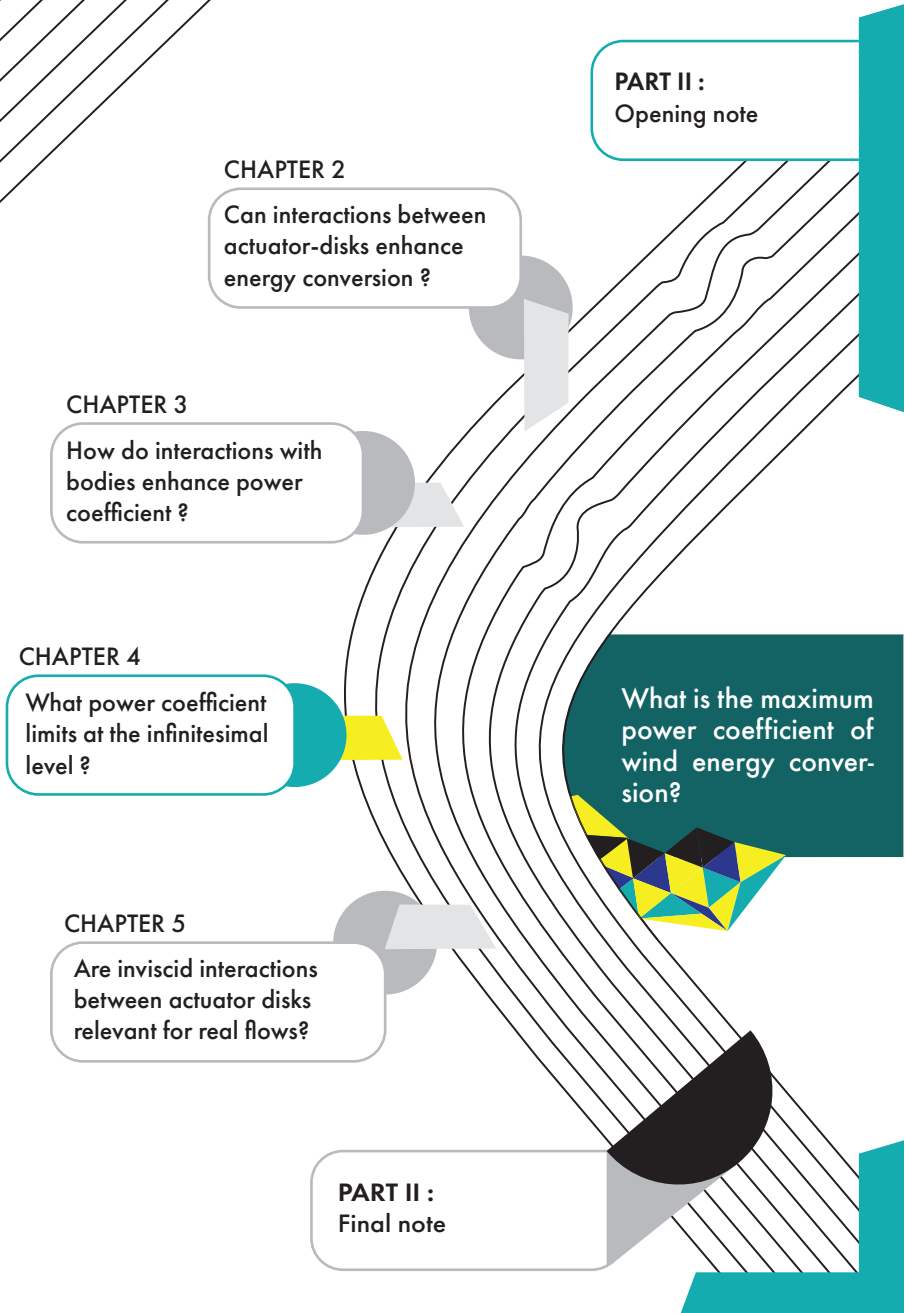
Planar or axisymmetric bodies do not exchange energy directly with ideal flows – they cannot exert shear forces, nor generate wakes through finite wing effects. They can, however, exert streamwise forces that channel flow onto an actuator disk leverage through virtual work mechanisms. Doing so shifts the actuator mass flow and increases achievable power coefficient beyond the Betz limit. This flow augmentation mechanism depends entirely on static enthalpy interactions – which represents the flow's potential energy – and that is why we call it passive.

RELATION WITH ACTIVE FLOW AUGMENTATION

Passive flow augmentation mechanisms, discussed in the present chapter, differ from active flow augmentation mechanisms discussed in chapter 2. Matched-actuator setups let the flow exchange energy with the outer world more than once, and thereby permit the construction of more complex total enthalpy fields. Total enthalpy completely describes interactions between actuators that stand infinitely far apart from each other. Actuators separated by a finite distance, however, interact simultaneously through static and total enthalpy perturbations. In that case, and this differs from what is observed with shrouding bodies, the effect of static enthalpy interactions hinders energy exchange.

COMBINING ACTIVE AND PASSIVE FLOW AUGMENTATION

The comparison between passive and active flow augmentation mechanisms raises new questions. One might for example ask whether shrouding bodies could potentially tailor interactions between subsequent actuator-disks? After all, it seems plausible that a duct placed between the actuators of a matched-actuator setup could accelerate wake recovery. Inter-actuator ducts could also help solve practical issues faced by matched-actuator setups, like the risk of wake misalignment, but would also lead to additional viscous losses. These challenges and opportunities should be the object of future studies.



4

TOWARDS A GENERAL POWER COEFFICIENT LIMIT

The Betz-Joukowsky limit does not apply to flows that experience external enthalpy changes before or when they cross an energy extraction surface. Can a unified analytical approach capture all determinants of energy exchange with steady flows of ideal fluids?

INTRODUCTION

Efforts to characterize the maximum power coefficient of wind energy conversion usually resort to *ex-ante* flow topology assumptions. The Betz-Joukowsky analysis, for example, assumes that wind energy is converted over an isolated actuation surface shedding a single homogeneous wake (Betz, 1920; Joukowski, 1929). The De Vries (1979) analysis, reviewed in chapter 3, broadens this setup to include bodies that exert streamwise pressure forces on the flow by interacting with the actuation surface. Matched-actuator setups, studied in chapter 2, depend on a different but equally restrictive configuration.

Can a general framework of power coefficient limits be established? One that would not depend on *ex-ante* flow topology assumptions? Doing so would require the ability to define the power coefficient without considering the macroscopic features of any particular energy conversion system. This is challenging because the projected surface of rotor swept area has traditionally been central to the notion of power coefficient. A partial workaround could consist in formulating power coefficient laws at the infinitesimal level: conversion efficiency would then be studied from a purely flow-based perspective.

Infinitesimal studies of energy exchange exist since the early days of rotor aerodynamics (Wilson and Lissaman, 1974; Burton et al., 2002). Most approaches, however, depend on strict topology assumptions. Infinitesimal annuli are central to both traditional

(Betz, 1919; Glauert, 1935; Theodorsen, 1948) and modern (Sharpe, 2010; Jamieson et al., 2018; Sorensen, 2016) momentum theories. Vortex theories make use of different, but equally restrictive, topological assumptions (Joukowski, 1929; Goldstein, 1929; Coleman et al., 1945; Conway, 1995; Bontempo and Manna, 2016).

The present chapter takes steps to relax the above restrictions by focusing on individual streamlines instead of the macroscopic flow configuration. The power coefficient is then defined at the streamline level instead of the system level. This is achieved by attaching infinitesimally thin tubular control volumes to arbitrary streamline segments. I then call infinitesimal streamtubes.

Section 4.1 formalizes the infinitesimal streamtube concept and shows how to use it for computing balances of the main conserved quantities with three mathematical lemmas. Section 4.2 completes the formulation with a formal definition of actuation surfaces. The approach is relatively abstract. Section 4.3 shows how to apply the infinitesimal streamtube formulation to the actuator-body system. This relates with the ongoing debate about the optimality of homogeneously loaded actuator-disks. Section 4.4 summarizes the main findings.

4.1. INFINITESIMAL STREAMTUBE FORMULATION

This section studies the exchange of energy with steady flows of inviscid incompressible fluids from the perspective of infinitesimal streamtubes. Infinitesimal streamtubes are small tubular volumes attached to flow streamlines like the ones depicted on figure 4.1. They are 3-manifolds with infinitesimal cross-section, and contain the streamline segments to which they are attached, which are 1-manifolds immersed in \mathbb{R}^3 .

Infinitesimal streamtubes can be attached to any streamline that experiences no flow reversal. These streamlines can change direction and even make U-turns but stagnation and bifurcation points should be absent. In their presence, streamtube cross-sections become locally singular and the concept would lose its relevance. The infinitesimal streamtube concept is meant to enable straightforward computation of mass, momentum and energy balances. The following subsections present three lemmas for doing so.

4.1.1. MASS CONSERVATION

Mass conservation is stated in terms infinitesimal streamtube cross-sections. Cross-sections are 2-manifolds $d\Omega \subset \mathbb{R}^3$ that correspond to the intersection of an infinitesimal streamtube $Y \subset \mathbb{R}^3$ with a reference surface $\Omega \subset \mathbb{R}^3$. Any 2-manifold $\Omega \subset \mathbb{R}^3$ traversed by the infinitesimal streamtube can be a reference surface.

$$d\Omega = Y \cap \Omega$$

Infinitesimal streamtubes become wider when the flow accelerates and narrower when it decelerates because of mass conservation. Lemma 1 describes this phenomenon with the continuity equation. Its proof is presented in appendix B.1 and figure 4.1 clarifies the notation.

Lemma 1. Consider a smooth solenoidal flow field $\mathbf{U} : \mathbb{R}^3 \rightarrow \mathbb{R}^3$:

$$\nabla \cdot \mathbf{U} = 0$$

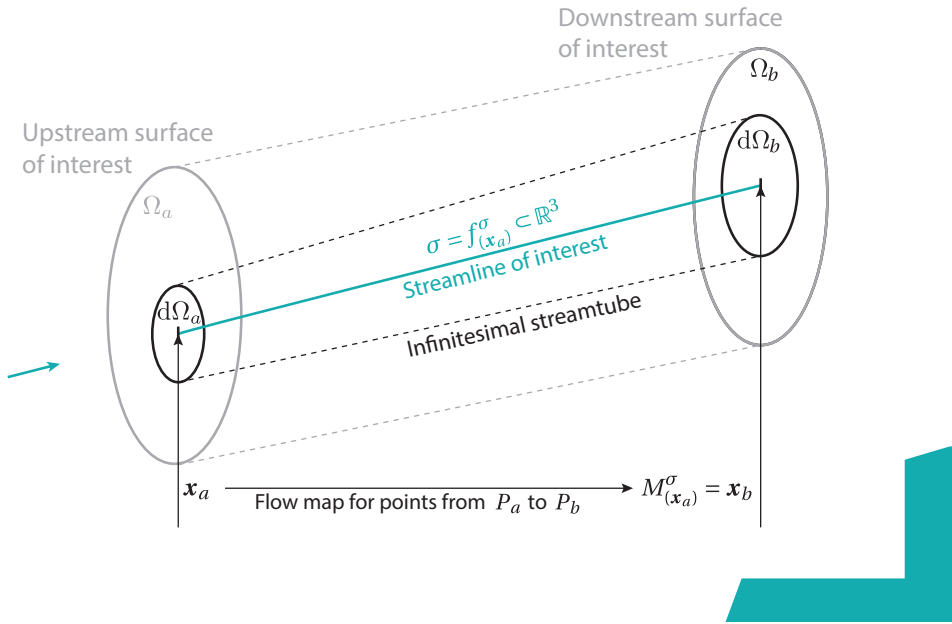


Figure 4.1: Arbitrary reference surfaces (P_a and P_b) considered in lemmas 1 and 2.

Let $P_a \subset \mathbb{R}^3$ be a smooth 2-manifold supporting the definition of a bijective map $f^\sigma : P_a \rightarrow \mathcal{P}(\mathbb{R}^3)$ that attaches a streamline $f^\sigma_{(x_a)} \subset \mathbb{R}^3$ to each point $x_a \in P_a$:

$$f^\sigma_{(x_a)} = \left\{ \mathbf{x}^\sigma \in \mathbb{R}^3 : \mathbf{x}^\sigma = \mathbf{x}_a + \int_0^\tau \mathbf{U}_{(\mathbf{x}^\sigma)} d\tau \quad , \forall \tau \in \mathbb{R} \right\}$$

Suppose $P_b \subset \mathbb{R}^3$ is a smooth 2-manifold for which a bijective map $M^\sigma : P_a \rightarrow P_b$ exists:

$$M^\sigma_{(x_a)} = \mathbf{x}_b \in \left(P_b \cap f^\sigma_{(x_a)} \right)$$

Volume conservation along infinitesimal streamtubes connecting P_a with P_b implies that:

$$\left(\mathbf{U}_{(x_a)} \cdot \mathbf{n}_a \right) dP_a = \left(\mathbf{U}_{(x_b)} \cdot \mathbf{n}_b \right) dP_b$$

Where \mathbf{n}_a and \mathbf{n}_b denote the normal unit vectors of the P_a and P_b surfaces at points x_a and x_b , with consistent choice of orientation.

4.1.2. MOMENTUM CONSERVATION

Momentum conservation dictates relations between flow velocity vectors \mathbf{U} at different stances of the infinitesimal streamtube. Lemma 2 makes these relations explicit from the Euler equations.

Lemma 2. Consider an incompressible flow governed by the steady variant of the Euler equations:

$$(\mathbf{U} \cdot \nabla) \mathbf{U} = -\frac{1}{\rho} \nabla p + \frac{1}{\rho} \mathbf{f}$$

Let $\sigma \subset \mathbb{R}^3$ be a smooth 1-manifold following a streamline between two points $\mathbf{x}_a, \mathbf{x}_b \in \mathbb{R}^3$ such that:

$$\sigma = \left\{ \mathbf{x} \in \mathbb{R}^3 : \mathbf{x}_{(\gamma)} = \mathbf{x}_a + \int_0^\gamma \mathbf{U}_{(\mathbf{x}_{(\tau)})} d\tau \wedge \mathbf{x}_{(\gamma_b)} = \mathbf{x}_b \right\}$$

If the velocity field $\mathbf{U} : \mathbb{R}^3 \rightarrow \mathbb{R}^3$ is smooth and no bifurcation occurs over σ :

$$|\mathbf{U}_{(\mathbf{x})}| \neq 0, \quad \forall \mathbf{x} \in \sigma$$

The following relation represents momentum conservation:

$$\mathbf{U}_{(\mathbf{x}_b)} - \mathbf{U}_{(\mathbf{x}_a)} = -\frac{1}{\rho} \int \frac{\nabla p}{|\mathbf{U}|} d\sigma + \frac{1}{\rho} \int \frac{\mathbf{f}}{|\mathbf{U}|} d\sigma$$

Where the integration is conducted from \mathbf{x}_a to \mathbf{x}_b .

Proof of lemma 2 is presented in appendix B.2. Despite its simplicity, this lemma is the heart of the infinitesimal streamtube formulation: it enables momentum balances to be conducted along streamlines.

4.1.3. ENERGY CONSERVATION

Energy conservation statements are often formulated along streamlines. The Bernoulli equation for inviscid incompressible flow and its generalized forms are obvious examples. Lemma 3, which is a simplified version of Crocco's theorem, expresses conservation of energy along infinitesimal streamtubes. Its proof follows the one by Greitzer et al. (2004) and is presented in appendix B.3.

Lemma 3. Consider a steady isentropic incompressible flow governed by the Euler equations and the fundamental thermodynamic relation:

$$(\mathbf{U} \cdot \nabla) \mathbf{U} = -\frac{1}{\rho} \nabla p + \frac{1}{\rho} \mathbf{f}, \quad dh = T ds + \frac{1}{\rho} dp$$

Let $\sigma \subset \mathbb{R}^3$ be a smooth 1-manifold following a streamline between two points $\mathbf{x}_a, \mathbf{x}_b \in \mathbb{R}^3$ such that:

$$\sigma = \left\{ \mathbf{x} \in \mathbb{R}^3 : \mathbf{x}_{(\gamma)} = \mathbf{x}_a + \int_0^\gamma \mathbf{U}_{(\mathbf{x}_{(\tau)})} d\tau \wedge \mathbf{x}_{(\gamma_b)} = \mathbf{x}_b \right\}$$

The following relation represents energy conservation along the streamline segment:

$$\left(h + \frac{1}{2} \mathbf{U} \cdot \mathbf{U} \right) \Big|_{\mathbf{x}_a}^{\mathbf{x}_b} = \frac{1}{\rho} \int \mathbf{f} \cdot \mathbf{r} d\sigma$$

where $\mathbf{r} \in T_\sigma$ denotes the tangent unit vector and h denotes the static enthalpy.

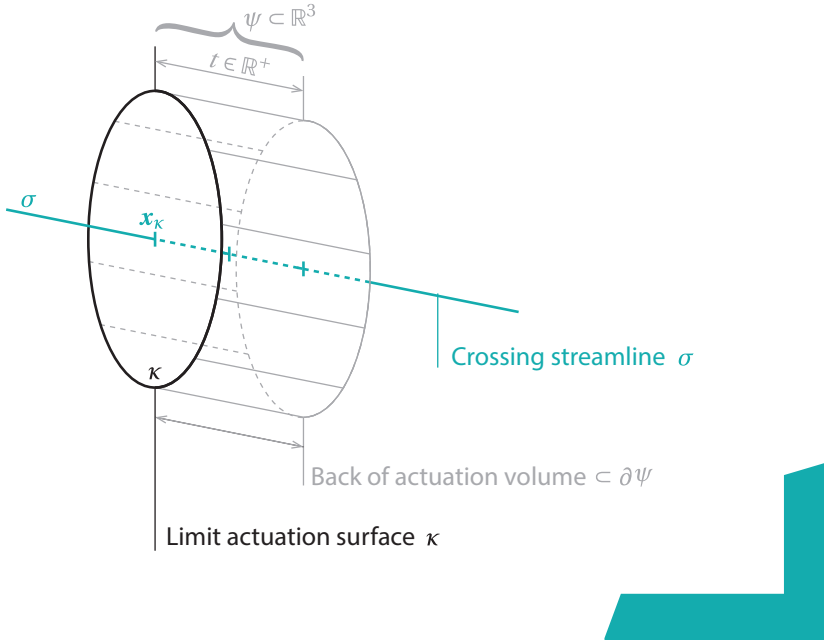


Figure 4.2: Actuation surface $\kappa \subset \mathbb{R}^3$ as asymptotic limit of actuation volume $\psi \subset \mathbb{R}^3$

4.2. FORMAL DESCRIPTION OF ACTUATION SURFACE

The actuator disk concept is extensively used in rotor aerodynamics. Even so, it lacks a consensual formal definition. Froude (Froude, 1889) conceptualized actuator-disks as surfaces over which a static pressure discontinuity occurs. Joukowsky (Joukowski, 1929), on the other hand, emphasized the role of the actuator disk as a surface that exerts external forces on the flow. The two approaches are generally consistent but lead to subtle formal differences. This work interprets actuation surfaces, of which actuator-disks are a particular case, from the perspective of externally imposed forces (denoted as \mathbf{f}). This approach is consistent with recent work of van Kuik (2014; 2015) but requires further specification for formal completeness.

We define actuation surfaces as 2-manifolds that correspond to the asymptotic limit of actuation volumes whose thickness tends to zero. The setup is clarified on figure 4.2. Forces are allowed to vary continuously over the actuation surface (κ) but chosen to be nearly constant across the thickness of the actuation volume (ψ). These assumptions are necessary to integrate actuation forces without ambiguity. This is necessary for applying lemmas 2 and 3 to the study of actuator disks and is with lemma 4.

Lemma 4. Consider a field of actuation forces $\mathbf{f} : \mathbb{R}^3 \rightarrow \mathbb{R}^3$ acting on a steady flow $\mathbf{U} : \mathbb{R}^3 \rightarrow \mathbb{R}^3$. Suppose all forces are exerted over an infinitesimally thin actuation volume $\psi \subset \mathbb{R}^3$ with thickness $t \in \mathbb{R}^+$ and let ψ tend to a twice differentiable 2-manifold $\kappa \subset \mathbb{R}^3$,

the actuation surface :

$$\kappa \in \lim_{t \rightarrow 0} \psi$$

Now describe actuation forces with a smooth vector field $\boldsymbol{\phi} : \kappa \rightarrow \mathbb{R}^3$:

$$\lim_{t \rightarrow 0} \int \mathbf{f} d\psi = \int \boldsymbol{\phi} d\kappa$$

Let $\sigma \subset \mathbb{R}^3$ denote a streamline that crosses the actuation surface once:

$$\sigma = \left\{ \mathbf{x} \in \mathbb{R}^3 : \mathbf{x}_{(\gamma)} = \mathbf{x}_\kappa + \int_0^\gamma \mathbf{U}_{(\mathbf{x}(\tau))} d\tau \right\}, \quad \mathbf{x}_\kappa = \sigma \cap \kappa$$

The integral of the body forces \mathbf{f} weighted with a smooth vector field $\mathbf{g} : \mathbb{R}^3 \rightarrow \mathbb{R}^n$ along streamline σ tends to:

$$\lim_{t \rightarrow 0} \int \mathbf{g}_{(\mathbf{x})} \mathbf{f}_{(\mathbf{x})} d\sigma = \frac{|\mathbf{U}_{(\mathbf{x}^\kappa)}|}{\mathbf{n}^\kappa \cdot \mathbf{U}_{(\mathbf{x}^\kappa)}} \mathbf{g}_{(\mathbf{x}^\kappa)} \boldsymbol{\phi}_{(\mathbf{x}^\kappa)}$$

Provided that forces are homogeneously distributed across the thickness of the actuation volume.

Lemma 4 is proved in appendix 3.4 and can be generalized to multiple actuation surfaces by summing the contribution of each crossing :

$$\lim_{t \rightarrow 0} \int \mathbf{g}_{(\mathbf{x})} \mathbf{f}_{(\mathbf{x})} d\sigma = \sum_j \frac{\mathbf{g}_{(\mathbf{x}^{x^j})} \boldsymbol{\phi}_{(\mathbf{x}^{x^j})}}{\mathbf{n}^{x^j} \cdot \mathbf{U}_{(\mathbf{x}^{x^j})}} \left| \mathbf{U}_{(\mathbf{x}^{x^j})} \right|$$

The integral of body forces from lemma 2 can be computed by setting the actuation force field as $\mathbf{f}_{(\mathbf{x})} = \mathbf{f}$ and $\mathbf{g}_{(\mathbf{x})} = \frac{1}{|\mathbf{U}_{(\mathbf{x})}|}$ as the weighting function. The formula of lemma 4 then reads:

$$\int \frac{\mathbf{f}}{|\mathbf{U}|} d\sigma = \lim_{t \rightarrow 0} \int \mathbf{g}_{(\mathbf{x})} \mathbf{f}_{(\mathbf{x})} d\sigma = \frac{\boldsymbol{\phi}_{(\mathbf{x}^\kappa)}}{\mathbf{n}^\kappa \cdot \mathbf{U}_{(\mathbf{x}^\kappa)}} \quad (4.1)$$

The integral of body forces present in lemma 3 can also be computed with lemma 4. To do so, commit a slight abuse of notation to set $\mathbf{g}_{(\mathbf{x})} = \mathbf{r} \cdot = \frac{\mathbf{U}_{(\mathbf{x})}}{|\mathbf{U}_{(\mathbf{x})}|} \cdot$ and $\mathbf{f}_{(\mathbf{x})} = \mathbf{f}$. The final expression of lemma 4 then reads:

$$\int \mathbf{f} \cdot \mathbf{r} d\sigma = \int \mathbf{g}_{(\mathbf{x})} \mathbf{f}_{(\mathbf{x})} d\sigma = \frac{\frac{\mathbf{U}_{(\mathbf{x})}}{|\mathbf{U}_{(\mathbf{x})}|} \cdot \boldsymbol{\phi}_{(\mathbf{x}^\kappa)}}{\mathbf{n}^\kappa \cdot \mathbf{U}_{(\mathbf{x}^\kappa)}} \left| \mathbf{U}_{(\mathbf{x}^\kappa)} \right| = \frac{\boldsymbol{\phi}_{(\mathbf{x}^\kappa)} \cdot \mathbf{U}_{(\mathbf{x})}}{\mathbf{n}^\kappa \cdot \mathbf{U}_{(\mathbf{x}^\kappa)}} \quad (4.2)$$

Expression 4.2 can be further simplified when the force density vector $\boldsymbol{\phi}$ is aligned with the normal of the actuation surface \mathbf{n}^κ :

$$\boldsymbol{\phi} \parallel \mathbf{n}^\kappa \quad \Rightarrow \quad \int \mathbf{g}_{(\mathbf{x})} \mathbf{f}_{(\mathbf{x})} d\sigma = (\pm) \left| \boldsymbol{\phi}_{(\mathbf{x}^{x^j})} \right| \quad (4.3)$$

When using the expression 3.4 care must be taken with the choice of the normal unit vector. It must be opposed to the flow ($\mathbf{n}^\kappa \cdot \mathbf{U} < 0$) and belong to the normal bundle of the actuation surface.

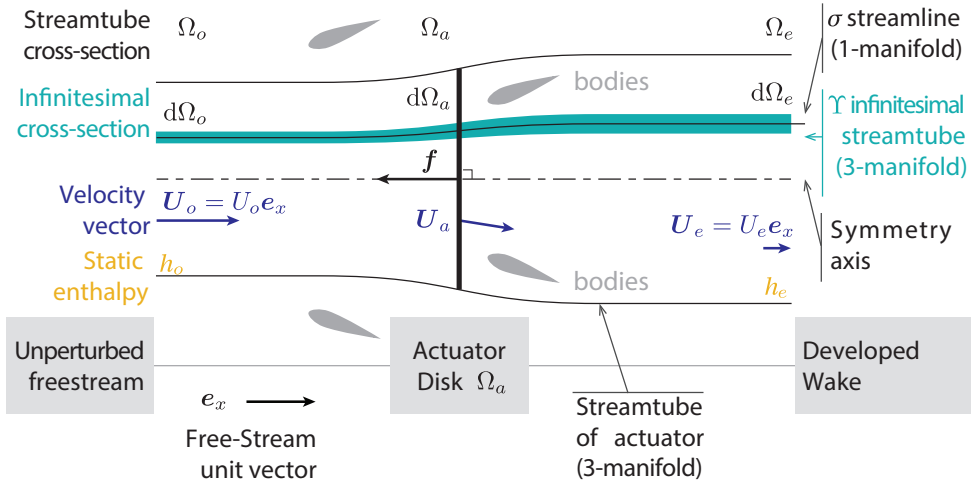


Figure 4.3: Flow configuration and nomenclature

4.3. APPLICATION TO ACTUATOR-DISK PROBLEM

The infinitesimal streamtube formulation consists of four lemmas that may seem rather abstract. This section demonstrates their application to a simple setup comprising a free-stream, a flat actuator-disk without swirl and a symmetric collection of bodies. The setup is depicted on figure 4.3 and is nearly identical to the one investigated in chapter 3. The loading density ($f_a = \varphi_a$) is now allowed to vary over the actuation surface (Ω_a).

4.3.1. MASS, MOMENTUM AND ENERGY BALANCES

The first step of the analysis consists in applying lemma 1 to a generic streamline that connects the inlet ($\Omega_o \subset \mathbb{R}^3$) to the actuation $\Omega_a \subset \mathbb{R}^3$ and outlet $\Omega_e \subset \mathbb{R}^3$ surfaces. The three reference surfaces are 2-manifolds and it is assumed that both the inlet and outlet lie asymptotically far away from the actuator.

$$(\mathbf{U}_{(x_o)} \cdot \mathbf{n}_o) d\Omega_o = (\mathbf{U}_{(x_a)} \cdot \mathbf{n}_a) d\Omega_a = (\mathbf{U}_{(x_e)} \cdot \mathbf{n}_e) d\Omega_e$$

$$\text{with } \mathbf{x}_o = M_{(x_a)}^{\sigma_{ao}} \text{ and } \mathbf{x}_e = M_{(x_a)}^{\sigma_{ae}} \quad (4.4)$$

$M^{\sigma_{ao}}$ and $M^{\sigma_{ae}}$ are bijections that follow streamlines to map points between reference surfaces, as in the proof of lemma 1.

MOMENTUM CONSERVATION

The bijections of expression 4.4 are also used to compute momentum balances with lemma 2. This is achieved by following a streamline segment, denoted as $\sigma \subset \mathbb{R}^3$, that connects a point on the inlet surface (Ω_o) to a point on the outlet surface (Ω_e).

$$\mathbf{U}_{(x_e)} - \mathbf{U}_{(x_o)} = -\frac{1}{\rho} \int \frac{\nabla p}{|\mathbf{U}|} d\sigma + \frac{1}{\rho} \int \frac{\mathbf{f}}{|\mathbf{U}|} d\sigma \quad (4.5)$$

The integral of external forces that appears in expression 4.5 is computed with lemma 4. It is applied by considering the crossing of a single actuation surface (Ω_a) whose normal unit vector (\mathbf{n}_a) is oriented against the freestream (\mathbf{U}_o):

$$\int \frac{\mathbf{f}}{|\mathbf{U}|} d\sigma = \frac{\boldsymbol{\phi}_{(\mathbf{x}_a)}}{\mathbf{U}_{(\mathbf{x}_a)} \cdot \mathbf{n}_a} \quad \text{with} \quad \mathbf{n}_a = -\mathbf{U}_o / |\mathbf{U}_o| = -\mathbf{e}_x \quad (4.6)$$

Function $\boldsymbol{\phi}_{(\mathbf{x}_a)}$ represents the surface density of forces exerted by the actuation surface at the streamtube intersection point (\mathbf{x}_a). It is a vector. To obtain a scalar relation, feed expression 4.6 into equation 4.5 and project the result on the normal of the actuation surface (\mathbf{n}_a):

$$\mathbf{U}_{(\mathbf{x}_e)} \cdot \mathbf{n}_a - \mathbf{U}_{(\mathbf{x}_o)} \cdot \mathbf{n}_a = - \left(\frac{1}{\rho} \int \frac{\nabla p}{|\mathbf{U}|} d\sigma \right) \cdot \mathbf{n}_a + \frac{1}{\rho} \frac{\boldsymbol{\phi}_{(\mathbf{x}_a)} \cdot \mathbf{n}_a}{\mathbf{U}_{(\mathbf{x}_a)} \cdot \mathbf{n}_a} \quad (4.7)$$

Now, consider a smooth parametrization of the actuation surface $\mathbf{s}^{\Omega_a} : (\eta, \xi) \rightarrow \Omega_a$ and use it to define a collection of useful functions:

$$\begin{aligned} \mathbf{U}_o : (\eta, \xi) &\rightarrow \mathbb{R} & \mathbf{U}_o &= \mathbf{U}_{(\mathbf{x}_o)} \cdot \mathbf{n}_a & \mathbf{x}_o &= M_{(\mathbf{x}_a)}^{ao} \\ \mathbf{U}_a : (\eta, \xi) &\rightarrow \mathbb{R} & \mathbf{U}_a &= \mathbf{U}_{(\mathbf{x}_a)} \cdot \mathbf{n}_a & \mathbf{x}_a &= \mathbf{s}_{(\eta, \xi)}^{\Omega_a} \\ \mathbf{U}_e : (\eta, \xi) &\rightarrow \mathbb{R} & \mathbf{U}_e &= \mathbf{U}_{(\mathbf{x}_e)} \cdot \mathbf{n}_a & \mathbf{x}_e &= M_{(\mathbf{x}_a)}^{ae} \\ \phi_a : (\eta, \xi) &\rightarrow \mathbb{R} & \phi_a &= \boldsymbol{\phi}_{(\mathbf{x}_a)} \cdot \mathbf{n}_a & & \end{aligned} \quad (4.8)$$

Denote the streamwise component of the resultant of pressure forces acting over the infinitesimal streamtube as ϕ_b :

$$\phi_b = \left(\left(\int \frac{\nabla p}{|\mathbf{U}|} d\sigma \right) \cdot \mathbf{n}_a \right) (\mathbf{U}_{(\mathbf{x}_a)} \cdot \mathbf{n}_a) \quad (4.9)$$

And use the notation of expressions 4.8 and 4.9 to rewrite equation 4.7 into a compact form:

$$(U_e - U_o) U_a = \frac{\phi_a}{\rho} - \frac{\phi_b}{\rho} \quad \Rightarrow \quad \phi_a = \rho (U_e - U_o) U_a + \phi_b \quad (4.10)$$

ENERGY CONSERVATION

Energy balances are obtained by applying lemma 3 between Ω_o and Ω_e :

$$\left(h + \frac{1}{2} \mathbf{U} \cdot \mathbf{U} \right) \Big|_{\mathbf{x}_o}^{\mathbf{x}_e} = \frac{1}{\rho} \int \mathbf{f} \cdot \mathbf{r} d\sigma \quad (4.11)$$

For symmetric flows without swirl like the one considered here, static enthalpy (h) returns to free-stream values as the wake develops (Jamieson et al., 2018). As result, all flow in the developed wake aligns with the free-stream:

$$\left. \begin{array}{l} h_e \rightarrow h_o \\ \text{symmetry} \end{array} \right\} \Rightarrow |\mathbf{U}_e| = \mathbf{U}_e \cdot \frac{\mathbf{U}_o}{|\mathbf{U}_o|} = \mathbf{U}_e \cdot \mathbf{e}_x \quad (4.12)$$

This boundary condition simplified equation 4.11 :

$$\frac{1}{2} (U_e^2 - U_o^2) = \frac{1}{\rho} \int \mathbf{f} \cdot \mathbf{r} d\sigma \quad (4.13)$$

The integral of actuation forces (\mathbf{f}) is computed with lemma 4 according to the procedure of expression 4.2.

$$\int \mathbf{f} \cdot \mathbf{r} d\sigma = \frac{\mathbf{U}_{(x_a)} \cdot \boldsymbol{\phi}_{(x_a)}}{\mathbf{U}_{(x_a)} \cdot \mathbf{n}_a} = \phi_a \quad \text{using} \quad \mathbf{g}_{(x)} \equiv \frac{\mathbf{U}_{(x)}}{|\mathbf{U}_{(x)}|}. \quad (4.14)$$

Inserting expression 4.14 into expression 4.13 leads to a compact statement for energy conservation at the local level:

$$\phi_a = \frac{1}{2} \rho (U_e^2 - U_o^2) \quad (4.15)$$

NORMAL FLOW VELOCITY AT ACTUATOR DISK

Two statements relate flow components with actuator loading ϕ_a : equation 4.10 represents momentum conservation and equation 4.15 corresponds to energy conservation. Simultaneous enforcement of both equations determines the normal flow velocity ($U_a = f(\eta, \xi)$) at the actuator intersection point (\mathbf{x}_a):

$$\begin{cases} \phi_a = \rho (U_e - U_o) U_a + \phi_b \\ \phi_a = \frac{1}{2} \rho (U_e^2 - U_o^2) \end{cases} \Rightarrow U_a = \frac{1}{2} (U_e + U_o) - \frac{\phi_b}{\rho (U_e - U_o)} \quad (4.16)$$

Expression 4.16 is best interpreted by defining adimensional groups that describe forces (ϕ_a, ϕ_b) and normal flow velocities (U_a, U_e):

$$\begin{aligned} u_a &= \frac{U_a}{U_o} : (\eta, \zeta) \rightarrow \mathbb{R} & C_{\phi_a} &= \frac{\phi_a}{\frac{1}{2} \rho U_o^2} : (\eta, \zeta) \rightarrow \mathbb{R} \\ u_e &= \frac{U_e}{U_o} : (\eta, \zeta) \rightarrow \mathbb{R} & C_{\phi_b} &= \frac{\phi_b}{\frac{1}{2} \rho U_o^2} : (\eta, \zeta) \rightarrow \mathbb{R} \end{aligned} \quad (4.17)$$

Inserting the groups of expression 4.17 into expression 4.16 leads to a description of relative normal speed (u_a) at the actuator in terms of the streamwise pressure force coefficient (C_{ϕ_b}) and the relative wake velocity (u_e). The relative wake velocity is uniquely determined by the actuation force coefficient (C_{ϕ_a}).

$$u_a = \frac{1}{2} \left((u_e + 1) - \frac{C_{\phi_b}}{(u_e - 1)} \right) \quad , \quad u_e^2 = C_{\phi_a} + 1 \quad (4.18)$$

4.3.2. POWER COEFFICIENT OF INFINITESIMAL STREAMTUBES

The power dP extracted from an infinitesimal streamtube corresponds to the product of the surface density of actuation forces ($\phi_a = \phi_a(\eta, \zeta)$), the normal speed ($U_a = U_a(\eta, \zeta)$) at the actuator, and the area ($d\Omega_a$) of its intersection of with the infinitesimal streamtube. This definition is consistent with formal balances of total flow enthalpy.

$$dP = \phi_a U_a d\Omega_a \quad (4.19)$$

Expression 4.19 is used to study extraction efficiency by defining a power coefficient (C^{dP}) for infinitesimal streamtubes. The chosen reference surface corresponds to the area ($d\Omega_a$) of the intersection between the infinitesimal streamtube and the actuator

disk. The projected area of the streamtube intersection on a plane normal to the free-stream would be an appropriate choice for curved or misaligned actuation surfaces.

$$C^{dP} = \frac{dP}{\frac{1}{2}\rho U_o^3 d\Omega_a} = \left(\frac{\phi_a}{\frac{1}{2}\rho U_o^2} \right) \left(\frac{U_a}{U_o} \right) \left(\frac{d\Omega_a}{d\Omega_a} \right) = C_{\phi_a} u_a \quad \text{given} \quad d\Omega_a = \left(-\mathbf{n}_a \cdot \frac{\mathbf{U}_o}{|\mathbf{U}_o|} \right) d\Omega_a \quad (4.20)$$

The power coefficient varies over the energy extraction surface ($C^{dP} : (\eta, \zeta) \rightarrow \mathbb{R}^3$). It can be parametrized with the approach of expression 4.8 or reworked into a convenient form using expression 4.17:

$$\begin{aligned} C^{dP} &= \frac{1}{2} (u_e + 1) ((u_e^2 - 1) - C_{\phi_b}) \\ &= \frac{1}{2} \left(1 + \sqrt{C_{\phi_a} + 1} \right) (C_{\phi_a} - C_{\phi_b}) \end{aligned} \quad (4.21)$$

Expression 4.21 describes the power coefficient of any infinitesimal streamtube that crosses the actuator disk. It depends on the terminal wake speed (u_e), which is entirely dictated by the actuator loading (C_{ϕ_a}) at the streamtube intersection point \mathbf{x}_a and the streamwise pressure force coefficient (C_{ϕ_a}).

RELATION WITH THE POWER COEFFICIENT LAW OF DE VRIES

The expression for the power coefficient of infinitesimal streamtubes that cross a single actuation surface (4.21), shares its structure with the expression for the power coefficient of a constant loading actuator disk surrounded by bodies (B.4). Despite their resemblance, these equations say different things.

The de Vries law (B.4) applies to the actuator disk as whole, whereas expression 4.21 applies locally to infinitesimal streamtubes. It is more general than expression B.4, which can also be obtained by integrating expression 4.21 over the entire actuator disk. The converse is not true and appendix B.5 clarifies the relation between the two expressions.

TRENDS IN LOCAL POWER COEFFICIENT

4.3.3. OPTIMAL LOADING DISTRIBUTION

The expression (4.21) for the power coefficient of an infinitesimal streamtube that crosses a single actuation surface, shares its structure (B.4) with the expression for the power coefficient of an homogeneously loaded actuator disk surrounded by bodies. This observation begs for troubling considerations.

Chapter 3 showed that the optimal loading (C_{F_a}) of an actuator-disk depends on the magnitude of streamwise pressure forces (C_{F_b}). It is therefore expectable that the magnitude of streamwise pressure forces (C_{ϕ_b}) that act on an infinitesimal streamtube affects its optimal loading (ϕ_a). Would it, then, be the case that the optimal loading distribution of an isolated actuator-disk depends on the streamwise pressure forces that infinitesimal streamtubes (or annuli) exert on each other?

The question has been asked before (Van Kuik et al., 2014) but, to the best of our knowledge, the optimality of homogeneous actuator loadings remains to be formally proven. We were unable to obtain a conclusive answer on that matter.

Variable		Numerical	Analytical	Relative error
Power coefficient of entire actuator-disk	$C_{\bar{p}}$	-0.5935	$-16/27$ ≈ -0.5926	0.15555%
Average normal velocity over entire actuator-disk	\bar{U}_a	0.6677	$2/3$ ≈ 0.6667	0.15555%
Average induction factor over entire actuator-disk	\bar{a}	0.3323	$1/3$ ≈ 0.3333	-0.3111%

Table 4.1: Accuracy of numerical solutions for isolated actuator disk flow with thrust coefficient $C_{Fa} = -8/9$ and unit free stream.

Even in the absence of definitive answers, the magnitude of potential gains that might arise from non-homogenous actuator loading distributions can be estimated by complementing the infinitesimal streamtube formulation with numerical solutions. Our estimation procedure is exactly that: an estimate. It does not guarantee that inhomogeneous actuator loadings can be advantageous, nor places a firm upper bound on the potential gains that they might bring. But it provides insight about their relevance, and contributes to the discussion about inhomogeneous flow features that arise on homogeneously loaded actuator-disks.

We proceed in three steps. The first step consists in using a numerical solver to predict the velocity distribution over a homogeneously loaded actuator disk with optimal thrust coefficient ($C_T = 8/9$). The second step consists in processing the velocity field to determine the magnitude of pressure forces that act on individual infinitesimal streamtubes. Finally, a new (tentatively) optimal actuator loading is determined from an extremum analysis based on the (unrealistic) assumption of an invariant pressure field. The magnitude of disparities between the initial, a newly determined actuator loading is

Velocity distributions over constant-loading actuator-disks can be obtained with semi-analytical (Conway, 1995; Bontempo and Manna, 2016), grid-based (Sorensen et al., 1998; Rethore et al., 2014) or vortex-based approaches (Van Kuik and Lignarolo, 2015; Gamme et al., 2017). The later option was chosen for the sake of convenience, used the steady-state vortex solver that was already used in chapters 2 and 3. The wake was discretized in 200 panels of constant vorticity up to a distance of 3000 actuator disk diameters. Naturally, the discretization was more refined near the actuator disk, and the shape of the wake was iterated to match the flow field. Power coefficient predictions, which function as a conservative measure for the accuracy of the numerical method, are compared against analytical predictions in table 4.1. They match to within a few tenths of percent and it is thought that disparities arise primarily from quadrature errors during the postprocessing of velocity fields, even if spatial discretization errors also have some significance (Gamme et al., 2017).

The magnitude of streamwise pressure forces exerted on infinitesimal streamtubes can be determined from the actuator-disk velocity distribution ($u_a : (\eta, \zeta) \rightarrow \mathbb{R}$) by inverting expression 4.17 :

$$C_{\phi_b} = (u_e + 1)(u_e - 1) - 2u_a(u_e - 1) \quad (4.22)$$

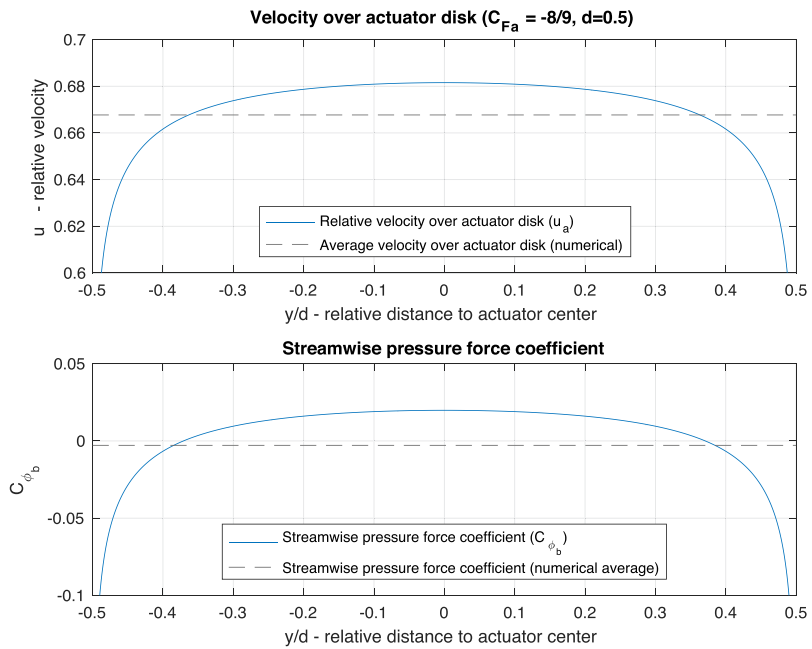


Figure 4.4: Velocity (*top*) and streamwise pressure force coefficient (*bottom*) over an isolated actuator-disk with diameter d and homogeneous loading leading to a thrust coefficient $C_{Fa} = -8/9$.

Results are plotted on figure 4.4. They show that infinitesimal streamtubes close to center of the actuator disk, between $y/d \approx -0.38$ and $y/d \approx +0.38$, are subject to net streamwise pressure forces that accelerate the flow ($C_{\phi_b} > 0$) and enhance power exchange ($u_a > \bar{U}_a$). The flow comprises no bodies that might support streamwise forces, so these pressure forces must be exerted by infinitesimal streamtubes located near the edge of the actuator disk. The action-reaction principle therefore subjects these streamtubes to streamwise pressure forces that decelerate the flow ($C_{\phi_b} < 0$) and hinder power exchange ($u_a < \bar{U}_a$).

The actuator-disk considered in the present numerical experiment is operating at the Betz limit. It has a homogeneous loading distribution, a thrust coefficient $C_{F_a} = -8/9$ and a global power coefficient $C_{\bar{p}} = -16/27$. But individual streamtubes, or actuator annuli, are not operating in these conditions. They operate below the Betz limit near the edges, and above in the central region of the actuator-disk. This is consistent with recent remarks by Jamieson (Jamieson et al., 2018).

Considering that streamwise pressure forces alter the optimal thrust coefficient of an homogeneously loaded actuator-disk, as was shown in chapter 3, one might wonder if it would make sense to tailor the actuator loading distribution to the needs of individual streamtubes. If streamwise pressure forces would remain constant, individual streamtubes subject to different streamwise pressure forces (C_{ϕ_b}) would reach their highest power coefficient at a different actuator loading ($C_{\phi_a}^{opt}$ given C_{ϕ_b}). A simple extremum analysis of expression 4.21, similar to that of section 4.21, then suggests that:

$$C_{\phi_a}^{opt} \Big|_{C_{\phi_b}} = \left(u_e^{opt} \Big|_{C_{\phi_b}} \right)^2 - 1 \quad \text{with} \quad u_e^{opt} \Big|_{C_{\phi_b}} = -\frac{1}{3} \left(1 - \sqrt{4 - 3C_{\phi_b}} \right) \quad (4.23)$$

Expression 4.23 is plotted on figure 4.5, for the distribution of streamwise pressure forces of figure 4.4. It suggests, but certainly does not prove, that actuator-disks should be more heavily loading at their edges to maximize power exchange.

The suggestions of expression 4.23 would only be exact if the distribution of streamwise pressure forces remained unaffected by changes in actuator loading. This is obviously not the case. But the ‘‘possibly optimal’’ actuator loading distribution serves as an indication of the order of magnitude of changes that one can possibly expect. And it suggests that such an inhomogeneous actuator loading would have a negligible effect on the power coefficient of the overall actuator. Expected changes fall below the precision of the numerical method.

4.4. NEW FINDINGS AND IMPLICATIONS

The infinitesimal streamtube formulation established in this chapter contains four lemmas. One enables integration of forces across energy-exchange surfaces, and the three others provide balances of conserved quantities. The formulation is rather general, but that comes with a price. Models are only closed for average values and relatively simple cases.

Strategies for applying the infinitesimal streamtube formulation were demonstrated on the simple problem of actuator-body interactions. The main result was an expression for the power coefficient of infinitesimal streamtubes. Unexpectedly, that expression

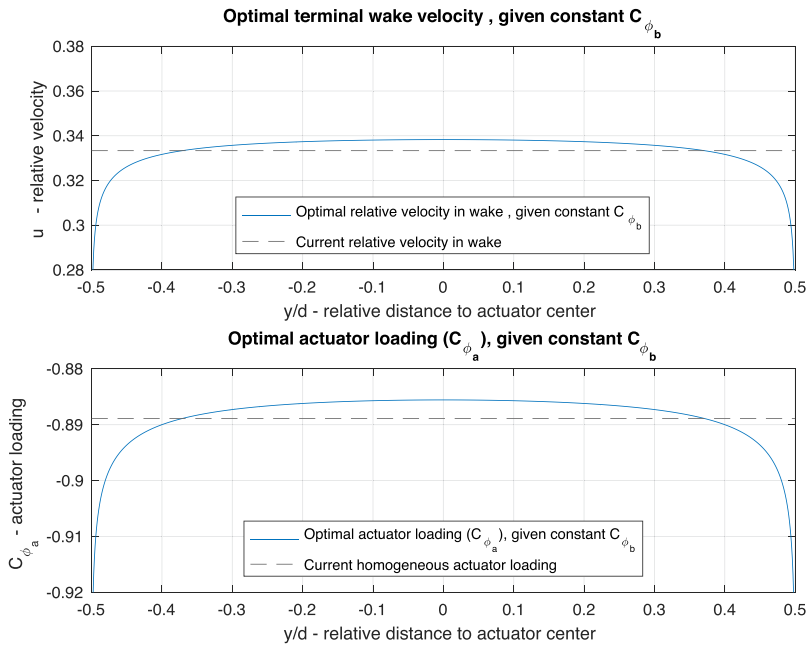


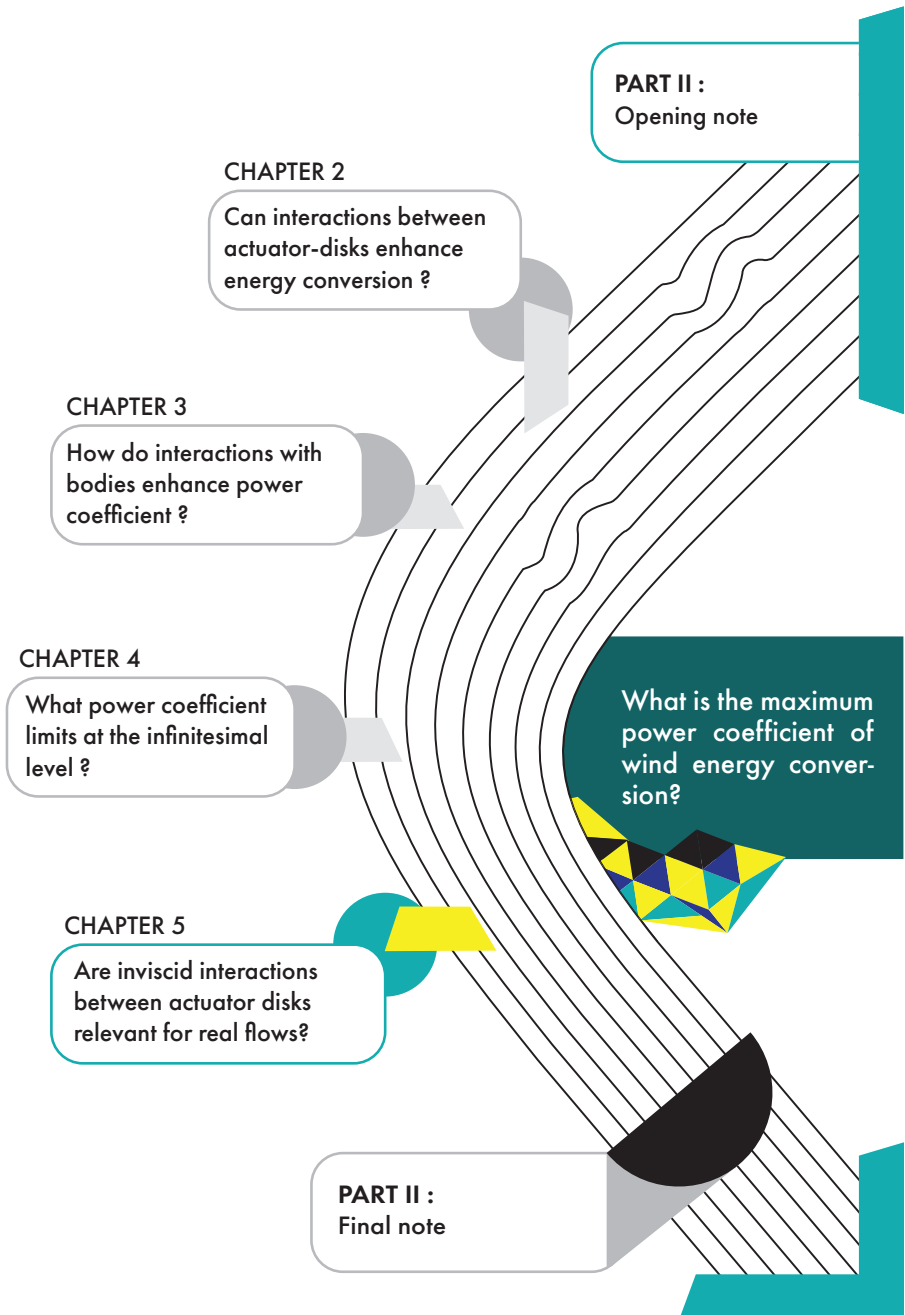
Figure 4.5: Possibly optimal terminal wake velocity and actuator loading, given constant C_{ϕ_b}

shared its structure with the power coefficient law of De Vries – which applies to the entire actuator.

An irresistible question then had to be asked. Given that infinitesimal streamtubes experience different pressure forces over constant loading actuator-disks, can non-homogeneous actuator loading distributions lead to enhanced energy extraction? The author was unable to provide a definitive answer. What became clear for isolated actuators, however, is that gains are likely to be negligible if they are possible at all. Repeating the exercise with a nearby body seems likely to lead to different results.

Applications of the infinitesimal streamtube formulation go beyond analytical work and actuator-body problems. Infinitesimal streamtubes can be used to benchmark CFD computations, validate PIV measurements and develop semi-analytical models of complex flow configurations. Future publications should clarify these points. The main aim of this formulation, however, is to provide a different viewpoint on energy. One that, the author hopes, may guide the optimisation of complex flow systems.

Study of flow streamlines highlights interactions that determine the performance of energy exchange. Several open problems in rotor aerodynamics could benefit from this kind of approach. A first problem that comes to mind concerns the study of boundary-layer ingestion propulsion setups. The second concerns the study of pressure force interactions between adjacent wind turbines and met masts. This phenomenon, which remains relatively undocumented, is attracting increasing attention.



5

EXPLOITING WAKE INTERACTIONS IN NON-CONSERVATIVE FLOWS

How do diffusive and dissipative flow phenomena affect the performance of matched actuator setups? Should the area of the largest actuator be used as a reference? Is inviscid theory relevant for non-conservative flows?

Matched-actuator setups are able to extract arbitrary amounts of energy per unit surface from steady flows of inviscid incompressible fluids. Are such inviscid flow considerations of any relevance to real flows? If that would be the case, active flow augmentation could possibly open new opportunities for advancing the efficiency of wind energy conversion. In the present state of knowledge, however, one might also argue that active flow augmentation is unlikely to be nothing more than a complicated way of showing the limited envelope of inviscid flow perspectives.

Inviscid design approaches powered the synthesis of subsonic rotors and aircraft for nearly a hundred years. Their main advantage is the ability to capture the dominant convective dynamics of a system by solving a simplified flow problem. Solutions of that problem are then perturbed to account for the effect of viscous or compressible flow phenomena (Lighthill, 1958; von Karman, 1941; Tsien, 1939). Perturbation strategies of that kind are well supported by formal arguments (Sychev et al., 1998; Cousteix and Mauss, 2007) and enabled the design of iconic aircraft like the Fokker-100 or the Osprey V-22 tilt-rotor (Rosenstein and Clark, 1986; Van Garrel, 2016). But inviscid design approaches can also be misleading: for example, viscous effects usually need to be considered from the first design step when dimensioning flow distribution networks, irrespective of the Reynolds number (Brederode, 2014).

The wind energy community holds diverse opinions about the value of inviscid flow metaphors. Blade and airfoil designers generally praise ideal flow perspectives for making sense of otherwise intractable rotor design problems. Windfarm designers, on the other hand, often disconsider convective dynamics to highlight the role of diffusive processes in wake mixing and recovery (Jensen, 1983); inviscid flow perspectives are then of limited value since macroscopic flow scales are dominated by non-conservative phenomena.

Which perspective should apply to the study of matched-actuator setups? There is no *a priori* answer because active flow augmentation mechanisms hinge on the ability to decouple fast convective dynamics from slow diffusive processes. The neglect of viscous diffusion and dissipation is a major objection to the inviscid treatment of matched-actuator setups. Another objection concerns the potentially detrimental effects of compressibility. Finally, a third and somehow unrelated issue concerns the choice of an appropriate reference area for defining the power coefficient.

The present chapter takes preliminary steps to address the above concerns. Section 5.1 studies the effect of non-conservative flow phenomena on the power coefficient of matched-actuator setups by representing them as arbitrarily prescribed total enthalpy losses. Section 5.2 repeats the exercise with an alternative reference area compatible with the conventions of wind farm design. Section 5.3 assesses expectable enthalpy and energy loss levels with various approaches. The main conclusions are summarized in section 5.4.

5.1. MATCHED-ACTUATOR SETUP WITH ENTHALPY LOSSES

The physical processes of wake diffusion and dissipation cannot be predicted with analytical approaches. Yet, their effect on the performance of matched actuator setups can be approximated by connecting two limit conditions:

- The inviscid limit – corresponds to the situation described in chapter 2 (section 5.11). The fluid opposes no resistance to shear so the wake of the first actuator persists indefinitely. Flow maintains the total enthalpy offset introduced by the first actuator until it reaches the second actuator. The second actuator recovers all the energy injected by the first actuator, and benefits from increased mass flow. The power coefficient of the entire setup is then written as:

$$C_{P_1}^{inv} = \frac{P_1}{\frac{1}{2} \rho S_2 U_0^3} = b(1 - a_2)(b^2 - 1) \quad (5.1)$$

$$C_{P_2}^{inv} = \frac{P_2}{\frac{1}{2} \rho S_2 U_0^3} = -b^3(4a_2)(1 - a_2)^2 \quad (5.2)$$

$$C_P^{inv} = \frac{P_1 + P_2}{\frac{1}{2} \rho S_2 U_0^3} \quad (5.3)$$

- The viscous limit – corresponds to the case in which the fluid opposes resistance to shear and actuators-disks are infinitely far apart. The wake of the first actuator diffuses and dissipates completely before reaching the downstream actuator,

which then operates exactly as it would in an unperturbed free-stream. The power coefficient of the entire setup is then written as:

$$C_{P_1}^{visc} = \frac{P_1}{\frac{1}{2}\rho S_2 U_0^3} = b(1 - a_2)(b^2 - 1) \quad (5.4)$$

$$C_{P_2}^{visc} = \frac{P_2}{\frac{1}{2}\rho S_2 U_0^3} = -(4a_2)(1 - a_2)^2 \quad (5.5)$$

$$C_P^{visc} = \frac{P_1 + P_2}{\frac{1}{2}\rho S_2 U_0^3} \quad (5.6)$$

Matched-actuator setups operate somewhere between the viscous and inviscid limits when their actuator-disks are separated by a large but finite distance and the fluids opposes a resistance to shear. Part of the total enthalpy offset introduced by the upstream actuator reaches the downstream actuator, while the other part is lost to wake diffusion and dissipation. The phenomenon can be described with an adimensional parameter γ :

$$\gamma : \quad \bar{h}_{a2}^t = \begin{cases} h_0^t & \gamma = 0 \quad \text{viscous limit} \\ h_0^t + \gamma(\bar{h}_{a1}^t - h_0^t) & 0 < \gamma < 1 \\ h_{a1}^t = h_0^t + \frac{1}{\rho}f_1 & \gamma = 1 \quad \text{inviscid limit} \end{cases} \quad (5.7)$$

The \bar{h}_{a1}^t and \bar{h}_{a2}^t symbols denote the average total enthalpies¹ integrated just behind the upstream actuator (Ω_{1a}) and in front of the downstream actuator (Ω_{2a}), respectively.

$$\bar{h}_{a1}^t = \frac{\int \left(\frac{1}{2} (\mathbf{U} \cdot \mathbf{U})^2 + \frac{p}{\rho} \right) \Omega_{1a}^{back}}{\int \Omega_{1a}^{back}}, \quad \bar{h}_{a2}^t = \frac{\int \left(\frac{1}{2} (\mathbf{U} \cdot \mathbf{U})^2 + \frac{p}{\rho} \right) \Omega_{2a}^{front}}{\int \Omega_{2a}^{front}}$$

Changes in total enthalpy can be represented by defining two speedup ratios: one defined from the total enthalpy of flow that just crossed the first actuator (b , equivalent to expression 2.20), and the other from the total enthalpy of flow just before it crosses the downstream actuator (b_{eff}).

$$b = \left(\frac{h_{a1}^t - h_0}{h_0^t - h_0} \right)^{\frac{1}{2}} = \left(1 + \frac{f_1}{\frac{1}{2}\rho U_0^2} \right)^{\frac{1}{2}}$$

$$b_{\text{eff}} = \left(\frac{\bar{h}_{a2}^t - h_0}{h_0^t - h_0} \right)^{\frac{1}{2}} = \left(1 + \frac{\gamma f_1}{\frac{1}{2}\rho U_0^2} \right)^{\frac{1}{2}} = (1 + \gamma(b^2 - 1))^{\frac{1}{2}} \quad (5.8)$$

The speedup ratios of expression 5.8 do not map directly into flow velocities. Instead, they are used to estimate the power coefficient of a matched-actuator setup by analogy with expressions 5.1 to 5.6:

¹Strictu sensu, variables \bar{h}_{a1}^t and \bar{h}_{a2}^t denote the mass density of mechanical energy instead of the total enthalpy. The internal energy component is neglected but this is not problematic because the flow is treated as incompressible and viscous dissipation is considered an irreversible loss.

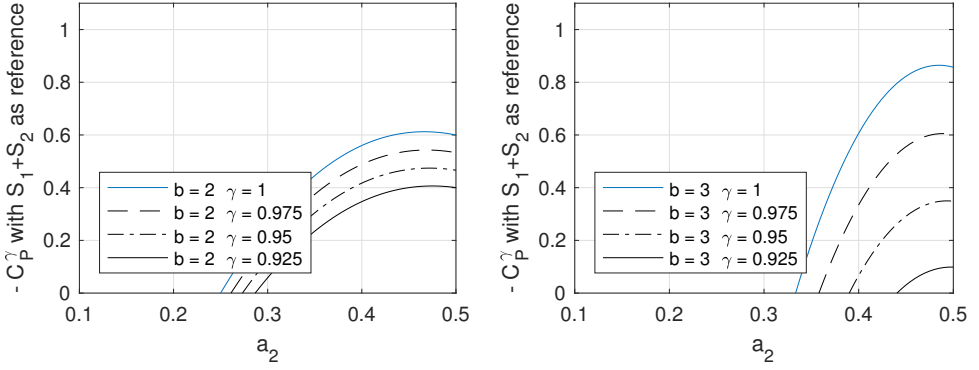


Figure 5.1: Power coefficient of matched actuator setup with inter-actuator energy losses and area of largest actuator as a reference, as given by expression 5.11.

$$C_{P_1}^\gamma = \frac{P_1}{\frac{1}{2}\rho S_2 U_0^3} = b(1-a_2)(b^2-1) \quad (5.9)$$

$$C_{P_2}^\gamma = \frac{P_2}{\frac{1}{2}\rho S_2 U_0^3} = -b_{\text{eff}}^3(4a_2)(1-a_2)^2 \quad (5.10)$$

$$C_P^\gamma = \frac{P_1 + P_2}{\frac{1}{2}\rho S_2 U_0^3} = b(1-a_2)(b^2-1) - (1+\gamma(b^2-1))^{\frac{3}{2}}(4a_2)(1-a_2)^2 \quad (5.11)$$

Figure 5.1 plots expression 5.11 for various values of the total enthalpy loss parameter. Before studying power coefficient trends, however, it is desirable to extend the analogy of expression 5.11 into a complete setup definition:

$$\begin{cases} \frac{f_1^\gamma}{\frac{1}{2}\rho U_0^2} = (b^2-1) \\ \frac{f_2^\gamma}{\frac{1}{2}\rho U_0^2} = -(4b_{\text{eff}}^2)(a_2(1-a_2)) \end{cases} \quad \text{and} \quad \frac{S_1}{S_2} = \frac{b(1-a_2)}{\frac{1}{2}(b+1)} \quad (5.12)$$

Expressions 5.12 can be used to derive 5.9-5.11 from control volume arguments. The procedure is trivial and if a homogeneous velocity is assumed across the wake. More interesting, however, is to look at the total enthalpy of flow leaving the downstream actuator (h_e^t):

$$h_e^t = h_{a_2}^t + \frac{1}{\rho} f_2 = h_0^t + \frac{\gamma}{\rho} f_1 + \frac{1}{\rho} f_2 \quad (5.13)$$

In real flows, that flow will progressively return to free-stream velocity and enthalpy levels because of viscous and turbulent wake mixing phenomena. But even then, it makes sense to map the h_e^t total enthalpy into an equivalent wake speed ($u_e^\gamma = U_e^\gamma/U_0$) whose value determines the likelihood of wake instabilities:

$$u_e^\gamma = \left(\frac{h_e^t - h_0}{h_0^t - h_0} \right)^{\frac{1}{2}} = b_{\text{eff}}(1-2a_2)$$

Like expression 2.30, the power coefficient law of expression 2.2.3.2 is only applicable if the following conditions are met (based on expression 2.33):

$$b > 0.2 \quad \text{avoid instability in inter-actuator region} \quad (5.14)$$

$$u_e^\gamma > 0.2 \quad \text{avoid instability of terminal wake} \quad (5.15)$$

Furthermore, expression 5.11 only applies if all flow velocities remain well below the speed of sound (a_0) because its precursors treated all fluid flow phenomena as incompressible:

$$M_0 = \frac{U_0}{a_0} < 0.3 \quad \text{(quasi)incompressible freestream} \quad (5.16)$$

$$bM_0 < 0.3 \quad \text{(quasi)incompressible inter-actuator flow} \quad (5.17)$$

The bound of expressions 5.16-5.17 is unlikely to be relevant. The speed of sound in air is $a_0=340.294 \text{ m/s}$ for standard atmosphere (ISA) conditions at mean sea level (MSL). A 12m/s wind then has Mach number $M_0 = 0.035$ and the Mach 0.3 criterion of expression 5.17 requires an inter-actuator speed ratio (b) smaller than 8.51. This is a fairly large number, corresponding to a thrust coefficient $C_T > 70$. Viscous energy losses, and the risk of chaotic breakdown, would probably rule out of such a flow condition anyway.

5.1.1. OPTIMAL SETUP WITH INTER-ACTUATOR ENTHALPY LOSSES

This section moves on to study the optimal performance of matched actuator setups subject to different levels of prescribed inter-actuator enthalpy losses. The idea is to identify the effect of different γ parameters on the minimum achievable power coefficient. Energy extraction corresponds to negative C_p^γ values. This is achieved by defining a constrained optimization problem from expression 5.11 and expressions 5.14 to 5.17:

$$\begin{aligned} \min_{(a_2, b)} \quad & C_p^\gamma = f_{(a_2, b, \gamma)} \\ \text{subject to} \quad & \text{prescribed } \gamma \\ & 0.2 < u_e^\gamma \\ & 0.2 < b < 8.5 \end{aligned} \quad (5.18)$$

The problem of expression 5.18 was solved numerically for 200 equally spaced values of the γ parameter spread over the $[0, 1]$ interval. Constraints were enforced with Lagrange multipliers to a tolerance of 1E-10 and the numerical procedure hinged on the hybrid interior-point algorithm proposed by Waltz et al. (2006). Gradients were estimated with central differences and the Hessian was approximated with the BFGS method. The optimization stopped when the optimality measure decreased to 1E-10 or when the step size between iterations vanished to 1E-14. Both criteria were considered valid convergence signals. The problem is not particularly difficult and can probably be solved analytically: future work should investigate that possibility and seek to obtain formal on problem convexity.

Results of the numerical optimization exercise are presented on figure 5.2. It suggests that it is beneficial to operate the first actuator in propeller mode ($b > 1$ implies $f_1 > 0$)

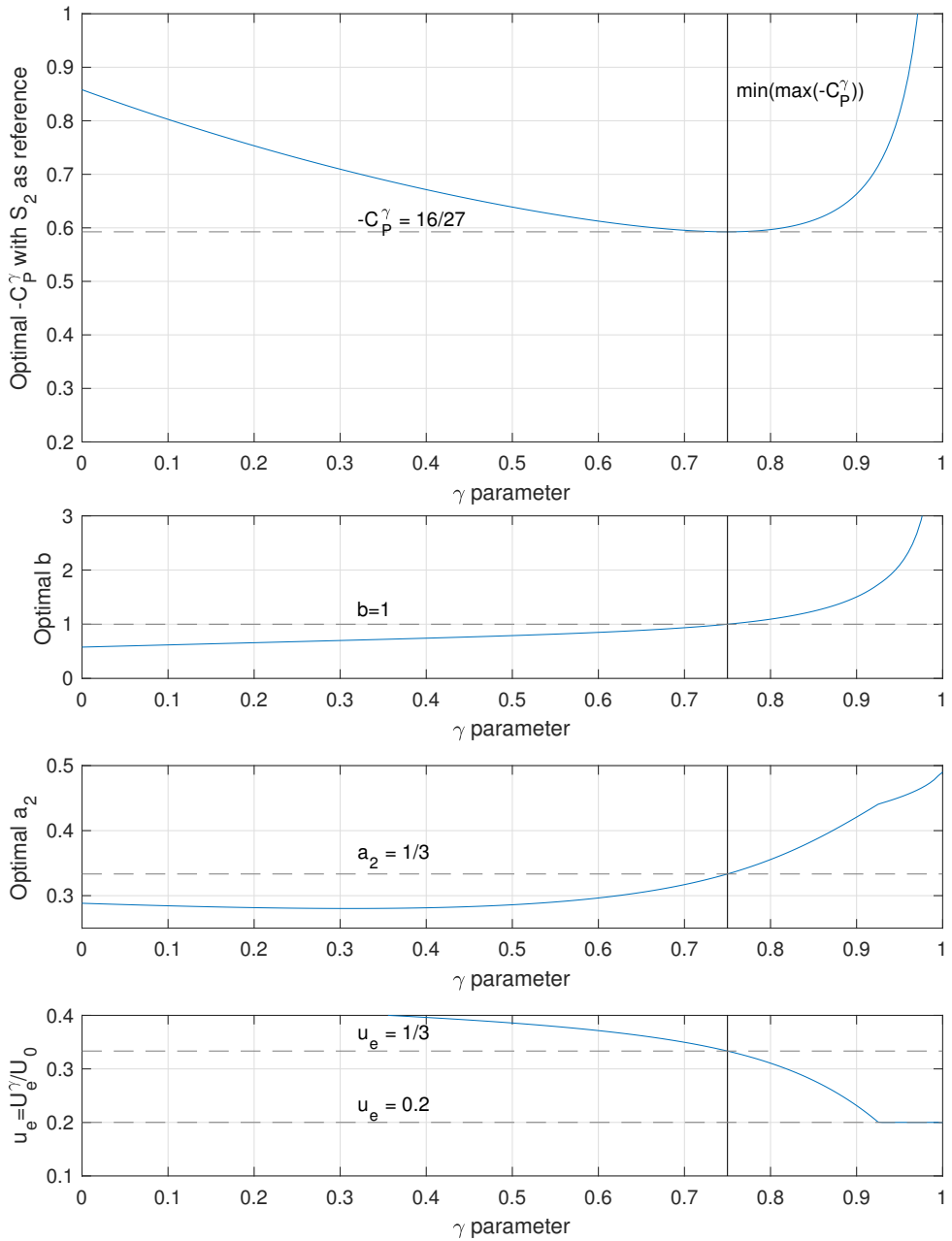


Figure 5.2: Effect of enthalpy loss parameter (γ) on optimal power coefficient of matched actuator setup, in the sense of problem 5.18. The area of the largest actuator is used as a reference.

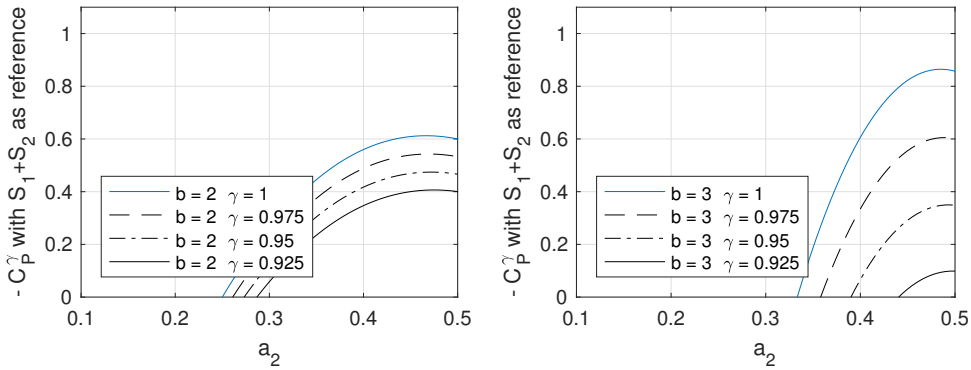


Figure 5.3: Power coefficient of matched actuator setup with inter-actuator enthalpy losses and sum of actuator areas as a reference, as given by expression 5.22.

when its slipstream has lost less than a quarter ($\gamma \approx 0.75$) of its total enthalpy offset by the time it reaches the downstream actuator. If diffusive and dissipative flow processes lead to a greater loss of total enthalpy, however, it is better to operate both actuators in wind turbine mode ($b < 1$ implies $f_1 < 0$). What remains to be determined, is the magnitude of the γ parameter. It will be investigated in section

According to figure 5.2, matched-actuator setups can reach power coefficients (C_p^γ) above $16/27$ for nearly all enthalpy loss parameter values, except around ($\gamma \approx 0.75$). That is because expression 5.11 ignores the area of the upstream actuator. That can lead to counter-intuitive situations. For example, when $\gamma = 0$, the two actuators operate without influencing each other from a physical perspective. But even then, the relative induction factor of the downstream actuator still influences the size of the upstream actuator (because of the (inviscid) matched actuator design choice, expression 5.12), which in turn affects its power extraction.

5.2. ALTERNATIVE REFERENCE AREA

Using the area of the largest actuator as a reference for adimensionalizing power exchange is consistent with other studies of complex wind energy conversion configurations – for example about vertical axis wind turbines (Madsen, 1982) or airborne wind energy systems (de Lellis et al., 2018) resort to conceptually similar approaches. Those studies use the projected area (on a plane normal to the free-stream) of all points swept by the machine as a reference, irrespective of its length in the free-stream direction .

When the actuators of a matched-actuator setup are very far from each other, however, they can also be seen as independent machines. It might then make more sense to adimensionalize the power coefficient of the complete setup with the sum of the two actuator areas. That approach would be consistent with the definition of array efficiency used in wind farm design studies.

Changing the reference area of expression 5.11 is trivial. The simplest way for doing

so involves reworking the area ratio of expression 5.12 into a convenient form :

$$\frac{S_2}{S_1 + S_2} = \frac{1}{\left(\frac{S_1}{S_2}\right) + 1} = \frac{(b+1)}{b(3-2a_2) + 1} \quad (5.19)$$

It then suffices to multiply expressions 5.9 to 5.11 by expression 5.19 to reach the desired result:

$$C_{P_1}^{\gamma J} = \frac{P_1}{\frac{1}{2}\rho(S_1 + S_2)U_0^3} = \frac{b(1-a_2)(b^2-1)(b+1)}{b(3-2a_2) + 1} \quad (5.20)$$

$$C_{P_2}^{\gamma J} = \frac{P_2}{\frac{1}{2}\rho(S_1 + S_2)U_0^3} = -\frac{b_{\text{eff}}^3(4a_2)(1-a_2)^2(b+1)}{b(3-2a_2) + 1} \quad (5.21)$$

$$C_P^{\gamma J} = \frac{P_1 + P_2}{\frac{1}{2}\rho(S_1 + S_2)U_0^3} = \frac{b(1-a_2)(b^2-1) - (1+\gamma(b^2-1))^{\frac{3}{2}}(4a_2)(1-a_2)^2}{(b+1)^{-1}(b(3-2a_2) + 1)} \quad (5.22)$$

Expressions 5.20 to 5.22 predict machine power in the same way as expressions 5.9 to 5.11, so their application is restricted by the same constraints (5.14 to 5.17).

Figure 5.23 plots expression 5.22 for two nominal speedup ratios ($b = 2$ and $b = 3$) and various γ parameter values. Comparison with figure 5.2, which plotted $C_P^{\gamma J}$ for $b = 1.5$ and $b = 2$ for a broader range of γ parameter values, shows that significant exceedance of the 16/27 threshold requires larger speedup ratios (b) when the area of both actuators is used as a reference. That is expectable, since $S_1 + S_2 > S_2$ for all possible design choices. Furthermore, system performance seems more sensitive to inter-actuator enthalpy losses when the area of the two actuators is used as reference.

5.2.1. OPTIMAL SETUP WITH ALTERNATIVE REFERENCE AREA

The choice of a different reference area also affects optimal actuator loadings because the area-ratio of expression 5.19 depends on the a_2 and b design parameters. It is therefore interesting to repeat the optimization exercise of section 5.1.1 using expression 5.22:

$$\min_{(a_2, b)} C_P^{\gamma J} = f_{(a_2, b, \gamma)}$$

$$\text{subject to } \text{prescribed } \gamma \quad (5.23)$$

$$0.2 < u_e^{\gamma}$$

$$0.2 < b < 8.5$$

As in section 5.12, numerical solutions were obtained for 200 prescribed γ parameter values covering the $[0, 1]$ interval. The main results are presented on figure 5.4. Expectably, the achievable power coefficient is lower when the sum of the area of the two actuators is used as a reference, instead of the area of the largest actuator (as in figure 5.2).

The $C_P^{\gamma J} = 16/27$ limit can be exceeded if enthalpy offset losses are very small, that is when $\gamma \gtrsim 0.97512$. This observation is relevant even if such high values of the γ parameter seem intuitively unlikely. It suggests, but does not prove or warrant, that non-conservative flow phenomena function as regular (and not singular) perturbations on

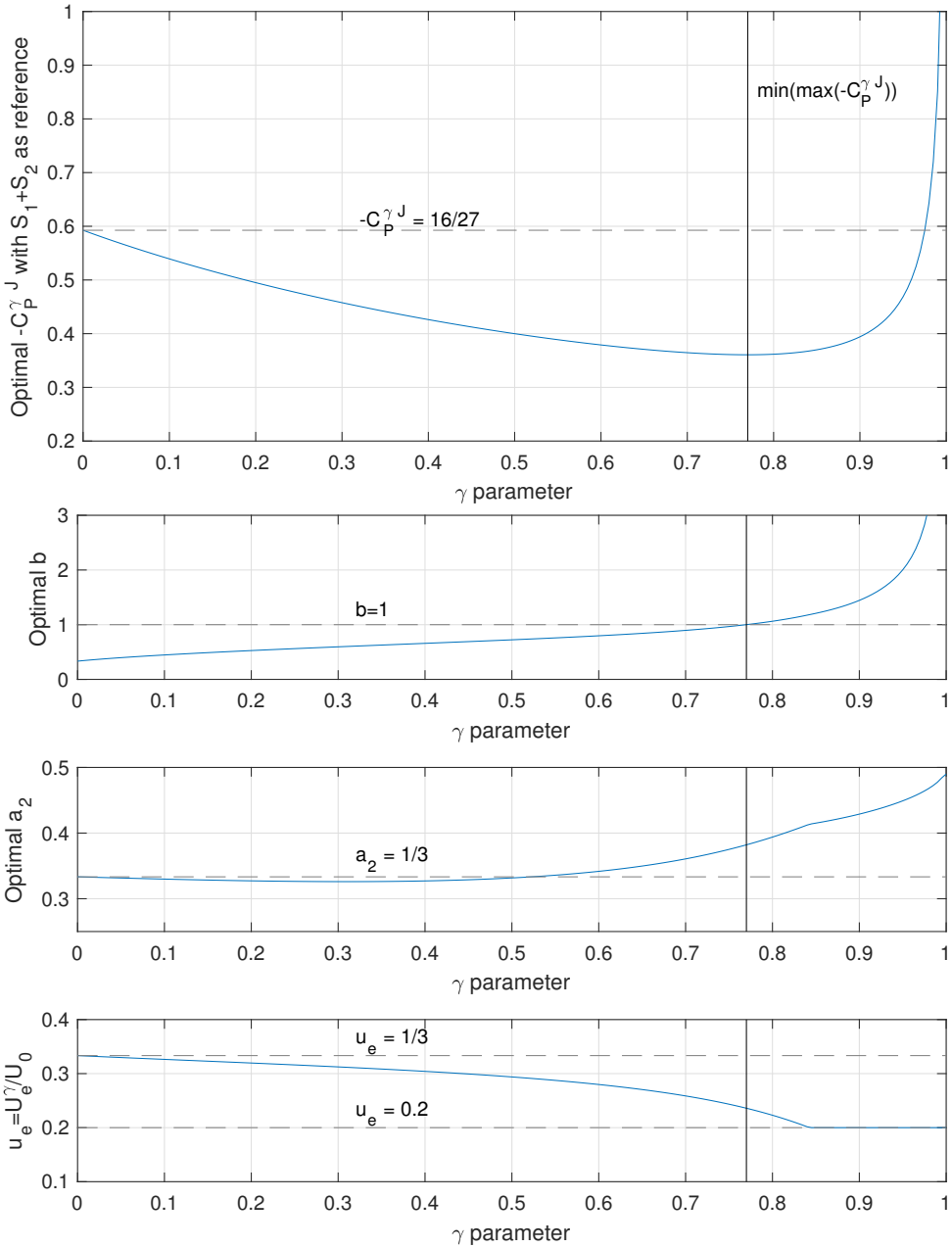


Figure 5.4: Effect of enthalpy loss parameter (γ) on optimal power coefficient of matched actuator setup, in the sense of problem 5.23. The sum of the area of the two actuators is used as a reference.

the ideal flow solutions of matched-actuator setups (in the sense described by [Kevorkian and Cole \(1996\)](#)). That would legitimate the inviscid treatment of matched-actuator setups from a formal standpoint.

The usage of the area of the two actuators as a reference leads to more intuitive results for low γ parameter values. With this choice of reference area, the optimal power coefficient corresponds to the Betz limit when $\gamma = 0$, in which case both actuators operate independently from each other with a thrust coefficient of 8/9.

$$\begin{aligned} b = 1/3 &\Rightarrow f_1 / (0.5\rho U_o^2) = 8/9 \\ \gamma = 0 \wedge a_2 = 1/3 &\Rightarrow f_1 / (0.5\rho U_o^2) = 8/9 \end{aligned}$$

It is worth observing that the enthalpy loss threshold at which it becomes beneficial to operate the first actuator in propeller mode ($f_1 > 0$) instead of wind turbine mode ($f_1 < 0$), is relatively insensitive to the choice of reference area. The threshold rises from $\gamma \approx 0.75$ in the former choice of reference area to $\gamma \approx 0.77$. If wake mixing is sufficiently slow for the inter-actuator enthalpy loss parameter to stay above that threshold, matched-actuator setups can extract more energy per unit area by energizing the flow to increase mass flow across the downstream actuator.

5.3. ESTIMATING INTER-ACTUATOR ENTHALPY LOSSES

This section seeks to characterize the magnitude of energy and enthalpy losses in actuator disk wakes. Subsection ... estimates the magnitude of the γ parameter with the Jensen wake model. Subsection .. adopts a slightly different perspective, and focuses on the total energy content of the wake instead of its local flow enthalpy. Section ... further investigates the matter with finite-volume solutions of the Navier-Stokes equations.

5.3.1. FIRST ESTIMATE

The Jensen model for the evolution of wind turbine wakes was derived by considering that wakes were inverted co-flow jets [Jensen \(1983\)](#). It is therefore not absurd to postulate that it might also be applicable to the wakes of actuator disks operated in propeller mode. This section does not discuss the validity of that postulate but instead restricts itself to the study of its implications.

The Jensen model is stated here after [Gocmen et al. \(2016\)](#). The notation was adapted to the match the conventions of the present work: U_a represents the speed in the wake of the actuation surface at downstream distance (x) scaled by the diameter (D) of the actuator disk, U_o is the velocity of the surrounding free-stream, D_a is the wake diameter, α is the semi-empirical wake expansion parameter, and C_T is the thrust coefficient ($C_T > 0$ corresponds to propeller mode).

$$u_a = \frac{U_{a,Jensen}}{U_o} = 1 - \frac{1 - \sqrt{1 + C_T}}{(1 + 2\alpha(\frac{x}{D}))} \quad (5.24)$$

$$\frac{D_a}{D} = 1 + 2\alpha\left(\frac{x}{D}\right) \quad (5.25)$$

There is no ambiguity in the definition of the wake diameter since the model assumes a constant velocity distribution across the wake radius. Furthermore, the Jensen model

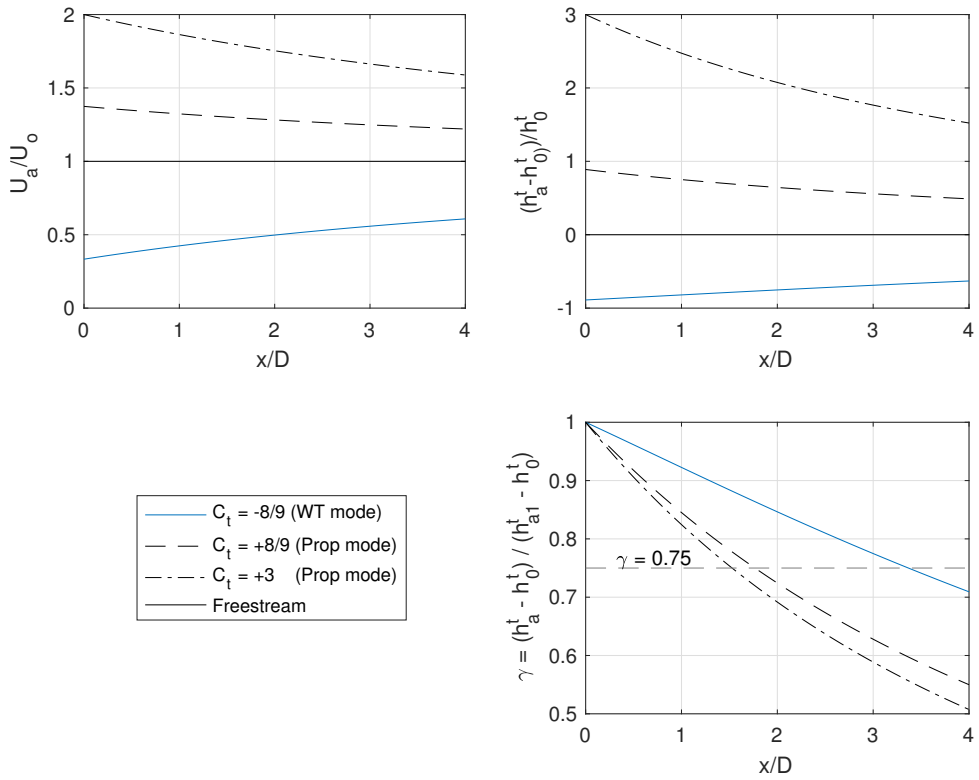


Figure 5.5: Jensen model predictions with ($\alpha = 0.038$) for wake velocity, total enthalpy offset and enthalpy loss parameter behind actuator disks with different thrust coefficients.

neglects the initial stages of wake development where potential and kinetic energy fields interact extensively. It predicts a velocity equivalent to that of the terminal wake at the actuator location:

$$\left(\frac{U_{a,Jensen}}{U_o} \right) \Big|_{x=0} = 1 - 2a \quad (5.26)$$

While that is unphysical, the velocity of expression 5.26 corresponds to the one the wake would reach after developing completely without mixing with the free-stream. That is, when it would have returned to the same static pressure as the free-stream ($p_o = \rho h_o$).

From the above perspective, it seems the Jensen model depicts the total enthalpy of flow behind the actuator more accurately than its flow velocity. That could be one of the reasons for its success. Let us now write the total enthalpy of flow in the wake of actuator disk from expression 5.24:

$$\begin{aligned} h_{a,Jensen}^t &= \frac{1}{2} U_{a,real}^2 + h_a = \frac{1}{2} U_{a,Jensen}^2 + h_o \\ &= \frac{1}{2} U_o^2 \left(1 - \frac{1 - \sqrt{1 + C_T}}{(1 + 2\alpha(\frac{x}{D}))} \right)^2 + h_o \end{aligned} \quad (5.27)$$

The γ enthalpy loss parameter can then be estimated by inserting expression 5.27 into its definition (5.7) and reworking:

$$\begin{aligned} \begin{cases} \bar{h}_{a2}^t = h_0^t + \gamma (\bar{h}_{a1}^t - h_0^t) \\ \bar{h}_{a1}^t \approx \left(h_{a,Jensen}^t \right) \Big|_{x=0} &= \frac{1}{2} U_o^2 (\sqrt{1 + C_T})^2 \\ \bar{h}_{a2}^t \approx \left(h_{a,Jensen}^t \right) \Big|_{x=\frac{x}{D}} &= \frac{1}{2} U_o^2 \left(1 - \frac{1 - \sqrt{1 + C_T}}{(1 + 2\alpha(\frac{x}{D}))} \right)^2 \end{cases} \\ \Rightarrow \gamma_{Jensen} = \frac{\bar{h}_{a2}^t - h_0^t}{\bar{h}_{a1}^t - h_0^t} \approx \frac{\frac{1}{2} \left(1 - \frac{1 - \sqrt{1 + C_T}}{(1 + 2\alpha(\frac{x}{D}))} \right)^2 - 1}{\frac{1}{2} U_o^2 (\sqrt{1 + C_T})^2 - 1} \end{aligned} \quad (5.28)$$

Figure 5.5 plots the wake velocity 5.26, the total enthalpy offset (based on expression 5.27) and the γ parameter (5.28) according to the Jensen model. The wake expansion parameter was taken as $\alpha = 0.38$ which corresponds to the fairly favorable case of a stable atmosphere at the Sexberium offshore wind farm (Peña et al., 2015). Three thrust coefficients were considered. The loading of the Betz limit case in wind turbine mode ($C_T = -8/9$), the same loading in propeller mode ($C_T = 8/9$ leading to $u_e \approx 1.3744$) mode, and a larger thrust in propeller mode ($C_T = 3$ leading to $u_e \approx 2$). A much larger thrust coefficient is needed to double the speed of the wake than to halve its velocity.

The predictions of figure 5.5 suggest the enthalpy loss parameter decreases quite fast when the distance between actuators grows. The γ parameter crosses the 0.75 threshold at $x/D = 1.76$ for $C_T = 8/9$ and $x/D = 1.53$ for $C_T = 3$. That hints actuators would need to be quite close to each other for active flow augmentation to be beneficial. They would also need to operate in each other's pressure field, which is an additional hurdle.

The predictions of figure 5.5 do not completely invalidate the feasibility of active flow augmentation principles. The $\gamma = 0.75$ threshold applies to matched actuator setups designed for inviscid flow conditions. As a result, in viscous flows, part of the energized

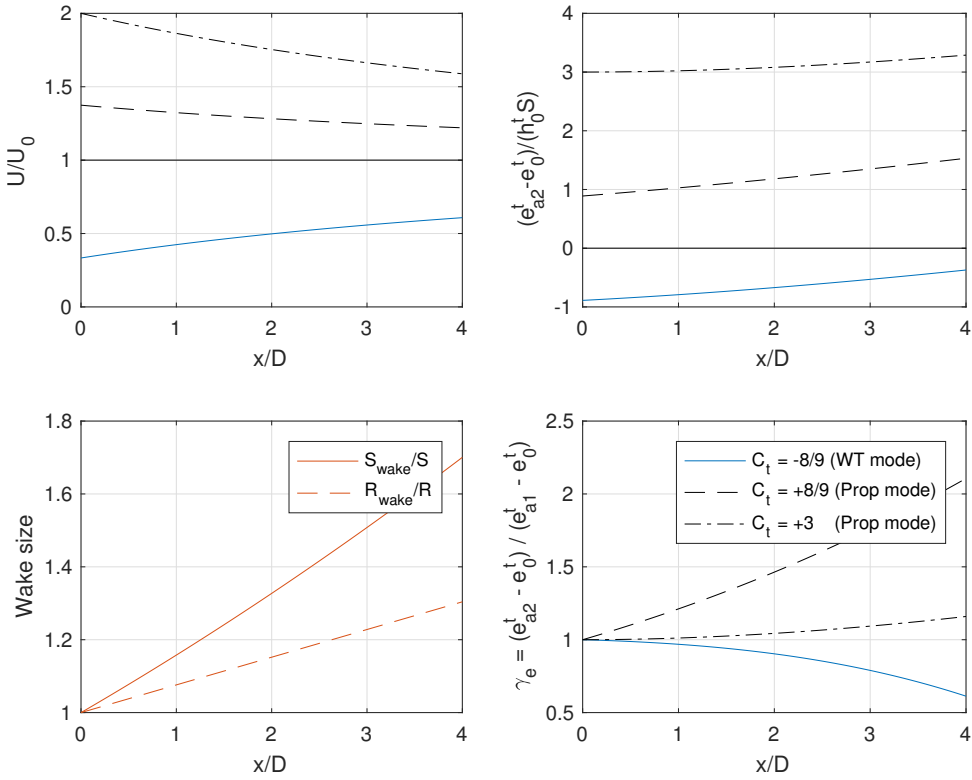


Figure 5.6: Jensen model predictions with ($\alpha = 0.038$) for wake velocity, energy offset and energy loss parameter (γ_e) behind actuator disks with different thrust coefficients. Predictions for actuator disks that accelerate the flow ($C_T > 0$) are obviously unphysical.

wake of the upstream actuator goes around the downstream actuator. This is a pointless waste of the energy.

A better design choice for real flows consist in enlarging the size of the second actuator until it covers all the wake of the upstream actuator. Including its widening due to the effect of viscous and turbulent diffusion.

5.3.2. SECOND ESTIMATE

This section estimates the extent to which inter-actuator energy losses might be mitigated by enlarging the second actuator, so that it covers all the (diffused) wake of the upstream actuator. The total enthalpy offset of the flow is now integrated over a plane normal to the free-stream (Ω). Two quantities are defined. First, the mechanical energy per unit length ($e_{\Omega_o}^t$) contained in the flow that lies on a plane in the unperturbed free-stream ($\Omega_o \subset \mathbb{R}^3$). Second, the mechanical energy per unit length ($e_{\Omega_a}^t$) contained in the flow that lies on a plane that crosses the wake of the actuator-disk ($\Omega_a \subset \mathbb{R}^3$).

$$e_{\Omega_o}^t = \int h^t d\Omega_o \quad , \quad e_{\Omega_a}^t = \int h^t d\Omega_a \quad (5.29)$$

The quantities of expression 5.29 are not powers, which correspond to fluxes of total enthalpy, but rather energy densities over a plane. Both $e_{\Omega_o}^t$ and $e_{\Omega_a}^t$ are infinite but the offset between them is finite and well defined:

$$e_{\Omega_a}^t - e_{\Omega_o}^t = \int h^t d\Omega_a - \int h^t d\Omega_o = \int h^t - h_o^t d\Omega_a \quad (5.30)$$

It can be used to define a new energy loss parameter γ_e similar to the enthalpy loss parameter (γ) of section 5.3.1:

$$\gamma_e = \frac{e_{\Omega_{a2}}^t - e_{\Omega_o}^t}{e_{\Omega_{a1}}^t - e_{\Omega_o}^t} \quad \text{where} \quad \begin{cases} \Omega_{a2} = \{\mathbf{x} \in \mathbb{R}^3 : x = \frac{x}{D}\} \\ \Omega_{a1} = \{\mathbf{x} \in \mathbb{R}^3 : x = 0\} \end{cases} \quad (5.31)$$

Where $e_{\Omega_{a1}}^t$ denotes the total energy offset of flow just behind the actuator disk and $e_{\Omega_{a2}}^t$ refers to the same quantity at a distance x/D behind the actuator, that is, at the location where another . The γ_Ω parameter is interesting because it isolates the two main effects of viscous stresses on flow energy:

- A diffusive effect - unlike inviscid fluids, viscous fluids oppose resistance to shear. For Newtonian fluids like air, the resulting forces are proportional to slip between fluid elements and usually represented as shear stress tensor (τ_{ij}). Shear stresses enable adjacent streamlines to transfer kinetic energy to each other whenever a transverse velocity gradient exists. Energy is always transferred from higher to lower speed streamlines: that explains the diffusion of actuator disk wakes from a steady flow perspective.

$$\tau_{ij} = \mu \left(\frac{\partial U_i}{\partial x_j} + \frac{\partial U_j}{\partial x_i} \right)$$

- A dissipative effect - the effect shear stresses is not limited to the transfer of energy between adjacent streamlines. Viscous stresses diffuse the velocity field by appearing as a laplacian ($\Delta = \nabla^2$) term in the Navier-Stokes equations:

$$\frac{d\mathbf{U}}{dt} + (\mathbf{U} \cdot \nabla) \mathbf{U} = -\frac{1}{\rho} \nabla p + \nu \Delta \mathbf{U}$$

The laplacian operator is not conservative when it applies to the velocity field, unlike in the context of the heat equation, because kinetic energy is proportional to the square of the velocity magnitude². Viscous stresses remove mechanical energy from the flow at a rate ($\tau : \nabla \mathbf{U}$) = $\nu \Phi$ per unit volume [Batchelor \(1967\)](#):

$$\begin{aligned} \Phi = & 2 \left[\left(\frac{\partial U}{\partial x} \right)^2 + \left(\frac{\partial V}{\partial y} \right)^2 + \left(\frac{\partial W}{\partial z} \right)^2 \right] \\ & + \left(\frac{\partial U}{\partial y} + \frac{\partial V}{\partial x} \right)^2 + \left(\frac{\partial V}{\partial z} + \frac{\partial W}{\partial y} \right)^2 + \left(\frac{\partial W}{\partial x} + \frac{\partial U}{\partial z} \right)^2 \end{aligned} \quad (5.32)$$

²Diffusion is a conservative process in the context of the heat equation because temperature is linearly correlated with thermal energy content. The laplacian operator conserves the diffused quantity (momentum) but not its higher moments (kinetic energy).

Because dissipation always removes energy from the flow ($\Phi > 0$), it affects wake development in different ways when actuator disks operate in wind turbine or in propeller mode. It delays wake recovery when the actuator disk extracts energy from the flow, and accelerates it when the actuator injects energy into the flow.

The energy loss parameter γ_e is not affected by viscous diffusion because it depends on the energy contained over an infinite plane. In that sense, it isolates the effect of dissipation. The way total enthalpy is spread over the plane does not affect the γ_e energy loss parameter. On the other hand, the γ enthalpy loss parameter is affected by both diffusion and dissipation.

It is tempting to try to estimate γ_e with the Jensen model since it includes an estimate of the width of the wake of the actuator disk. The obvious way to do so would consist in reworking expression 5.30 with expressions 5.27 and 5.25 :

$$\begin{aligned} e_{\Omega a}^t - e_{\Omega o}^t &= \int h^t - h_o^t d\Omega_a \\ &\approx (h_a^t - h_o^t) \left(\frac{\pi}{4} D_a^2 \right) \\ &\approx \left(\frac{1}{2} U_o^2 \left(1 - \frac{1 - \sqrt{1 + C_T}}{(1 + 2\alpha(\frac{x}{D}))} \right)^2 - h_o^t \right) \left(\frac{\pi D^2}{4} \right) \left(1 + 2\alpha \left(\frac{x}{D} \right) \right)^2 \end{aligned} \quad (5.33)$$

Just behind the actuator ($x/D = 0$), the energy offset is written as:

$$e_{\Omega a1}^t - e_{\Omega 0}^t = \left(\frac{1}{2} U_o^2 (1 + C_T) - h_o^t \right) \left(\frac{\pi D^2}{4} \right) = \frac{1}{2} U_o^2 C_T \left(\frac{\pi D^2}{4} \right) \quad (5.34)$$

It then seems that γ_e parameter might be approximated by inserting expressions 5.33 and 5.34 into expression 5.31 :

$$\gamma_e = \frac{e_{\Omega a2}^t - e_{\Omega 0}^t}{e_{\Omega a1}^t - e_{\Omega 0}^t} = \left(\left(1 - \frac{1 - \sqrt{1 + C_T}}{(1 + 2\alpha(\frac{x}{D}))} \right)^2 - 1 \right) \frac{(1 + 2\alpha(\frac{x}{D}))^2}{C_T} \quad (5.35)$$

Figure 5.6 plots expressions 5.24, 5.24, 5.33 and 5.35 for the same conditions as figure 5.5. Jensen model predictions are unphysical when it comes to the energy content of wake of an actuator disk that injects energy into the flow. The energy offset can by no means grow in such a flow: it should decrease monotonically as the distance to the actuator grows, just like the wake energy parameter (γ_e). Figure 5.6 should therefore be disregarded.

5.3.3. THIRD ESTIMATE

Unlike diffusive processes, energy dissipation is generally thought to have negligible impact on overall flow features. Literature on the matter is therefore rather sparse and, to the best of the author's knowledge, there are no semi-analytical models dedicated to the description of energy content in actuator-disk wakes. As such, it was decided to assess the magnitude of the γ_e parameter with finite-volume solutions of the Reynolds Averaged Navier Stokes equations.

Numerical Schemes (Step 3)			
gradSchemes		RANS	Gauss linear
		Laminar	Gauss leastSquares
divSchemes	Fluxes (phi)	k and ε	Gauss linear
		U	Gauss linearUpwind cellLimited <> 1
		Limiter	leastSquares
	$\nabla(v_{\text{eff}}\text{dev}(\nabla U^T))$	RANS	Gauss linear
		Laminar	Gauss linear limited corrected 0.5

Convergence criteria (Residuals)				
	Solver	Variable	Step 1	Step 2 and 3
Inner	GAMG	p	1e-8	1e-9
	smoothSolver	$U k \varepsilon$	1e-9	1e-10
Outer	SIMPLE	p	1e-3	1e-5
		$U k \varepsilon$	1e-4	1e-6

Table 5.1: Numerical setup used for simpleFoam solution of actuator-disk flows.

5.3.4. NUMERICAL SETUP

Computations were carried out with version 6 of the OpenFoam package distributed by the OpenFoam foundation and meshes were constructed with version 3.11 of the Gmsh open source mesher. A wedge domain with 5 degrees angle was adopted to take advantage of the axisymmetric nature of actuator disk flows. The mesh had two actuator disks but only one was used in this study. The domain radius was 60 times larger than the radius of the actuator disk ($R = 0.5D$), and the inlet boundary was 8D upstream of the actuation surface while the outlet boundary was 20D downstream. Flows regions close to the actuator disk were discretized with a structured mesh with radius 1.5D, which extended 2.5D upstream and 15D downstream of the actuator disk. The rest of the domain was covered with a tetrahedral mesh that matched the structured mesh at its interfaces, and became coarser near domain boundaries, where the typical spacing between nodes was about 0.25D. Four meshes were considered: the *coarse* mesh covered the radius of the actuation surface with 24+1 nodes, the *medium* mesh with 48+1 nodes, the *fine* mesh with 96 nodes and the *finer* mesh with 192 nodes. If extended into a full cartesian domain representation, the *finer* mesh would cover the actuation surface with 13184 cells ($192 \times 360/5$).

The actuation surface was not represented with the standard OpenFoam actuator-disk force model, which suffers from recurrent issues in weakly diffusive flows: pressure wiggles over the actuation surface and velocity wiggles on adjacent cells. Methods for mitigating this issue have been discussed in Wahono's (2014) excellent report but they seem hard to put in practice without access to commercial meshing software.

Since solutions were sought for a wide range of Reynolds numbers (including laminar cases), and the domain was simple enough for structured meshes, it seemed sensible to represent the actuator disk as an explicit pressure discontinuity. This was achieved by making use of a cyclic jump boundary condition applied to a baffle that covered the actuation surface, and had been defined explicitly during the meshing process. That

Case ID	Inflow			Turbulence model	
	Reynolds number	Turbulence intensity	Turbulence length scale	Model	Coefficients
HiRe, $C_\mu = 0.03$	1.61E8	12%	$l = 0.07D$	$k - \varepsilon$	$C_\mu = 0.03$ $C_1 = 1.21$
HiRe, $C_\mu = 0.09$	1.61E8	12%	$l = 0.07D$	$k - \varepsilon$	$C_\mu = 0.09$ $C_1 = 1.44$
MiRe, $C_\mu = 0.03$	1.88E5	2%	$l = 0.07D$	$k - \varepsilon$	$C_\mu = 0.03$ $C_1 = 1.21$
MiRe, $C_\mu = 0.09$	1.88E5	2%	$l = 0.07D$	$k - \varepsilon$	$C_\mu = 0.09$ $C_1 = 1.44$
LoRe	1.00E4	–	–	Laminar	–
VLRe	1.00E3	–	–	Laminar	–

Table 5.2: Flow conditions studied with the simpleFoam flow solver.

choice proved appropriate: solutions exhibit clean pressure and velocity fields with no observable artifacts for all four meshes, even when no turbulence model is present.

Solutions were sought with the SIMPLE algorithm using the simpleFoam solver. Numerical results were obtained in three steps. In step 1, relaxed convergence criteria (see table 5.1) were employed to obtain a preliminary flow solution with upwind schemes. Step 2 kept these schemes but drove the solution to lower residuals thanks to stricter linear solver convergence criteria. Step 3 started from that point to obtain the final solution using the schemes described in table 5.1.

5.3.5. CONSIDERED CASES

Four different flow conditions were considered: two corresponding to turbulent flow and two corresponding to either laminar or nearly laminar flows. Table 5.1 describes flow conditions in detail, with Reynolds numbers written by using the actuator disk diameter as a reference ($Re_D = U_o D / \nu$).

The high Reynolds (HiRe) cases correspond to the typical operation conditions of the world's largest rotor, the GE Haliade X offshore wind turbine. The medium Reynolds (MiRe) cases resemble flow condition in the TU-Delft OJF wind tunnel during the actuator-disk experiment of Lignarolo, even if the tunnel is known to have a lower turbulence intensity and smaller turbulent length scale than the ones prescribed here. Both flow conditions were investigated with the $k - \varepsilon$ turbulence model, with two choices of model constants: the $C_\mu = 0.09$ cases use

The (LoRe) and very low (VLRE) Reynolds number cases correspond to quasi-laminar and laminar flow conditions. The threshold at which jets become turbulent is often quoted after [McNaughton and Sinclair \(1966\)](#): they define the weakly diffused laminar jet range for $300 < Re < 1000$ and the transition to fully turbulent flow at $Re = 3000$. Yet, [Gauntner et al. \(1970\)](#) points that [Gardon and Cobonpue \(1963\)](#) observed a higher transition threshold, at $Re = 14000$. It seemed interesting to distinguish the effect of viscous stresses from that turbulent stresses.

5.3.6. MESH INDEPENDENCE

The numerical campaign sought to compute estimates of the γ_e parameter at various distances (x/D) downstream of the actuator-disk. It was computed with ParaView ver-

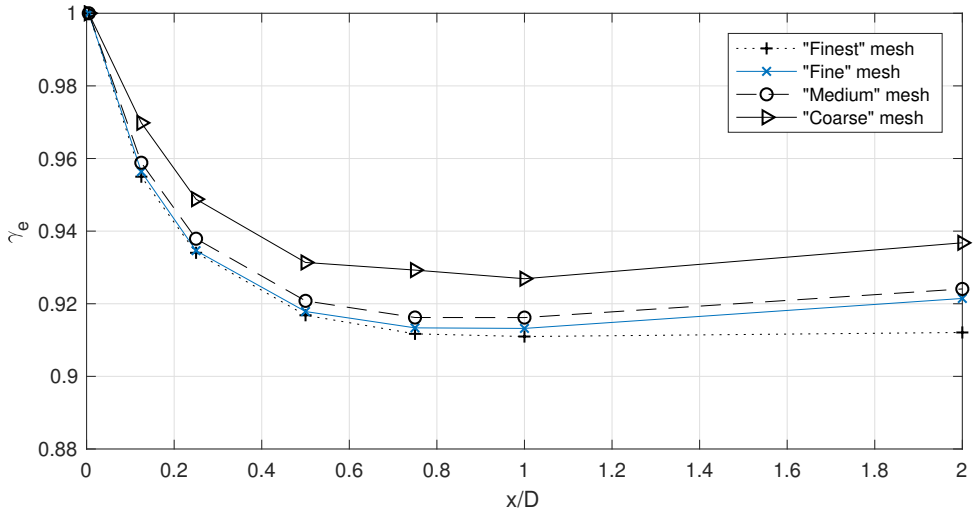


Figure 5.7: Mesh independence study for HiRe ($C_\mu = 0.03$) flow conditions with $C_T = 8/9$ (propeller mode). The *coarse* mesh splits the radius of the actuation surface with 24 cells, the *medium* mesh with 48 cells, the *fine* mesh with 96 cells and the *finer* mesh with 192 cells.

sion 5.4 by integrating the total enthalpy offset over a line that samples point data over 1000 points, spread from the axi-symmetry axis to a distance of 4 actuator disk radii. Varying the integration distance or number of sampling points did not alter estimates in relevant ways.

Figure 5.7 shows the results of the mesh independence study conducted for the HiRe ($C_\mu = 0.03$) flow conditions with all four considered meshes for a thrust coefficient $C_T = +8/9$ (propeller mode). Numerical estimates of the γ_e parameter are roughly consistent for the *fine* and *finer* meshes in the early stages of wake development but discrepancies grow with downstream distance. Large eddy simulation (LES) studies of wind farm interactions sometimes use comparable meshes but employ higher order schemes that lead to much more reliable results (Sarlak et al., 2014; Lignarolo et al., 2016).

It is far more difficult to estimate energy dissipation in the wake of an actuator-disk than to predict its power coefficient. The *medium* mesh leads to very accurate power coefficient predictions despite its shortcomings for estimating γ_e . For example, when used in quasi inviscid flow conditions ($Re = 1.88e5$ with no turbulence model) with $C_T = -8/9$ the medium mesh a power coefficient of 0.58943. That corresponds to an error of 0.53%, below the reference 16/27 value, which is similar to the accuracy of reference potential flow solutions Van Kuik and Lignarolo (2015).

The employed numerical schemes can easily lead to misleading results because are not energy-conserving. It would have been desirable to conduct the entire study with the *finer* mesh and energy conserving numerical schemes. Those options, however, were not compatible with the available time and computing resources. The *fine* mesh was used as a reference for all calculations presented on figures 5.8 and 5.9 due to time constraints. Their predictions should therefore be regarded as a weak and fragile preliminary inquiry. One that calls for computations to be repeated with a finer mesh and energy conserving

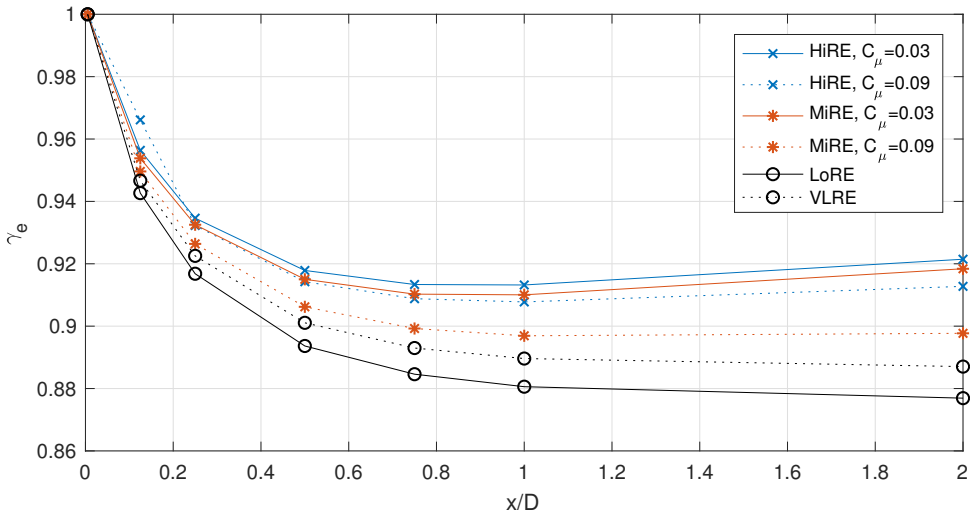


Figure 5.8: Evolution of γ_e parameter in different flow conditions for actuators with $C_T = +8/9$ (propeller mode).

numerical schemes.

5.3.7. INTERPRETATION OF NUMERICAL RESULTS

Figure 5.8 plots the evolution of the γ_e parameter when the actuator has a thrust coefficient $C_T = +8/9$ (propeller mode) for all flow conditions of table 5.2. These results should not be taken as firm conclusions but some trends seem to make sense. For instance, energy dissipation is strongest in very early stages of wake development, for $x/D \lesssim 0.5$, where velocity gradients are greatest.

The dissipation term of expression 5.2 was computed from the derivatives of the velocity field and plotted on figure 5.10 for the HiRe ($C_\mu = 0.03$) case using the *finer* mesh. The figure also plots an order of magnitude estimate for the rate at which energy moves from the Reynolds-averaged field to the turbulent kinetic energy field (k)³. In both cases, dissipation is much larger near actuator edges than anywhere else in the flow.

Figure 5.11. plots the velocity, pressure and total enthalpy fields for the same case as figure 5.10. The wake diffuses quite rapidly and reaches the edges of the structured mesh region (a $r=1.5R$) quite early, at around two diameters ($2D = 4R$) downstream of the actuator disk. That could explain why the γ_e parameter grows slowly again after $x/D > 1.5$ for the coarser meshes in turbulent flow – that is unphysical since, in the absence of flow reversal, γ_e must decrease monotonically as the flow moves downstream because energy dissipation per unit volume (Φ) is always positive. The laminar flow solutions suffered less from that issue because laminar wakes widen at a much smaller pace.

The evolution of the γ_e parameter in laminar flow conditions is plotted on figure 5.9

³ $(\mu + \mu_t) \Phi$ does not accurately represent the loss of mechanical energy due to turbulent phenomena because μ_t varies in space (unlike μ). Better ways to estimate this would involve: deriving the full tensor, using the production term of the turbulence model, or exploring the $(\nabla \cdot k)$ quantity.

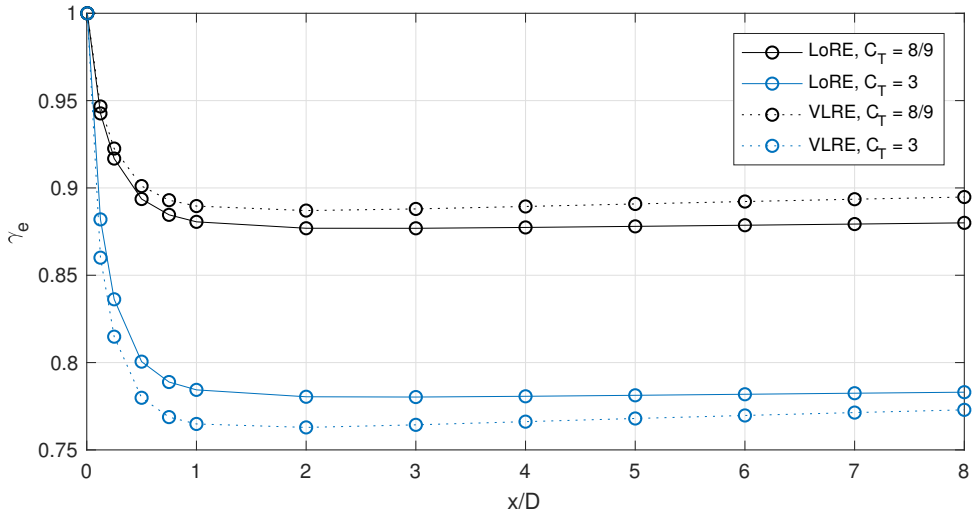


Figure 5.9: Evolution of γ_e parameter for two actuator loadings in laminar and (quasi)laminar flow conditions.

for two different thrust coefficients and up to $x/D = 8$. The thrust coefficient of the actuator disk has a profound effect on the evolution its wake and of the γ_e parameter. A higher thrust coefficient corresponds to a faster wake, which leads to higher shear, and hence higher energy dissipation. It should be noted that, for $C_T = 3$, the predictions of figure 5.9 are far less optimistic than those of the Jensen model (figure 5.5). Specially considering γ should, in principle, be smaller than γ_e .

5.4. MAIN FINDINGS

There remains considerable uncertainty regarding the magnitude of inter-actuator energy losses that can be expected in a matched actuator setup. It does not seem impossible, however, that some (few) conditions exist in which matched actuator setups might actually produce more power by operating the upstream actuator in propeller mode.

Naïve transposition of active flow augmentation to practical flows is probably impossible. Viscous effects and other sources of irreversibility are hard to quantify but generally rule out immediate practical benefits. Yet, the existence of active flow augmentation mechanisms deserves to be shared with the scientific community. They clarify the implications of the disparity between the rate at which static and total enthalpy perturbations decay in space. These insights can also advance the understanding of wake-ingestion propulsion setups.

Last, but not least, the flows discussed in the past chapters show that the maximum efficiency of wind energy conversion is not bounded by static inviscid phenomena when multiple energy extraction surfaces are considered. This is paradoxical since such a bound, the Betz limit, exists (and remains unchallenged) for isolated energy extraction surfaces. This finding strengthens arguments suggesting that the optimal efficiency of wind turbine arrays is primarily bounded by viscous and unsteady phenomena.

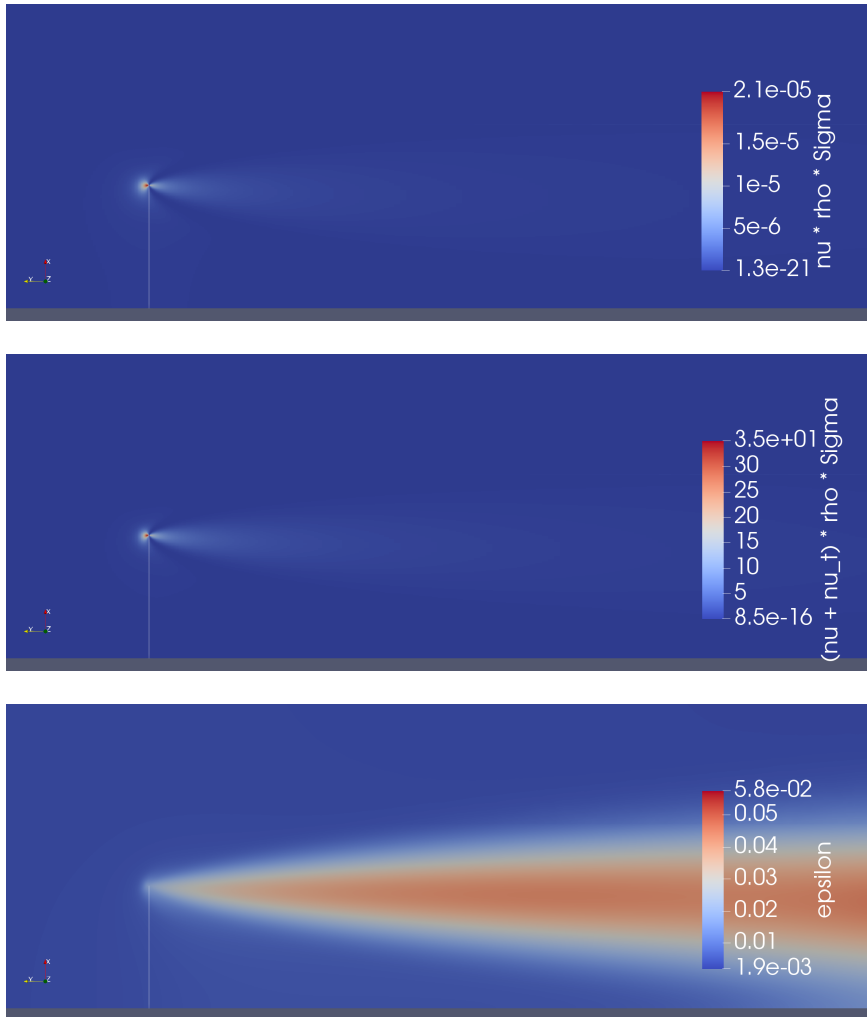


Figure 5.10: Viscous dissipation of mechanical energy from the averaged flow field ($\mu\Phi$), order of magnitude estimate of energy transfer to the thermal and turbulent fields ($(\mu + \mu_t)\Phi$) and dissipation of turbulent kinetic energy (ϵ); all for HiRe ($C_\mu = 0.03$) flow conditions with $C_T = +8/9$ (propeller mode) using the *finer* mesh. The white line is not part of the flow solution and represents the actuator disk (half diameter).

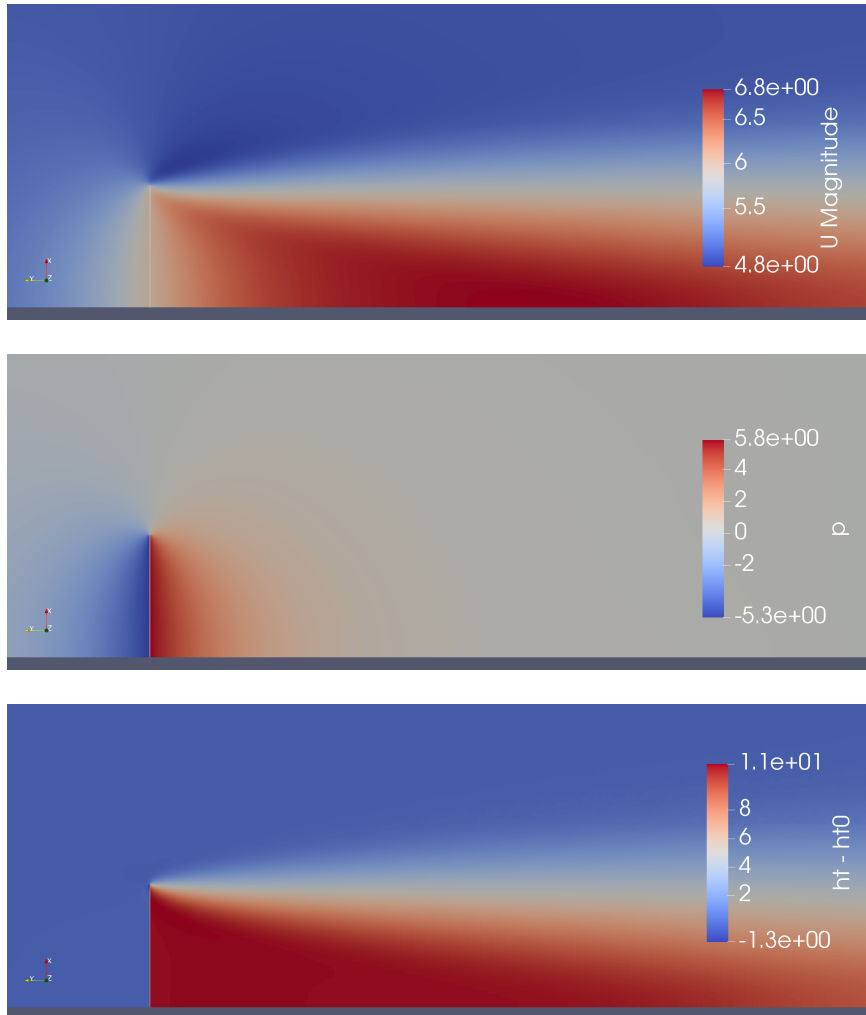
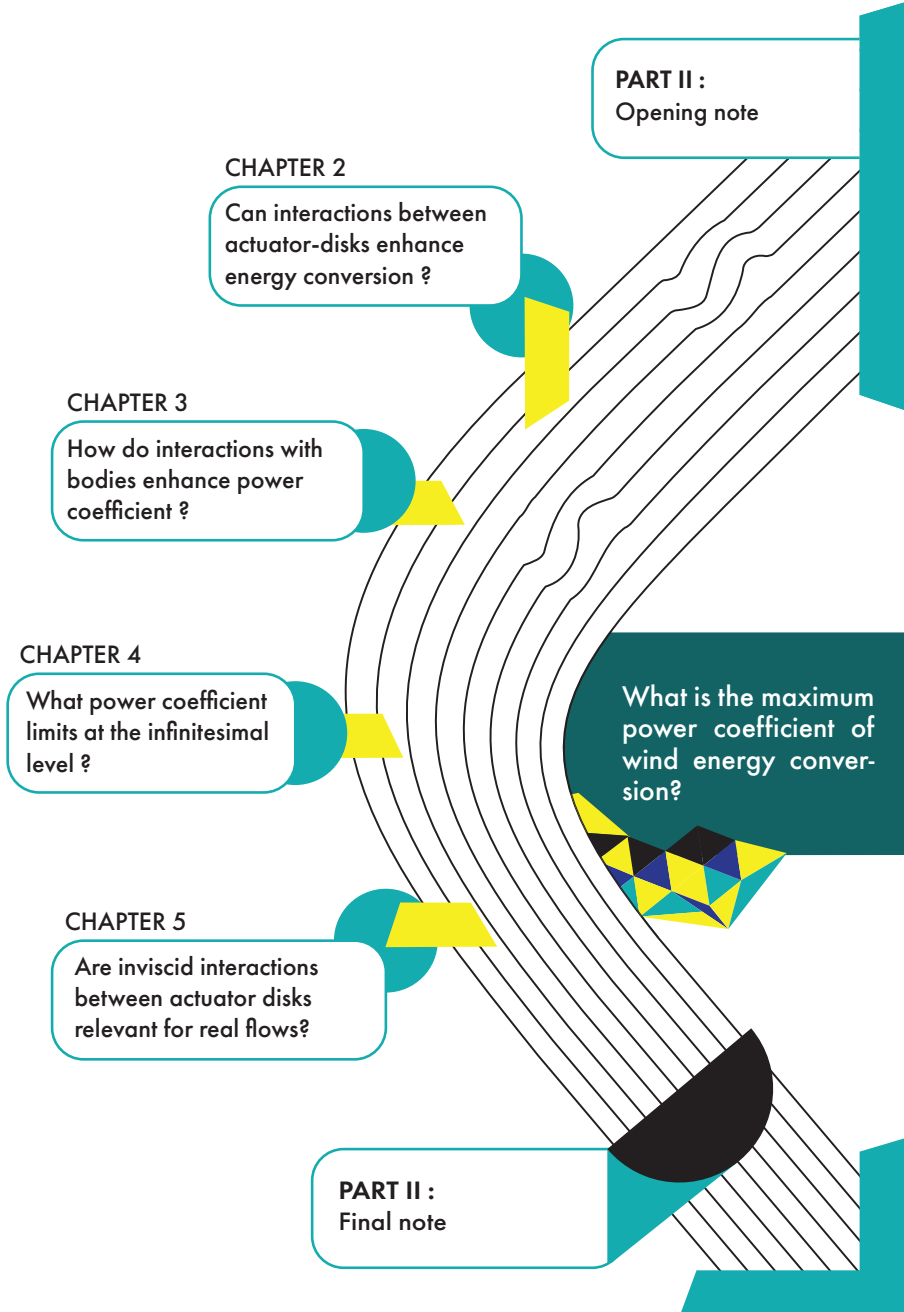


Figure 5.11: Velocity magnitude (U), pressure (p) and total enthalpy (h^t) computed in HiRe ($C_\mu = 0.03$) flow conditions with $C_T = +8/9$ (propeller mode) using the *finer* mesh. The white line is not part of the flow solution and represents the actuator disk (half diameter).



CLOSING NOTE

Maximum power coefficient

Active and passive flow augmentation mechanisms demonstrate that the Betz limit is not universal. Passive exceedance mechanisms operate by shifting the static enthalpy field over the energy extraction surface. They have been known since the 1920s and justify the development of shrouded and diffuser augmented wind turbines. Active exceedance mechanisms function differently, by shifting the total enthalpy of the flow before it reaches the energy extraction surface. That generally requires upstream energy injection, but injected energy can, in principle, be recovered by a downstream energy extraction surface that processes more flow to extract more energy.

ACTIVE FLOW AUGMENTATION

Active flow augmentation allows dramatic increases in the power coefficient of wind energy for ideal flow conditions. Applications, however, may be hindered by the viscous nature of real fluids. That implies wakes diffuse and imperfect energy transfer between actuation surfaces. The rate at which wakes diffuse, which depends on turbulence levels and molecular diffusivity, sets a first adverse constraint on the feasibility of active flow augmentation. The second major constraint is related to the onset of the turbulent wake state. Real rotors are made of a finite number of blades and shed helical instead of tubular wakes. Would the accelerated wake of an upstream rotor remain stable as it crosses a downstream (energy extracting) rotor? To which extent would chaotic breakdown alter overall flow topology? These questions should be the object of future research.

No practical demonstration of the active flow augmentation concept has been attempted. Construction of naïve matched-actuator setups poses obvious and immense practical challenges. The implications of active flow augmentation are not practical but intellectual.

Active flow augmentation principles could affect the design of every system in which flow crosses more than one actuation surface. Wind farms are the obvious example, but other arrangements are also concerned. The bottom row of figure I.B depicts single-rotor machine concepts that would exploit active augmentation principles. The middle row suggests using bodies to accelerate wake development between the surfaces of

matched-actuator setups. Finally, the layouts of the top row are straightforward multi-rotor systems. Additional research is needed to determine the best path towards active flow augmentation.

PASSIVE FLOW AUGMENTATION

Implications of passive flow augmentation also extend beyond the design of diffuser augmented wind turbines. Chapter 3 showed that static enthalpy interactions, like those due to bodies, affect the loading at which actuator disks extract most energy from the flow. Chapter 4 transformed that insight into a formal approach, suggesting that optimal actuator-disk loading distributions are not forcefully homogeneous. What does that mean for practical applications?

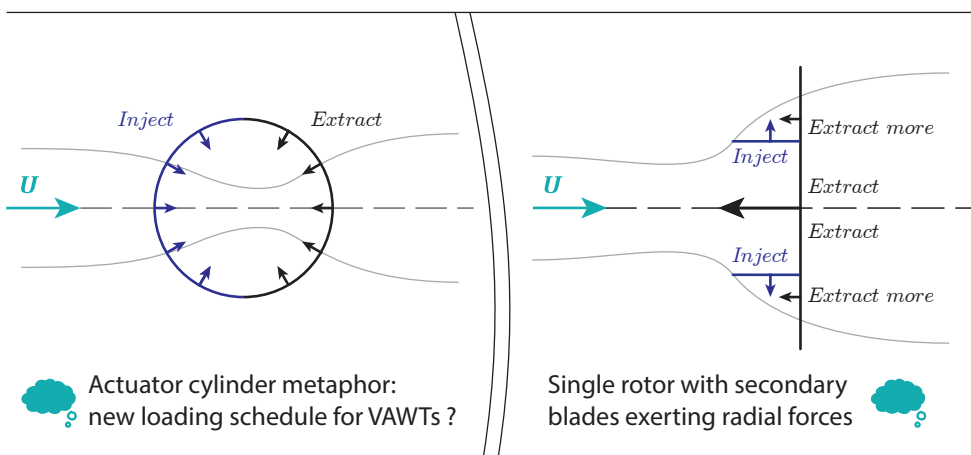
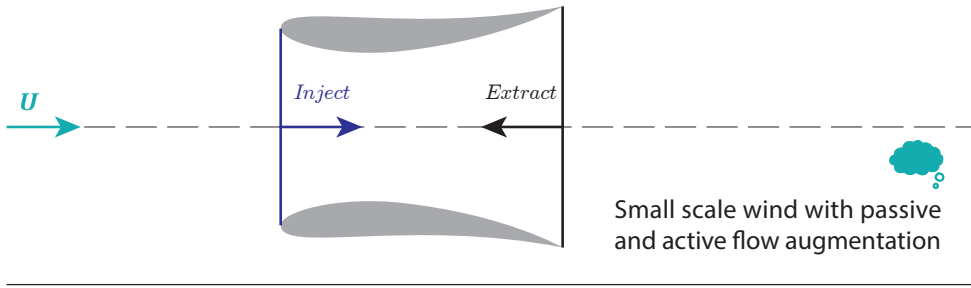
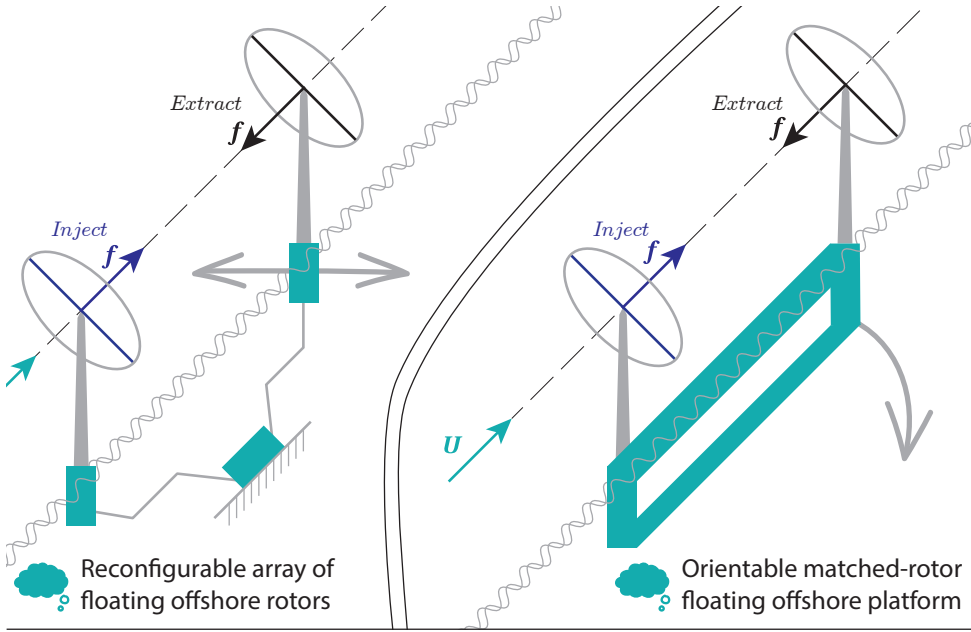
Probably not much for conventional wind turbines, because they operate essentially alone. Hub height is substantially larger than rotor radius, so potential gains from non-homogeneous axial actuator loading distributions seem either negligible or inexistent. On such machines, the aerodynamic case for inhomogeneous loading seems restricted to wake rotation and finite blade-count issues. These phenomena were not studied in this thesis, but excellent work is already being conducted on the matter.

Static enthalpy interactions affect the efficiency of flow energy conversion systems that operate in spatially constrained environments. That occurs when natural or human-built landscapes are used to channel flow onto energy extraction devices: small-scale urban wind turbines mingled with buildings, wind turbines sited to exploit relief effects or tidal turbine arrays whose performance depends on the seabed's ability to channel flow. For all these cases, selection of a lower thrust coefficient (than $C_T = 8/9$) will generally enhance power extraction.

EXPECTED IMPACT TIMESCALE

Moonshot innovation is conceivable in wind energy – that was the takeaway message of the past three chapters. Materialising such a vision might however take several decades. However, wind energy is happening now, and its efficiency is not only about big ideas: it is to a large extent about getting an innumerable collection of details right.

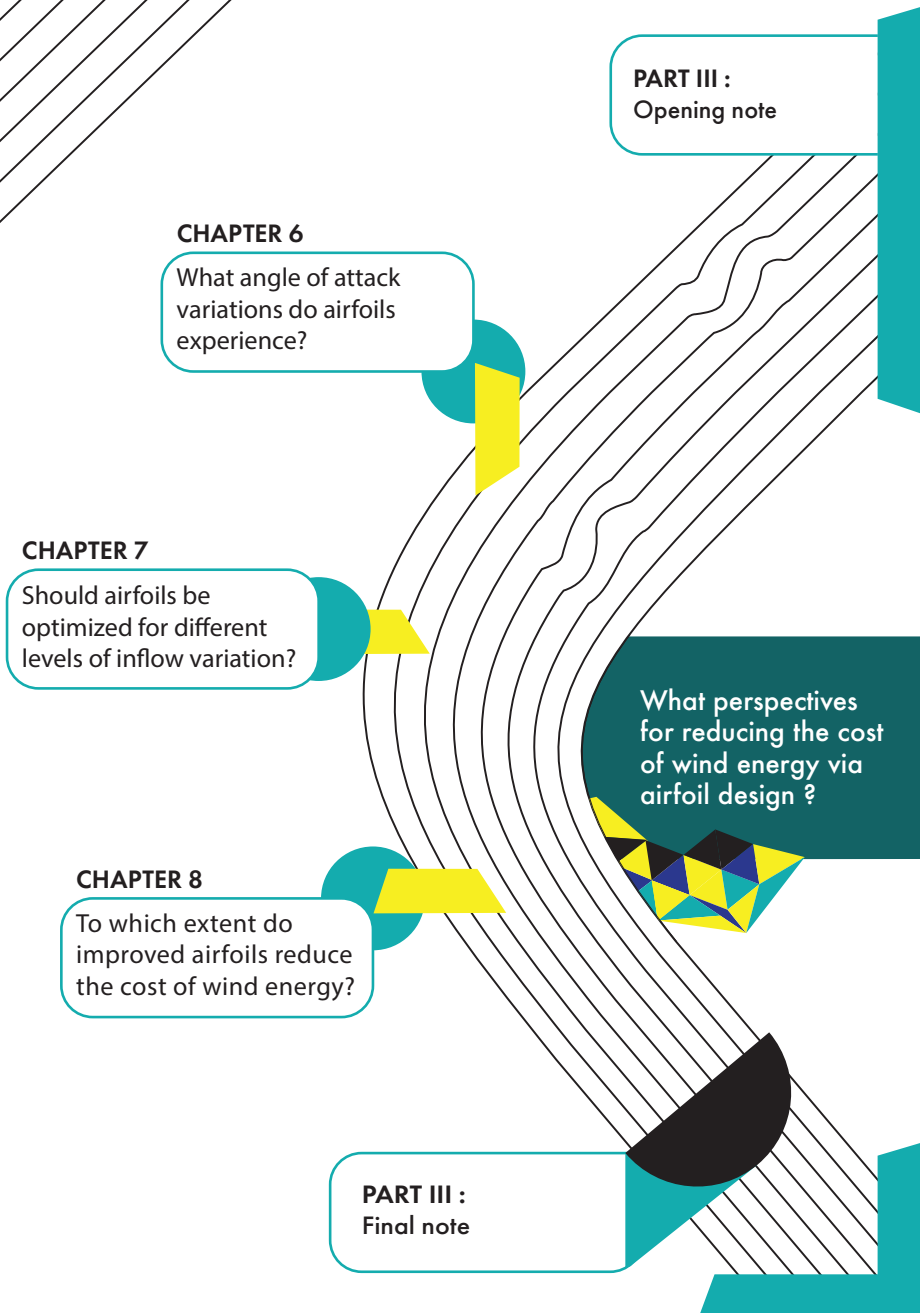
Modern wind turbines have thousands of parts, and each of them must operate efficiently to maximise power coefficient or economic yield. No individual study can cover the subtleties of every element that contributes, or hinders, the efficiency of wind energy conversion. This thesis is no exception, but it would be profoundly incomplete if it did not delve into the details of a particular design block. That will be the purpose of the next three chapters, which focus on the relation between airfoil design and wind turbine performance.



Naïve transposition of matched-actuator setups to offshore environments (top), duct for accelerated wake development in matched-actuator setup (middle) and application of active flow augmentation to single rotor vertical axis (bottom, left) or horizontal axis (bottom, right) machines.

III

EFFICIENCY OF WIND TURBINE AIRFOILS



OPENING NOTE

Efficiency of wind turbine airfoils

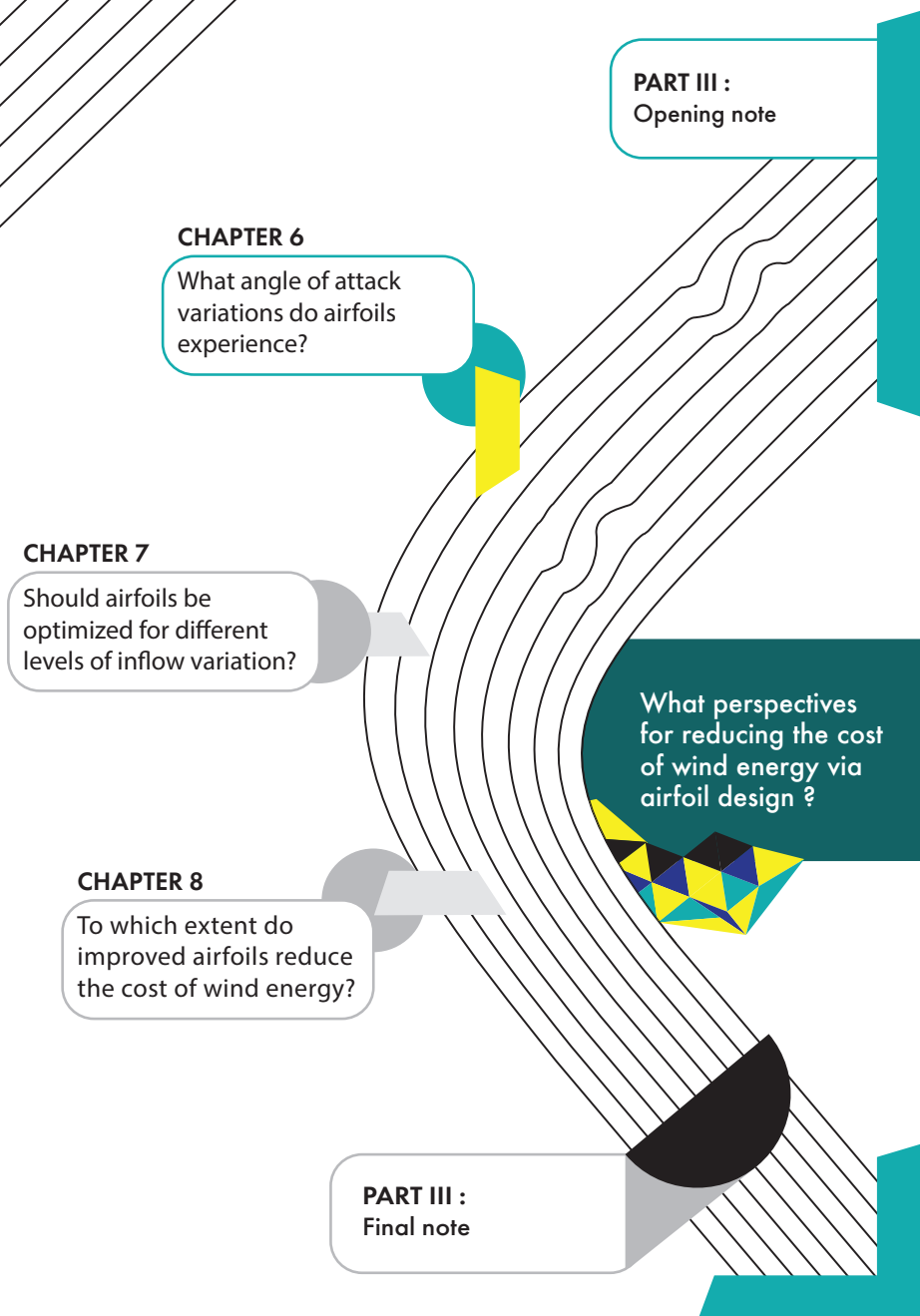
Can improvements in airfoil design still improve the aerodynamic efficiency of current wind-turbines? Horizontal-axis wind turbines are the primary workhorse of wind energy conversion. Far from the abstract considerations of part II, this part of the thesis seeks to understand the remaining scope for improving their efficiency through improved airfoil design.

The primary goal is to estimate the order magnitude of efficiency gains that can arise from improved wind turbine airfoils. A secondary goal is to try to account for the effect of unsteady inflow conditions during airfoil design. The approach is structured around the particular case of the DTU reference wind turbine and seeks to answer three questions.

Are there simple means for estimating the effect of inflow fluctuations on airfoil performance? Chapter 2 derives a semi-analytic probability distribution for angle-of-attack perturbations experienced by wind turbine blade sections. The probability distribution depends on local flow and operational conditions: yaw misalignment, wind shear and turbulence intensity. It is used to produce quasi-static polar curves of expected values for airfoil lift and drag that help answer the next question.

Should the effect of angle of attack variations be considered during airfoil design? Chapter 3 uses multi-objective airfoil optimisation techniques to quantify shifts in achievable performance due to angle-of-attack fluctuations. The first set of cases explores the design space with relatively formal design goals. Obtained insight is then used to design new airfoils for the tip of the DTU reference wind turbine, in a way that accounts for the effect of inflow perturbations.

How do improved airfoil designs affect the cost of wind energy? Chapter 4 attempts to answer by observing shifts in Pareto fronts of efficient rotor designs obtained with different sets of airfoils. Results are confronted with constant-cost isolines produced with a stylised, and overly simplified, cost model.



6

EFFECT OF INFLOW PERTURBATIONS

What fluctuations in angle-of-attack do wind turbine blade sections experience? Can their effect be estimated from static lift and drag polars?¹

INTRODUCTION

Wind turbine blades experience continuous variations of the angle of attack (AOA). Inflow variations arise from deterministic phenomena, like wind shear or rotor-misalignment, and from atmospheric boundary layer turbulence. Varying inflow causes fluctuating loads that induce transient structural deformation and additional unsteadiness. In wind farms, the wakes of upstream rotors create additional inflow inhomogeneity.

Fluctuations in the angle of attack mean that point design airfoils (Liebeck, 1976) are inadequate for wind turbine blades (Timmer, 2009a). That is why the design of wind turbine airfoils always starts by specifying the desired performance range (Vila and Alfaro, 2015; Zahle et al., 2014). Together with the relative importance of different operating points, that range is usually estimated by expert designers that resort to heuristic arguments (Timmer and Van Rooij, 2003; Li et al., 2017). Can objective guidelines for the range of operational angles of attack be formulated? Are there simple ways to determine how angle-of-attack perturbations affect airfoil performance?

¹Parts of this chapter were published in *Journal of Physics Conference Series* 1037(2) with co-authors G. de Oliveira, R.B. Pereira, W.A. Timmer and E. Quaeghebeur under the title "Probabilistic Design of Airfoils for Horizontal Axis Wind Turbines.". It is also related to "Design of HAWT airfoils tailored for Active Flow Control", published in *Wind Energy* with R. Pereira, W.A. Timmer, G. de Oliveira and G.J.W. van Bussel.

Probabilistic descriptions of the wind field are common (Kelly et al., 2014), but few efforts attempted to develop probability distributions for airfoil angle of attack and loads (Rinker, 2016; Rezaeihaa et al., 2017). Such descriptions are relevant, however, because angle-of-attack fluctuations cause disparities between average airfoil lift and static lift in average inflow conditions (Bernardy, 2002; Weismuller, 2011). This fact is considered in aircraft performance models (Bernardy, 2002; Boermans, 2008) but seldom accounted for during the design of wind turbine airfoils. The work of (Grasso et al., 2017) is a notable exception.

This chapter proposes a probabilistic description of angle-of-attack perturbations experienced by wind turbine blades. Section 6.1 uses inflow diagrams to address three different sources of AOA perturbations: wind shear, yaw misalignment, and inflow turbulence. Section 6.2 integrates the three sources of perturbation into a probability distribution function whose predictions are compared to higher fidelity models. Finally, section 6.3 assesses the effect of angle-of-attack perturbations on the performance of wind turbine airfoils. Implications for airfoil design will be discussed in the next chapter.

6.1. ANGLE OF ATTACK PERTURBATIONS

This section relates perturbations in angle-of-attack experienced by blades of horizontal-axis wind turbines with operational environment. Three sources of perturbation are considered: wind shear, rotor misalignment and atmospheric boundary layer misalignment.

6.1.1. ROTOR MISALIGNMENT

Wind turbine rotors are rarely aligned with incoming flow. First, the rotor axis is generally tilted upward to secure sufficient tip clearance. Second, wind direction sensors placed on the turbine nacelle are subject to perturbations that can mislead the yaw control system into erroneous orientations.

The yaw misalignment problem is described with figures 6.1 (a) and 6.1 (c). They show the rotor-fixed orthogonal reference frame XYZ , the yaw misalignment angle (β) and the rotor azimuthal angle (ψ). Rotor coning and prebend are ignored. Blades are considered straight and infinitely stiff to justify the assumption that all blade sections rotate in the same plane.

The free-stream (\vec{U}) is considered parallel to the ground but its magnitude (U) varies with height due to wind shear. It is written with a base of unit vectors (e_X, e_Y, e_Z) attached to the rotor reference frame:

$$\vec{U} = U_X \vec{e}_X + U_Y \vec{e}_Y + U_Z \vec{e}_Z \quad \text{with} \quad \begin{cases} U_X = U \cos \beta \\ U_Y = -U \sin \beta \\ U_Z = 0 \end{cases} \quad (6.1)$$

The geometric effect of yaw misalignment on U_X and U_Y corresponds to the advancing and retreating blade effect Schepers (2012). The wind speed at the rotor, denoted as U_r for radial position r , is written by parametrizing apparent wind speed in terms of azimuth angle:

$$U_{rX} = U_X(1 - \bar{a} - K \sin \psi) \quad \text{and} \quad U_{rY} = U_Y. \quad (6.2)$$

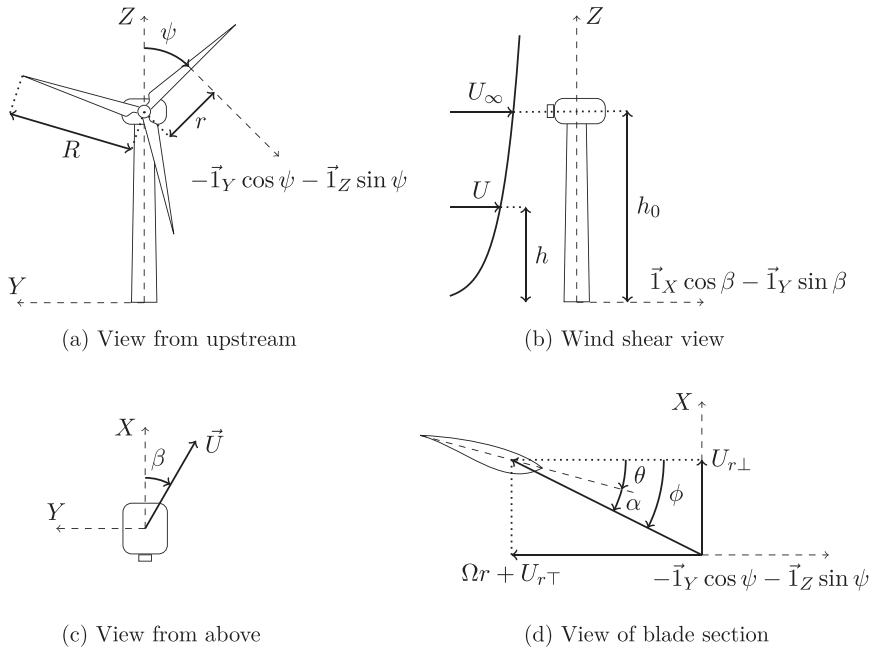


Figure 6.1: Setup overview and notation.

The axial X -component U_{rX} of the wind speed at the rotor plane includes the azimuthally varying induction felt at the rotor. That phenomenon, sometimes called skewed wake effect, is approximated with the model by [Pitt and Peters \(1981\)](#). Symbol \bar{a} denotes the azimuthally and radially averaged axial induction factor. Finally, R denotes the rotor radius and K is a parameter that depends on radial coordinate (r) and yaw misalignment angle:

$$K = \frac{15\pi}{32} \frac{r}{R} \tan\left(\frac{\beta(0.6\bar{a} + 1)}{2}\right), \quad (6.3)$$

Expression 6.2 ignores the Y -component of rotor induction, which is negligible for small yaw misalignment angles.

In order to estimate fluctuations in the angle of attack, it is necessary to express wind speed components reference frame of blade sections. Recalling the assumption that all blade sections rotate in the same plane and leads to a simple coordinate transformation:

$$U_{r\perp} = U_{rX} \quad \text{and} \quad U_{r\top} = U_{rY} \cos\psi, \quad (6.4)$$

The procedure is justified by figures 6.1(a) and (d). Subscripts \perp and \top denote directions normal and tangential to the plane of rotation.

6.1.2. WIND SHEAR

Wind shear is modeled with a logarithmic atmospheric boundary layer profile [Manwell et al. \(2002\)](#). Local inflow velocity can then be written in terms of height (h), undisturbed wind speed at hub height (U_∞), and roughness length (z_0):

$$U = U_\infty \frac{\ln h - \ln z_0}{\ln h_0 - \ln z_0} \quad (6.5)$$

Blade section height (h) is written in terms of radial coordinate (r), azimuth angle (ψ) and hub height (h_0) using figure 6.1(b).

$$h = h_0 + r \cos\psi \quad (6.6)$$

Inserting expression 6.6 into 6.5 leads to a useful relation between inflow speed and azimuth angle, all other parameters remaining equal.

$$U = U_\infty \frac{\ln(h_0 + r \cos\psi) - \ln z_0}{\ln h_0 - \ln z_0}, \quad (6.7)$$

6.1.3. ATMOSPHERIC TURBULENCE

The effect of atmospheric turbulence is described in terms of relative perturbations (δ) to the X direction of the wind speed, as described in [Pereira et al. \(2017\)](#). This is justified because:

1. The intensity of the longitudinal component (aligned with X) of turbulence is much larger than the lateral one (aligned with Y) ([Wagenaar and Eecen, 2010](#))
2. Longitudinal inflow perturbations influence AOA to a greater extent than lateral or vertical ones, as can be inferred from the inflow diagram of 6.1(d)

Turbulent wind velocity (\vec{V}) is therefore described in terms of normal and tangential components by adding instantaneous perturbations ($U_{r\perp}\delta$) to the normal component.

$$V_{r\perp} = U_{r\perp}(1 + \delta) \quad \text{and} \quad V_{r\top} = U_{r\top}, \quad (6.8)$$

Following the IEC (2005) standard, instantaneous inflow perturbations are described in terms of a normal probability distribution whose standard deviation corresponds to the turbulence intensity (I).

$$p(\delta) = \frac{1}{\sqrt{2\pi}I} \exp\left(-\frac{1}{2}\left(\frac{\delta}{I}\right)^2\right) \quad (6.9)$$

Expression 6.9 has been extensively criticized (van den Boz and Sanderse, 2017) despite its usage for certification purposes (IEC, 2005). It is expected to provide reasonable estimations for the average effect of turbulent phenomena, and to be blatantly inaccurate for modeling extreme events.

6.1.4. COMBINED INFLOW

The effects of rotor misalignment, wind shear and atmospheric turbulence are superposed by combining equations 6.1, 6.7 and 6.8 with the inflow diagram of figure 6.1(d). This results in expressions for perturbed (ϕ) and unperturbed (ϕ_0) inflow angle.

$$\tan\phi = \frac{V_{r\perp}}{\Omega r + V_{r\top}} = (1 + \delta) \tan\phi_0 \quad \phi_0 = \text{atan}\left(\frac{\cos\beta(1 - \bar{a} - K \sin\psi)}{\lambda_r - \sin\beta \cos\psi}\right) \quad (6.10)$$

Where K was defined in equation 6.3 and λ_r corresponds to the local speed ratio:

$$\lambda_r = \frac{\Omega r}{U} = \frac{\Omega r}{U_\infty} \frac{\ln h_0 - \ln z_0}{\ln(h_0 + r \cos\psi) - \ln z_0} \quad (6.11)$$

Equations 6.10 and 6.11 suppose that the occurrence of turbulent inflow perturbations (δ) is independent of blade position (ψ , r) and misalignment angle (β). Again, this approach can be questioned even if it is supported by wind turbine certification standards (IEC, 2005). It is deemed accurate enough for order-of-magnitude estimates.

6.1.5. EFFECT OF ABL TURBULENCE ON ANGLE OF ATTACK

We now assume that the control system does not adjust blade pitch θ or rotational speed Ω in response to perturbations due to atmospheric turbulence. In other words, there is no individual pitch control and the rotor is large enough for its rotational inertia to damp turbulent gusts. Figure 6.1(d) then leads to a simple expression for the perturbation-dependent angle of attack (α):

$$\alpha = \phi - \theta = \text{atan}\left((1 + \delta) \tan\phi_0\right) - \theta \quad (6.12)$$

Angle-of-attack perturbations (α_δ) are defined in terms of a reference angle of attack (α_0):

$$\alpha_0 = \phi_0 - \theta \quad \alpha_\delta = \alpha - \alpha_0 = \text{atan}\left((1 + \delta) \tan\phi_0\right) - \phi_0. \quad (6.13)$$

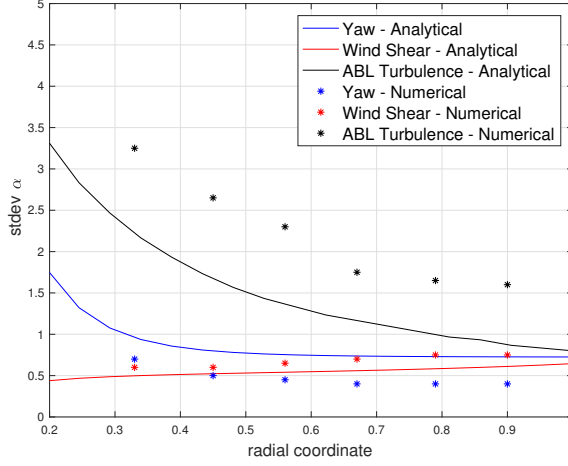


Figure 6.2: Comparison of standard deviation of angles-of-attack in numerical and semi-analytical approach. Numerical results produced by [Rezaeihaa et al. \(2017\)](#)

The arctangent function is invertible over the range of interest, so expression 6.13 can be inverted to express perturbations in wind speed due to turbulence ($U_{r\perp}$) as function of the perturbation angle of attack (α_δ):

$$\delta = \frac{\tan(\phi_0 + \alpha_\delta) - \tan \phi_0}{\tan \phi_0} \quad \text{for} \quad \phi_0 + \alpha_\delta = \text{atan}((1 + \delta) \tan \phi_0) \in \left] -\frac{\pi}{2}, \frac{\pi}{2} \right[\quad (6.14)$$

6.2. PERTURBATION PROBABILITY DISTRIBUTION

The probability distribution function (q) for the occurrence of angle-of-attack perturbations is obtained by applying the change of variables of expression 6.14 to the probability distribution of expression 6.9:

$$\begin{aligned} q(\alpha_\delta|\psi) &= \left| \frac{d\delta}{d\alpha_\delta} \right| p(\delta) = \left| \frac{1 + \tan^2(\phi_0 + \alpha_\delta)}{\tan \phi_0} \right| p\left(\frac{\tan(\phi_0 + \alpha_\delta) - \tan \phi_0}{\tan \phi_0} \right) \\ &= \frac{1}{\sqrt{2\pi} |\tan \phi_0|} |1 + \tan^2(\phi_0 + \alpha_\delta)| \exp\left(-\frac{1}{2} \left(\frac{\tan(\phi_0 + \alpha_\delta) - \tan \phi_0}{I |\tan \phi_0|} \right)^2 \right) \end{aligned} \quad (6.15)$$

Expression 6.15 depends directly on the turbulence intensity I and the ‘no-disturbance’ inflow angle ϕ_0 , defined in equation 6.10. This angle is a function of yaw misalignment (β), surface roughness (z_0), radial position (r) and azimuthal position (ψ). That is why equation 6.15 describes the probability of angle-of-attack perturbations conditional to azimuth angle – variables that do not vary in time (β, z_0, r) are considered parameters of the probability distribution.

		Value	Unit
Rotor radius	R	89	<i>m</i>
Hub height	h_0	119	<i>m</i>
Rotational speed	Ω	1	<i>rad/s</i>
Wind at hub height	U_∞	10.6	<i>m/s</i>
Roughness length	z_0	0 to 0.6	<i>m</i>
Yaw misalignment angle	β	0 to 10	<i>deg</i>
Turbulence intensity	I	0 to 0.16	–

Table 6.1: Numerical simulation parameters considered by [Rezaeihaa et al. \(2017\)](#)

The probability distribution of azimuthal positions (w) is uniform since the blade rotates cyclically and the rotational speed is assumed to be constant. It is written in terms of Heavyside functions (H):

$$w(\psi) = \frac{1}{2\pi} (H_{(\psi)} - H_{(\psi-2\pi)})$$

The marginal probability of angle of attack perturbations therefore corresponds to the integral of equation 6.15 over a complete revolution, i.e. for all possible values of the azimuthal angle ψ .

$$q(\alpha_\delta) = \int_{-\infty}^{+\infty} q(\alpha_\delta|\psi) w(\psi) d\psi = \frac{1}{2\pi} \int_0^{2\pi} q(\alpha_\delta|\psi) d\psi \quad (6.16)$$

Expression 6.16 is integrated numerically with a simple quadrature scheme. It combines the effect of angle of attack perturbation due to rotor misalignment, wind shear and ABL turbulence. It can be used to compute the standard deviation (σ_α) of angle-of-attack perturbations:

$$\sigma_\alpha = \left(\int_{-\infty}^{+\infty} (\alpha_\delta^2 q(\alpha_\delta)) d\alpha_\delta - \mu_{\alpha_\delta}^2 \right)^{\frac{1}{2}} \quad \mu_{\alpha_\delta} = \int_{-\infty}^{+\infty} (\alpha_\delta q(\alpha_\delta)) d\alpha_\delta \quad (6.17)$$

6.2.1. VALIDATION OF SEMI-ANALYTICAL PROBABILITY DISTRIBUTION

This section compares the predictions of equation 6.16 with results from aero-structural simulations of the DTU 10MW machine. These numerical simulations were performed by [Rezaeihaa et al. \(2017\)](#) and employed the *HAWC2* software. Their numerical study assessed a total of 34 load scenarios with different sources of angle-of-attack perturbation : tower shadow, yaw misalignment, wind shear and a range of ABL turbulence intensities. Table 6.1 summarizes operational conditions.

Figure 6.2 plots the standard deviation of angle-of-attack perturbations (σ_α) observed in the numerical simulations of [Rezaeihaa et al. \(2017\)](#) next to that predicted by expression 6.17 . Analytical predictions compare reasonably well with aero-structural simulations. For fluctuations induced by wind-shear, the small slope of increase of σ_α towards larger radial positions display is of comparable order-of-magnitude for both analytical and numerical predictions. The two methods also compare favorably regarding the effect of yaw misalignment: there is a clear trend of increasing AOA fluctuations towards

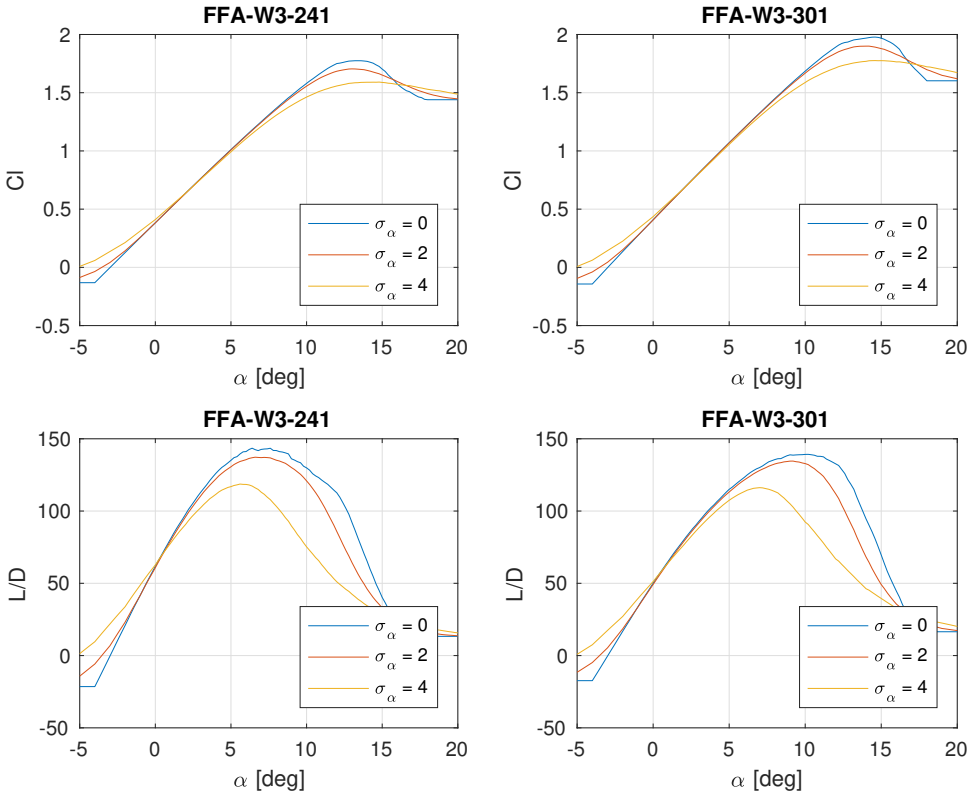


Figure 6.3: Expected lift, and expected lift over expected drag ratio, for two FFA airfoils subject to angle of attack fluctuations by a normal distribution with different standard deviation (σ_α). Transition was free and Reynolds number was equal to $9e6$ for all cases.

inboard HAWT blade stations. Finally, in both approaches, the effect of atmospheric turbulence dominates other perturbation sources.

The trend of decreasing σ_α towards larger radial positions is clear in numerical and analytical results, but the magnitude is not well captured. Differences in the magnitude of σ_α may be attributed to the fact that the analytical approach ignores structural dynamics, unsteady aerodynamics and tower shadow effects, which were included in the numerical approach. In addition, the numerical data was obtained over a range of wind speeds while the analytical approach was only applied to the rated wind speed.

6.3. EXPECTED WIND TURBINE AIRFOIL LOADS

If a probability distribution for angle-of-attack fluctuations experienced by wind turbine blade sections is available, and if a function relating section loads with angle-of-attack exists (the airfoil polar), then a probability distributions for blade loads can also be established.

Consider for the drag polar, which describes the drag coefficient (C_d) in terms of a

monotonic function of angle-of-attack h such that $C_d = h(\alpha)$. The probability of occurrence of drag values conditional to azimuth, denoted as $s_{(C_d|\psi)}$, can be written from the average angle-of-attack ($\bar{\alpha} = \alpha - \alpha_\delta$) and from the probability of occurrence of angle-of-attack values conditional to azimuth (from expression 6.15) :

$$s_{(C_d|\psi)} = q\left(\left(h_{(C_d)}^{-1} - \bar{\alpha}\right)|\psi\right) \left| \frac{d h_{(C_d)}^{-1}}{d C_d} \right|$$

The procedure is slightly more complex for lift values, because the lift polar is not monotonous. In any case, the most interesting quantities are the expected values (average) of the lift and drag coefficient. They depend on the polar curve ($C_l = g(\alpha)$ and $C_d = h(\alpha)$), the average angle of attack ($\bar{\alpha}$), and the probability distribution ($q(\alpha)$) for angle-of-attack perturbations :

$$\begin{aligned} \bar{C}_l(\bar{\alpha}) &= g(\bar{\alpha} + \alpha_\delta) \star q(\alpha_\delta) = \int_{-\infty}^{\infty} \left(g(\bar{\alpha} + \alpha_\delta) \star q(\alpha_\delta) \right) d\alpha_\delta \\ \bar{C}_d(\bar{\alpha}) &= h(\bar{\alpha} + \alpha_\delta) \star q(\alpha_\delta) = \int_{-\infty}^{\infty} \left(h(\bar{\alpha} + \alpha_\delta) \star q(\alpha_\delta) \right) d\alpha_\delta \end{aligned} \quad (6.18)$$

Expression 6.18 was integrated numerically for the polars of two popular wind turbine airfoils employed on the DTU reference wind turbine blade. For the sake of simplicity, the probability distribution of angles of attack was approximated with a normal distribution (\mathcal{N}) with standard deviation σ_{α} and integration bounds were trimmed to capture 90% of all angle of attack occurrences (α):

$$\begin{aligned} \bar{C}_l(\bar{\alpha}) &= g(\bar{\alpha} + \alpha_\delta) \star q(\alpha_\delta) \approx \frac{1}{0.9} \int_{-1.645\sigma}^{+1.645\sigma} \left(g(\bar{\alpha} + \alpha_\delta) \mathcal{N}(\alpha, \bar{\alpha}, \sigma_{\alpha}) \right) d\alpha_\delta \\ \bar{C}_d(\bar{\alpha}) &= h(\bar{\alpha} + \alpha_\delta) \star q(\alpha_\delta) \approx \frac{1}{0.9} \int_{-1.645\sigma}^{+1.645\sigma} \left(h(\bar{\alpha} + \alpha_\delta) \mathcal{N}(\alpha, \bar{\alpha}, \sigma_{\alpha}) \right) d\alpha_\delta \end{aligned} \quad (6.19)$$

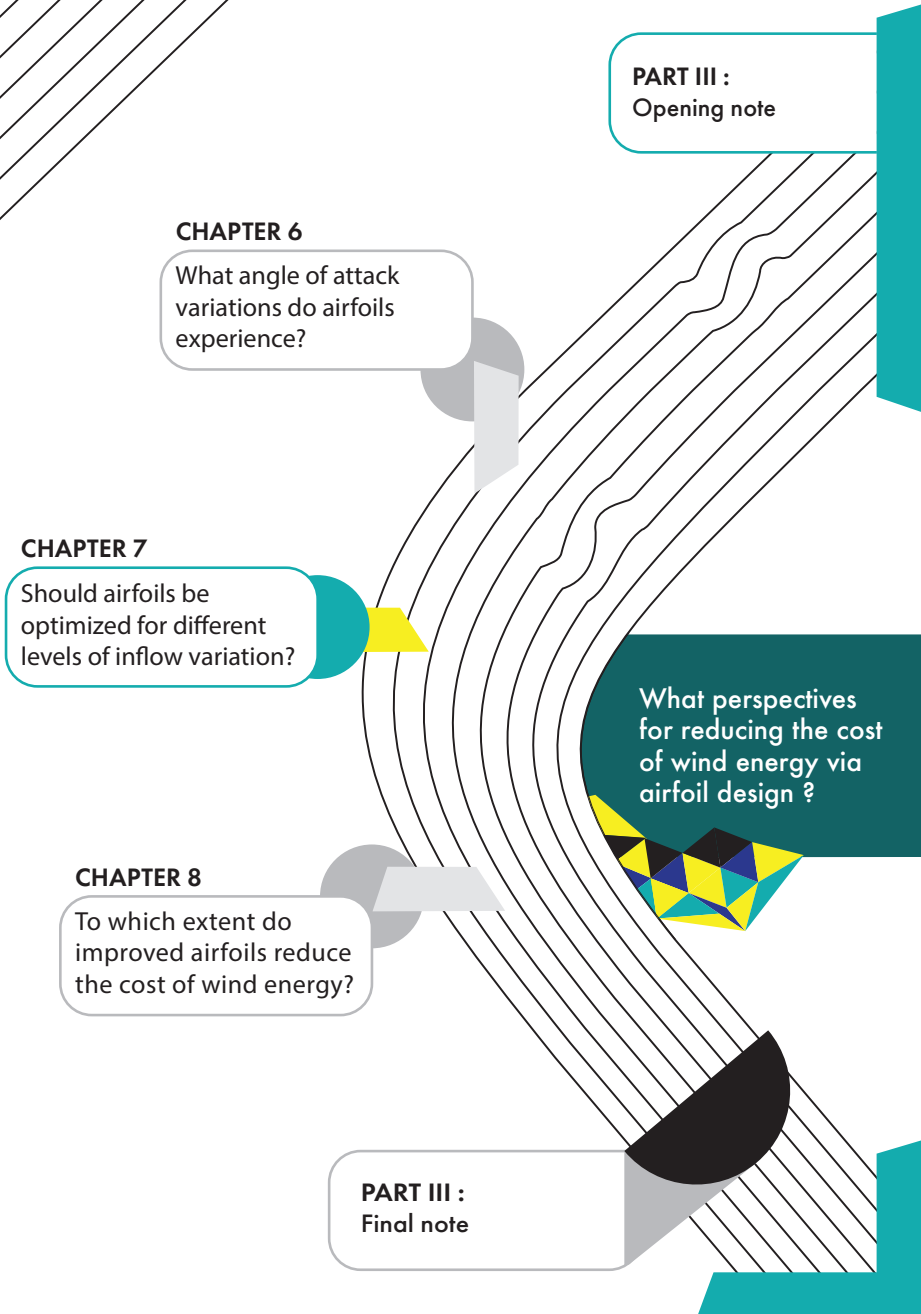
Results are shown on figure 6.3. The blue line corresponds to the traditional static polar ($\sigma = 0$) whereas the red and yellow lines correspond to standard deviations of 2 and 4 degrees, comparable to conditions found near the tip or root of the DTU-RWT blade (as shown on figure 6.2). Expectably, the lines overlap each other in the linear region of the airfoil polar. Close to stall, however, inflow fluctuations average non-linear lift variations and shave the peak of the lift polar. This suggests that angle of attack variations reduce the actual maximum lift that wind turbine airfoils can reach in turbulent inflow conditions. This phenomenon is well-known to glider pilots (Bernardy, 2002; Boermans, 2008; Weismuller, 2011).

Of course, figure 6.3 does not give a complete picture of the effect of inflow fluctuations on the performance of wind turbine airfoils. The approach of expression 6.18 is quasi-static and neglects many important unsteady phenomena: variations in angle of attack lead to important circulatory and added mass effects (Katz and Plotkin, 2006; Reeh et al., 2014), spectral components of inflow turbulence can disrupt boundary layer transition processes (Bertolotti, 1999; Reeh and Tropea, 2015), and history effects can lead to dynamic stall phenomena (Rasmussen et al., 1999). Despite gross oversimplifications, quasi-static treatments like those of equation 6.18 are known to provide reasonable estimations for the effect of inflow variations due to atmospheric turbulence (Weismuller, 2011). Fluctuations due to wind shear and yaw misalignment should be less

problematic, because these phenomena occur at lower reduced frequencies on multi-MW rotors.

The quasi-static treatment of figure 6.3 suggests that inflow variations shift the angle of attack at which airfoils reach the highest expected (average) glide-ratio. One might therefore wonder about the angle of attack at wind turbine airfoils should operate. Should it be the angle that maximizes static glide-ratio, as is the case in most current designs, or the angle that maximizes expected (average) glide ratio for the envisioned inflow inhomogeneity level? Chapter 8 will seek to answer to this question.

The magnitude of glide-ratio shifts caused by inflow perturbations differs across airfoils — it is larger for the FFA-W3-301 than for the FFA-W3-241, in terms of both angle-of-attack and effective glide-ratio. One might then ask whether airfoils should be designed to minimize the performance loss due to inevitable inflow variations. That will be subject of the next chapter (7).



7

TAILORING AIRFOILS TO INFLOW CONDITIONS

How do fluctuations in operational angle of attack affect the realization of airfoil design goals?¹

INTRODUCTION

Airfoils employed on horizontal axis wind turbines must satisfy conflicting aerodynamic requirements (Li et al., 2017; de Oliveira, 2011; Fuglsang et al., 2004). A large glide-ratio is essential to power production (Tangler and Somers, 1987; Somers, 1997; Vila and Alfaro, 2015) while aerodynamic damping requirements call for smooth stall (Grasso et al., 2017) and large design lift (Rasmussen et al., 1999; Zahle et al., 2014). Resilience to leading edge roughness is also fundamental (Bak et al., 2008; Van Rooij and Timmer, 2003) because soiling and erosion of the blade surface are inevitable (Schramm et al., 2017). Finally, trailing-edge noise (Oerlemans, 2011) should be limited to avoid the need for derating turbines to comply with nuisance regulations (Oerlemans and Fuglsang, 2012).

Airfoils with a large stall margin – the distance from the design angle-of-attack to the angle of maximum lift – are more resilient to inflow fluctuations (Boorsma et al., 2015) but reach lower glide-ratios (Liebeck, 1976; Eppler, 1979). It could therefore make sense to choose airfoils with higher glide-ratio (and hence lower stall margin) for sites where

¹Parts of this chapter were published in *Journal of Physics Conference Series 1037(2)* with co-authors G. de Oliveira, R.B. Pereira, W.A. Timmer and E. Quaeghebeur under the title “Probabilistic Design of Airfoils for Horizontal Axis Wind Turbines.”. It is also related to “Design of HAWT airfoils tailored for Active Flow Control”, published in *Wind Energy* with R. Pereira, W.A. Timmer, G. de Oliveira and G.J.W. van Bussel.

clean inflow is expected. The opposite thought would apply to sites where large angle of attack perturbations are expected.

Different wind turbines operate in different wind or soiling conditions (Draxl and Mayr, 2010; El-din and Diab, 2016). Agricultural flatlands, for example, display much cleaner inflow than mountainous sites with ridges or forest coverage (Arnqvist, 2013; Dragomir et al., 2016). Offshore, wind turbines face different levels of incoming turbulence depending on their location in the windfarm array (Argyle et al., 2015). These factors are taken into account when specifying ultimate load cases (IEC, 2005) but seldom considered explicitly during airfoil design. Should it be the case? Should airfoils be designed for specific levels of inflow inhomogeneity?

This chapter answers with Pareto fronts of airfoil designs that maximize the same performance metrics for different levels of inflow variation. The idea is that differences in optimized airfoils indicate whether design procedures should account explicitly for expected angle-of-attack perturbations. Section 7.1 describes the multi-objective optimization approach. Section 7.2 assesses the effect of inflow perturbations on non-inferior compromises between clean and soiled airfoil performance. Section 7.3 designs new airfoils for the tip of the DTU 10MW reference wind turbine. Key findings are summarized in section 7.4.

7.1. MULTI-OBJECTIVE AIRFOIL OPTIMIZATION

The airfoil optimization strategy employed in this chapter was developed over several years has now become relatively mainstream (de Oliveira, 2011; Pereira et al., 2017). Airfoil design is interpreted as a multi-objective optimization problem solved with a combination of genetic and gradient-descent algorithms. Design goals are translated into cost functions and the design space is approximate with a parametrization.

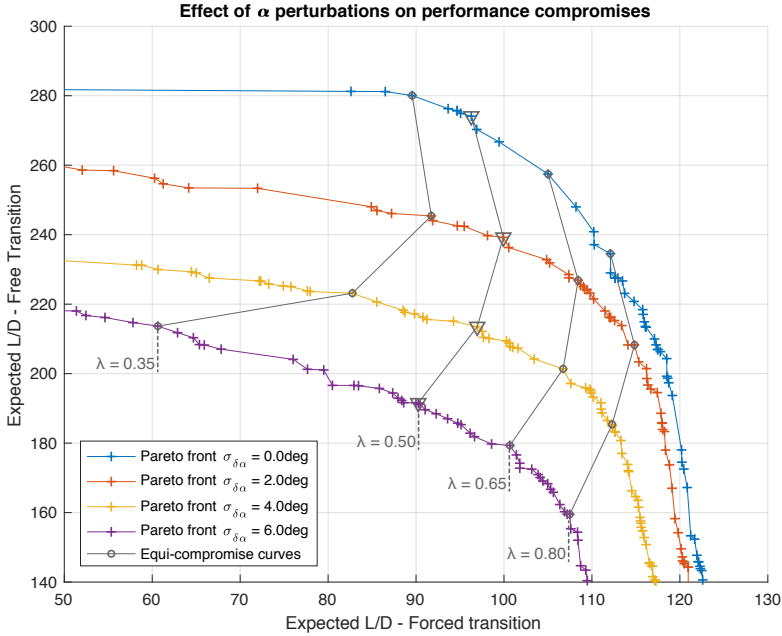
7.1.1. SHAPE PARAMETRIZATION

Airfoil shapes are parametrized with the class shape transformation (CST) method (Kulfan and Bussoletti, 2006b; Kulfan, 2007). Each airfoil is described with 19 shape parameters (A_i): 8 parameters for the upper side, 8 for the lower side and 1 for trailing edge thickness. Admissible upper and lower bounds for shape parameters are found with a data-driven approach described in de Oliveira (2011).

Stiffness and manufacturability constraints are enforced according to the method outlined by Pereira et al. (2017). Airfoil thickness is required to exceed a lower threshold in the trailing edge region, approximately 3.6% t/c at a relative chordwise position $x/c = 0.7$. This value was determined to correspond to about 60% of the trailing-edge thickness of typical wind energy airfoils with 21% thickness to chord ratio.

7.1.2. COMPUTATION OF AERODYNAMIC POLARS

Two lift and drag polars are calculated for each airfoil candidate, corresponding to *clean* and *rough* configurations. Aerodynamic polars are calculated with the Rfoil viscous-inviscid interaction (VII) flow solver (van Rooij, 1996a). The airfoil is discretized with 240 panels and the flow is solved for angles of attack between -5 and 20 degrees in steps of 0.2 degrees. Transition of the boundary layer from laminar to turbulent flow is com-

Figure 7.1: Optimization Results - Pareto Fronts for different σ_α

puted with the linear e^N method for the *clean* configuration ($N = 9$), while it is forced at $x/c = 0.05$ on the upper surface and $x/c = 0.1$ on the lower surface for the *rough* configuration.

7.2. MAXIMIZING GLIDE-RATIO ACROSS INFLOW PERTURBATIONS

This section studies the effect of inflow variations on the compromise between performance in clean and soiled conditions. Structural considerations left aside, that compromise is a primary driver of wind turbine airfoil design.

7.2.1. OBJECTIVE FUNCTIONS

Two objective functions were considered: one represents performance in clean conditions while the other does the same for soiled conditions. Performance is approximated as the expected value of the glide ratio, which corresponds to the convolution of the glide-ratio function with the probability distribution of angle-of-attack occurrences.

$$\frac{\bar{L}}{D}(\alpha_{\text{des}}) = \frac{1}{0.9} \int_{\alpha_{\text{DES}} - 1.64\sigma_{\delta\alpha}}^{\alpha_{\text{DES}} + 1.64\sigma_{\delta\alpha}} \frac{C_l(\alpha)}{C_d(\alpha)} p(\alpha) d\alpha \quad (7.1)$$

Unlike in the previous chapter, expression 7.1 resorts to a normal probability distribution for angle-of-attack perturbations. That accelerates computations, and introduces negligible errors because perturbations due to atmospheric turbulence dominate over other AOA fluctuation sources.

$$\alpha \approx N(\alpha_{des}, \sigma_\alpha)$$

The design angle of attack $\alpha_{DES} = 7$ degrees was chosen to match typical DU airfoils. It corresponds to the expected value of angle-of-attack occurrences. Limits of integration are chosen to capture 90% of all occurrences. Bounds are considered large enough to have a negligible effect on optimisation results.

Performance objectives are translated into cost functions because the chosen numerical optimization algorithm operates on minimisation problems. A minus sign is introduced such that the optimizer maximizes aerodynamic performance by minimizing the cost functions, which are also scaled to a unit order of magnitude.

$$CF_1 = -\frac{1}{100} \frac{\bar{L}}{D} (\alpha_{DES}) \Big|_{\text{clean}} \quad \text{and} \quad CF_2 = -\frac{1}{100} \frac{\bar{L}}{D} (\alpha_{DES}) \Big|_{\text{rough}}$$

Cost function CF_1 is computed with an aerodynamic polar computed for free-transition conditions, whereas cost CF_2 employs an aerodynamic polar for forced transition conditions. The effect of inflow fluctuations is included by considering different values of the standard of deviation σ_α of angle-of-attack perturbations.

7.2.2. STAGGERED SOLUTION PROCEDURE

Four standard deviations of angle-of-attack perturbations were considered (0,2,4 and 6degrees), and a double objective optimization problem was solved for each of them. Each problem was solved in four steps:

1. A collection of three initial guesses was generated with a gradient algorithm based on the interior point method. Results from this run were then added to the initial population of the genetic algorithm used in the next step.
2. The double objective problem was then tackled with the NSGA-II genetic algorithm with a population size of 160 individuals. The algorithm was allowed to run for 40 generations, and it departed from an initial population that combined 60 well known airfoil designs, the three designs generated in step 1, and 97 randomly generated designs. A Pareto fraction of 45% and mutation rate of 2% were used to ensure broad coverage of the design space.
3. Three members of the Pareto front were then drawn and fed as initial guesses to the gradient algorithm, which pushed them to extremes of the Pareto front.
4. The double objective problem was then tackled again with the NSGA-II genetic algorithm. The algorithm was again allowed to run for 40 generations but population-size was increased to 200 individuals and the Pareto fraction was increased to 60%. The mutation rate was maintained.

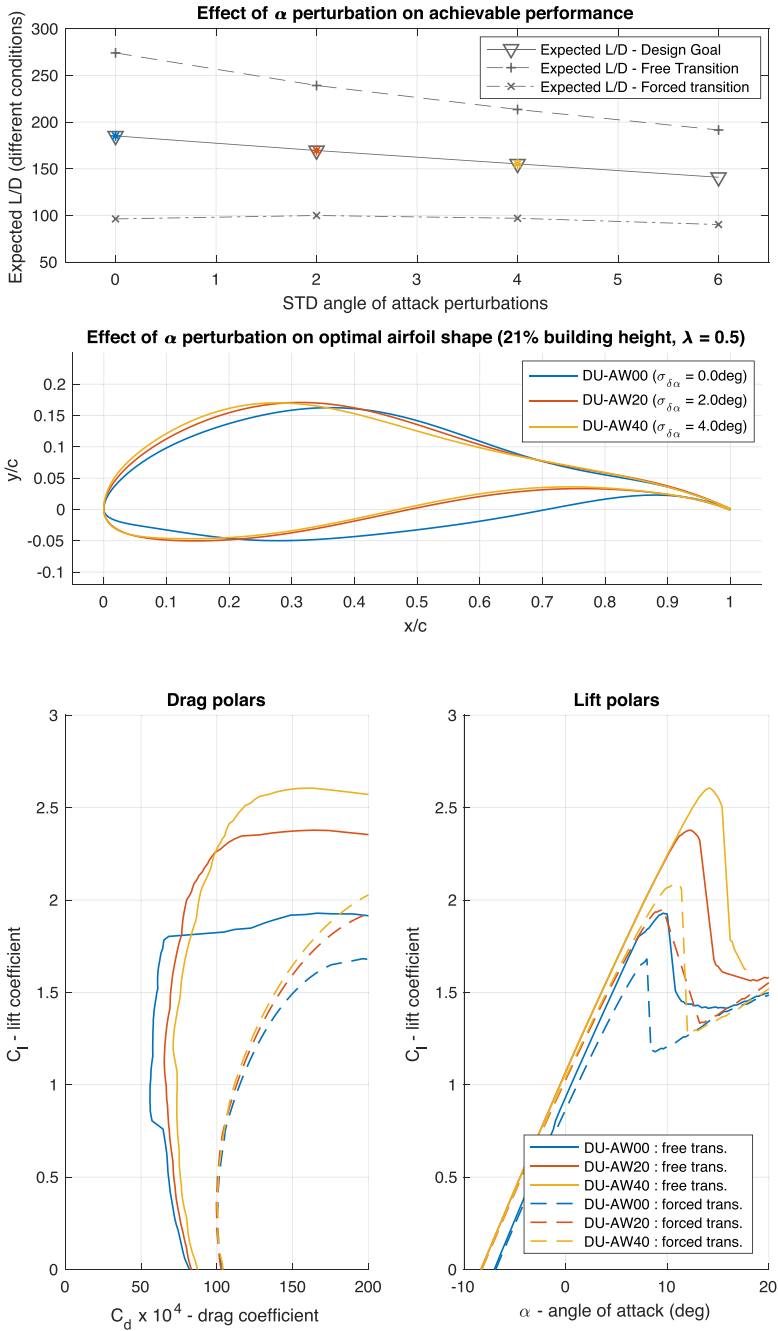


Figure 7.2: Optimization Results - Airfoil sections and cost function variation with AOA standard deviation.

7.2.3. PARETO FRONT

Optimization results are presented on figure 7.1 and 7.2. Figure 7.1 displays the Pareto fronts obtained for different standard deviations of angle-of-attack fluctuations. The Pareto front is a feasibility frontier: each marker corresponds to an efficient airfoil design, that is, an airfoil for which improving clean performance (CF_1) is only possible at the expense of a loss in soiled performance (CF_2). Ideally, on

Figure 7.1 shows that cost function values decrease for larger values of σ_α . This results from the lower values of the expected L/D , but also from the fact that the optimization objectives on figure 7.1 show the expected value of the lift to drag ratios considering different ranges of angle of attack, thus necessarily decreasing the cost function values as larger AOA fluctuations are considered. Figure 7.1 also displays circle markers that correspond to the airfoil sections whose geometry and performance are shown in figure 7.2.

7.2.4. EQUI-COMPROMISE LEVELS

Levels of compromise between clean and rough performance were identified by re-processing the Pareto front. Every solution of the multi-objective optimization problem is also a solution to a simpler scalar minimization problem. Designs (A_i^λ) that correspond to particular compromise levels (λ) are therefore found by searching the Pareto front for minima of a composite cost function:

$$A_i^\lambda : \min_{A_i} (1 - \lambda)CF_{(A_i)}^1 + \lambda CF_{(A_i)}^2 \quad (7.2)$$

Airfoil with a larger CF_1 ($\lambda = 0$) exhibit poor performance in tripped flow conditions and very good performance in clean conditions. They resemble have a point-design shape (Liebeck, 1976) typical of laminar flow airfoils (Fuglsang et al., 2004; Reeh and Tropea, 2015). Towards the right of each Pareto front ($\lambda = 1$) the difference between the *clean* and *rough* performance is much smaller, leading to a more robust type of airfoil. In this case, robustness means that the airfoil performance does not degrade significantly when the turbulent boundary layer is tripped. Early onset of turbulent flow is frequent on large wind turbines. It results from leading edge soiling and erosion.

7.2.5. AIRFOIL SHAPE

Figure 7.2 focuses on the region of interest for horizontal axis wind turbine airfoil, but recasts optimization results to show the variation of airfoil performance with standard deviation of angle of attack. This may be interpreted as the degree of robustness, but related to good airfoil performance over a range of α . The airfoil sections and respective performance shown in figure 7.2 correspond to a clean/rough compromise level $\lambda = 0.5$ (illustrated by triangles in figure 7.1). Regarding airfoil geometry, it is clear that the point of maximum upper thickness moves towards the leading edge when larger standard deviations of angle-of-attack are considered. This geometric feature promotes earlier transition of the boundary layer (Bak et al., 2008), which suggests that airfoils robust to angle-of-attack fluctuations are also robust to leading-edge soiling.

Airfoils optimized for smaller values of σ have narrower drag buckets and lower minimum drag. In other words, designing with smaller AOA deviations leads to 'point-design' airfoils with higher peak performance for very specific conditions (Liebeck, 1976). It is

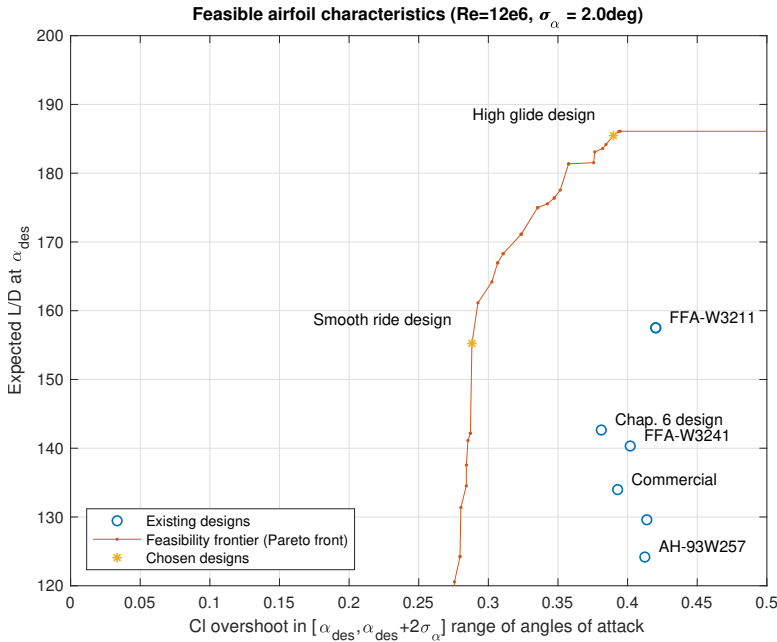


Figure 7.3: Feasibility frontier of compromise between expected glide ratio and lift overshoot for airfoils with 24% relative thickness at $Re = 12e6$ with 2deg standard deviation of angle of attack.

long known, however, that such designs fail to realize their promises in realistic flow conditions (Eppler, 1979). This is particularly true for wind energy applications where design stability (robustness) is of primary importance, as stressed by (Li et al., 2017).

7.2.6. EFFECT OF INFLOW ON STALL MARGIN

The airfoils of figure 7.2 display a sharp decrease in lift after the maximum lift point. This goes against general intuition suggesting that robust designs are associated with soft stall characteristics. In fact, the opposite trend is observed: the design optimised for $\sigma = 4.0$ has sharper stall than designs optimized for $\sigma = 2.0$ and $\sigma = 0.0$.

The optimization algorithm sought airfoils with long linear runs to compensate for large variations in angle-of-attack. The resulting designs exhibit stable glide-ratio across a wide variety of angles of attack, and therefore fulfill the demanded design goal. Because of their larger stall margin, however, these airfoils are likely to cause increased transient loads. Practical wind turbine airfoils include soft-stall or load exceedance requirements (Vila and Alfaro, 2015).

7.3. COMPROMISE BETWEEN GLIDE-RATIO AND LIFT OVERSHOOT

The design goal of improving airfoil performance across a wide angle of attack range is opposed to the design goal of reducing lift overshoot during gusts. Both goals are relevant because they respond directly to rotor design requirements: increasing power pro-

Goal 1	Aerodynamic performance (“Finesse”) $CF_1 = -\frac{1}{100} \bar{L}\bar{D}(\alpha_{des})$
Goal 2	Minimization of lift overshoot (“Gust ride”) $CF_2 = \max_{\alpha \in G_\alpha} \left(C_{l(\alpha)}^{clean} - C_{l(\alpha_{des})}^{clean} \right)$
Definition 1	Ratio between expected lift and drag $\bar{L}\bar{D}(\bar{\alpha}) = \frac{\int_{\bar{\alpha}-1.64\sigma_\alpha}^{\bar{\alpha}+1.64\sigma_\alpha} C_1^{clean}(\bar{\alpha}+\alpha_\delta) \mathcal{N}(\alpha_\delta, \bar{\alpha}, \sigma_\alpha) d\alpha_\delta}{\int_{\bar{\alpha}-1.64\sigma_\alpha}^{\bar{\alpha}+1.64\sigma_\alpha} C_d^{clean}(\bar{\alpha}+\alpha_\delta) \mathcal{N}(\alpha_\delta, \bar{\alpha}, \sigma_\alpha) d\alpha_\delta}$
Definition 2	Design angle of attack : $\alpha_{des} : \bar{L}\bar{D}(\alpha_{des}) = \max_{\alpha_{des}}$
Definition 3	Lift overshoot range : $G_\alpha = [\alpha_{des}, \alpha_{des} + 2\sigma]$
Constraint 1	Resilience to forced transition $\left(C_{l(\alpha_{des})}^{soiled} - C_{l(\alpha_{des})}^{clean} \right) < 0.05$
Constraint 2	Thickness fixed to 24% chord
Conditions	Mach number $M = 0$ Reynolds number $Re = 12e6$ Angle of attack standard deviation $\sigma_\alpha = 2deg$
Clean case	Free transition with critical $N = 9$
Soiled case	Transition forced at 5% chord on suction side, and 10% chord on pressure side

Table 7.1: Designs goals, constraints and conditions for quantifying the compromise between expected glide-ratio and lift overshoot.

duction through enhanced glide-ratio, and reducing costs by reducing loads and blade structural requirements. Both goals are affected by the standard deviation of angle-of-attack variations.

We propose to assess the tension between expected glide-ratio and lift overshoot, defined as the maximum increase in lift within a range of two standard deviations from the design angle of attack. Details about the design goals are presented in table 7.1. The design angle of attack is now left free, and chosen to maximize the ratio between expected lift and expected drag. Finally, resilience to leading edge roughness is no longer treated as a goal but as a constraint. Losses in lift at the design angle of attack are required to be as small as on popular wind energy airfoils like the FFA-W3 (Bjorck, 1990) and classic DU series (Timmer and Van Rooij, 2003).

Results are shown on figure 7.3. The red line forms a Pareto front by connecting non-inferior airfoil designs. Each red dot corresponds to a design for which increases in expected glide-ratio can only be achieved at the cost of additional lift overshoot. Ideal but unfeasible designs would lie at the upper left of the figure. Established designs display substantial margin for improvement in the considered goals. They do, however, incorporate additional design constraints that were not considered here (Timmer and Van Rooij, 2003; Vila and Alfaro, 2015; Pereira et al., 2017).

Figure 7.4 shows the shapes and polar curves of two designs sampled from the Pareto front of figure 7.3. The so-called “high glide” and “smooth glide” designs correspond to different levels of compromise between aerodynamic performance and gust response — estimated to be at 0.40 and 0.08 respectively. Both designs incorporate considerations for the reduction of C_l overshoot, even if the high glide design lies on at the edge of the displayed Pareto front. That is why both exhibit relatively soft stall behavior, and will be employed to redesign the tip of the DTU reference wind turbine in chapter 8.

7.4. FINDINGS AND IMPLICATIONS

Efficient airfoil designs differ across flow conditions. Airfoils designed for static inflow achieve higher peak performance in controlled conditions, but fail to realize their promises in practical field conditions. Airfoil designers have long been aware of this fact, and generally demand that airfoils satisfy a handful of manually selected performance indexes at different angles of attack. Selection of these criteria, which stem from experience and intuition, is the kern of the art of airfoil design.

This chapter sought to formalize some of the unsaid wisdom behind wind turbine airfoil design criteria. The idea was that, by using a probability distribution of operational points, one would obtain a formal description of the relative importance of different operational points. This approach succeeded in highlighting that optimal airfoil designs differ across flow conditions. Yet, it is clear that naive transposition of performance design-goals does not suffice to produce commercially viable designs.

Related approaches with smaller level of formalism and more practical considerations result in more attractive airfoil designs. One may contend, that commercial wind turbine airfoils will continue to be designed with relatively informal goals. The author hopes, however, that informal airfoil design practices can be influenced by formal insight about the effect of inflow fluctuations on airfoil performance and design requirements.

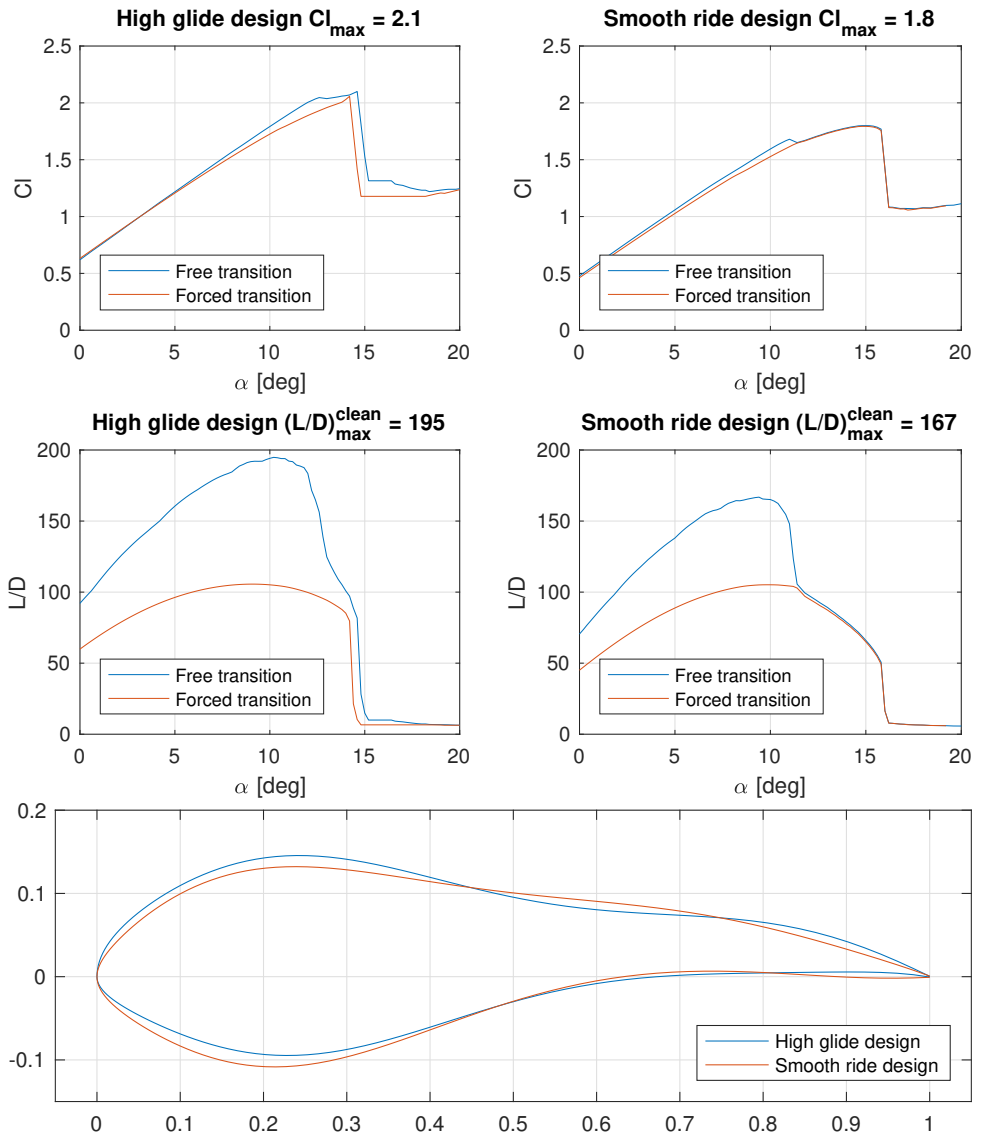
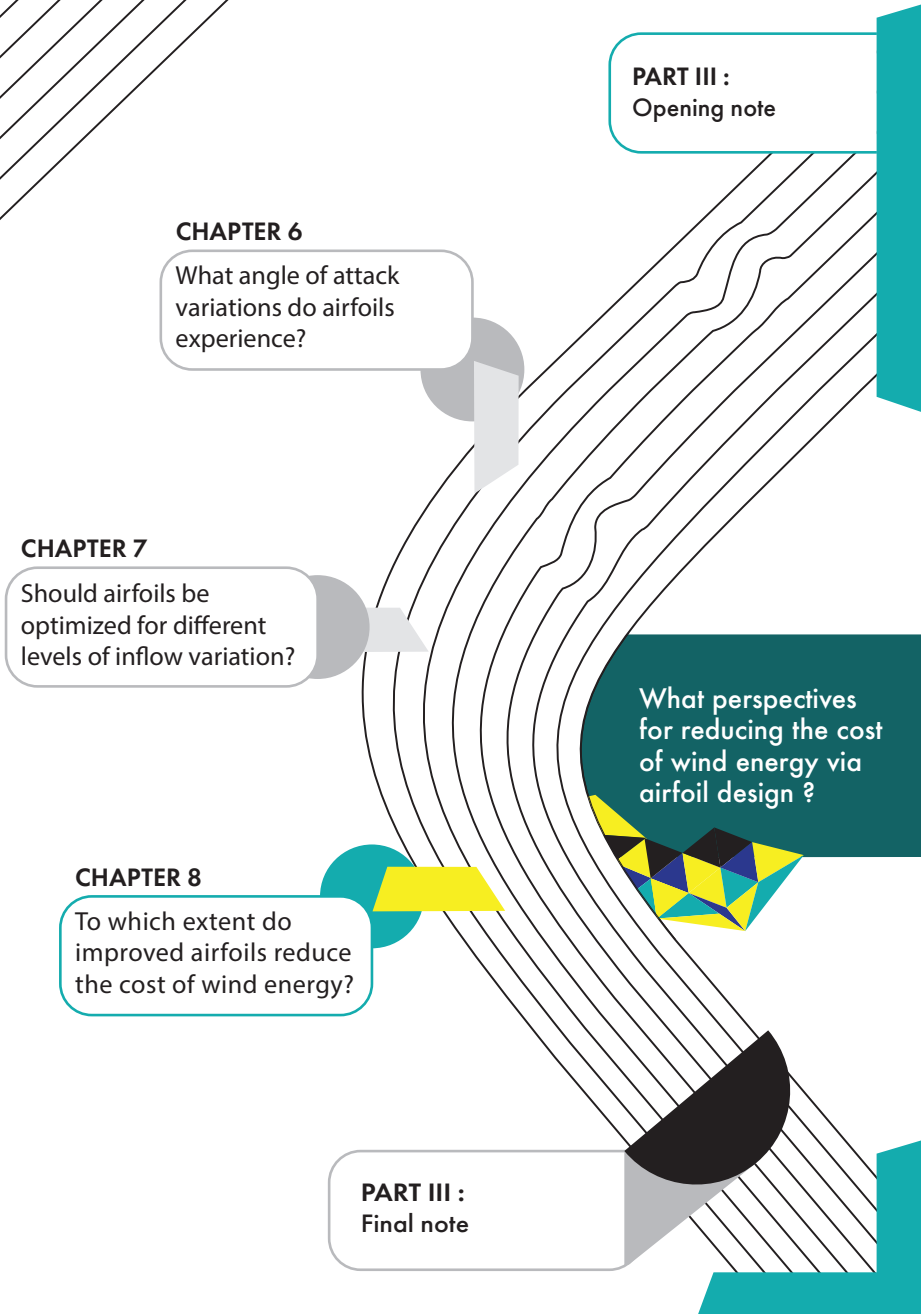


Figure 7.4: Polar curves for chosen tip airfoil designs



8

IMPACT OF TAYLORED AIRFOILS ON COST OF ENERGY

To which extent do optimized airfoil designs lead to more efficient rotors? How does that affect the cost of wind energy?

Some research agendas recommend continued development of wind turbine airfoil designs. Others suggest indirectly that aerodynamic progress is no longer determinant to the penetration of wind energy. Despite strong opinions, a long time has passed since the last assessment of the impact of increased glide-ratio on the cost of wind energy. This chapter addresses this gap with a stylized analysis. The idea is not to obtain a definitive answer regarding the merits of a particular airfoil. Instead, the aim is to understand the magnitude of rotor efficiency gains that are achievable through airfoil design, in general and by considering the effect on inflow inhomogeneities in particular.

A starting postulate is that a rotor is aerodynamically efficient if all means of improving its power conversion lead to increased loads or nuisance. It follows that differences in rotor efficiency correspond to shifts in the feasibility frontier of rotor planform designs. The relative advantages of different airfoil designs are therefore assessed by comparing Pareto fronts of efficient rotor planforms that result from their use.

The chapter is built around the particular case of the DTU reference wind turbine. Section 8.1 summarizes the multi-objective planform optimization approach and section 8.2 presents the main optimization results and answers the first research question. Section 8.3 describes a linearized cost model, which is used to answer the second research question in section 8.4.

8.1. ROTOR PLANFORM OPTIMIZATION APPROACH

Rotors must satisfy two fundamental design compromises: maximizing power production and minimizing loads. Practical rotors consider additional design goals, like noise, but this design exercise only means to estimate an upper bound for the order of magnitude of efficiency gains that airfoil design can achieve. That is why rotor design goals are chosen to be particularly favorable to the considered airfoils.

8.1.1. STATIC DESIGN SCENARIO

Two rotor design scenarios are considered: the static scenario corresponds to the canonical multi-objective design problem of maximizing rotor power coefficient and minimizing the root bending moment of out-of-plane (thrust) forces. All rotor properties are kept fixed during the optimization apart from the planform (twist and chord) of the outer half of the blade. The tip speed ratio is fixed at nominal value (7.5) and no interactions with the controller are considered. The objective functions correspond to maximizing power coefficient (C_P) and minimizing root-bending-moment coefficient (C_Q^{RBM}):

$$CF_1 = -C_P = -\frac{P}{\frac{1}{2}\rho(\pi R^2)U^3}, \quad CF_2 = C_Q^{RBM} = \frac{Q^{RBM}}{\frac{1}{2}\rho(\pi R^2)U^2 R} \quad (8.1)$$

Where power (P) and root bending moment (Q^{RBM}) are computed from a Blade-Element-Momentum (BEM) solution with static lift and drag polars ($C_l = g(\alpha)$ and $C_d = h(\alpha)$):

$$\begin{aligned} P &= \int \frac{1}{2}\rho c W^2 (C_l \sin(\phi) - C_d \cos(\phi)) dr \\ &= \int \frac{1}{2}\rho c W^2 (g_{(\phi-\theta)} \sin(\phi) - h_{(\phi-\theta)} \cos(\phi)) dr \\ Q^{RBM} &= \int \frac{1}{2}\rho c W^2 (C_l \cos(\phi) + C_d \sin(\phi)) r dr \\ &= \int \frac{1}{2}\rho c W^2 (g_{(\phi-\theta)} \cos(\phi) + h_{(\phi-\theta)} \sin(\phi)) r dr \end{aligned}$$

Where W and r denote local airspeed and radius respectively, and c denotes section chord. The inflow angle is denoted as ϕ and is used to estimate the angle of attack ($\alpha = \phi - \theta$) from the blade twist angle (θ). The procedure corresponds to standard blade element momentum BEM practice.

8.1.2. PROBABILISTIC SCENARIO

The probabilistic design scenario is a variation of the static scenario. The compromise between power production and loads is explored again, but from a slightly different angle. Two BEM solutions are generated to evaluate each design. The first one is solved using expected value airfoil polars, as defined in expressions 6.18 and 8.2 :

$$\begin{aligned} \bar{C}_l &= \bar{g}(\bar{\alpha}, \sigma_\alpha) = \bar{g}(\phi - \theta, \sigma_\alpha) \\ \bar{C}_d &= \bar{h}(\bar{\alpha}, \sigma_\alpha) = \bar{h}(\phi - \theta, \sigma_\alpha) \end{aligned} \quad (8.2)$$

They are used to solve the BEM problem, and to estimate the rotor power extraction:

$$\begin{aligned} \bar{P} &= \int \frac{1}{2}\rho c W^2 (\bar{C}_l \cos(\phi) + \bar{C}_d \sin(\phi)) r dr \\ &= \int \frac{1}{2}\rho c W^2 (\bar{g}_{(\phi-\theta, \sigma_\alpha)} \cos(\phi) + \bar{h}_{(\phi-\theta, \sigma_\alpha)} \sin(\phi)) r dr \end{aligned} \quad (8.3)$$

Expression 8.3 supposes that airfoil angle of attack fluctuations occur on a much shorter timescale than period at which the rotor wake adapts. It is consistent with the philosophy behind probabilistic models of glider and aircraft performance (Boermans, 2008; Weismuller, 2011). Standard deviation values for angle-of-attack perturbations were extracted from the numerical dataset of Rezaeihaa et al. (2017).

The second BEM computation uses the traditional static polars ($\sigma_\alpha = 0$), but seeks to estimate the root-bending-moment in a gust situation that would cause a homogeneous upward perturbation of two standard deviations to the angle of attack:

$$\begin{aligned} Q_{max}^{RBM} &= \int \frac{1}{2} \rho c W^2 (C_l \cos(\phi) + C_d \sin(\phi)) r dr \\ &= \int \frac{1}{2} \rho c W^2 (g_{(\phi-\theta+\sigma_\alpha)} \cos(\phi) + h_{(\phi-\theta+\sigma_\alpha)} \sin(\phi)) r dr \end{aligned}$$

Such an approach is obviously questionable. The IEC (2005) coherent gust is heavily criticized for its unphysical nature (van den Boz and Sanderse, 2017), and the present gust is even worth from that standpoint. Even if it is somewhat arbitrary, it is effective for introducing considerations about rotor dynamic behavior into the design process. Objective functions are set to maximize the power coefficient (C_P) and minimize the root-bending-moment coefficient (C_Q^{RBM}):

$$CF_1 = -C_{\bar{P}} = -\frac{\bar{P}}{\frac{1}{2} \rho (\pi R^2) U^3}, \quad CF_2 = C_Q^{RBM} = \frac{Q_{max}^{RBM}}{\frac{1}{2} \rho (\pi R^2) U^2 R} \quad (8.4)$$

8.1.3. PLANFORM PARAMETERIZATION

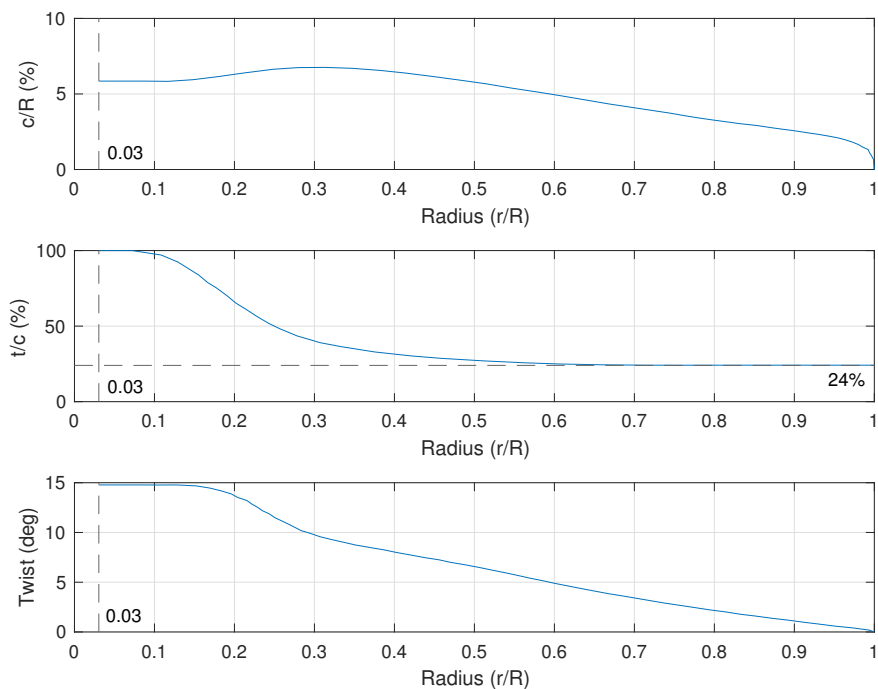
The blade planform is parametrized with an 8th order class shape transformation (CST) approach (Kulfan and Bussoletti, 2006b; Kulfan, 2007). The original chord and twist distributions of the Innwind DTU-RWT blade are used as class functions ($c_{(r/R)}^0$ and $\theta_{(r/R)}^0$), and deformed with shape functions (S^c and S^θ) that depend on 8 parameters each. The chord and twist distribution ($c_{(r/R)}$ and $\theta_{(r/R)}$) of rotor planform design candidates is given by expression 8.5.

$$\begin{aligned} c_{(r/R)} &= (c_{(r/R)}^0 - c^\delta) S_{(r/R, A_i^c)}^c + c^\delta \\ \theta_{(r/R)} &= (\theta_{(r/R)}^0 - \theta^\delta) S_{(r/R, A_i^\theta)}^\theta + \theta^\delta \end{aligned} \quad (8.5)$$

Shape functions (S^c and S^θ) correspond to the linear combination of a seventh degree Bernstein polynomial basis ($M = 7$) with eight coefficients ($N = M + 1 = 8$):

$$\begin{aligned} S_{(r/R, A_i^c)}^c &= \sum_{i=0}^{i=M} A_{i+1}^c s_{(r/R)}^{Mi} \\ S_{(r/R, A_i^\theta)}^\theta &= \sum_{i=1}^{i=M} A_{i+1}^\theta s_{(r/R)}^{Mi} \end{aligned} \quad with \quad s_{(r/R)}^{Ni} = \binom{M}{i} \left(\frac{r}{R}\right)^i \left(1 - \frac{r}{R}\right)^{M-i}$$

Upper and lower bounds are depicted on figure 8.1 next to the original design. It corresponds to the Innwind DTU-RWT blade and is recovered by setting all shape coefficient to unity ($A_i^c = 1$ and $A_i^\theta = 1$). Expression 8.5 includes constant offsets ($\theta^\delta = 6$ deg and $c^\delta = 0$) to ensure that regions of zero twist can be manipulated by the optimization algorithm.



Thickness	60%	48%	36%	30%	24%
Airfoil	Scaled		FFA-W3-360	FFA-W3-301	FFA-W3-241
Typical Re	6e6	10e6	10e6	10e6	12e6

Figure 8.1: DTU reference wind turbine (RWT) blade chord, twist, thickness and airfoil distributions.

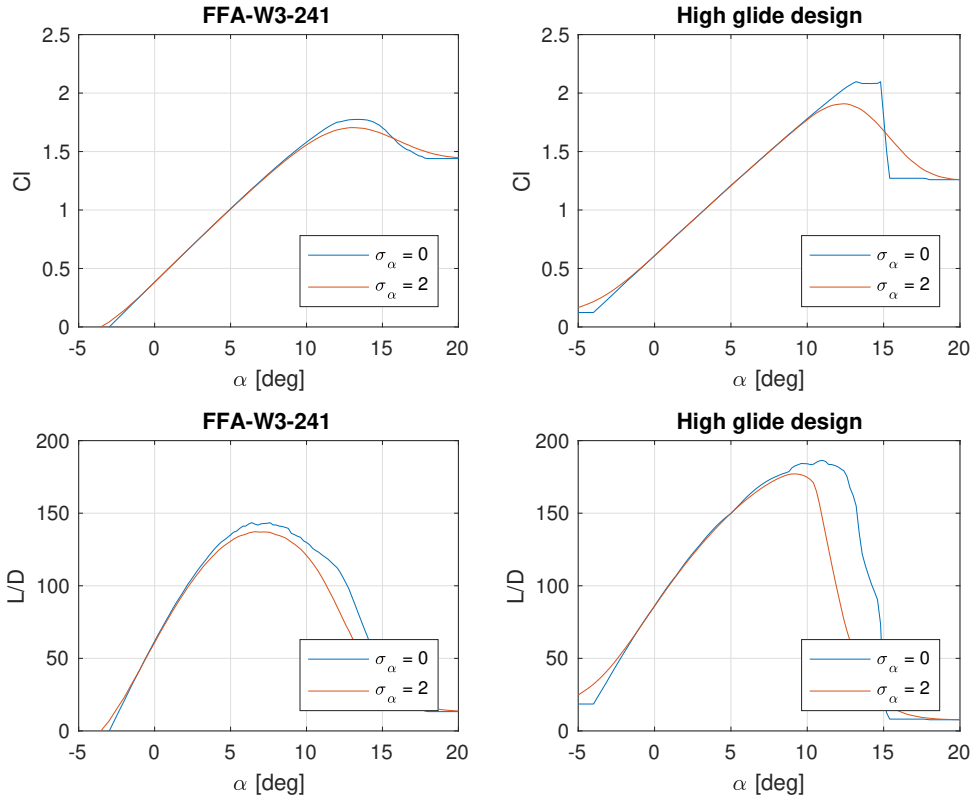


Figure 8.2: Comparison between free-transition polar curve of FFA-W3-241 airfoil and high glide design of figure 7.4.

8.1.4. SOLUTION OF MULTI-OBJECTIVE PROBLEM

Rotor planform optimization problems were solved with the NSGA-II genetic multi objective optimization algorithm (Fletcher, 2001). Cases ran for 80 generations with a population size of 240 individuals, a Pareto fraction of 40% and a mutation rate of 2%. Blade-element method (BEM) solutions were computed for each candidate design and ranked according to the goals of expressions 8.1 or 8.4, depending on the design scenario.

The BEM equations were solved in weak formulation with a line-search gradient algorithm (Byrd et al., 1997; Waltz et al., 2006). The Prandtl tip loss factor and Glauert thrust coefficient correction were implemented according to the recommendations of Buhl (2005).

8.2. EFFECT OF AIRFOILS ON ROTOR FEASIBILITY FRONTIER

Four sets of non-inferior rotor designs were generated for each design scenario. The first set of cases used the original DTU-RWT airfoil distribution, based on the FFA-W3 family. The second and third sets of cases replaced the 24% thick FFA airfoil by the “smooth ride” and “high glide” designs of the previous chapter (see figures 7.3 and 7.4). Figure

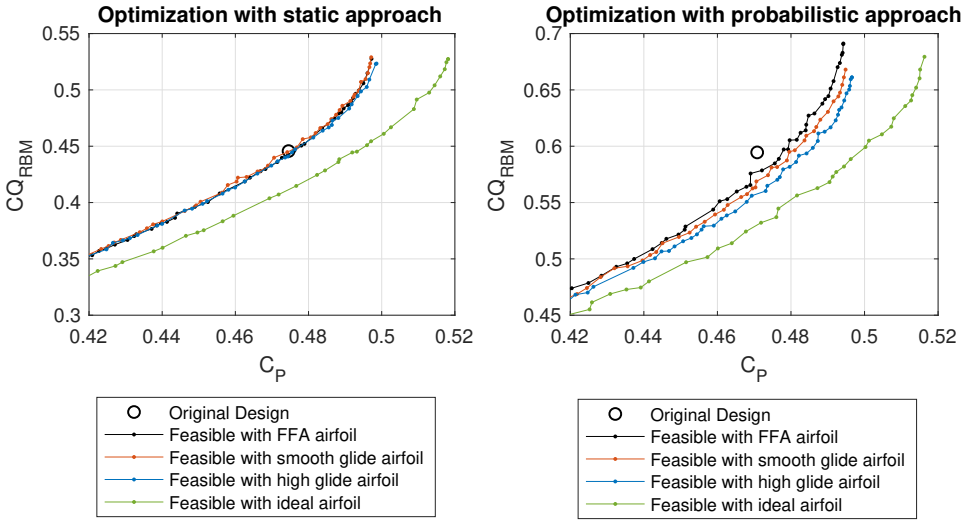


Figure 8.3: Effect of airfoil choice on compromises between rotor design goals.

8.2 compares the polars curves of the “high glide” airfoil with the original 24% airfoil of the DTU-RWT (FFA-W3-241). Finally, a fourth set of cases was generated by replacing the 24% FFA airfoil with an ideal airfoil. All other airfoils, with thicknesses between 30 and 60% remained identical across optimization cases.

8.2.1. IDEAL AIRFOIL POLAR

The ideal airfoil does not have a shape. It is an abstract polar used to study the upper bound of rotor performance gains that can be achieved through airfoil design. Our ideal polar has zero drag and an inviscid lift curve with the same zero-lift angle as the original 24% thick airfoil:

$$\begin{cases} C_l &= 2\pi \sin(\alpha) \cos(\alpha) + C_l^0 \\ C_d &= 0 \end{cases} \quad \text{with} \quad C_l^0 = 0.39 \quad (8.6)$$

The polar of expression 8.6 has great advantages: the absence of drag contribution to inplane forces means that the same torque can be realized with a lower lift than with a realistic airfoil. Furthermore, because it reaches very high lift coefficients, the ideal airfoil can damp the effect of gusts on root-bending-moment via reduced chord. These desirable features are unreachable in practice, but they point to the ultimate limit of what airfoils might achieve for rotor efficiency.

8.2.2. STATIC DESIGN SCENARIO

Figure 8.3 depicts the results of the rotor optimization exercises. Results from the static design scenario are presented on the left whereas results from the probabilistic design scenario appear on the right.

The static design scenario shows very limited scope for improving rotor efficiency through airfoil design. The three Pareto fronts based on realistic airfoil designs overlap

each other. The only substantial shift of the feasibility frontier is achieved with the ideal airfoil that has absolutely no drag.

8.2.3. PROBABILISTIC DESIGN SCENARIO

The probabilistic design scenario shows a greater scope for improving rotor efficiency through airfoil design. Both the “high glide” and “soft ride” designs shift the feasibility frontier in favorable ways. The question is about how relevant these shifts are. The answer comes in section 8.4, after introducing the cost model.

8.3. LINEARIZED MODEL FOR COST OF ENERGY

In practical design settings, compromises between power production and rotor loads are chosen with detailed structure and cost models. The goal consists in selecting an rotor that minimizes levelised cost of energy (LCOE). This section presents a subset of the Innwind turbine cost model (P.K. Chaviaropoulos and Lekou, 2013) that results in cost indifference curves that will be used to select points from Pareto fronts. It is deliberately oversimplified, but complex enough to illustrate the role of fixed costs and interest rate in the selection of optimal power coefficient.

Levelised cost of energy is approximated as capital expenditure (CAPEX) – including wind turbine and balance of plant costs – divided by the total energy production discounted over the plant lifetime of $N = 25$ years, and supplemented by a constant levelised cost of maintenance (LCOM) per MWh . Derating of turbine power output with machine age is ignored until the end of system lifetime, $N=25$ years. Annual energy production (AEP) is considered constant in time and the annual interest rate is denoted as $r = 7.34\%$.

$$LCOE = \frac{CAPEX}{AEP} \left(\sum_{i=1}^{i=N} (1+r)^{-i} \right)^{-1} + LCOM \quad [\text{Eur}_{2012}/MWh] \quad (8.7)$$

Capital expenditure consists of a fixed component (C_{WT}^{fix}), which represents the cost of components that are independent from blade loads, and a dependent component (C_{WT}^{dep}) which represents the cost of components that are affected by blade loads. A fraction ($\gamma = 0.3$) of these costs scales linearly with blade mass, while the other ($1 - \gamma$) remains constant.

$$CAPEX = C_{WT}^{fix} + C_{WT}^{dep} (1 - \gamma) + C_{WT}^{dep} \gamma \left(\frac{m}{m_0} \right) \quad [\text{Eur}_{2012}] \quad (8.8)$$

Symbol m_0 denotes the mass of the Innwind reference blade, while m refers to the mass of new designs that support a different root bending moment (C_Q^{RBM}). Contributions to fixed and dependent costs are summarized in tables 8.1a and 8.1b, and were extracted from the Innwind RWT cost model (P.K. Chaviaropoulos and Lekou, 2013).

We treat some costs that vary in upscaling studies as fixed because the turbine design remains fundamentally identical throughout the design exercise. Generator costs for example, are primarily determined by nominal power and rotational speed. So they should not, and do not, vary across the optimized blade designs presented on figures

	Cost type	Value	Description
Rotor	Fixed	18134	<i>pitch mechanism, nose cone</i>
	Variable	2140360	<i>blades, hub</i>
Nacelle and Drive Train	Fixed	3783241	<i>generator, brakes, power electronics, etc</i>
	Variable	731507	<i>low speed shaft, main bearing, bed plate</i>
Tower	Variable	2071193	
Other costs	Fixed	1069742	<i>control, safety, marinization</i>
Assembly multiplier	–	1.4	<i>ratio between cost of complete turbine and cost of components</i>

(a) Cost of wind turbine turbine components and assembly

	Cost type	Value	Description
Wind turbine	Fixed	6819563.8	
	Variable	6920284	
Balance of Plant	Fixed	7452803	<i>transportation, scour protection, etc</i>
	Variable	9496800	<i>foundation system</i>
Total CAPEX	Fixed	14272366.8	C_{WT}^{fix}
	Variable	16417084	C_{WT}^{var}

(b) Capital expenditure (CAPEX) of wind turbine plus installation

Table 8.1: Fixed and variable costs in linearized cost model of the Innwind RWT turbine. All values in constant euros, with 2012 purchasing power parity.

8.3 and 8.4 . Expression 8.8 linearizes the Innwind cost model for the sole purpose of selecting compromises between blade loads and power production. It is not applicable to different design scenarios.

If tip clearance is the determinant design driver, then blade mass (m) should depend primarily on the out-of-plane root bending moment (Q_{RBM}). Correlations between blade mass and bending moment can either be inferred from beam analogies, or by reworking scaling trends from literature

$$\left. \begin{array}{l} Q_{RBM} \propto R \gamma_R^{RBM} \\ m \propto R \gamma_R^m \end{array} \right\} \Rightarrow \left(\frac{m}{m_0} \right) = \left(\frac{Q_{RBM}}{Q_{RBM}^0} \right)^{\gamma_{RBM}^m} \quad \text{with} \quad \gamma_{RBM}^m = \frac{\gamma_R^m}{\gamma_R^{RBM}} \quad (8.9)$$

The scaling exponents ($\gamma_{RBM}^m = 1.04$) were chosen to match the conventional scaling scenario of Ashuri (2012). This scenario is close to physical expectations (Chaviaropoulos et al., 2003) for constant technology levels. The capital expenditure of the entire system can then be stated as a function of root bending moment, by inserting expression 8.9 into expression 8.8 :

$$C_{WT} = C_{WT}^{fix} + (1 - \gamma) C_{WT}^{dep} + \gamma C_{WT}^{dep} \left(\frac{Q_{RBM}}{Q_{RBM}^0} \right)^{\gamma_{RBM}^m} \quad (8.10)$$

The Innwind cost model also provides a simple tool for estimating annual energy production of the wind turbine as a function of rotor power coefficient (C_p^{rotor}) at nominal

tip-speed ratio ($\lambda = 7.5$). It resorts to a Weibull wind distribution with shape factor $k = 2$ and form factor $C = 10.38 m/s$ for a site with $9.2 m/s$ mean wind speed. Mechanical and electrical losses are included. When using this simple model with invariant rotational speed schedules, which is consistent with the design choice of keeping rotor tip speed ratio fixed, results for annual energy production can be approximated with a piecewise linear dependency on rotor power coefficient:

$$AEP = a + bC_p^{rotor} \text{ [GWh]} \quad \text{with} \quad \begin{cases} a = 25.068 & C_p < 0.5234 \\ b = 40.482 & C_p < 0.5234 \\ a = 28.774 & C_p \geq 0.5234 \\ b = 31.196 & C_p \geq 0.5234 \end{cases} \quad (8.11)$$

Finally, inserting expressions 8.10 and 8.11 into expression 8.7 leads to a relation between LCOE, power coefficient at design tip speed ratio and flapwise bending moment (Q_{RBM}):

$$LCOE = \frac{C_{WT}^{fix} + C_{WT}^{var} \left(\frac{Q_{RBM}}{Q_{RBM}^0} \right)^{\gamma_{RBM}^m}}{(a + bC_p^{rotor}) \left(\sum_{i=1}^{i=N} (1+r)^{-i} \right)} \quad (8.12)$$

Expression 8.12 can be inverted to draw lines of constant levelised cost of energy, as plotted on figure 8.4. Different combinations of rotor power coefficient and flapwise bending moment can lead to identical levelised cost of energy.

8.4. SELECTION OF OPTIMAL DESIGN

Optimal designs minimize levelised cost of energy. These designs can be identified graphically by plotting curves of constant levelised cost of energy (LCOE) over of the feasibility frontiers of figure 8.3. Designs that lead to lower cost of energy lie closer to the downward left corner of figure 8.4. They reach lower isocost lines.

The black line depicts the feasibility frontier of rotor designs based on the original airfoil distribution of the DTU reference wind turbine. It suggests that redesigning the rotor planform while keeping the FFA-W3 airfoils can lead to 0.4% reduction in the levelised cost of wind energy. Switching tip airfoils to the “high glide” design (red line, illustrated on figure 8.2) can lead to an additional 0.4% decrease in the cost of wind energy. The offset between black and red Pareto fronts is nearly constant and corresponds roughly to the spacing between isocost lines.

Finally, replacing the thinner airfoils of the DTU wind turbine with an ideal airfoil without drag and with extremely high lift, permits as 1.6% reduction in the levelised cost of wind energy. That is probably a gross overestimate, but a fair upper bound for what airfoil design can do to reduce the cost of wind energy.

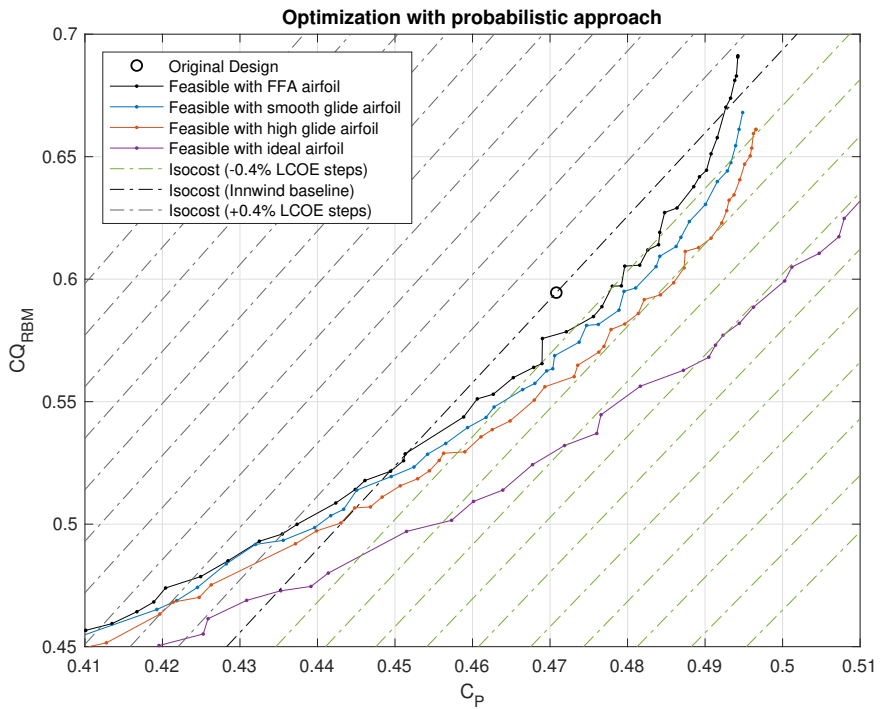
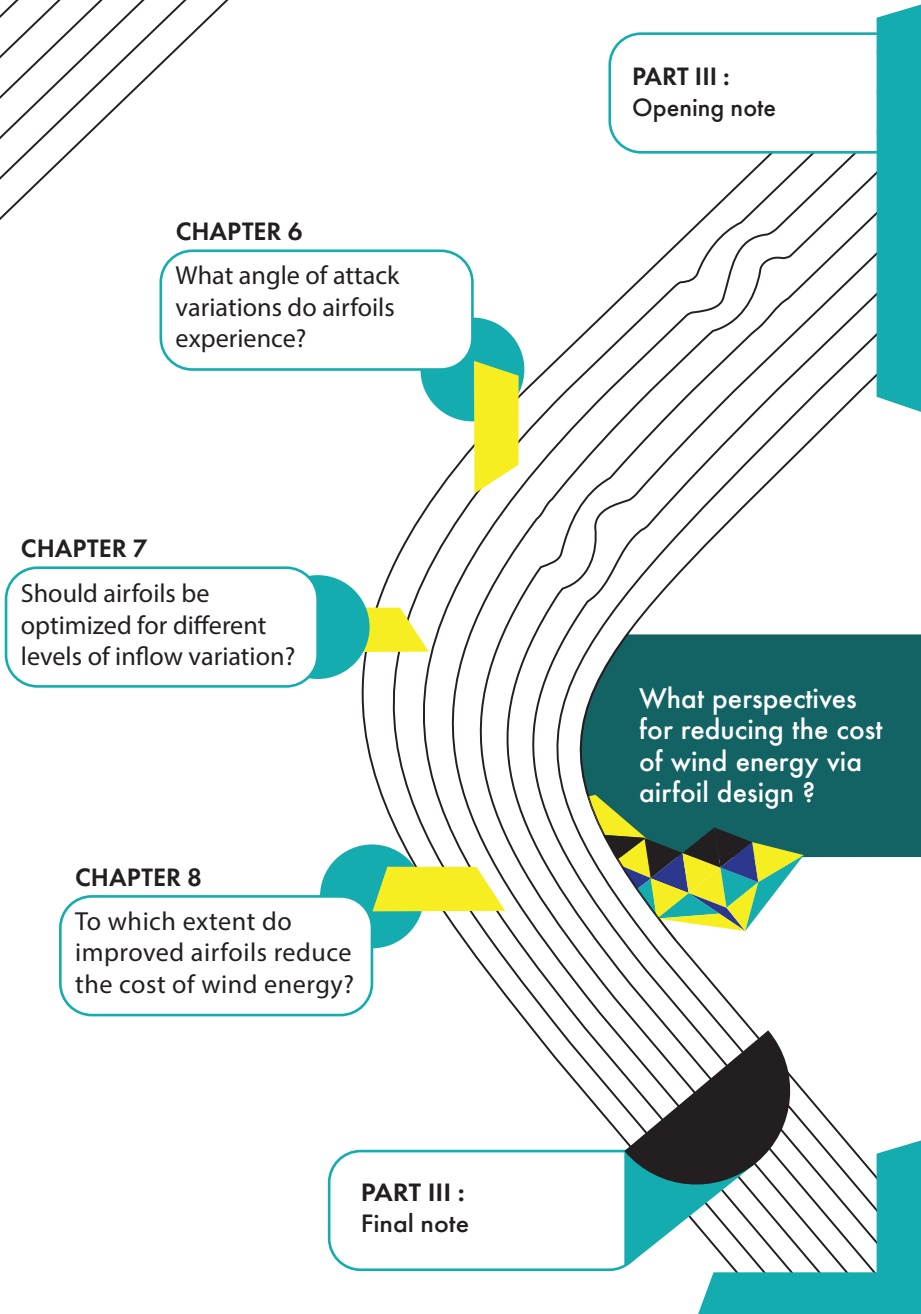


Figure 8.4: Effect of airfoil choice on cost of energy for DTU reference wind turbine



CLOSING NOTE

Efficiency of wind turbine airfoils

Current wind turbine blades already reached a remarkable level of aerodynamic efficiency. The optimization exercises conducted in part III of this thesis showed that, from a static flow perspective, even free designs like the DTU Reference Wind Turbine lie on the Pareto front. That observation reinforces previous insight suggesting that improvements to the efficiency of horizontal-axis wind turbines will stem primarily from multi-disciplinary considerations.

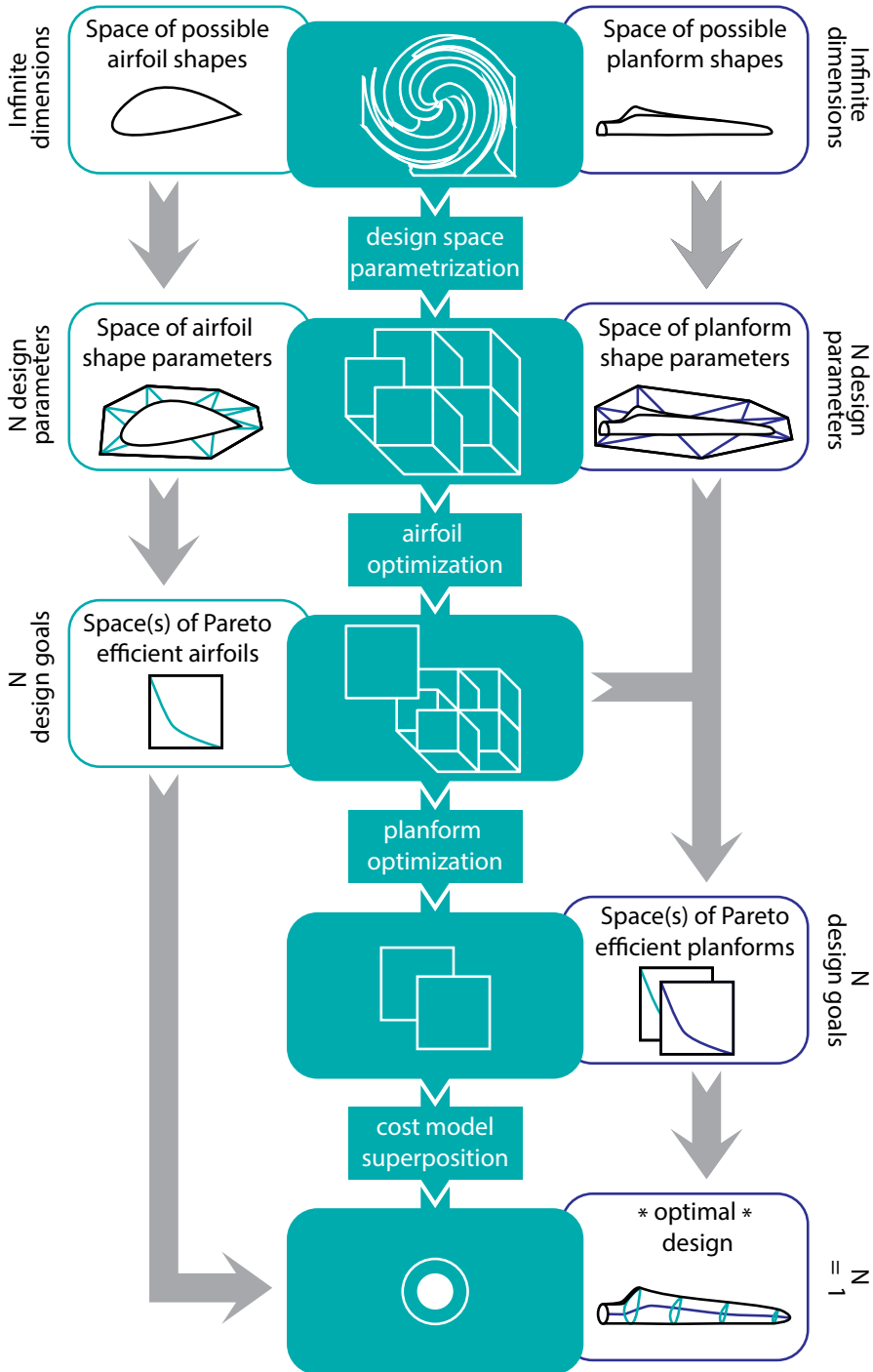
A simple analysis based on quasi-static representations of unsteady aerodynamic phenomena shows that some margin remains for improving current aerodynamic designs. Considering the effect of inflow inhomogeneity from the first stages of conceptual airfoil and rotor planform design might reduce the cost of wind energy in the order of a few tenths of a per cent.

The design exercise of chapter 8 showed that replacing the tip airfoils of the DTU reference wind turbine with an optimized design of the same thickness (24% chord) could lead to a 0.2% reduction in the levelised cost of energy. That was achieved by increasing annual energy production by 0.55% via a 1.25% increase in maximum rotor power coefficient. Improvements of that kind may seem modest, but they are relevant.

Global wind power generation capacity currently stands at 539GW (GWEC) with an average capacity factor of 28% (IRENA, 2017). Industry-wide implementation of a 0.55% increase in capacity factor would lead to the additional generation of about 7200GWh per year. That would be sufficient to cover the electricity needs of about 2.3 million people at the global per capita electricity usage of 3200kWh per year (Bank/OECD/IEA Bank/OECD/IEA (2018))

The impact of airfoil and planform design optimization is even more significant when one considers that cost reductions drive additional demand for wind energy capacity.

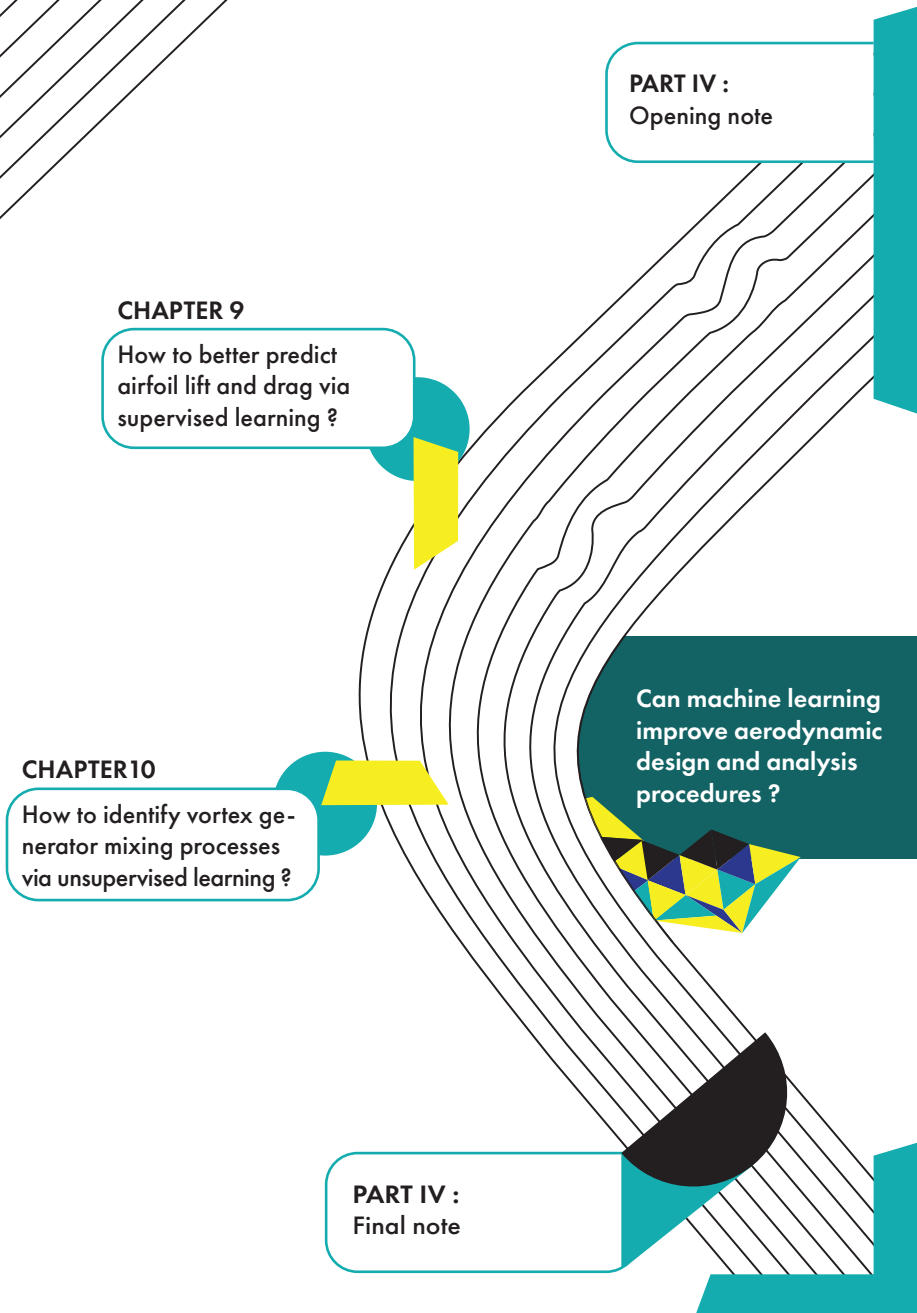
Even so, implementation of such minute changes in rotor performance is challenging. Unit percent changes in maximum power coefficient stand close to the typical error margin of flow simulation and power curve measurement techniques. That explains, in part, why some wind turbine manufacturers can be reluctant to adopt new rotor or airfoil designs.



Progressive compression of design space through successive stages of multi-objective optimization.

IV

MINIMIZATION OF FLOW SIMULATION UNCERTAINTIES



Minimization of flow simulation uncertainties

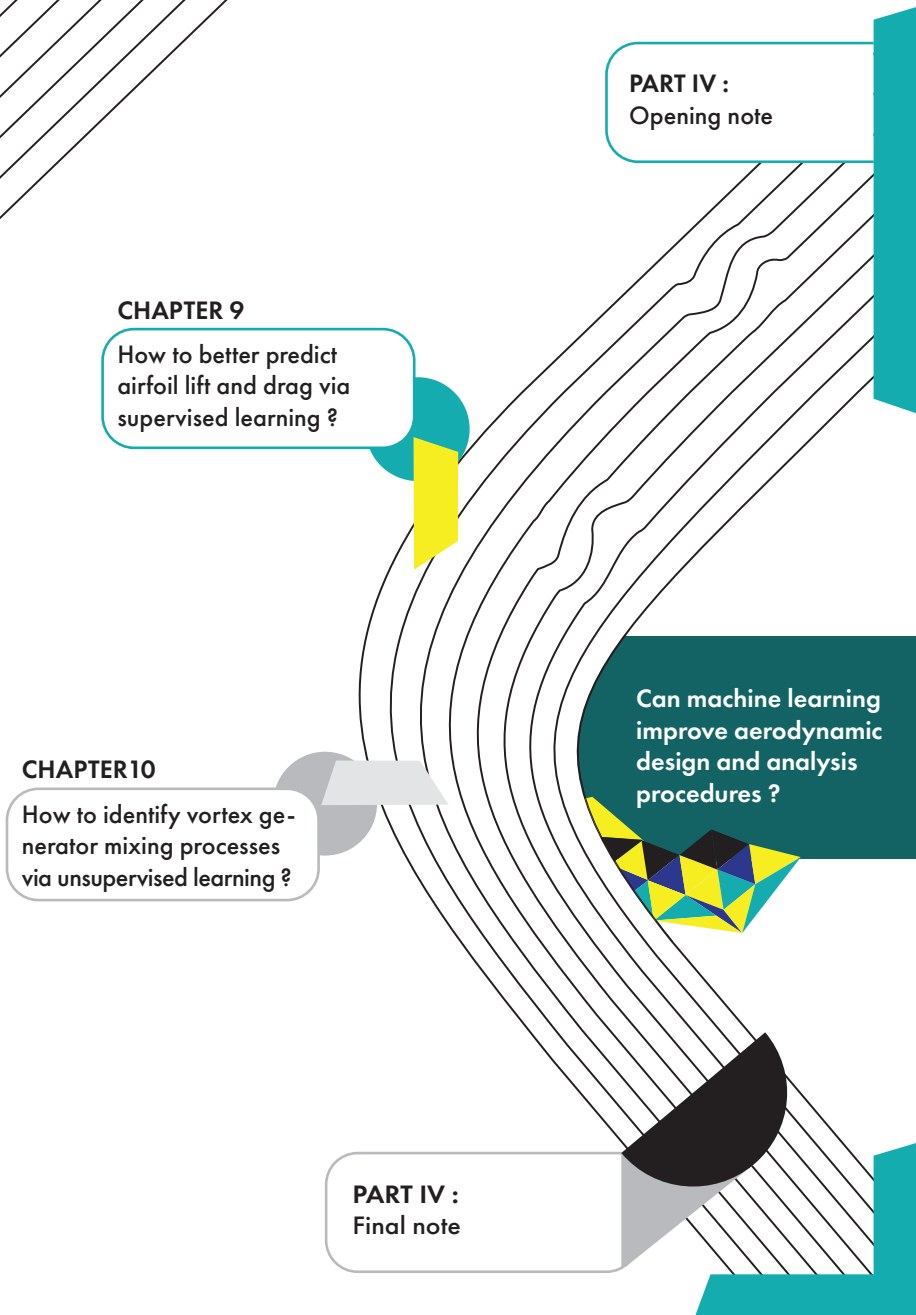
Industrial players seek strong guarantees before they invest in moulds to produce wind turbine blades with new airfoil designs. A passage through the wind tunnel, often in more than one location, is almost obligatory. Because of their cost, in finance and time, wind tunnel tests delay the adoption of new airfoil designs. That functions as a short-term obstacle to the efficiency of wind energy conversion; even if wind tunnels are the cradle of long-term aerodynamic creativity.

The EAWE research agenda states that the reduction of flow prediction uncertainties is critical to the adoption of optimized rotor and airfoil designs (Bottasso and Muskulus, 2017). Flow simulation techniques staged sustained progress across the past decades. Improvements result from increases in raw computational power and innovation in numerical schemes. Even so, accurate prediction of turbulent processes remains exceptionally challenging for very high Reynolds number flows found in wind energy applications.

The NASA CFD Vision 2030 report (Slotnick et al., 2014) suggests that high-Reynolds turbulent phenomena will remain intractable to first principles simulation for the next two decades. Unless the growth of computational power surpasses previously observed trends in extreme ways. While that is not impossible, it seems unlikely given the current prospects for quantum computing. It is therefore expected that the wind energy community will continue to rely on compact flow models for at least one or two more decades.

Part IV of this thesis explores two opportunities for enriching compact flow models with data-driven strategies. Both applications concern the prediction of turbulent boundary layer flows. Chapter 9 demonstrates the usage of advanced regression techniques for learning turbulent boundary layer closure relations from airfoil polar curves. Results are immediately applicable in industrial environments, but the method depends on the availability of sufficient experimental data. Chapter 10, combines asymptotic

analysis tools with unsupervised learning techniques to identify similarity patterns in boundary layers with streamwise vortices, like those created by vortex generators. The final note sketches future research perspectives.



9

MACHINE-LEARNING OF TURBULENT CLOSURE RELATIONS

Airfoil flows are hard to predict when the Reynolds number is high because turbulent eddies overwhelm computing capabilities. The resulting uncertainties create barriers to the adoption of optimized airfoil designs. Can machine-learning improve this situation?¹

Wind turbine airfoils operate in high Reynolds flows with intricate eddies that cannot be resolved in practical simulations. Flow solvers model the effect of unresolved turbulent phenomena by combining mechanistic insight with closure relations. Closures inject empirical knowledge into simulations and dominate errors in airfoil load prediction (Althaus, 1993; Sorensen et al., 2016; Sarlak, 2017) – be it for Viscous-Inviscid (VII) (Drela, 1989b; van Rooij, 1996b), Reynolds Averaged Navier-Stokes (RANS) (Wilcox, 2006), Large-Eddy (LES) (Lu and Rutland, 2016) or Lattice-Boltzman (Sagaut, 2010) environments. But good closures matter: less uncertainty means better design optimization and lower cost of wind energy (Abdallah et al., 2015).

Current understanding of turbulence is shaped by a century of dialogue between statistic (Reynolds, 1894; Prandtl, 1925; Taylor, 1935; Tennekes and Lumley, 1972), structural (Schubauer and Skramstad, 1948; Lumley, 1981), and deterministic (Lorenz, 1963; Ruelle, 1981) perspectives (Chapman and Tobak, 1985; McDonough, 2007). Advances in turbulence thinking have limited impact on engineering approaches despite industrial

¹Parts of this chapter were published in *Journal of Physics Conference Series 1037(2)* with co-authors G. de Oliveira, R.B. Pereira, W.A. Timmer and R.P.J.M. van Rooij under the title “Improved airfoil polar predictions with data-driven boundary-layer closure relations”. It is also related to “Laminar Boundary Layer Flow with DBD Plasma Actuation: A Similarity Equation”, published in *Springer Lecture Notes in Computational Science 120* with G. de Oliveira, M. Kotsonis and B.W. Van Oudheusden.

demand (Wilcox, 2006; Lesieur, 2008; Durbin, 2018). Moreover, direct numerical simulation (DNS) of high Reynolds flows is still two decades from maturity (Slotnick et al., 2014). How can models improve until then? Tracey (Tracey et al., 2013, 2015), Durasaimy (Durasaimy et al., 2017; Zhang and Durasaimy) and Ling (Ling and Templeton, 2015; Ling et al., 2016a) are advocating for data-driven approaches: using minimization algorithms to learn turbulent closures from high-fidelity simulations and experimental data (Kutz, 2017; Durbin, 2018; Bose and Park, 2018). Results for RANS (Wang et al., 2017; Weatheritt and Sandberg, 2017; Singh and Durasaimy, 2017; Singh et al., 2017) and LES (Barone et al., 2017; Maulik and San, 2017; Vollant et al., 2017) frameworks are encouraging, but applications of machine-learning to viscous-inviscid frameworks remain sparse.

Can data teach the effect of turbulence on skin-friction? Are airfoil polars exploitable for this purpose? Viscous-inviscid interaction (VII) codes like Rfoil (van Rooij, 1996b) and Xfoil (Drela, 1989b) are ideal to answer these questions: they have modest computational requirements, take a structural view on turbulence, and use the e^N method (Van Ingen and Kotsonis, 2011) to predict laminar-turbulent transition accurately (Sorensen et al., 2016; Yilmaz and et al., 2017).

This chapter answers the above questions by learning new turbulent closure relations for the Rfoil code from experimental airfoil polar curves. Section 9.1 reviews Rfoil's physical basis to identify error sources and machine-learning opportunities. Section 9.2 describes the supervised learning method: it is crude by modern standards and does not use neural networks. Results comprise a tailored Rfoil code and closure relations for turbulent skin friction (C_f) and energy shape factor (H^*). Section 9.3 checks the physical consistency of the new closures and assesses their impact on polar predictions.

9.1. BOUNDARY LAYER TREATMENT IN RFOIL

Rfoil is derived from Xfoil and solves an approximate form of the Navier-Stokes (NS) equations obtained by truncating a matched asymptotic expansion (Kevorkian and Cole, 1996; Veldman, 2008). The outer expansion concerns convectively-dominated flow in the far field whereas the inner expansion deals with shear-flow near the airfoil surface. Outside deep-stall, the inner flow is approximately governed by the boundary-layer partial-differential-equations (BL-PDE) (Morino et al., 1995; Veldman, 2008):

$$\begin{cases} U \frac{\partial U}{\partial x} + V \frac{\partial U}{\partial y} = -\frac{1}{\rho} \frac{\partial P}{\partial x} + \nu \left(\frac{\partial^2 U}{\partial y^2} \right) \\ \nabla \cdot \mathbf{U} = 0 \quad \wedge \quad \frac{\partial P}{\partial y} = 0 \end{cases} \quad \text{with } BCs = \left\{ \begin{array}{l} \text{prescribed } U_e \\ \text{edge velocity} \end{array} \right\} \quad (9.1)$$

The boundary-layer (BL) flow is solved with an integral method based on the Von Karman equations Schlichting and Gersten (2017); Veldman (2008):

$$\begin{cases} \frac{\partial \theta}{\partial x} = \frac{C_f}{2} - (H_{12} + 2) \frac{\theta}{U_e} \frac{\partial U_e}{\partial x} \\ \frac{\partial H_{32}}{\partial x} = \frac{2C_D}{\theta} - \frac{H_{32}}{\theta} \frac{C_f}{2} + (H_{12} - 1) \frac{H_{32}}{U_e} \frac{\partial U_e}{\partial x} \end{cases} \quad \text{with } BCs = \left\{ \begin{array}{l} \text{prescribed } \\ U_e = f(x) \end{array} \right\} \quad (9.2)$$

These equations (9.2) are obtained by integrating the BL-PDEs (9.1) analytically in the normal direction (y). No approximations are involved in this procedure. But while the BL-PDEs (9.1) are closed, system (9.2) comprises two ordinary differential equations (ODEs) that depend on five variables (see table 9.1 for notation). Solving system (9.2)

δ^*	$= \int_0^\infty \left(1 - \frac{U}{U_e}\right) dy$	Displacement Thickness	H	$= \frac{\delta^*}{\theta}$	Shape Factor
θ	$= \int_0^\infty \frac{U}{U_e} \left(1 - \frac{U}{U_e}\right) dy$	Momentum Thickness	H^*	$= \frac{\delta^{**}}{\theta}$	Energy Factor
δ^{**}	$= \int_0^\infty \frac{U}{U_e} \left(1 - \frac{U^2}{U_e^2}\right) dy$	Energy Thickness	C_f		Friction Coeff.
Re_θ	$= \frac{U_e \theta}{\nu}$	Momentum Reynolds	C_D		Dissipation Coeff.

Table 9.1: Integral boundary layer variables (see reference [Schlichting and Gersten \(2017\)](#) for detailed definitions)

therefore requires additional connections between variables, and these are known as closure relations.

9.1.1. LAMINAR AND TURBULENT CLOSURE RELATIONS

Rfoil resorts to different closure relations for each flow region – laminar BL, turbulent BL and wake. Transition between flow regions is predicted with a supplementary ODE for the growth of Tollmien-Schlichting waves ([Van Ingen and Kotsonis, 2011](#)) and matching laws are used at interfaces – near stagnation, laminar-turbulent transition and the trailing edge.

Laminar closure relations are backed by solid theory ([Oleinik and Samokhin, 1999](#)). Similarity conditions allow the construction of two-state velocity profiles ([Blasius, 1950](#); [Falkner and Skan, 1931](#)) that originate consensual closure datasets ([Farell et al., 2000](#)). These closures are only exact for specific pressure histories ([de Oliveira et al., 2017](#)) but laminar flows have limited memory. Departure from similarity has negligible effects in the absence of turbulent eddies ([Emanuel, 2001](#)).

The theory of turbulent closure relations is weaker ([Zagarola and Smits, 1998](#); [Chorin, 1998](#); [Castillo and Wang, 2004](#)). Rfoil uses two-state closures for turbulent skin friction (C_f) and energy factor H^* :

$$C_f^{org} = f_{(H, Re_\theta)} \quad , \quad H^{*org} = f_{(H, Re_\theta)} \quad (9.3)$$

Bivariate closures of this kind assume Clauser equilibrium ([Clauser, 1954](#)) but airfoil pressure histories ([Bradshaw, 1969](#); [Perry, 1966](#)) are often far from this condition ([Perry et al., 1998](#); [Marusic and Perry, 1995](#)). Turbulent boundary layers require additional descriptors for history effects, and this is acknowledged with the shear-lag equation:

$$\frac{\delta}{C_\tau} \frac{\partial C_\tau}{\partial x} = K_C \left(C_\tau^{\frac{1}{2}} - C_{\tau EQ}^{\frac{1}{2}} \right) + \left\{ \begin{array}{l} \text{diffusive} \\ \text{terms} \end{array} \right\} \quad (9.4)$$

This ODE adds a state related to flow memory, the turbulent shear stress coefficient (C_τ). It is derived from Green's approximation ([Green et al., 1977](#)) of Bradshaw's equation ([Ferriss et al., 1967](#)) for the transport of turbulent kinetic energy. And enables computation of the dissipation coefficient (C_D) with a (C_τ) that lags behind equilibrium values (C_τ^{eq}) inferred from the Clauser $G - \beta$ relation ([Coles, 1956](#); [Drela and Giles, 1987](#)).

$$G = A \sqrt{1 + B\beta} \quad (9.5)$$

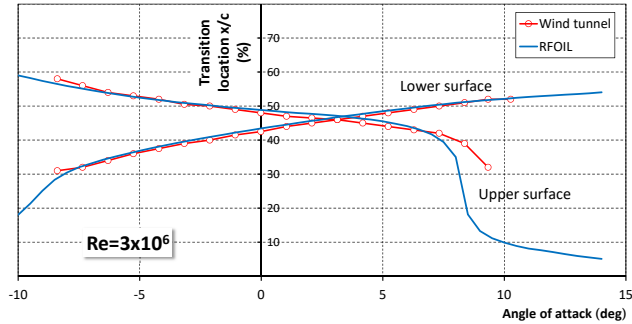


Figure 9.1: Transition location on a 24% thick airfoil measured in TU-Delft's LTT.

But the shear-lag approach is attackable (Ramanujam et al., 2016; Althaus, 1993): it depends on a shear stress profile that contradicts experimental evidence (Perry et al., 1998; Marusic and Perry, 1995), its diffusive term is debated (Ramanujam et al., 2016; Drela and Giles, 1987) and the K_C factor encompasses substantial uncertainty (van Rooij (1996b)).

9.1.2. SOURCES OF PREDICTION ERROR

Mechanistic arguments suggest that turbulent closures are the greatest source of error in Rfoil's polar predictions. Rfoil underestimates drag in most conditions (Timmer, 2009a), and the issue is greatest on airfoils with early transition, and hence longer turbulent runs.

Accurate prediction of the transition location requires accurate flow solutions of every flow region but the turbulent boundary layer and wake. And Rfoil predicts transition accurately, as can be seen on the illustrative case of figure 1. It corresponds to an airfoil with 24% thickness measured in TU-Delft's LTT that was published in reference (?), and functions as an experimental hint for the problematic nature of Rfoil's turbulent closures.

Airfoil designers circumvent shortcomings in the turbulent closure with various workarounds. Some designers tailor the $G - \beta$ relation (9.5) to specific cases, others use custom skin-friction relations (9.3), and yet others correct the polar curve directly. Typical corrections depend on airfoil thickness, leading-edge radius, extent of laminar run or Reynolds number (Timmer, 2009a). Semi-empirical correction methods suggest airfoil polar data can reveal systematic trends that remain unexploited by closure relations.

9.1.3. MACHINE LEARNING OPPORTUNITIES

Unexploited information and epistemic uncertainty signal machine-learning opportunities. But what is machine-learning? According to Mitchell (1997):

"A computer program is said to learn from experience E with respect to some class of tasks T and performance measure P , if its performance at tasks in T , as measured by P , improves with experience." Mitchell (1997)

Think of a task (T) that consists in predicting airfoil polars. Learning could use experi-

ence (E , predictions with different settings) to modify a flow solver (*Rfoil*) in ways that improve its performance (P accuracy against reference results). Such a setup is typical of supervised-learning and could be used to improve several terms in *Rfoil*'s turbulent closure:

1. Matching rules at boundary layer interfaces
2. Shape and coefficients of the $G - \beta$ closure relation (9.5)
3. Diffusive terms and slip-velocity closure of the shear-lag equation (9.4)
4. Enhanced skin friction (C_f) and energy shape-factor (H^*) closure relations (9.3)

The present contribution narrows its scope to the last, and simplest, option of the above list.

9.2. SUPERVISED LEARNING OF CLOSURE RELATIONS

We use airfoil polar data to learn new closure relations for turbulent skin friction (C_f) and energy shape-factor (H^*). The two-state dependency $f(H, Re_\theta)$ is maintained despite its shortcomings and the new closures are defined parametrically:

$$C_f^{learn} = f_{(H, Re_\theta; \psi^{C_f})} \quad , \quad H^{*learn} = f_{(H, Re_\theta; \psi^*)} \quad (9.6)$$

Learning consists in finding parameters (ψ) that lead to improved closure relations. What are better closures? Traditional approaches (Clauser, 1954; Schlichting and Gersten, 2017) emphasize agreement with detailed boundary layer data. Recent work (Althaus, 1993; van Rooij, 1996b; Tracey et al., 2015) argues better closure relations lead to better flow predictions. We assume the definitions correlate well and learning outcomes will tell if that holds true.

Formally, we seek to learn by minimizing the expectation (\mathbb{E}) of a measure for *Rfoil*'s inaccuracy (\mathcal{L}) in the prediction of airfoil polar curves ($f_{(x,\beta)}^P$). The problem is formalized after Goodfellow (Goodfellow et al., 2016):

$$\min_{\psi} \mathbb{E}_{(x,y) \sim p_{data}} \mathcal{L} \left(f_{(x,\psi)}^P, \mathbf{y} \right) \quad \approx \quad \min_{\psi \in D} \frac{1}{m} \sum_{i=1}^{i=m} \mathcal{L} \left(f_{(x_i,\psi)}^P, \mathbf{y}_i \right) \quad (9.7)$$

Experimental reference (\mathbf{y} - reference aerodynamic coefficients) and conditions (\mathbf{x} - airfoil coordinates, Mach, Reynolds) would ideally span the entire data generating distribution (p_{data}) of the physical world. This is impossible, so the expected inaccuracy norm of *Rfoil*'s polar predictions is approximated over a discrete collection $\{\mathbf{x}_i, \mathbf{y}_i\}$ of $i = 1 \dots m$ of experimental samples.

9.2.1. EXPERIMENTAL REFERENCE

Reference data is sampled from airfoil polar curve measurements of Abbot and Van Doenhoff (Abbott et al., 1945). A database was constructed using digitized data (Siemens, 1994) from the NACA TR824 report (Abbott et al., 1945) that spans several 4, 5 and 6 digit NACA airfoils. Reynolds numbers range from 3 to 9 million, airfoil coordinates were

regenerated with the NACA456 code (Carmichael, 2011), and aerodynamic coefficients were reinterpolated into $C_l - \alpha$, $C_d - \alpha$ and $C_m - \alpha$ curves. Rough leading edge and thin airfoil ($t/c < 0.1$) cases were excluded to limit overcompensation risks.

9.2.2. INACCURACY MEASURE

Inaccuracy is measured with a combination of least square error norms that confront Rfoil's predictions with a training dataset sampled from the experimental reference. The global inaccuracy measure $\mathcal{L} = f(\psi)$ is a scalar that combines topical error norms for lift, drag and moment coefficients.

Norms for each coefficient (\mathcal{L}^{C_l} , \mathcal{L}^{C_d} and \mathcal{L}^{C_m}) are scaled with reference values ($\mathcal{L}_{ref}^{C_{\dots}}$) computed at the beginning of the learning process.

$$\mathcal{L} = \left(\frac{\mathcal{L}^{C_l}}{\mathcal{L}_{ref}^{C_l}} \right)^2 + \left(\frac{\mathcal{L}^{C_d}}{\mathcal{L}_{ref}^{C_d}} \right)^2 + \left(\frac{\mathcal{L}^{C_m}}{\mathcal{L}_{ref}^{C_m}} \right)^2 \quad (9.8)$$

Coefficient norms ($\mathcal{L}^{C_{\dots}}$) are computed separately for each aerodynamic coefficient and combine inaccuracy measures from all experimental cases ($\mathcal{L}_i^{C_{\dots}}$) in the training set:

$$\mathcal{L}^{C_{\dots}} = \left(\frac{1}{m} \sum_{i=1}^m \left(\mathcal{L}_i^{C_{\dots}} \right)^2 \right)^{\frac{1}{2}} \quad (9.9)$$

Each experimental case represents a unique combination of airfoil and Reynolds number. Case inaccuracy norms ($\mathcal{L}_i^{C_{\dots}}$) correspond to the root mean square integral of the difference between predicted (C_{\dots}^{num}) and measured (C_{\dots}^{exp}) aerodynamic coefficients over the range of experimental angles of attack (α):

$$\mathcal{L}_i^{C_{\dots}} = \left(\frac{\int \left(C_{\dots(x_i, \psi)}^{num} - C_{\dots(x_i)}^{exp} \right)^2 d\alpha}{\int d\alpha} \right)^{\frac{1}{2}} \quad (9.10)$$

9.2.3. PARAMETRIC CLOSURE RELATIONS

Closure relations are parametrized with a variant of the Class Shape Transformation (CST) (Kulfan, 2007). The idea consists in using a shape function (S^{dM}) that modifies the original closure relations (C_f^{org} and H^{*org}) in arbitrary ways:

$$\begin{aligned} C_f^{learn} \left(H, Re_\theta, \psi_i^{cf} \right) &= S^{dM} \left(H, \psi_i^{cf} \right) \left(C_f^{org} \left(H, Re_\theta \right) + \delta^{C_f} \right) - \delta^{C_f} & \text{with } \delta^{C_f} = 0.004 \\ H_{(H, Re_\theta, \psi_i^*)}^{*learn} &= S^{dM} \left(H, \psi_i^* \right) \left(H_{(H, Re_\theta)}^{*org} + \delta^{H^*} \right) - \delta^{H^*} & \text{with } \delta^{H^*} = 0 \end{aligned}$$

The S^{dM} function is constructed by linear combination of the M^{th} degree Bernstein polynomial basis. Its behavior is controlled by $M + 1$ parameters $(\psi_i^{cf}, \psi_i^* \in \mathbb{R}^{M+1})$:

$$S_{(H, \psi_i)}^{dM} = \begin{cases} A_0 & 0 < \eta(H) \\ \sum_{i=0}^{M} \psi_{i+1} B_{(H)}^{Mi} & 0 < \eta(H) < 1 \\ A_{M+1} & 1 < \eta(H) \end{cases} \quad with \quad \begin{cases} B_{(x)}^{Mi} = \binom{M}{i} x^i (1-x)^{M-i} \\ \eta(H) = \frac{H-H_{lb}}{H_{ub}-H_{lb}} \end{cases}$$

Closure relation modifications are confined to a relatively narrow interval $[H_{lb}, H_{ub}]$ of shape factors. The lower bound is set at the vanishing boundary layer limit ($H_{lb} = 1$) and the upper bound corresponds to separated flow ($H_{ub} = 6$). Two constraints are enforced:

1. First derivative discontinuities at the upper bound are limited by aggregating the last shape parameters $(\psi_M^{cf} = \psi_{M+1}^{cf}$ and $\psi_M^* = \psi_{M+1}^*)$
2. Original closure relation values at the vanishing boundary layer limit are maintained $(\psi_1^{cf} = \psi_1^* = 1)$ to preserve asymptotic behavior

Bernstein polynomials of very modest order ($M + 1 = 6$) were used, but these shape functions allow progressive refinement across multivariate polynomial spaces and the generality of the method can be proven (Kulfan, 2007).

9.2.4. SOLUTION ALGORITHM

Closure relations are learned by changing the parameters until the inaccuracy norm is minimized. This is achieved with a gradient descent algorithm based on the interior point method (Byrd et al., 1997; Waltz et al., 2006): the algorithm starts from the original closures $(\psi_i^{cf} = \psi_i^* = 1, \forall i)$ and combines conjugate gradient steps with line search iterations to find sensible moves (Waltz et al., 2006). Gradients are estimated with fixed-step central differences, the hessian matrix is approximated through the dense BFGS method and numerical noise is carefully attenuated. Together with a parsimonious parametrization and tractable dataset, these measures enable the obtention of formally converged minima.

9.3. RESULTS AND DISCUSSION

The minimization algorithm reduced the scalar inaccuracy measure of expression 9.8 from an initial value of $\sqrt{3} \approx 1.7321$ to 1.5725. Coefficient accuracy measures, defined in expression 9.9, improved for all three aerodynamic coefficients:

		Before learning	After learning	Improvement
Lift inaccuracy measure	\mathcal{L}^{C_l}	0.0813	0.0667	18.0%
Drag inaccuracy measure	\mathcal{L}^{C_d}	8.7649e-04	8.0302e-04	8.40%
Moment inaccuracy measure	\mathcal{L}^{C_m}	0.0178	0.0174	1.90%

The training dataset comprised 1524 datapoints spread over 33 experimental cases for NACA 4-series airfoils with relative thickness above 10%. Inaccuracy measures improved differently for each experimental case and figure 9.2 shows histograms of drag and lift prediction errors at the case level, as given by expression 9.10.

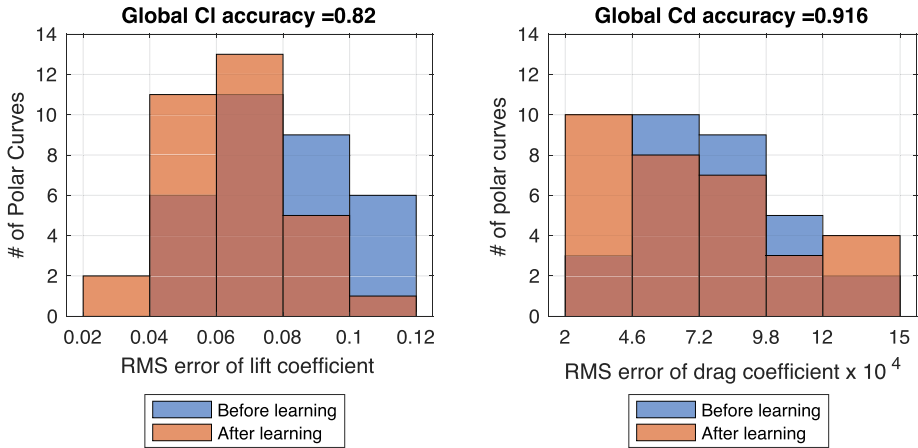


Figure 9.2: Effect of learning on standard deviation of lift and drag predictions over training set.

Learning shifts error histograms to the left and that is desirable. The drag inaccuracy measure improved for all but two cases in the training set. The two spurious points of the drag histogram correspond to situations in which Rfoil predicted transition too early. The width of the laminar drag bucket was then underestimated, and led to a paradoxical situation in which turbulence model improvements degraded the overall drag accuracy measure. The present work used a critical amplification factor of $N = 9$ for all simulations, but different values are probably more appropriate for the Langley LTPT tunnel.

9.3.1. EFFECT OF LEARNING ON POLAR PREDICTIONS

Polar predictions improved in qualitative terms for all airfoils in the training set. Figure 9.3 shows the effect of learning on the NACA2415 airfoil at a Reynolds number of 9 million. Rfoil's traditional drag under-prediction was attenuated and maximum-lift approached the experimental reference. Differences in the slope of the lift curve remained throughout the learning process but that is probably due to experimental shortcomings: early lift measurements in the Langley LTPT were obtained by integrating wall pressures over a small number of orifices. Combined with primitive correction methods, that probably lead to systematic underestimation of the lift curve slope (Timmer, 2009a).

Figure 9.4 compares polar curves for the DU96-W180 airfoil at a Reynolds number of $3e6$, as measured in TU-Delft's Low Turbulence Tunnel (LTT) (Timmer and Van Rooij, 1998). Improvements in drag prediction are clear and suggest that learning enhanced the predictive power of Rfoil: the DU96-W180 case functions as a verification because it did not belong to the training set.

Maximum-lift predictions deteriorated slightly for the verification case. The reasons for this are still misunderstood: it could be due to biases in the training set, over-compensation, under-fitting, or simply the price to pay for better drag predictions. Future efforts can elucidate these hypotheses by using more dependable datasets and by letting the algorithm learn deeper features of Rfoil's turbulent closure.

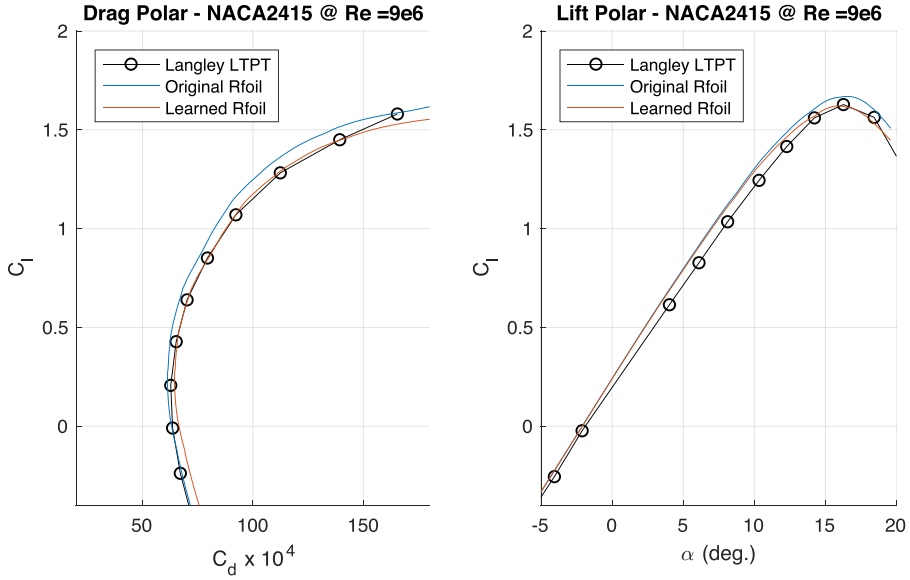


Figure 9.3: Effect of learning on polar prediction for airfoil in training set.

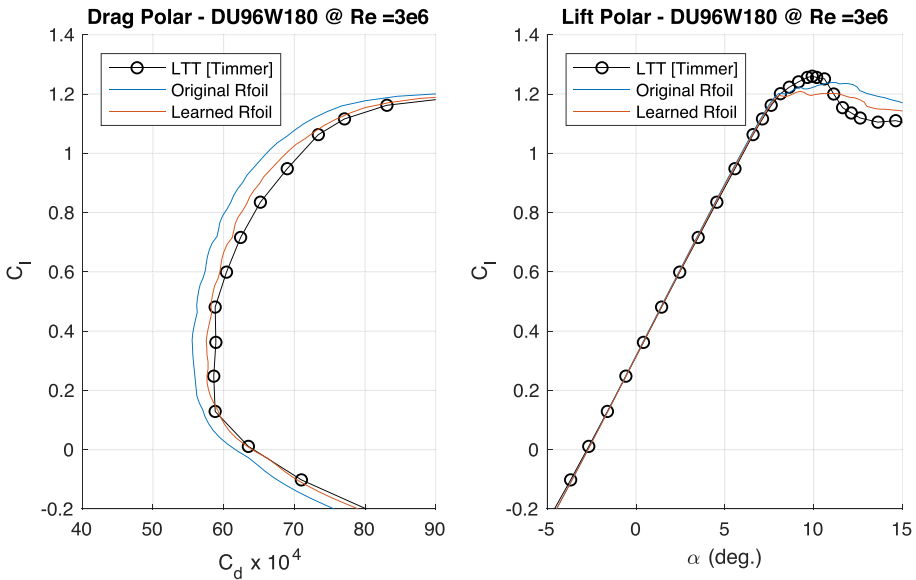


Figure 9.4: Effect of learning on polar prediction for airfoil outside training set.

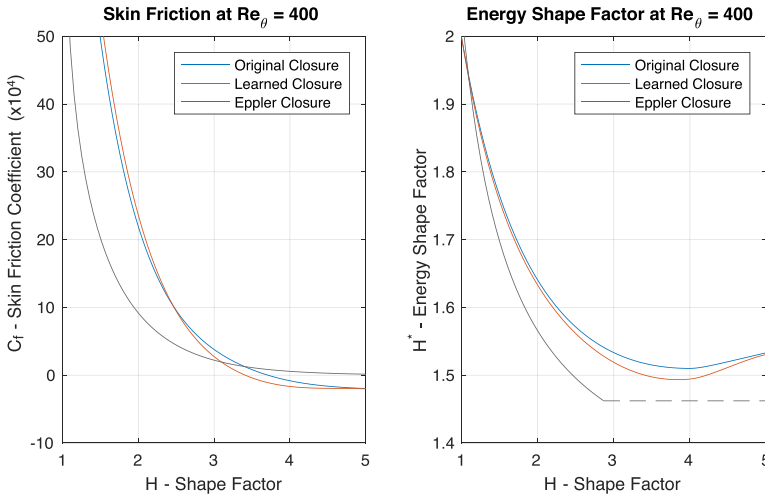


Figure 9.5: Effect of learning on skin friction and energy shape-factor closures

9.3.2. EFFECT OF LEARNING ON CLOSURE RELATIONS

Figure 9.5 shows the effect of learning on closure relations. A modest momentum Reynolds number was chosen to enable comparison with the closures of the Eppler airfoil prediction code (Eppler and Somers, 1980). Even if these changes had substantial effect on polar predictions, they remained within the range of uncertainty associated with historical (Schlichting and Gersten, 2017) boundary layer measurements.

The new closure predicts higher skin friction values than the original one. This makes sense because older boundary layer studies (Coles, 1956; Clauser, 1954) underestimated skin friction in adverse pressure gradients: skin friction was traditionally estimated by extrapolation pitot or hot-wire measurements with incorrect law-of-the-wall assumptions (Perry and Schofield, 1973; Marusic and Perry, 1995; Perry et al., 1998). Oil film interferometry measurements and direct numerical simulations (DNS) do not depend on law of the wall assumptions, and produce higher skin friction estimates that are now believed to be more accurate.

Figure 9.6 compares the learned skin friction closure with recent DNS results published by Vinuesa et al. (2017). It shows that improved agreement of closure relations with detailed BL data correlates well with improvements in polar predictions. This corresponds to what we had hoped for in section 3, and confirms that the effects of turbulence on skin friction can indeed be learned from airfoil polar data.

9.3.3. LEARNING EXERCISES

Variations in the learning method did not affect learning outcomes in substantial ways, but lead to methodological insights:

- **Inaccuracy norm:** The approach described here provides stable gradients and agrees well with heuristic understandings of code accuracy. Most importantly,

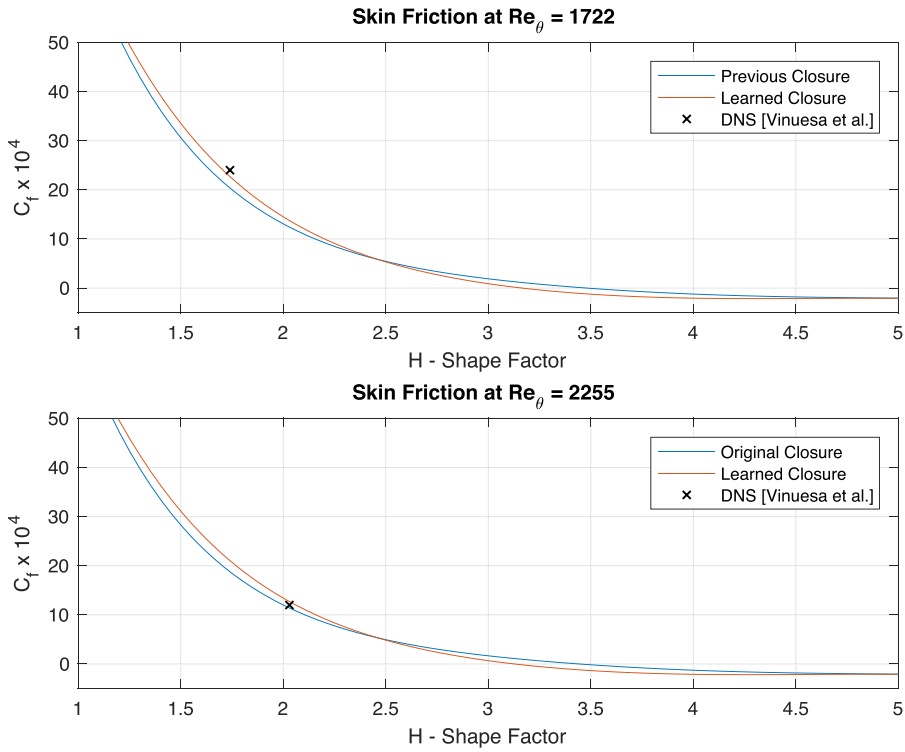


Figure 9.6: Comparison of learned skin friction closure with DNS data of Vinuesa et al. [Vinuesa et al. \(2017\)](#).

it uses all available data points. This may appear inefficient because some data points hold limited information about what we want to learn. Think of lift measurements in the linear region. But these points are important for machine-learning because they teach physical consistency.

- **Parametric representation:** The current parametrization is restrictive and leads to some underfitting. Future studies should use more parameters by increasing the order of the H parametrization, using a bivariate shape function that includes Re_θ effects, or accounting for equilibrium departure with a trivariate closure. Extension of the parametrization is straightforward, but broader design spaces are only advantageous if the training set contains sufficient information. We decided not to learn an Re_θ dependency from the TR824 dataset because its coverage of the data-generating distribution seemed narrow: low Re_θ and H values are too correlated because all polars were measured at high chord Reynolds numbers.
- **Solution Algorithm:** Results obtained with different full batch deterministic gradient algorithms are similar. The learning problem (9.7) is formally non-convex but the original convergence basin seems wide and slightly shallow. Alternative convergence basins were identified with simulated annealing algorithms (Ingber, 1995) but these lead to narrow unphysical minima. Stochastic gradient (SGD) algorithms (Goodfellow et al., 2016) proved inefficient on small datasets like the ones used here (Hinton et al., 2016).
- **Training dataset:** Attempts for using larger training datasets were made. The largest one had 7157 datapoints sampled randomly from the experimental database's 11976 datapoints; but it contained spurious airfoil shape reconstructions that hindered the learning process. It was also noticed that learning became less robust when using airfoils with longer laminar runs.

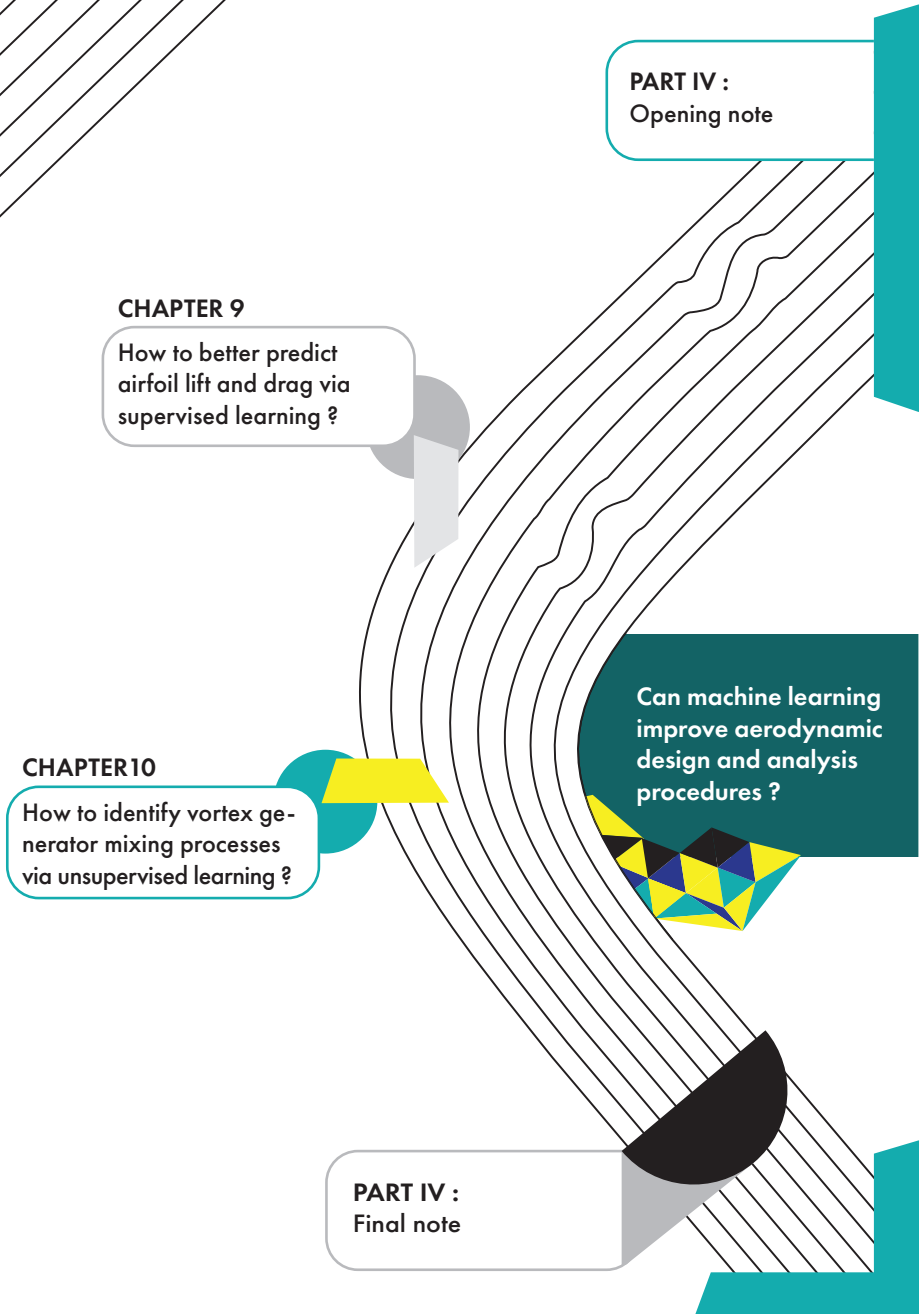
9.4. FINDINGS AND FUTURE PERSPECTIVES

Airfoil polar curves contain exploitable information about turbulent boundary layers. A relatively small dataset was able to teach a better skin friction closure to the Rfoil code. The new closure relation agrees with direct numerical simulation data that was not used for training. It leads to better drag predictions for airfoils inside and outside the training set.

Lift predictions remained identical for the linear region, but a decrease in maximum-lift estimations was observed. The extent to which this is desirable, or physically sound, remains unclear. On the one hand, lift inconsistencies created by the new closure relations may point to limitations in Rfoil's handling of turbulent history effects. On the other hand, the experimental dataset used for training is known to contain zero-lift angle inconsistencies. Future work should employ better datasets, even if that comes at the cost of public replicability.

Reliable data is scarce, but it seems more important to learn from reliable data than from big data. Turbulence learning is therefore likely to benefit from the use of parsimonious parametric representations. Variants of the CST parametrization could then be appealing compared to neural-networks. These methods are less general than modern

machine-learning predictors, but that could be an advantage when the inaccuracy norm is computationally expensive and susceptible to robustness issues. Applications extend beyond viscous-inviscid interaction: future efforts can build on the current method to improve RANS or LES predictions of airfoil flows and wind turbine wakes.



10

MACHINE-LEARNING OF SIMILARITY IN VORTEX GENERATOR FLOWS

We demonstrate the usage of unsupervised learning techniques to identify mixing mechanisms in boundary layers with streamwise vortices. Results contribute to the understanding of vortex generators used on wind turbine blades.¹

INTRODUCTION

Vortex generators are ubiquitous on modern wind turbines. They create streamwise vortices [Bradshaw \(1987a\)](#); [Metha and Bradshaw \(1988\)](#) that enhance boundary-layer mixing ([Schubauer and Spangenberg, 1960](#); [Shabaka et al., 1985](#)) and were first exploited to delay separation in internal flows [Taylor \(1948\)](#); [Valentine and Carrol \(1951\)](#). Today, streamwise vortices are extensively used to enhance the lift characteristics of wind turbine airfoils [Griffin \(1996\)](#); [Fernandez-Gamiz et al. \(2018\)](#); [Bak et al. \(2018\)](#) but their effect remains hard to predict. As a result, few, if any, blade sections are designed to make optimal use of vortex generators.

¹Parts of this chapter were published in the proceedings of the 52nd 3AF International Conference on Applied Aerodynamics (2017) with co-authors G. de Oliveira, W. A. Timmer and B.W. van Oudheusden. under the title “Integral Equations for Boundary Layers with Streamwise Vortices”. It is also related with “Similarity in boundary-layers with forced-mixing by streamwise vortices.” which is being submitted to the Journal of Fluid Mechanics with co-authors G. de Oliveira, R. Pereira, D. Ragni and B.W. van Oudheusden.

Mechanisms for the generation and development of vortex filaments are well understood, but there are substantial challenges to the prediction of their mixing effect. Vortex-induced mixing is often simulated with finite-volume solvers of the Reynolds Averaged Navier Stokes (RANS) equations (Dudek, 2010; Florentie et al., 2014; Trolldborg et al., 2015). In source-term approaches Kunik (1986); Bender et al. (1999), streamwise vortices are synthesized by prescribing external forces at vane locations (May, 2001; Wallin and Eriksson, 2006; Jirasek, 2004; Waithe, 2003). Local mesh refinement is needed to protect filaments from artificial diffusion but requirements are less stringent than for explicit meshing of vortex-generator vanes (Fernandez-Gamiz et al., 2014; Manole-sos et al., 2016). Even so, mesh dependence issues are sometimes problematic Florentie et al. (2016). Statistical approaches address these issues by adopting a different perspective: vortex filaments are no longer resolved but represented as an increase in turbulent diffusion Tornblom and Johansson (2007). This translates into a modified closure of the Reynolds stress tensor (Stilffried et al., 2010, 2013) for RANS frameworks, and into an additional entrainment term Kehro and Kramer (2003); D.Tavernier et al. (2018) for integral boundary layer (IBL) frameworks Drela and Giles (1987); Green (1976). But statistical representations of streamwise vortices are incomplete: they suppose mixing is known beforehand and only assess its implications on the remaining flow.

The only compact deterministic description of a boundary layer with streamwise vortices was constructed by Smith (1994). He obtained a small perturbation version of the turbulent boundary layer equations that accounted for the presence of vortex-generators. These equations are rich in physical insight but depend on restrictive assumptions that make it difficult to incorporate results from detailed structural studies. This is regrettable, since accurate structural descriptions of streamwise vortices are available Jones (1957); Squire (1965); Wendt (2001); Fernandez-Gamiz et al. (2016). Furthermore, structural models for the evolution of unactuated shear layers are also extensively documented (Schlichting, 1979, 7th Ed). What is missing, is a pluggable connection between vortex filament descriptions and shear-layer alterations

We address this gap in three steps. First, we extend the asymptotic stack of classic boundary layer theory to include structural representations of forced-mixing effects. Then, we connect existing structural models to predict the generation and development of streamwise vortices. Finally, we use unsupervised machine-learning techniques to identify the universal features of forced-mixing by streamwise vortices. This last step can be interpreted as a sophisticated way of identifying flow similarity patterns. Taken together, results from the three steps provide a complete deterministic description of boundary layers with streamwise vortices. This is new and unique. It is expected to contribute to the betterment of vortex generator design procedures.

The chapter is organized in five sections. Section 10.1 decomposes the flow and its governing equations into shear and vortical components. It also obtains a partial differential equation whose solutions approximate the streamwise-momentum difference between boundary-layers with and without mixing vortices. This new equation is coupled with structural shear-layer and streamwise vortex models in section 10.2. Section 10.3 validates solutions of the asymptotic model against particle image velocimetry (PIV) measurements. Finally, section 10.4 uses proper-orthogonal decomposition (POD) and artificial neural network (ANN) techniques to identify flow features common to a broad

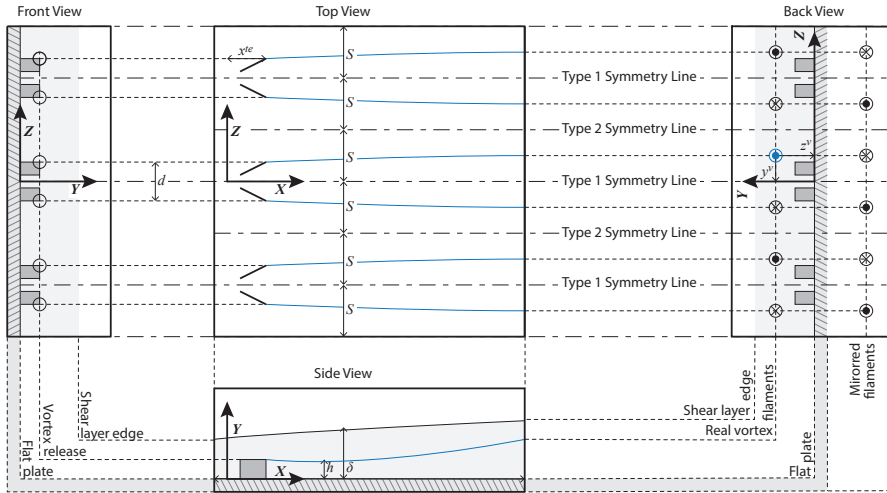


Figure 10.1: Shear-layer with periodic vortex system.

range of flows with forced mixing by streamwise vortices.

10.1. ASYMPTOTIC DEVELOPMENT

We focus on flow over flat plates with wide arrays of vortex-generator pairs. Figure 10.1 clarifies the setup and its spatial scales. The thickness of the shear-layer is denoted as δ and the distance between pairs of counter-rotating vortices is denoted as S . It is assumed that the flow develops over a long distance $L \gg \{\delta, S\}$ and that vortex-filament cores are separated from the wall by a distance (Y_v) comparable to boundary layer thickness $O[Y_v] = O[\delta]$.

10.1.1. FLOW DECOMPOSITION

The main postulate is that the flow is dominated by two interacting structures. A free shear layer that develops over the wall and a periodic system of counter-rotating streamwise vortices. Pressure and velocity fields can be decomposed to separate flow structures and reconnect them with an interaction term:

$$\begin{aligned}
 U &= \tilde{U} + \tilde{U} + \dot{\tilde{U}} \} InteractionField \\
 V &= \tilde{V} + \tilde{V} \\
 W &= \tilde{W} + \tilde{W} \\
 P &= \underbrace{\tilde{P}}_{Shear\ Layer} + \underbrace{\tilde{P}}_{VorticalFlow}
 \end{aligned}
 \tag{10.1}$$

All phenomena will be treated from the perspective of steady incompressible flow governed by the Navier Stokes equations. The equations can be decomposed with expression 10.1 to identify the key features of each flow component:

$$\begin{cases} ((\vec{U} + \vec{U}) \cdot \nabla)(\vec{U} + \vec{U}) = -\frac{1}{\rho} \nabla P + \nu \Delta (\vec{U} + \vec{U}) \\ \nabla \cdot (\vec{U} + \vec{U}) = 0 \end{cases} \quad (10.2)$$

The magnitude of shear flow components is assessed by combining spatial scales with order of magnitude analyses of the continuity equation. Orders of magnitude for vortical flow components, on the other hand, are estimated from the induced field of an infinite streamwise vortex filament with circulation Γ per unit length Jones (1957) .

$$\begin{aligned} O[X] &= L & O[\vec{U}] &= U_e & O[\vec{U}] &= 0 \\ O[Y] &= \delta & O[\vec{V}] &= \frac{\delta U_e}{L} & O[\vec{V}] &= \frac{\tilde{\Gamma}}{2\pi} \frac{1}{S} \\ O[Z] &= S & O[\vec{W}] &= 0 & O[\vec{W}] &= \frac{\tilde{\Gamma}}{2\pi} \frac{1}{\delta} \\ & & O[\vec{P}] &= \rho U_e^2 & O[\vec{P}] &= \frac{\rho}{\delta^2} \left(\frac{\tilde{\Gamma}}{2\pi} \right)^2 \end{aligned} \quad (10.3)$$

Shear components (\vec{U}, \vec{V}) are dominate flow in the $(X - Y)$ plane. The chosen shear-layer scales are consistent with laminar boundary layer practice and differ from those used by Smith Smith (1994). He considered the effect turbulence from the beginning of his analysis while the present study re-introduces it at a later stage. [verify this]

Streamwise vortices dominate flow in the $(Y - Z)$ plane but induce negligible velocities in the streamwise direction. They do, however, affect streamwise velocities (U) by advecting high-speed flow from the edge of the boundary-layer ($U = U_e$ at $Y = \delta$) to the wall ($Y = 0$) .

Forced-mixing is described in terms of an interaction field \vec{U} that represents the offset in streamwise momentum between a boundary-layer with and without forced mixing. In order of magnitude terms, the interaction term is expected to grow proportionally to the time over which mixing occurs $(O[X]/O[\vec{U}])$ and to the rate of forced mixing – which is itself proportional to the product of the vortical advection velocity $O[\vec{V}]$ with the inhomogeneity of the shear field $O[\partial\vec{U}/\partial Y]$:

$$O[\vec{U}] \propto \underbrace{\left(\frac{\tilde{\Gamma}}{2\pi S} \right)}_{O[\vec{V}]} \underbrace{\left(\frac{U_e}{\delta} \right)}_{O\left[\frac{\partial\vec{U}}{\partial Y}\right]} \underbrace{\left(\frac{\tilde{L}}{U_e} \right)}_{\frac{O[X]}{O[\vec{U}]}} = \left(\frac{\tilde{\Gamma}}{2\pi S} \right) \left(\frac{\tilde{L}}{\delta} \right) \quad (10.4)$$

The gauges of expressions 10.3 and ?? can be used to map the flow into a normalized non-dimensional space.

$$\begin{aligned} x &= \frac{X}{L} & \tilde{u} &= \frac{\vec{U}}{U_e} & \tilde{u} &= \frac{\vec{U}}{\left(\frac{\tilde{\Gamma}}{2\pi S} \right) \left(\frac{\tilde{L}}{\delta} \right)} & \tilde{p} &= \frac{\vec{P}}{\rho U_e^2} \\ y &= \frac{Y}{\delta} & \tilde{v} &= \frac{\vec{V}}{U_e} \left(\frac{L}{\delta} \right) & \tilde{v} &= \frac{\vec{V}}{\left(\frac{\tilde{\Gamma}}{2\pi S} \right)} & \tilde{p} &= \frac{\vec{P}}{\frac{\rho}{\delta^2} \left(\frac{\tilde{\Gamma}}{2\pi} \right)^2} \\ z &= \frac{Z}{S} & \tilde{w} &= \frac{\vec{W}}{O[\vec{W}]} & \tilde{w} &= \frac{\vec{W}}{\left(\frac{\tilde{\Gamma}}{2\pi} \frac{1}{\delta} \right)} \end{aligned} \quad (10.5)$$

Expression 10.5 defines a transformation that maps the decomposed Navier Stokes equations (10.2) into non-dimensional space:

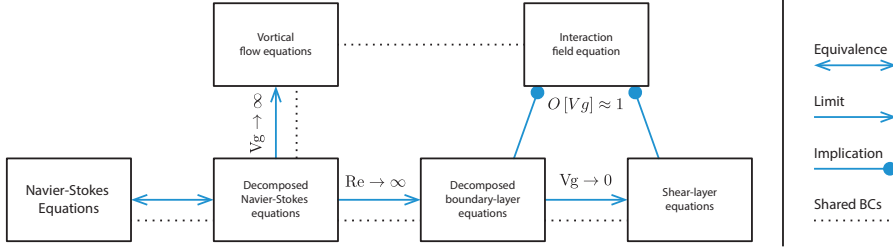


Figure 10.2: Complementary asymptotic development program.

$$\left\{ \begin{aligned}
 & (\bar{u} + \bar{u}Vg) \left(\frac{\partial \bar{u}}{\partial x} + \frac{\partial \bar{u}}{\partial x} Vg \right) + (\bar{v} + \bar{v}Vg) \left(\frac{\partial \bar{u}}{\partial y} + \frac{\partial \bar{u}}{\partial y} Vg \right) + \bar{w} \frac{\partial \bar{u}}{\partial z} Vg^2 = \\
 & = - \left(\frac{\partial \bar{p}}{\partial x} + \left(\frac{S}{L} \right)^2 \frac{\partial \bar{p}}{\partial x} Vg^2 \right) + \frac{1}{Re} \left(\frac{\partial^2 \bar{u}}{\partial x^2} + \left(\frac{L}{\delta} \right)^2 \frac{\partial^2 \bar{u}}{\partial y^2} \right) + \\
 & \quad + \frac{Vg}{Re} \left(\frac{\partial^2 \bar{u}}{\partial x^2} + \left(\frac{L}{\delta} \right)^2 \left(\frac{\partial^2 \bar{u}}{\partial y^2} + \left(\frac{\delta}{S} \right)^2 \frac{\partial^2 \bar{u}}{\partial z^2} \right) \right) \\
 & (\bar{u} + \bar{u}Vg) \left(\frac{\partial \bar{v}}{\partial x} + \frac{\partial \bar{v}}{\partial x} Vg \right) + (\bar{v} + \bar{v}Vg) \left(\frac{\partial \bar{v}}{\partial y} + \frac{\partial \bar{v}}{\partial y} Vg \right) + \bar{w} \frac{\partial \bar{v}}{\partial z} Vg^2 = \\
 & = - \left(\frac{L}{\delta} \right)^2 \left(\frac{\partial \bar{p}}{\partial y} + \left(\frac{S}{L} \right)^2 \frac{\partial \bar{p}}{\partial y} Vg^2 \right) + \frac{1}{Re} \left(\frac{\partial^2 \bar{v}}{\partial x^2} + \left(\frac{L}{\delta} \right)^2 \frac{\partial^2 \bar{v}}{\partial y^2} \right) + \\
 & \quad + \frac{Vg}{Re} \left(\frac{\partial^2 \bar{v}}{\partial x^2} + \left(\frac{L}{\delta} \right)^2 \frac{\partial^2 \bar{v}}{\partial y^2} + \left(\frac{\delta}{S} \right)^2 \left(\frac{L}{\delta} \right)^2 \frac{\partial^2 \bar{v}}{\partial z^2} \right) \\
 & \left((\bar{u} + \bar{u}Vg) \left(\frac{\partial \bar{w}}{\partial x} Vg \right) + (\bar{v} + \bar{v}Vg) \left(\frac{\partial \bar{w}}{\partial y} Vg \right) + \left(\bar{w} \frac{\partial \bar{w}}{\partial z} Vg^2 \right) \right) = \\
 & = - \frac{\partial \bar{p}}{\partial z} Vg^2 + \frac{Vg}{Re} \left(\frac{\partial^2 \bar{w}}{\partial x^2} + \left(\frac{L}{\delta} \right)^2 \frac{\partial^2 \bar{w}}{\partial y^2} + \left(\frac{L}{\delta} \right)^2 \left(\frac{\delta}{S} \right)^2 \frac{\partial^2 \bar{w}}{\partial z^2} \right) \\
 & \left(\frac{\partial \bar{u}}{\partial x} + \frac{\partial \bar{v}}{\partial y} \right) + \left(\frac{\partial \bar{u}}{\partial x} + \frac{\partial \bar{v}}{\partial y} + \frac{\partial \bar{w}}{\partial z} \right) Vg = 0
 \end{aligned} \right. \quad (10.6)$$

System 10.6 depends on the non-dimensional Reynolds (Re) and Vortex strength (Vg) numbers:

$$Re = \frac{U_e L}{\nu} \quad , \quad Vg = \frac{1}{U_e} \left(\frac{\Gamma}{2\pi S} \right) \left(\frac{L}{\delta} \right)$$

The vortex strength number characterizes the relative strength of the vortical component compared to the shear-flow component. When Vg tends to ∞ , streamwise vortices dominate the flow. On the other hand, streamwise vortices have a negligible effect when Vg tends 0. In typical applications, the magnitude of the vortex strength number is close to unity ($O[Vg] = 1$). In the Wendt [Wendt \(1997, 2001\)](#) datasets spanning 56 vortex generator flows, for example, Vg numbers vary between 0.29 and 1.94 while the vane height Reynolds number varies between 28 and 491.

The flow decomposition introduces more variables than governing equations. Clear definitions and governing equations are therefore needed for shear, vortical and interac-

to both sides of system ?? and rewriting the result into dimensional variables.

$$\left\{ \begin{array}{l} (\tilde{U} + \dot{U}) \frac{\partial \tilde{V}}{\partial X} + \tilde{V} \frac{\partial \tilde{V}}{\partial Y} + \tilde{W} \frac{\partial \tilde{V}}{\partial Z} = -\frac{1}{\rho} \frac{\partial \tilde{P}}{\partial Y} + \nu \left(\frac{\partial^2 \tilde{V}}{\partial Y^2} + \frac{\partial^2 \tilde{V}}{\partial Z^2} \right) \\ (\tilde{U} + \dot{U}) \frac{\partial \tilde{W}}{\partial X} + \tilde{V} \frac{\partial \tilde{W}}{\partial Y} + \tilde{W} \frac{\partial \tilde{W}}{\partial Z} = -\frac{1}{\rho} \frac{\partial \tilde{P}}{\partial Z} + \nu \left(\frac{\partial^2 \tilde{W}}{\partial Y^2} + \frac{\partial^2 \tilde{W}}{\partial Z^2} \right) \\ \frac{\partial \tilde{V}}{\partial Y} + \frac{\partial \tilde{W}}{\partial Z} = -\frac{\partial \dot{U}}{\partial X} \end{array} \right. \quad (10.9)$$

In principle, all normalized terms that do not multiply with the Vg number should have been dropped. But an exception was introduced for streamwise convective terms whose singular nature arises from imperfections in the interaction field gauge. System 10.9 can be restated in terms of a Lagrangian derivative for the streamwise (X) direction and a nabla symbol for the crossflow ($Y - Z$) plane.

$$\frac{D}{DT_x} = \frac{\partial}{\partial T} + U \frac{\partial}{\partial X} = (\tilde{U} + \dot{U}) \frac{\partial}{\partial X} \quad \nabla^{yz} = \left(\frac{\partial}{\partial Y}, \frac{\partial}{\partial Z} \right) \quad (10.10)$$

The differential operators of expression 10.10 make system 10.9 more compact:

$$\left\{ \begin{array}{l} \frac{D}{DT_x} (\tilde{V}, \tilde{W}) + ((\tilde{V}, \tilde{W}) \cdot \nabla^{yz}) (\tilde{V}, \tilde{W}) = -\frac{1}{\rho} \nabla^{yz} (\tilde{p}) + \nu \nabla_{yz}^2 (\tilde{V}, \tilde{W}) \\ \nabla^{yz} \cdot (\tilde{V}, \tilde{W}) = -\frac{\partial \dot{U}}{\partial X} \end{array} \right. \quad (10.11)$$

Defining $\tilde{\omega} = \nabla^{yz} \times (\tilde{V}, \tilde{W})$ as the vorticity of the vortical flow and reworking leads to a very intuitive form of system .. :

$$\left\{ \begin{array}{l} \frac{D\tilde{\omega}}{DT_x} + ((\tilde{V}, \tilde{W}) \cdot \nabla^{yz}) \tilde{\omega} = \nu \nabla_{yz}^2 (\tilde{\omega}) \\ \nabla^{yz} \cdot (\tilde{V}, \tilde{W}) = -\frac{\partial \dot{U}}{\partial X} \end{array} \right. \quad (10.12)$$

It states that streamwise vortices are advected along the streamwise direction (D/DT_x terms) which functions as a time . While they move forward in space, vortex cores convect ($((\tilde{V}, \tilde{W}) \cdot \nabla^{yz}) (\tilde{V}, \tilde{W})$) under their own influence and diffuse ($\partial^2/\partial Y^2 + \partial^2/\partial Z^2$) in the cross-flow plane.

Curiously, the streamwise rate of change of the interaction field introduces a light divergence into the vortical field. Velocity fields can still be reconstructed from the vorticity field but, to be exact, the complete Helmholtz decomposition should be considered and two Poisson equations should be solved [Cottet and Koumotsakos \(2000\)](#); [Speck \(2011\)](#) :

$$(\tilde{V}, \tilde{W}) = \nabla^{yz} \times \boldsymbol{\phi} + \nabla^{yz} \cdot \boldsymbol{\varphi} \quad \Rightarrow \quad \left\{ \begin{array}{l} \nabla_{yz}^2 \boldsymbol{\varphi} = \frac{\partial \dot{U}}{\partial X} \\ \nabla_{yz}^2 \boldsymbol{\phi} = \tilde{\omega} \end{array} \right.$$

In most flow regions of practical boundary layers, however, streamwise

$$\left. \begin{array}{l} \frac{\partial \tilde{V}}{\partial Y} \gg \frac{\partial \dot{U}}{\partial X} \\ \frac{\partial \tilde{W}}{\partial Z} \gg \frac{\partial \dot{U}}{\partial X} \end{array} \right\} \Rightarrow \quad \nabla^{yz} \cdot (\tilde{V}, \tilde{W}) \approx 0$$

Solutions of system 10.9 can be sought with convergent numerical methods [Cottet and Koumotsakos \(2000\)](#) or approximated from a compact set of vortex descriptors ([Westphal et al., 1987](#)).

10.1.5. INTERACTION EQUATION

This section presents an approximate equation for the interaction flow component (\dot{U}), which is defined as the offset in streamwise velocity (momentum) between shear-layers with and without forced-mixing:

$$\dot{U} = U - \bar{U}$$

It is tempting to subtract the streamwise equation of the shear-flow system (10.8) to the corresponding equation of the decomposed boundary layer equations (10.7). The result is written in dimensional form:

$$(\bar{U} + \tilde{U}) \frac{\partial \tilde{U}}{\partial X} + \left(\tilde{U} \frac{\partial \tilde{U}}{\partial X} + \tilde{V} \frac{\partial \tilde{U}}{\partial Y} + \tilde{W} \frac{\partial \tilde{U}}{\partial Z} \right) + \left(\tilde{V} \frac{\partial \tilde{U}}{\partial Y} + \tilde{W} \frac{\partial \tilde{U}}{\partial Z} \right) = \nu \left(\frac{\partial^2 \tilde{U}}{\partial Y^2} + \frac{\partial^2 \tilde{U}}{\partial Z^2} \right) \quad (10.13)$$

Longitudinal variations of the streamwise component of the shear flow are slow in zero-pressure gradient flows. It is therefore expectable that:

$$O\left[\frac{\partial \tilde{U}}{\partial X}\right] \ll O\left[\frac{\partial \tilde{U}}{\partial Y}\right] \left. \vphantom{O\left[\frac{\partial \tilde{U}}{\partial X}\right]} \right\} \Rightarrow \tilde{U} \frac{\partial \tilde{U}}{\partial X} + \tilde{V} \frac{\partial \tilde{U}}{\partial Y} \approx \tilde{V} \frac{\partial \tilde{U}}{\partial Y} \quad (10.14)$$

The normal component of the shear flow is then equally small, given that \tilde{V} and $\partial \tilde{U} / \partial X$ are coupled by the continuity equation through the wall impermeability condition. The convective terms of equation 10.13 will be negligibly small in flows with mild pressure gradients.

$$O\left[\frac{\partial \tilde{U}}{\partial Y}\right] \approx O\left[\frac{\partial \tilde{U}}{\partial Y}\right] \left. \vphantom{O\left[\frac{\partial \tilde{U}}{\partial Y}\right]} \right\} \Rightarrow \tilde{V} \frac{\partial \tilde{U}}{\partial Y} + \tilde{W} \frac{\partial \tilde{U}}{\partial Z} \approx \tilde{V} \frac{\partial \tilde{U}}{\partial Y} \quad (10.15)$$

The approximations of expressions 10.14 and 10.15 simplify equation 10.13 into equation 10.16:

$$(\bar{U} + \tilde{U}) \frac{\partial \tilde{U}}{\partial X} + \left(\tilde{V} \frac{\partial \tilde{U}}{\partial Y} \right) + \left(\tilde{W} \frac{\partial \tilde{U}}{\partial Z} \right) = \nu \left(\frac{\partial^2 \tilde{U}}{\partial Y^2} + \frac{\partial^2 \tilde{U}}{\partial Z^2} \right) \quad (10.16)$$

Equation 10.16 is best interpreted the custom differential operators of expression .. , which recast it into equation 10.17:

$$\frac{D\tilde{U}}{Dt_x} + \underbrace{\left((\tilde{V}, \tilde{W}) \cdot \nabla^{yz} \right)}_{\text{advection}} \tilde{U} = \underbrace{\nu \nabla_{yz}^2 \tilde{U}}_{\text{diffusion}} - \underbrace{\tilde{V} \frac{\partial \tilde{U}}{\partial Y}}_{\text{source}} \quad (10.17)$$

Equation 10.17 displays the typical structure of a 2d advection-diffusion equation with source terms. Advection and diffusion take place in the YZ plane, while the X coordinate functions as a time. The mixed flow field \tilde{U} departs from homogenous initial conditions ($\tilde{U} = 0$ at $X = X_0$) and receives momentum through a source term that is proportional to the normal vortical component \tilde{V} and the inhomogeneity $\partial \tilde{U} / \partial Y$ of the shear flow \tilde{U} .

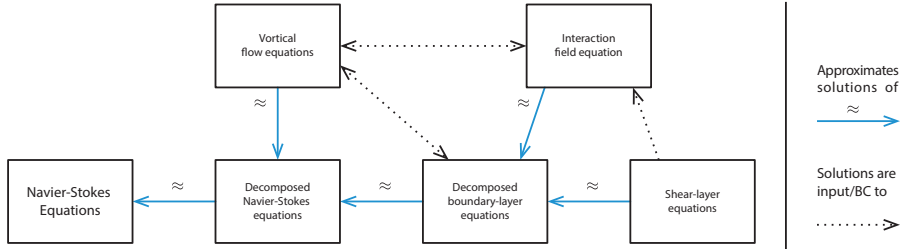


Figure 10.3: Reconstruction of flow solutions from asymptotic components.

10.2. RECONSTRUCTION OF FLOW STRUCTURES

The asymptotic developments presented in this article aim to reconstruct approximate solutions of the Navier Stokes equations from knowledge about flow structures and mechanisms. Solutions of equations 10.8, 10.12 and 10.17 can either be approximated with full-field numerical solvers or reconstructed from structural flow models. The former option is followed for the interaction field while the later is followed for shear and vortical flow components.

10.2.1. SHEAR LAYER

Several integral representations of the shear-layers exist. The Von Karman system of ordinary equations enjoys the most frequent use and is obtained by integration system 10.8 along the vertical (Y) direction:

$$\begin{cases} \frac{\partial \theta}{\partial X} = \frac{C_f}{2} - (H_{12} + 2) \frac{\theta}{U_e} \frac{\partial U_e}{\partial x} \\ \frac{\partial H_{32}}{\partial X} = \frac{2C_D}{\theta} - \frac{H_{32}}{\theta} \frac{C_f}{2} + (H_{12} - 1) \frac{H_{32}}{U_e} \frac{\partial U_e}{\partial x} \end{cases} \quad (10.18)$$

The shear-flow is then described with the well-known integral variables of planar boundary layers (Schlichting, 1979, 7th Ed) :

$$\begin{aligned} \delta_1 &= \int_0^\infty \left(1 - \frac{\tilde{U}}{U_e}\right) dY & C_f &= \frac{1}{\frac{1}{2} \rho U_e^2} \left(\mu \frac{\partial U}{\partial Y} \right) \Big|_{Y=0} \\ \theta &= \int_0^\infty \left(\frac{\tilde{U}}{U_e} \left(1 - \frac{\tilde{U}}{U_e}\right) \right) dY & C_D &= \frac{\mu}{\rho U_e^3} \int_0^\infty \left(\frac{\partial U}{\partial Y} \right)^2 + \left(\frac{\partial U}{\partial Z} \right)^2 dY \\ \delta_3 &= \int_0^\infty \left(\frac{\tilde{U}}{U_e} \right) \left(1 - \left(\frac{\tilde{U}}{U_e} \right)^2 \right) dY & & \\ H_{12} &= \delta_1 / \theta & H_{32} &= \delta_3 / \theta \end{aligned} \quad (10.19)$$

Velocity profiles can be reconstructed from integral quantities for both laminar Falkner and Skan (1931); de Oliveira et al. (2017) and turbulent (Schlichting, 1979, 7th Ed; Swafford, 1982) flows. The present work uses the Swafford turbulent profile (Swafford, 1982) and a related set of closure relations described in references. Skin friction and energy shape factor closure relations depend on shape factor H_{12} and momentum Reynolds

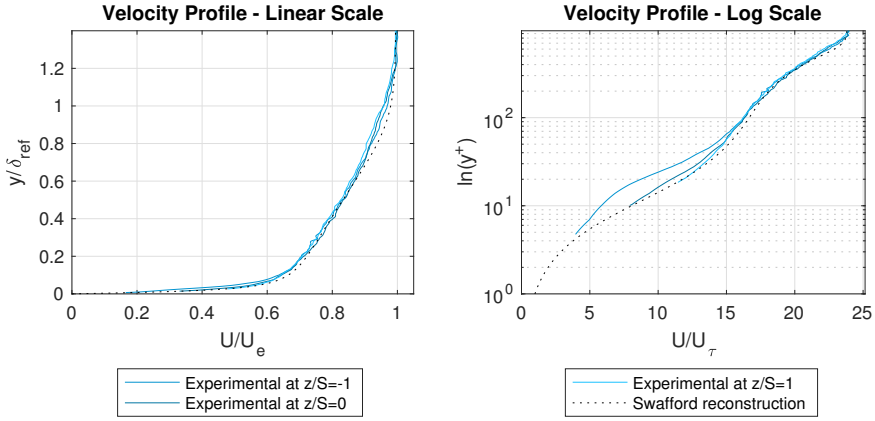


Figure 10.4: Velocity profiles at streamwise stance of vane trailing edge. Comparison with unactuated base-flow from experiment of Baldacchino [Baldacchino et al. \(2015\)](#).

number Re_θ . An additional entrainment ODE is used to close the dissipation coefficient, as in reference [Drela and Giles \(1987\)](#).

10.2.2. STREAMWISE VORTICES

Westphal [Westphal et al. \(1987\)](#) showed that three quantities — circulation per unit length Γ , peak vorticity ω^{max} and vortex core position (Y^v, Z^v) — suffice to completely describe the local features of streamwise vortices. Vortex descriptors can be combined with structural flow models to approximate solutions of equation . . . In doing so, streamwise vortices are explicitly reconstructed to predict vortical velocity field (\tilde{V}, W) .

RELEASE OF VORTICITY

Vortex generator vanes function like finite wings: they generate spanwise forces that manifest to farfield flow as a bound vortex attached to the quarter-chord line. The vortex system does not end at the vane tip but continues as a filament of trailing vorticity. The circulation of trailing vortices can therefore be approximated with Prandtl's lifting line solution. Prandtl's solution captures the vorticity-generating phenomenon but ignores secondary effects. Namely, the roots of vortex-generator vanes are close to wall and perceive slower velocities than the tips. Also, vane aspect ratios are usually small compared to lifting-line assumptions[].

Modern structural studies [] circumvent the limitations of the Prandtl vortex system with a data-driven expression proposed by Wendt [Wendt \(1965\)](#):

$$\Gamma_v = \left(\frac{k_1 \alpha_v c_v U_e}{1 + \frac{k_2}{AR}} \right) \tanh \left(k_3 \left(\frac{h}{\delta} \right)^{k_4} \right) \quad (10.20)$$

He used four constants to match results from an experimental campaign ([Wendt, 1997, 2001](#)) conducted at the Langley internal flow facility ([Porro et al., 1991](#)). This dataset was important: it also served to reinforce previous insight suggesting that the vorticity distribution of filament cores resembled a Lamb vortex [Squire \(1965\)](#). In doing so, it en-

abled the deployment of angular momentum arguments to formulate a semi-empirical expression for the initial peak vorticity (ω_0^{max}) of vortex filaments that depends on a single constant (β):

$$\omega_0^{max} = \frac{\Gamma_v^3 (\beta-1)^2}{2\pi^3 (\alpha_v h_v c_v U_e)^2} \quad with \quad \beta = \frac{1}{2\xi^2 \left(1 - e^{-\frac{1}{2}}\right)^2} \approx 0.29 \quad (10.21)$$

DIFFUSION OF VORTEX CORES

The right side of equation .10.12 indicates that viscous stresses diffuse vorticity in the crossflow plane as filaments move downstream. The result is two-fold: vortex cores smoothen due to shear forces of their own induced field and exchange vorticity due to shear forces that result from mutual interactions [Cottet and Koumotsakos \(2000\)](#). The former phenomenon was first analysed by Squire [Squire \(1965\)](#) who related it to Lamb's solution for the time evolution of a planar vortex. Peak vorticity is first with the age of vortex cores, denoted as t^v :

$$\omega^{max} = \frac{\Gamma}{4\pi\nu} \frac{1}{t^v} \quad (10.22)$$

Expression 10.22 is then recast into a system of ordinary differential equations by restating vortex core age in terms of streamwise stance (X) and velocity ($U_v = \bar{U}_v + \dot{U}_v$) [Wendt et al. \(1995\)](#):

$$\begin{cases} \frac{d\omega^{max}}{dt^v} = -\frac{\Gamma}{4\pi\nu} \left(\frac{1}{t^v}\right)^2 \\ \frac{dt^v}{dX} = \frac{1}{U_v} \end{cases} \quad with \quad \begin{cases} \omega_{(t_0^v)}^{max} = \omega_0^{max} \\ t_0^v = \frac{\Gamma}{4\pi\nu\omega_0^{max}} \\ X_0 = x^{TE} \end{cases} \quad (10.23)$$

Initial conditions are found by matching system 10.23 with expressions 10.20 and 10.21 at the vane trailing edge. Vortex cores start with non-zero age ($t^v > 0$) because they form over the entire chord of the vane tip ([Oon, 1973](#)).

DEFORMATION OF VORTEX FILAMENTS

The left side of equation 10.12 describes the transport of filament vorticity in space. Core movement is dominated by streamwise advection but cores also convect under their mutual induction. This phenomenon was first modeled by Jones ([Jones, 1957](#)): he considered a periodic vortex system, enforced wall impermeability with the method of images and used inviscid induction functions. [Wendt \(Wendt et al., 1995\)](#) and [Logdberg \(Logdberg et al., 2009\)](#) refined his analysis and restated it as ODEs for the crossflow movement of vortex core positions (Y_v, Z_v).

$$\begin{cases} \frac{dY^v}{dX} = \frac{\tilde{V}_v}{U_v} \\ \frac{dZ^v}{dX} = \frac{\tilde{W}_v}{U_v} \end{cases} \quad with \quad \begin{cases} Y_0^v = h^{vg} \\ Z_0^v = d^{vg}/2 \end{cases} \quad (10.24)$$

Initial conditions (Y_v, Z_v) correspond to the trailing edge of vane tips and vortical velocities at core centers are denoted as (\tilde{V}_v, \tilde{W}_v). This approach is reported to yield accurate predictions of vortex filament development ([Pearcey, 1961](#)) until the occurrence of chaotic breakdown ([Logdberg et al., 2009](#)).

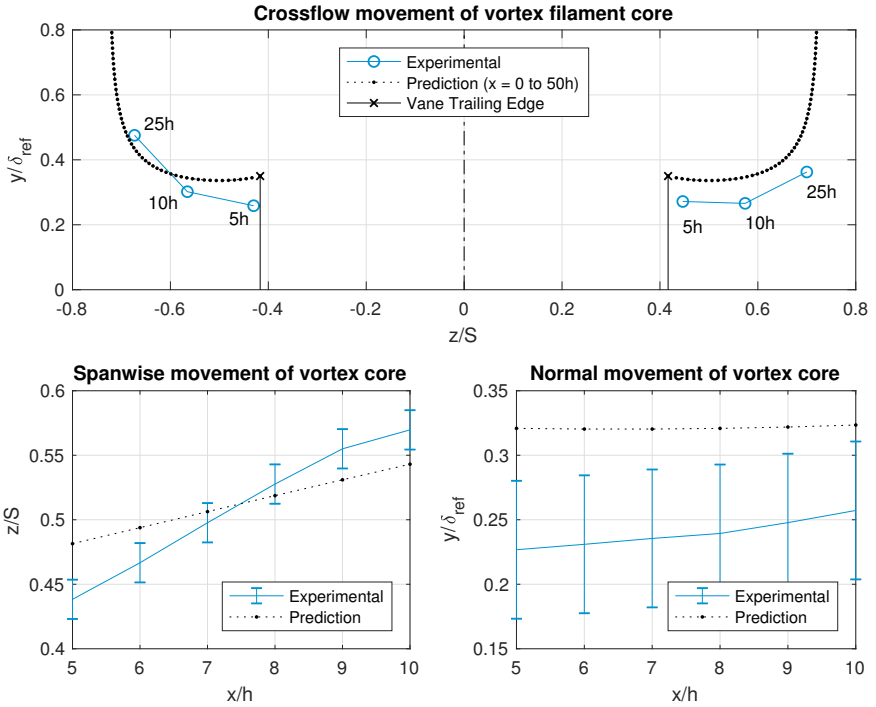


Figure 10.5: Crossflow movement of vortex cores. Comparison with experiment of Baldacchino [Baldacchino et al. \(2015\)](#).

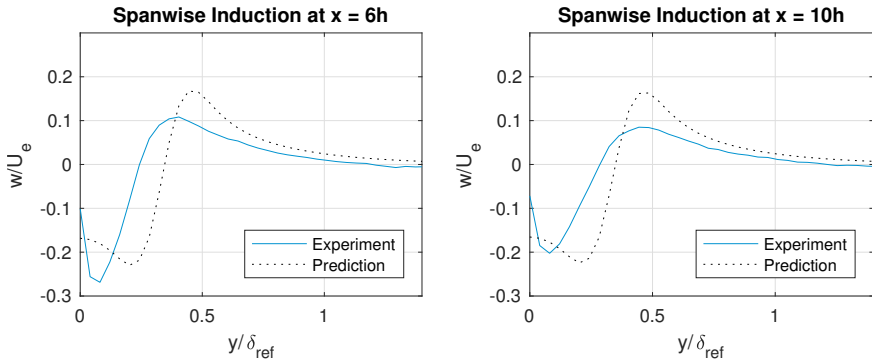


Figure 10.6: Spanwise velocity across vortex core along vertical lines. Cores and plotting locii where at $z_{exp}^v = -0.46S$ and $z_{num}^v = -0.50S$ for experimental and numerical cases corresponding to the $x = 6h$ streamwise stance. For $x = 10h$ cores were at spanwise stance $z_{exp}^v = -0.57S$ and $z_{num}^v = -0.55S$.

VORTEX-INDUCED VELOCITY FIELD

Logdberg (Logdberg et al., 2009) recommends that the vortical velocity field be reconstructed by numerical superposition of Lamb induction functions:

$$|\tilde{V} + \tilde{W}| = \frac{\Gamma}{2\pi r} \left(1 - e^{\left(-\frac{\pi\omega^{max}}{\Gamma} r^2\right)} \right)$$

The distance between the vortex core and the induction point is denoted as r . More sophisticated reconstructions can be achieved from the insights of Velte (Velte, 2013) and Gamiz (Fernandez-Gamiz et al., 2016).

10.2.3. EFFECT OF TURBULENCE ON INTERACTION FIELD

Streamwise vortices promote transition to turbulence so most applications of forced mixing occur in turbulent flow. Turbulent processes are immensely complex but can be approximated with a simplified form of the Reynolds stress tensor. The simplest form of Prandtl's mixing-length model follows Boussinesq's approximation to describe turbulent effects in terms of a supplementary viscosity (Launder and Spalding (1972):

$$v_t = \rho l_m^2 \left| \frac{\partial U}{\partial Y} \right| \quad \text{with} \quad l_m = \begin{cases} \kappa y & \frac{y}{\delta} < 0.02 \\ 0.02 \delta & \frac{y}{\delta} \geq 0.02 \end{cases}$$

This form is known to provide reasonable approximations for homogeneous shear layers with small or negligible pressure gradients. It fails, however, to capture increases in turbulence intensity near the core of vortex filaments. This issue can be circumvented by following the inner-layer approach of the Baldwin-Lomax algebraic model to replace the shear term with the magnitude of the vorticity vector (Baldwin and Lomax (1978):

$$v_t = \rho l_m^2 \Omega \quad \text{with} \quad \Omega = \sqrt{\nabla \times \mathbf{U}}$$

Equation 10.17 is then restated as:

$$\frac{D\tilde{U}}{DT_x} + \underbrace{\left((\tilde{V}, \tilde{W}) \cdot \nabla^{yz} \right) \tilde{U}}_{\text{advection}} = \underbrace{\left(v + v_t \right) \nabla_{yz}^2 \tilde{U}}_{\text{diffusion}} - \underbrace{\tilde{V} \frac{\partial \tilde{U}}{\partial Y}}_{\text{source}} \quad (10.25)$$

In the next section, solutions of equation ... approximated with a finite-difference method – described in appendix A – are compared with experimental measurements. Means for describing interaction flow structures with a compact set of descriptions are assessed later, in section ...

10.3. VALIDATION AGAINST PIV MEASUREMENTS

Several measurements of boundary layers with streamwise vortices are reported in literature. The experiments of Schubauer (Schubauer and Spangenberg, 1960), Westphal (Westphal et al., 1987) and Bradshaw (Shabaka et al., 1985; Bradshaw, 1987a; Metha and Bradshaw, 1988) marked the era of hot-wire anemometry. Direct measurements of skin friction, for example with oil flow interferometry, are extremely scarce for boundary-layers with streamwise vortices. Recent experiments have been favoring the use of Particle Image

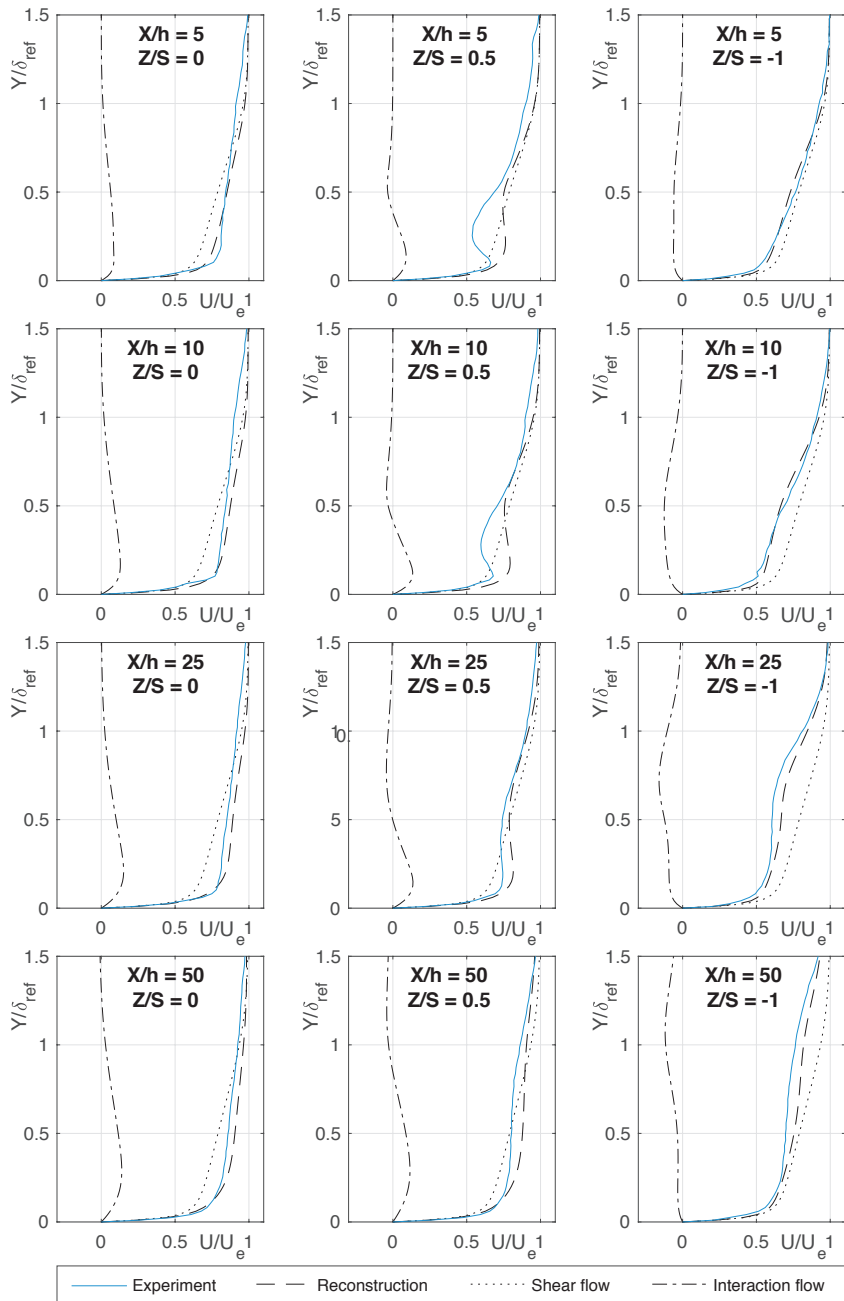


Figure 10.7: Measured and reconstructed velocity profiles for experiment of Baldacchino et al. (2015).

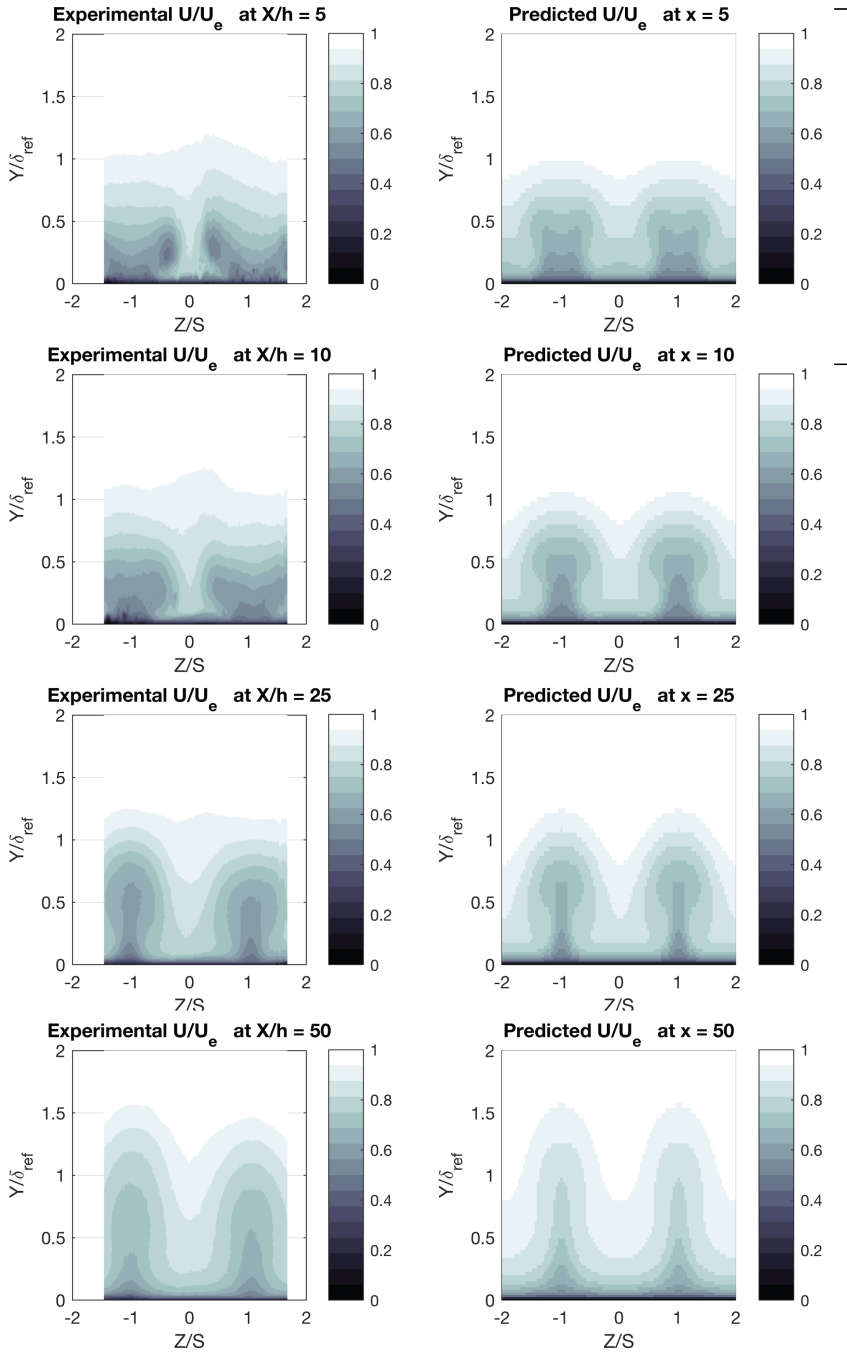


Figure 10.8: Measured (left) and reconstructed (right) streamwise velocity fields.

Vortex Generators			PIV Setup	
Vane Height	h	5 mm	Window width	47 mm
Vane Chord	c	12.5 mm	Window height	33 mm
T.E. Separation	d	12.5 mm	Pixel size	0.09 mm
Vane Nominal AOA	α	18°	Plane orientation	crossflow, centered on vane pair symmetry line
Symmetry Width	S	15 mm	Plane location	$x = 5, 6, 7, 8, 9, 10, 25$ and $50h$ behind vane
Inflow Properties				
Edge Velocity	U_e	15.16 m/s		

Table 10.1: Experimental conditions for experiment of Baldacchino [Baldacchino et al. \(2015\)](#).

Velocimetry (PIV) ([Di Cicca et al., 2002](#); [Godard and Stanislas, 2006](#); [Velte et al., 2008](#); [Logdberg et al., 2009](#); [Shim et al., 2015](#); [Manolesos and Voutsinas, 2015](#)).

A recent series of PIV measurements were conducted in TU-Delft's Boundary Layer Tunnel (BLT) by Baldacchino [Baldacchino et al. \(2015\)](#). The BLT is a closed windtunnel with a long (5.4 m) and wide ($1.25\text{ m} \times 0.25\text{ m}$) test-section preceded by a settling chamber with 16:1 area ratio ([Dobbinga, 1968](#)). Flat plate flows are measured on a side of the test-section while the other is deformed to control the pressure gradient. Experimental details are found in reference [Baldacchino et al. \(2015\)](#).

Baldacchino measured several boundary-layers with different streamwise vortex generators in null and adverse pressure gradients with straight or yawed inflow. The simplest case is ideal for validating asymptotic expansions and flow reconstructions presented in the preceding sections. It consists in an array of rectangular vanes packed in pairs and placed in a turbulent boundary layer with zero pressure gradient.

10.3.1. UNACTUATED FLOW

The base-flow was measured at the location of the vane trailing edge before vortex generators were placed [Baldacchino et al. \(2015\)](#). Boundary-layer thicknesses were first estimated by trapezoidal integration but results varied with spanwise stance. Spanwise variations had two origins: a true but minor inflow inhomogeneity and a misorientation of the PIV camera. Velocities were improperly resolved close to the wall and base-flow velocities had to be shifted via law of the wall extrapolation. The procedure was repeated for every vertical stance. It results in an upward shift of 0.0737 mm for the left ($z = S$) side of the PIV window, and 0.6958 mm for the right side ($z = -S$).

Shape factor (H_k) and momentum Reynolds number (Re_θ) values are as initial conditions for the numerical solution. They were determined by fitting a Swafford velocity profile to measurements with a Levenberg-Marquardt algorithm. This procedure proved more robust than naïve integrals: values of $H_k = 1.41$ and $Re_\theta = 2499$ were retained with a standard deviation of ... and ... percent. The reference scale for boundary layer thickness was estimated at $\delta_{ref} = 14.3\text{ mm}$ with the closure relation of Green [Green \(1976\)](#).

The Swafford [Swafford \(1982\)](#) profile yields a fair reconstruction of the shear velocity field from averaged shape factor (H) and momentum Reynolds number (Re_θ) values. The main disparity concerns the wake function [Coles \(1956\)](#), which seems stronger in the real flow than in the Swafford profile reconstruction. As in most PIV studies, near wall resolution was insufficient to verify skin friction predictions.

10.3.2. STREAMWISE VORTICES

The key dynamics of vortex filament movement are captured. Figure 10.5 compares numerical predictions with experimental measurements. Experimental locations of the vortex core were determined by manual analysis of quiver plots. Error bars represent the 90% confidence level based on a normal probability distribution of errors. Vortex cores first move towards the wall, then away from each other and finally bounce off the wall. Predictions display systematic bias in height because the numerical method assumes that vortex filaments are formed at the upper edge of the vortex-generator vane. It is well known that vortices form slightly upstream and at a lower height [Kroo and Smith \(1990\)](#).

10.3.3. SPANWISE FLOW

Spanwise velocities, shown on 10.6, are largely dominated by vortical induction. Vortex filament strength is slightly over-predicted and the effect of core height (y_v) overestimation is quite explicit. Also, over-estimation of peak vorticity seems stronger at $x = 10h$ than $x = 6h$. Reasons could be twofold. On the one hand, Squire's model may underestimate the rate at which vortex cores smoothen because it neglects turbulent diffusive processes. On the other hand, real flows are subject to no-slip wall conditions for both streamwise and spanwise velocity components. The present formulation permits spanwise slip at the wall, and therefore neglects viscous vorticity exchanges between the wall and streamwise vortices. These exchanges not only accelerates core smoothing in real flows, but also provoke to the progressive decay of filament circulation.

10.3.4. FORCED MIXING

Streamwise vortices mix flow from upper strata of the shear-layer with de-energized flow from lower strata. Behind vortex vanes ($z = 0, \pm 2S$), advection displaces streamwise momentum from the edge of the boundary-layer to the wall and forms a region of accelerated flow. The effect is opposite between vane pairs ($z = \pm S$), where vortical advection moves flow from the wall into a higher region of decelerated flow. Figure 10.7 compares predicted velocity profiles with measurements. Agreement is best on symmetry planes. Intermediate flow regions ($z = 0.5S$) exhibit greater disparities but the asymptotic model captures the distinctive S-shape of velocity profiles.

Disparities between predictions and measurements diminish as the flow develops downstream of the vortex-generator vanes. Figure 10.8 compares streamwise velocity fields. Agreement is best at 25 vane heights but numerical velocity fields maintain thinner flow structures that are absent from the flow measurements. Also, flow reconstructions exhibit narrower decelerated flow regions. These differences could be related to mismatches in the prediction of vortex filament positions and turbulent diffusive processes.

10.4. UNIVERSAL FEATURES OF FORCED-MIXING

The asymptotic approach developed in section 10.2 and validated in section 10.3 showed that the mixing effect of streamwise vortices could be approximated as an externally imposed advective process. This advective process leads to the accumulation of an offset in streamwise momentum, which describes the difference between a boundary with and

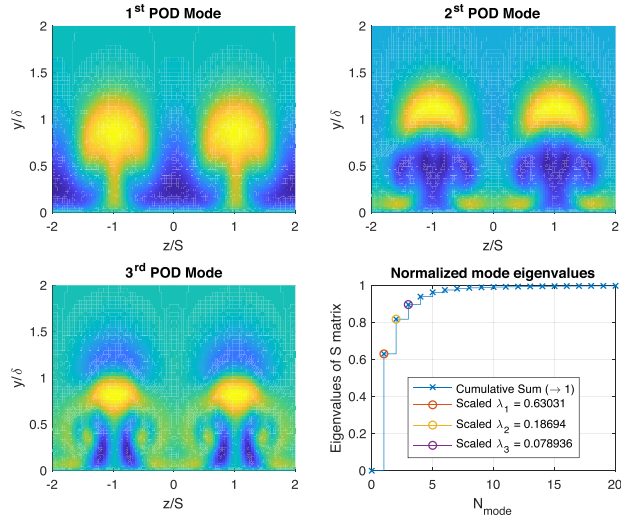


Figure 10.9: Proper Orthogonal Decomposition of interaction (\hat{U}) flow field

without streamwise vortices.

The question that arises is whether this advective process can be described with a compact set of descriptors. Observation of figure .. shows that the offset in streamwise momentum changes in shape as the flow develops. The regions of accelerated flow that forms between vortex filaments is initially narrow, and widens as the flow moves downstream. It is therefore clear that no simple similarity pattern exists.

10.4.1. PROPER ORTHOGONAL DECOMPOSITION

The absence of easily observable similarity patterns does not rule out the possibility of describing the mixing field with a compact set of parameters. Figure 10.9 shows the dominant modes of a proper orthogonal decomposition (POD) of the mixing field, conducted on a collection of 240 snapshots sampled from the flow shown on figure 10.8.

The first three modes capture more than 94% of the kinetic energy of the mixing field. The first mode highlight contains 80% of the information and is easily interpreted as a representation of the main mixing process. It is capable of creating a region of accelerated flow between vortex pairs, and a region of decelerated flow in the middle of each vortex pair. The second mode functions as a correction for the first mode, enabling to narrow or widen the accelerated flow region, and move it up or down. The third mode is less instinctive, and may correspond to somehow spurious flow features. It contains less than 3% of the of the kinetic energy of the mixing field, and hence of its information content, as measured by an L_2 norm.

These first four POD modes were then employed to generate a reduced order model. This model was found to be stable and to describe the mixing field of the flow depicted on figure 10.8 accurately. Differences between the original asymptotic solutions and the reduced order model solutions were virtually invisible. This model was also found to

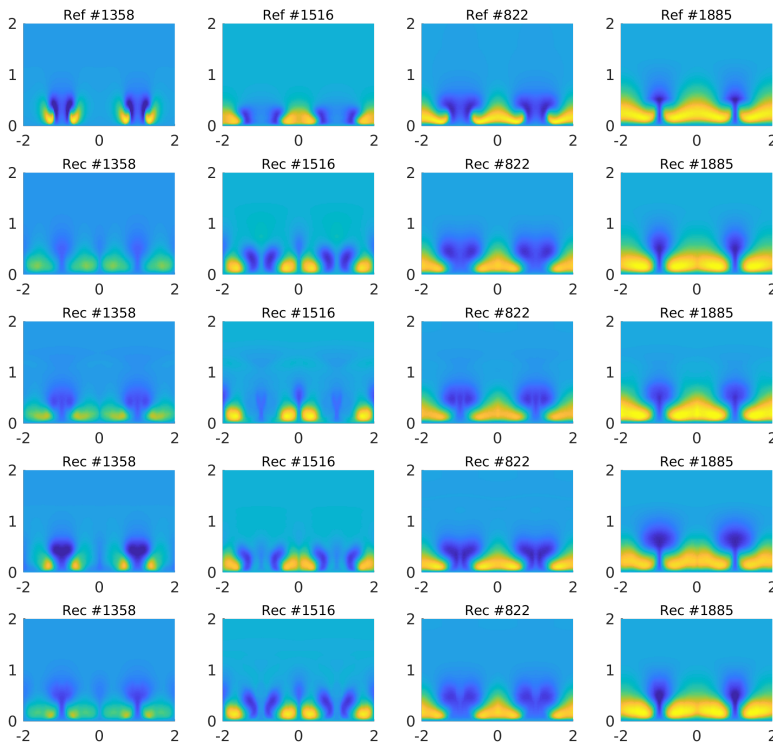


Figure 10.10: Select snapshots from validation set: original (*top*), POD reconstruction (*second row*), Lin-lin autoencoder (*third row*), SigLog-Lin autoencoder (*fourth row*), SigLog-SigLog autoencoder (*fifth row*).

provide reasonable results for modeling vortex generator flows with different pressure distributions, as long the spacing and height of vortex generators was kept invariant.

10.4.2. GENERALIZATION TO ARBITRARY GEOMETRIES

A new collection of numerical experiments was conducted to gather 2200 snapshots of mixing fields obtained from a variety of representative flows with streamwise vortices. Vortex generator properties – relative height, relative spanwise spacing and – were sampled from 12 different experiments described in literature (Logdberg et al., 2008; Metha and Bradshaw, 1988; Wendt, 1997; Baldacchino et al., 2015), and mixing field snapshots were generated with the asymptotic model from sections 10.2 and 10.3.

The proper orthogonal decomposition was unable to find effective bases for representing mixing phenomena once flows with different geometric features were considered. The first 4 modes contain less than 40% of the total kinetic energy of the mixing field, and 60 modes would have been needed to capture 90% of the kinetic energy of all

snapshots. We therefore turned our quest for the common features of forced mixing to a different dimensionality reduction.

Autoencoding neural networks are well-known generalization of the proper orthogonal decomposition (POD) technique. The principle is relatively simple. A feed-forward network with three layers was constructed: The input and output layers had the same size as the input data (128x128 datapoints), whereas the intermediate layer had a much smaller size. We chose that it would have mere 4 neurons to try to identify four modes that would describe the mixing field. The network was then trained to minimize the difference between input and outputs for 1600 of the 2200 snapshots. These 1600 snapshots corresponded to randomly sampled training set, whereas the remaining 600 snapshots were kept for validation purposes.

Three different networks were trained for 40.000 epochs with a sequential quadratic programming (SQP) gradient algorithm. The loss function corresponded to the L2 norm of the difference between network inputs and outputs averaged over all snapshot in an epoch. Results were evaluated by comparing the reconstruction of several snapshots from the validation set that exhibited fairly different flow features. A selection of insightful reconstructions is presented on figure 10.10 . Columns correspond to the same image whereas rows correspond to different reconstructions, except for the top one which presents the original image.

The three networks shared the same feedforward topology but different in the choice of neuron activation functions. The first network (Lin-Lin) had linear activation function for both the input and output layers, whereas the second network (SigLog-Lin) had a logistic sigmoid input layer and linear output layer. Finally, the third network (SigLog-SigLog) had logistic sigmoid layers for both input and output. These networks are ordered in terms of their growing complexity, and generality. The Lin-Lin network is supposed to produce results comparable to a POD decomposition but without orthogonality guarantees, whereas the SigLog-Lin and SigLog-SigLog networks are in principle able to extract non-linear trends from the data.

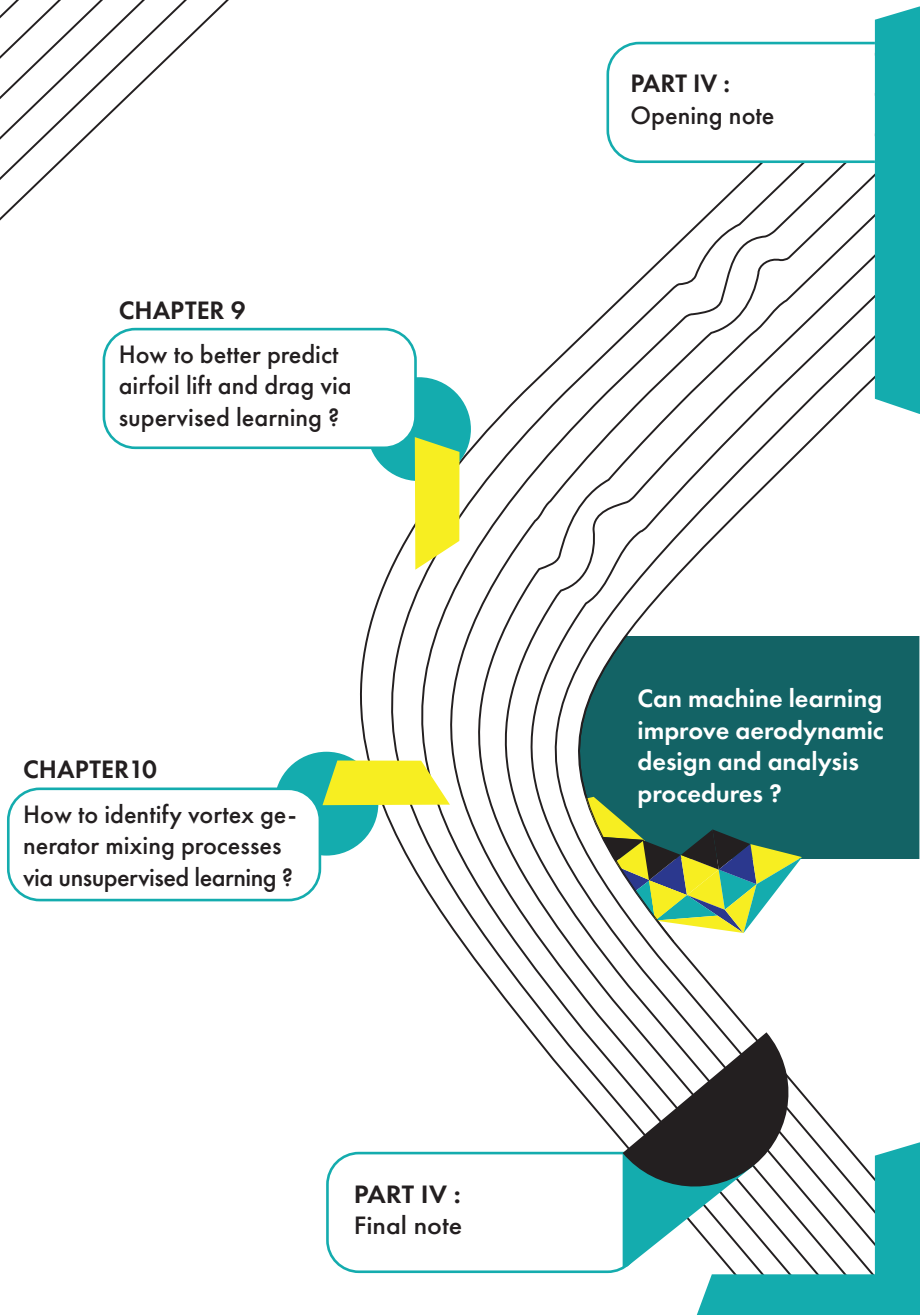
The results of figure 10.10 show that linear dimensionality reduction techniques struggle to find common features amidst very diverse snapshots of vortex-mixing fields. The POD and Lin-Lin autoencoder reconstructions of the leftmost snapshot comprise several spurious features and fail to represent the narrow circular regions of accelerated flow from the original snapshot. This stands in stark contrast with the results of the LogSig-LogSig and Lin-LogSig autoencoders which were able to capture these features. The Lin-LogSig autoencoder seems to perform best, as he is capable of reconstructed all main flow features of the selected snapshots while introducing less spurious elements than the LogSig-LogSig autoencoder.

The ability to reconstruct mixing field snapshots from a very diverse set of vortex generator flow with non-linear autoencoders whose inner contains only 4 neurons indicated that 4 parameters could suffice to describe the entire basis of forced-mixing fields. This indicates that some form of similarity exists in vortex generator flows.

10.5. FINDINGS AND FUTURE PERSPECTIVES

The present chapter showed that compact deterministic modeling of vortex generator flows is possible. First, a flow decomposition was proposed and expanded to comple-

mentary asymptotic limits to identify the fundamental phenomena vortex-generator driven mixing of the boundary-layer. Then, numerical solutions of the asymptotic system of equations were validated against experimental measurements. Finally, a broader set of numerical solutions was generated to seek common features in the streamwise momentum offset of different vortex-generator flows with non-linear dimensionality reduction techniques. Results from this last step suggest that four parameters might be sufficient to describe a broad variety of forced mixing occurrences.



CLOSING NOTE

Minimization of flow simulation uncertainties

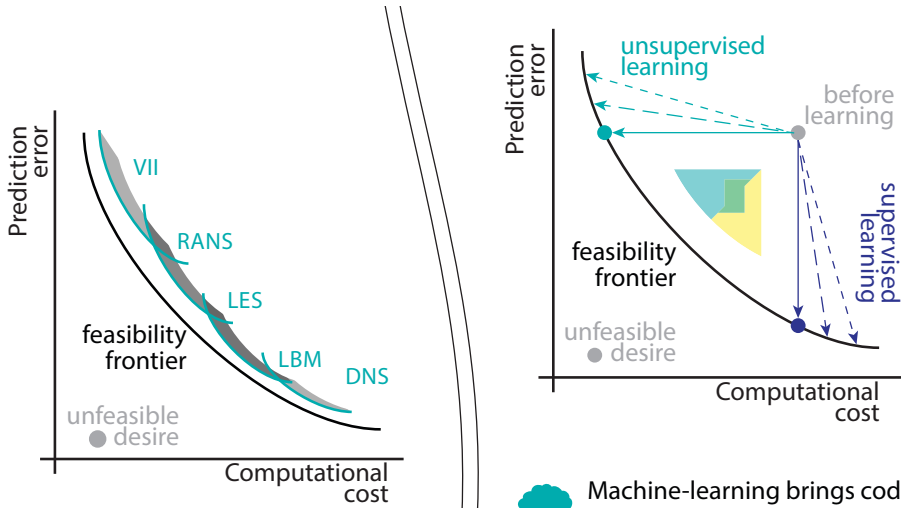
What do the techniques demonstrated here mean for wind energy? How do they relate to the question of efficiency?

Each method in the palette of flow simulation techniques strikes a different compromise between accuracy and computational cost. Most simulation codes, however, fail to realise their full potential due to imperfect calibration or numerical implementation. Machine learning can address both issues.

Supervised-learning approaches can determine optimal closures by solving regression problems. In that case, optimality corresponds to the minimisation of a metric for prediction inaccuracy. Code inaccuracy is quantified against a set of known reference results. If the set of reference reliable results is large enough, a numerical code that minimises the inaccuracy metric achieves the most accurate predictions permitted by its physical models. Chapter 9 used supervised learning to learn closure relations for the turbulent boundary layer from experimental airfoil polar data. The approach was a success, in the sense that it improved the prediction of drag polars with the Rfoil code. Even so, it became clear that scarcity of reliable experimental data hinders the general application of supervised learning techniques.

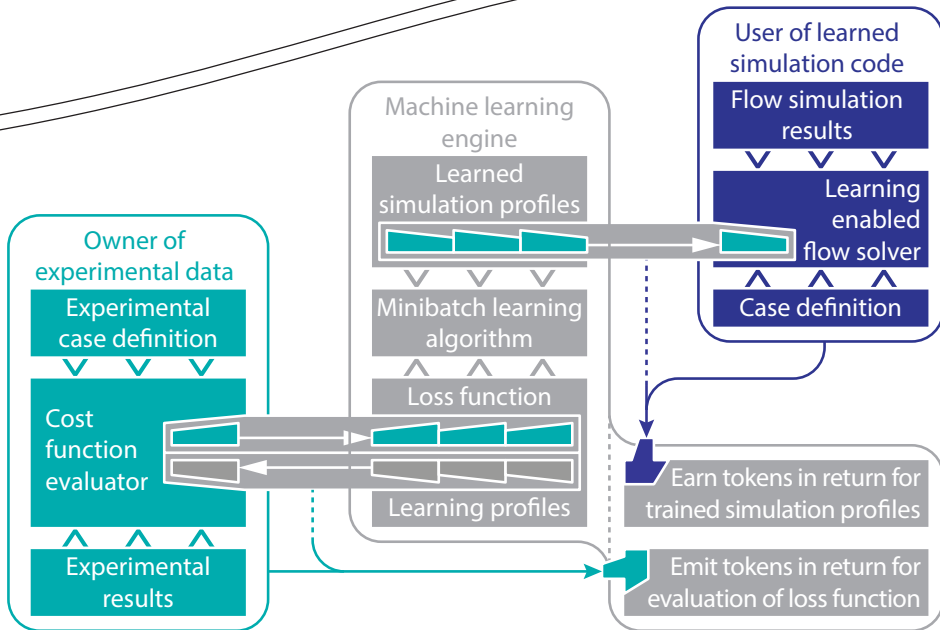
Unsupervised-learning has different applications and does not require access to labelled sets of experimental data. It was used to identify hidden similarity patterns in a boundary layer with streamwise vortices, like those that created by vortex generators. That is relevant to wind energy since vortex generators are ubiquitous on the thicker sections of modern wind turbine blades. It is hoped that the ability to describe the effect of vortex generators with compact descriptors enables the development of better designs and placement strategies.

Machine-learning offers substantial opportunities for improving flow prediction techniques used in wind energy. However, it is no panacea: the results are only as good as the data they are based on. Good data is scarce. That is why new mechanisms for sharing experimental data are needed for widespread development of data-driven flow predictions. The human challenge is at least as large as the technical one.



Efficient codes strike non-inferior compromises between accuracy and computational cost

Machine-learning brings codes closer to their feasibility frontier



Minibatch algorithms create demand and opportunities for data exchange

V

CONCLUSION

CONCLUSION

Where are the main opportunities for improving the aerodynamic efficiency of wind energy conversion? Is disruptive progress physically possible? Does progress in airfoil design still impact cost of wind energy? Can barriers to the adoption of new designs be lifted?

The efficiency of wind energy cannot be resumed to the sole question of aerodynamic performance. New research and changing socio-technical conditions constantly redefine the meaning of efficiency. In the broadest sense, efficient wind energy systems respond to the needs of individuals and communities. That goes far beyond aerodynamics: it is about reducing sound nuisance, designing lean structures, employing recyclable materials, facilitating maintenance, enabling synergies with electricity storage and promoting universal energy access. The list of multi-disciplinary considerations is endless. But the physical processes of fluid flow remain the immutable starting point of wind energy conversion.

PHYSICAL LIMITS TO WIND ENERGY EFFICIENCY

Part I of this thesis showed that there are no physical objections to the achievement of unbounded power coefficients in steady flows of inviscid incompressible fluids if multiple energy exchange surfaces are coordinated. Real flows are neither inviscid, nor incompressible or steady, so the practical feasibility of such a strategy is at best uncertain. But it could have a deeper, almost cultural, impact on the way we think about the efficiency of wind energy conversion. The Betz limit, which remains unchallenged for isolated rotors, was built on the ideal flow framework and served as a compass for maximum wind energy efficiency during the past hundred years. It should be complemented with a greater awareness about the fact that other flow layouts might reach extract even more energy per unit surface. Even if they are not feasible advantageous in practice.

Limits to the achievable aerodynamic efficiency of wind energy conversion stem from other considerations once multiple rotors are considered. Realistic interactions between rotors and wakes differ considerably from ideal flow predictions. In real flows, wakes diffuse and induce increased turbulence levels that lead to strong detrimental loads between interacting wind turbines. They may also collapse into chaotic movements and interact with the surrounding atmosphere in complex ways. These are the factors that limit the achievable efficiency of wind energy conversion on a multi-rotor arrangement like a wind farm.

The framework of inviscid incompressible flow solutions remains useful to the study of wind energy conversion nonetheless. Its value arises from the ability to isolate macroscopic convective processes from all other physical phenomena. Even if it is no longer the limiting factor, convection remains the primary determinant of wind energy conversion. That is why ideal flow metaphors enabled this thesis to show that:

1. **Interactions between rotors and wakes are not necessarily detrimental to wind energy conversion**
2. **The thrust coefficient that maximizes energy extraction depends on the surrounding flow**
3. **Inhomogeneous actuator loading distributions may be advantageous in certain settings**

The above insights do not translate into immediate changes to the way wind turbines and wind farms are built. Their impact is envisioned to occur on a longer timescale. It is thought that a better understanding of energy exchange processes broadens the scope of imaginable renewable energy solutions. That last observation echoes to the EAWE call for curiosity driven research.

REFINEMENT OF CURRENT WIND TURBINE BLADES

Part II of this thesis showed horizontal-axis wind turbines already reached a remarkable level of aerodynamic efficiency. Rotors must at the same time maximize power production and minimize static loads, dynamic loads and noise emission. Procedures for generating non-inferior compromises between these goals are effective and well known. The open question, and major challenge, concerns the selection of appropriate compromises between goals.

From a steady flow perspective, standard wind turbine airfoils and rotor planforms already approach aerodynamic optima. However, improvements might still be possible by considering the effect of inflow inhomogeneities across all stages of rotor and airfoil design. Specifically, we showed that:

1. **The order of magnitude of inflow fluctuations experienced by wind turbine airfoils can be described with a simple semi-analytical tools**
2. **Inflow fluctuations shift the angle-of-attack at which wind turbine airfoils realize the highest effective glide-ratio**
3. **Design of optimized wind turbine airfoils enables modest but relevant reductions in the cost of wind energy**

IMPROVEMENT OF FLOW SIMULATION TECHNIQUES

The prediction of turbulent phenomena is an old problem that admits no simple or universal solutions. Machine-learning techniques provide effective, even if imperfect, replacements for the absence of reliable mechanistic models describing turbulent phenomena. This thesis used supervised machine-learning to improve the calibration of a viscous-inviscid airfoil analysis code. In doing so, it found that:

1. **Airfoil polar data contains information about turbulent boundary layer flow features**
2. **Traditional boundary layer closures underestimate skin friction**

3. It is more important to learn from reliable data than from big data, even if reliable data is scarce

Machine-learning techniques are not restricted to the calibration of aerodynamic codes from experimental data. Unsupervised learning techniques can be combined with asymptotic analysis to identify common features across flow structures. Specifically, for the case of boundary-layers with streamwise vortices, they enabled us to show that:

- 1. Streamwise vortices act as on the boundary layer as an externally imposed convective process**
- 2. Offsets in streamwise momentum introduced by forced-mixing with vortex-generators display a substantial level of similarity**

The above insights are expected to improve the design wind turbine airfoils and passive flow control devices.

FINAL WORD

Discussions about the aerodynamic efficiency of wind energy conversion do not fit in three questions. Yet, the issues raised in this thesis show that aerodynamic challenges remain determinant to the progress of wind energy efficiency. Disruptive progress in the efficiency of wind energy conversion is not physically impossible, even if the Betz limit puts a firm and unchallenged bound on the power coefficient of isolated wind turbines. Pursuit of such a revolutionary agenda, however, requires long term investments that would be easier to obtain if flow simulation techniques were more accurate. Short term improvements in wind turbine performance are more easily achieved by tailoring wind turbine airfoils to local site conditions, but even these modest steps are constrained by the limited accuracy of turbulence models. Attempts to introduce minor improvements on current wind turbines could therefore drive demand for new simulation techniques that would facilitate the development of disruptive wind energy conversion systems. Evolution and revolution are not contradictory.

A Pareto tale about the social relevance of wind energy

Imagine that Assetou, a Malian citizen, thinks Europeans should stop flying for holidays because climate change causes draught in her rainfed agricultural fields. And that Andrew, a European citizen, defends that developing countries should instead constrain their population to curb future emissions. Andrew and Assetou hold different, and apparently irreconcilable views about optimal resource allocation.

Reality is, fortunately, not as manicheist as our characters. Let us map Andrew's welfare into the per capita gross national product of European citizens: they cannot go back on living standards and need growth to maintain social cohesion despite an ageing population – their demands correspond to the yellow area. Assetou's welfare, on the other hand, represents the satisfaction of basic needs for 980 million rural poor: they often live in the tropics and urge for access to food, shelter and healthcare – their ambitions lie in the blue area. Figure 10.12(a) sketches compromises between Andrew's and Assetou's interests as a feasibility frontier: a line of efficient compromises between stakeholder interests given present technology levels.

Andrew's and Assetou's ambitions are both legitimate, but anthropogenic changes of the climate system stress the tension between them. Climate change affects the fluxes of ecosystemic services on which Assetou and the world's poor depend – irregular rainfall patterns disrupt the productivity of rainfed agriculture, droughts accelerate desertification, and rising ocean salinity tarnishes the productivity of fisheries. The list is endless and ills go beyond Assetou's livelihood. Andrew and European citizens also lose welfare to climate change – Dutch dikes face harsher storms, Swiss ski stations disappear, French oak forests need to be rethought and Portuguese wetlands collapse. Loss of welfare shifts the feasibility frontier to the origin, as shown on figure 10.12(b), and makes both stakeholders worse off.

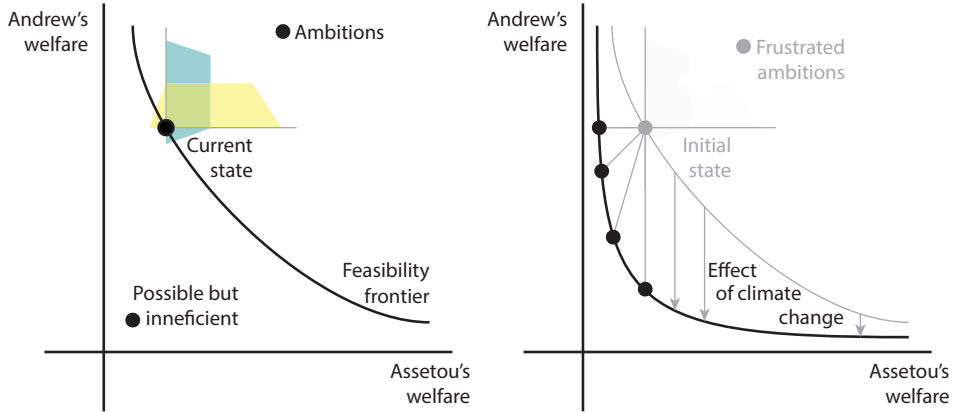


Figure 10.11: Welfare feasibility frontier (left) and adverse effects of climate change (right).

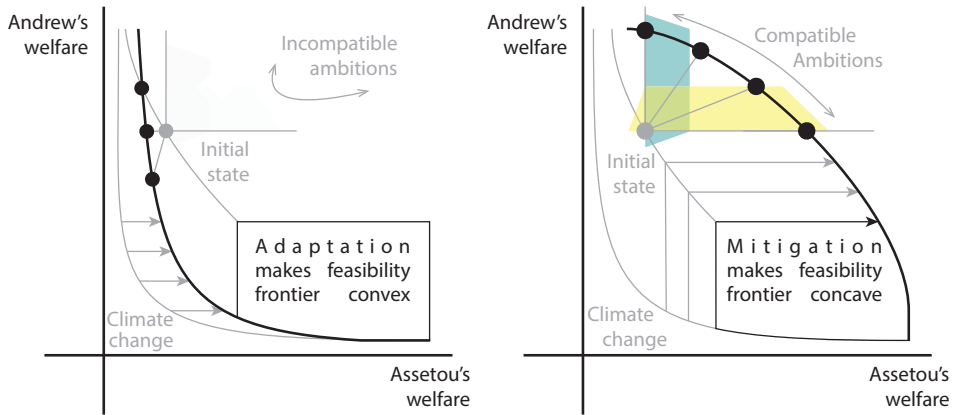


Figure 10.12: Restoration of welfare through adaptation (left) and mitigation (right).

Welfare lost to climate change can be partially recovered with adaptation technologies. Measures like reinforcing dikes or developing precision agriculture shift the feasibility frontier back the right, as figure 10.12(a) shows. But successful adaptation requires substantial investments: stakeholders with more capital have better chances of adapting than those with less capital. Adaptation based strategies make the feasibility frontier more convex unless explicit redistributive policies are applied. They exacerbate the conflict between stakeholder interests .

Mitigation technologies have the opposite effect, shown on the right side of figure 10.12, because they decouple economic growth from the generation of climatic forcings. Also, they tend to replace usage of exhaustible resources by labour and technology, which are intrinsically redistributive compared to resource rents. Mitigation creates jobs in industrialized countries and therefore enhances Andrew's welfare. Simultaneously, it reduces greenhouse gas emissions and thereby protects the ecosystems that support the livelihoods of the world's most vulnerable populations. Mitigation strategies make the welfare feasibility frontier more concave and relax the tension between conflicting interests. That explains how research to increase the efficiency of mitigation technologies, like wind energy, contributes to the reduction of climate injustice.

APPENDIX

A

MATCHED ACTUATOR SETUPS

A.1. DIMENSIONS, SETS AND SMOOTHNESS

The Euler (2.1) and total enthalpy (2.2) equations apply equally to planar ($n = 2$) and tridimensional ($n = 3$) flows. So do all deductions presented up to subsection 2.3.1, provided that set descriptions are interpreted in a suitable manner:

- Control volumes ($\Omega \subset \mathbb{R}^n$) are n -manifolds over which the momentum equations (2.1) are integrated into algebraic statements.
- Streamlines are 1-manifolds ($\sigma \subset \mathbb{R}^n$) over which the total-enthalpy equation (2.2) is integrated to obtain energy conservation statements.
- Cross-sections and actuation surfaces ($\phi \subset \mathbb{R}^n$) are interpreted as $(n-1)$ -manifolds. Actuators span surfaces (2-manifolds) in 3-d flow and lines (1-manifolds) in planar flow.

All configurations studied in the article are considered symmetric around the centreline of both actuators, which is itself aligned with the free-stream.

A.1.1. INTEGRATION SETS

All sets are contained in a Euclidean space \mathbb{R}^n with $n = 2$ or 3. It is implicitly assumed that control volumes are open sets:

$$\partial\Omega_{01} \notin \Omega_{01} \quad \partial\Omega_{1a} \notin \Omega_{1a} \quad \partial\Omega_{a2} \notin \Omega_{a2} \quad \partial\Omega_{2e} \notin \Omega_{2e}$$

Actuation surfaces correspond to the intersection of subsequent control volumes. So does the cross-section of the recovery region (ϕ_a):

$$\begin{aligned}\phi_1 &= \partial\Omega_{01} \cap \partial\Omega_{1a} \\ \phi_a &= \partial\Omega_{1a} \cap \partial\Omega_{a2} \\ \phi_2 &= \partial\Omega_{a2} \cap \partial\Omega_{2e}\end{aligned}$$

Wake edges correspond to the boundaries of the union of all but the first control volume (Ω_{1a}), excluding cross sections:

$$\bar{\omega} = \partial(\Omega_{1a} \cup \Omega_{a2} \cup \Omega_{2e}) \setminus \phi \quad \text{with} \quad \phi = \phi_1 \cup \phi_a \cup \phi_2 \cup \phi_e$$

In the above expression, ϕ_e denotes the cross-section of the terminal wake.

A.1.2. SMOOTHNESS ASSUMPTIONS

Actuator forces are lumped over actuation surfaces and introduce discontinuities in the static pressure $p : \mathbb{R}^n \rightarrow \mathbb{R}$ and enthalpy $h : \mathbb{R}^n \rightarrow \mathbb{R}$ fields. Both fields are assumed to be smooth outside actuation surfaces ($\phi_1 \cup \phi_2 \subset \mathbb{R}^n$):

$$\begin{aligned} p &\in C^k(\mathbb{R}^n \setminus (\phi_1 \cup \phi_2)) \\ h &\in C^k(\mathbb{R}^n \setminus (\phi_1 \cup \phi_2)) \end{aligned}, \quad k \geq 1 \quad (\text{A.1})$$

Vorticity is shed from the edges of actuation surfaces and remains on $(n-1)$ -manifolds in the absence of viscous shear forces. Vortex sheets introduce velocity discontinuities and the velocity field $\mathbf{U} : \mathbb{R}^n \rightarrow \mathbb{R}^n$ is assumed to be smooth everywhere but across wake edges ($\bar{\omega} \subset \mathbb{R}^n$):

$$\mathbf{U} \in C^k(\mathbb{R}^n \setminus \bar{\omega}), \quad k \geq 1 \quad (\text{A.2})$$

Wakes enclose regions of different constant total-enthalpy. The total-enthalpy field $h^t : \mathbb{R}^n \rightarrow \mathbb{R}$ is therefore discontinuous across wake edges and actuation surfaces:

$$h^t \in C^0(\mathbb{R}^n \setminus (\phi_1 \cup \phi_2 \cup \bar{\omega})) \quad (\text{A.3})$$

A.2. ASYMPTOTIC CONFIGURATION

The term asymptotic configuration refers to matched-actuator setups with infinite length ($D_x \rightarrow \infty$).

A.2.1. RELATIVE VELOCITIES AND ACTUATOR LOADINGS

The relative normal speed over the downstream actuator is restated in terms of non-dimensional parameters (a_2, b) by feeding definitions 2.19 and 2.20 into equation 2.11:

$$\begin{cases} \frac{U_2}{U_a} = (1 - a_2) \\ b = \frac{U_a}{U_0} \end{cases} \Rightarrow \frac{U_2}{U_0} = \frac{U_a}{U_0} \frac{U_2}{U_a} = b(1 - a_2) \quad (\text{A.4})$$

Reworking equation 2.11 and inserting the above together with expression 2.20 leads to the expression for the relative terminal wake speed:

$$\begin{aligned} U_2 = \frac{U_a + U_e}{2} &\Leftrightarrow \frac{U_e}{U_0} = 2 \frac{U_2}{U_0} - \frac{U_a}{U_0} = 2b(1 - a_2) - b \\ &\Leftrightarrow \frac{U_e}{U_0} = b(1 - 2a_2) \end{aligned} \quad (\text{A.5})$$

The mean relative speed over the upstream actuator is obtained by inserting definition 2.20 into equation 2.15:

$$U_1 = \frac{U_a + U_0}{2} \Rightarrow \frac{U_1}{U_0} = \frac{1}{2} \left(\frac{U_a}{U_0} + 1 \right) = \frac{1}{2} (b + 1) \quad (\text{A.6})$$

Actuator loadings (f_1, f_2) can be stated in terms of the relative induction factor a_2 and intermediate speed ratio b by reworking expressions 2.7 and 2.14 with the relative speed expressions (A.4-A.6).

$$f_1 = \rho (h_a^t - h_0^t) = \frac{1}{2} \rho U_0^2 (b^2 - 1) \quad (\text{A.7})$$

$$f_2 = \rho (h_e^t - h_a^t) = \frac{1}{2} \rho U_0^2 b^2 ((1 - 2a_2)^2 - 1) \quad (\text{A.8})$$

$$= -\frac{1}{2} \rho U_0^2 (4b^2) (a_2 (1 - a_2)) \quad (\text{A.9})$$

Summing leads to the total-enthalpy jump imposed on the flow by the complete setup:

$$\frac{f_1 + f_2}{\rho} = (h_e^t - h_0^t) = \frac{1}{2} U_0^2 ((b^2 - 1) - 4b^2 a_2 (1 - a_2)) \quad (\text{A.10})$$

A.2.2. CONSISTENCY WITH SINGLE ACTUATOR MODELS

The power coefficient law for matched actuator setups with infinitely distant actuators (2.30) is consistent with isolated actuator models when the downstream actuator exerts no force ($a_2 = 0$).

To verify consistency, let us define the induction factor of the upstream actuator a_1 and relate it to the intermediate speedup ratio b through expression A.6:

$$a_1 : U_1 = (1 - a_1) U_0 \quad \Rightarrow \quad b = 1 - 2a_1 \quad (\text{A.11})$$

Feeding this relation into the power coefficient expression (2.30) with $a_2 = 0$ leads to an unusual power coefficient law:

$$C_P|_{a_2=0} = -4a_1 (1 - 2a_1) (1 - a_1) \quad (\text{A.12})$$

It cannot be compared directly with the classical power coefficient law, because it uses the area of the second actuator as a reference. Let us then define an alternative power coefficient, using the area of the upstream actuator as a reference:

$$C_P^{S_1} = \frac{P_1 + P_2}{\frac{1}{2} \rho S_1 U_0^3} = \frac{P_1 + P_2}{\frac{1}{2} \rho S_2 U_0^3} \frac{S_2}{S_1} = \frac{S_2}{S_1} C_P \quad (\text{A.13})$$

The area ratio can be recovered from expression 2.24 and reworked in terms of a_1 for $a_2 = 0$:

$$\frac{S_2}{S_1} = \frac{\frac{1}{2} (b + 1)}{b(1 - a_2)} = \frac{(1 - a_1)}{b(1 - a_2)} \quad \Rightarrow \quad \left. \frac{S_2}{S_1} \right|_{a_2=0} = \frac{1 - a_1}{b} = \frac{1 - a_1}{1 - 2a_1} \quad (\text{A.14})$$

Feeding all this into the power coefficient of the upstream actuator leads to a familiar expression, consistent with the Betz-Joukowski model:

$$\begin{aligned} C_P^{S_1} \Big|_{a_2=0} &= \frac{S_2}{S_1} C_P|_{a_2=0} = \left(\frac{1 - a_1}{1 - 2a_1} \right) (-4a_1 (1 - 2a_1) (1 - a_1)) \\ &= -4a_1 (1 - a_1)^2 \end{aligned} \quad (\text{A.15})$$

A.2.3. COMPLIANCE WITH CONSERVATION OF ENERGY

Expression 2.30 predicts that matched-actuator setups with asymptotically distant actuators can reach power coefficients above unity. This is intriguing because the power coefficient has often been compared to an efficiency. But exceeding unity does not imply violating energy conservation. Let us write an inequality stating that extracted power must be smaller than the power carried by the flow:

$$\dot{m} \left(\frac{1}{2} U_0^2 \right) + P > 0 \quad (\text{A.16})$$

We will now prove that matched-actuator setups extract less energy than that contained in the flow. The inequality (A.16) is restated into non-dimensional groups by inserting expressions 2.27, 2.30, A.4 and 2.30:

$$\begin{aligned} \Leftrightarrow \quad & \rho S_2 U_2 \left(\frac{1}{2} U_0^2 \right) + \frac{1}{2} \rho S_2 U_0^3 C_P > 0 \\ \Leftrightarrow \quad & \left(\frac{U_2}{U_0} \right) + C_P > 0 \quad \forall \rho, S_2, U_0 > 0 \\ \Leftrightarrow \quad & b(1 - a_2) + b(1 - a_2)(b^2 - 1) - b^3(4a_2)(1 - a_2)^2 > 0 \\ \Leftrightarrow \quad & b(1 - a_2)(1 + (b^2 - 1) - b^2(4a_2)(1 - a_2)) > 0 \end{aligned}$$

The avoidance of flow reversal bounds the design space with $b > 0$ and $a_2 < \frac{1}{2}$. Therefore, it holds that:

$$b(1 - a_2) > 0 \quad , \quad \forall \quad \begin{matrix} b > 0 \\ a_2 < \frac{1}{2} \end{matrix}$$

Reworking leads to an expressive form of inequality A.16 :

$$\begin{aligned} \Leftrightarrow \quad & 1 + (b^2 - 1) - b^2(4a_2)(1 - a_2) > 0 \\ \Leftrightarrow \quad & b^2(1 - (4a_2)(1 - a_2)) > 0 \\ \Leftrightarrow \quad & 1 - (4a_2)(1 - a_2) > 0 \\ \Leftrightarrow \quad & (1 - 2a_2)^2 > 0 \end{aligned}$$

This condition is fulfilled at every point (a_2, b) in the design space, which proves that matched actuator setups never violate energy conservation. Corollary: matched-actuator setups extract energy over an area that is greater than their projected area when the power coefficient exceeds unity.

A.3. COMPLEMENTARY CONFIGURATION

The term complementary configuration refers to matched-actuator setups with vanishing distance between actuators ($D_x \rightarrow 0$).

A.3.1. ACTUATOR LOADING

For the complementary configuration, a relation between the \bar{a} induction factor and the total-enthalpy jump imposed on the fluid elements crossing the machine can be established:

$$\frac{f_1 + f_2}{\rho} = (h_e^t - h_0^t) = -2U_0^2 \bar{a}(1 - \bar{a}) \quad (\text{A.17})$$

The division of loading between actuators has no effect on induction or power coefficient. The total enthalpy jump uniquely determines the performance of a matched actuator setup with infinitesimal separation between its actuators.

A.3.2. CORRESPONDENCE WITH ASYMPTOTIC CONFIGURATION

Expression A.17 can be compared with its equivalent for machines whose actuators are infinitely far away from each other. In that case, expression A.10 relates the total-enthalpy jump with the intermediate speedup ratio b and the relative induction factor a_2 :

$$\frac{f_1 + f_2}{\rho} = (h_e^t - h_0^t) = \frac{1}{2} U_0^2 ((b^2 - 1) - 4b^2 a_2 (1 - a_2)) \quad (\text{A.18})$$

Expressions A.17 and A.10 can be matched to establish a correspondence between double actuator machines with infinitesimally and infinitely spaced actuators:

$$\begin{aligned} \Leftrightarrow \quad & \begin{aligned} (h_e^t - h_0^t) &= (h_e^t - h_0^t) \\ -2U_0^2 \bar{a} (1 - \bar{a}) &= \frac{1}{2} U_0^2 ((b^2 - 1) - 4b^2 a_2 (1 - a_2)) \end{aligned} \\ \Rightarrow \quad & \bar{a} = \frac{1}{2} \left(1 - \sqrt{1 - (4b^2 a_2 (1 - a_2) - (b^2 - 1))} \right) \end{aligned} \quad (\text{A.19})$$

This expression is particularly useful when assessing the effect of actuator spacing on the machine performance.

A.4. TOTAL ENTHALPY AND ENERGY CONSERVATION

The usage of total-enthalpy emphasizes the energy content of the incoming free-stream. By definition, total-enthalpy (h^t) represents the total energy contained in each unit of fluid mass - it is generally quantified in Joules per Kilogram. My focus is on the particular case of non-reacting inviscid incompressible fluids, so I to treat internal (thermal and chemical) energy (ϵ) as an arbitrary constant offsetted to zero. Offsetting to zero eases manipulation without loss of generality.

Total enthalpy (h^t) then represents the mechanical energy per unit mass: kinetic energy held exclusively in the fluid velocity field ($\frac{1}{2} \mathbf{U} \cdot \mathbf{U}$) and potential energy held exclusively in the fluid pressure field ($h = p/\rho$). Static enthalpy (h) represents potential energy per unit mass. The flux of mechanical energy (power, P_0) crossing a $(n-1)$ -manifold $\phi_0 \subset \mathbb{R}^n$ (surface) immersed in the unperturbed free-stream is therefore written as:

$$P_0 = \int h^t (\mathbf{U} \cdot \mathbf{n}) d\phi_0$$

Only a limited share of this energy can be extracted. It is customarily assumed — and this work makes no exception — that static pressure and enthalpy perturbations vanish in the far field. Every parcel of flow must then return to its original potential energy state at some point. No power can be extracted from the flux of potential energy (P_0^{pot}), and that poses a first bound on the maximum amount of energy (P_0^{max}) that can be extracted from the fluid that crosses the ϕ_0 cross-section:

$$P_0^{max} < \int (h^t - h) (\mathbf{U} \cdot \mathbf{n}) d\phi_0 = P_0 - P_0^{pot} \quad (\text{A.20})$$

Local exchanges between the kinetic and potential energy fields are possible as long as the balance of potential energy exchanges comes back to zero for every fluid parcel. Actuator disks induce static enthalpy discontinuities across themselves. Energy is then exchanged with the potential energy field, which exchanges it back with the kinetic energy field, and thereby drives the wake to a different speed (kinetic energy state).

Condition A.20 is incomplete - it is necessary but not sufficient. Power can only be extracted from the kinetic energy field, but not all kinetic energy can be extracted. Kinetic energy per unit mass (h^k) and its flux across the ϕ_0 cross-section (P_0^{kin}) are written as:

$$h^k = \frac{1}{2}(\mathbf{U} \cdot \mathbf{U}) = h^t - h \quad \Rightarrow \quad P_0^{kin} = \int h^k (\mathbf{U} \cdot \mathbf{n}) d\phi_0 = P_0 - P_0^{pot}$$

The wake would come to a standstill if all kinetic energy was extracted. Wakes collapse into chaotic motions well before this happens. The maximum power that can be extracted from the fluid crossing the ϕ_0 cross-section is therefore bounded by the ability of wakes to resist the onset of chaos, as suggested by Mikkelsen [Mikkelsen et al. \(2014\)](#). There is no well defined threshold for the minimum speed below which wakes breakdown, but denoting it as U_{turb} makes inequality A.20 more comprehensive.

$$P_0^{max} < \int \frac{1}{2}((\mathbf{U} \cdot \mathbf{U}) - U_{turb}^2)(\mathbf{U} \cdot \mathbf{n}) d\phi_0 < \int (h^t - h)(\mathbf{U} \cdot \mathbf{n}) d\phi_0 \quad (\text{A.21})$$

Matched-actuator setups fulfill inequality A.21 at every point $(a_2, b) \in D$ in the design space (2.34) — so long as that the Glauert threshold (a_{turb}) is chosen so that $U_{turb} = (1 - 2a_{turb})U_0$.

A.4.1. UNBOUNDED POWER COEFFICIENT

Inequality A.21 does not eliminate the possibility of reaching unbounded power coefficients because:

“The share of energy that can be extracted from each parcel of fluid is bounded, not that the amount of fluid from which energy can be extracted is bounded.”

To see how this plays out, consider a matched-actuator setup with asymptotically distant actuators operated in the prescribed a_2 optimality regime (section 2.2.4.2). The speed-ratio $b^{(a_2)}$ is chosen according to expression 2.35 for any given induction factor that fulfills the conditions of expression 2.34. Actuator loadings are found by feeding the optimality condition (2.35) into the expressions for the loading of each actuator (A.7 and A.7):

$$\Rightarrow \begin{cases} b = b^{(\bar{a}_2)} = \frac{\sqrt{3}}{3(1-2\bar{a}_2)} \\ a_2 = \bar{a}_2 \\ f_1 = \rho(h_a^t - h_0^t) = \frac{1}{2}\rho U_0^2(b^2 - 1) \\ f_2 = \rho(h_e^t - h_a^t) = -\frac{1}{2}\rho U_0^2(4b^2)(a_2(1 - a_2)) \end{cases} \quad (\text{A.22})$$

$$\Rightarrow \begin{cases} \frac{f_1}{\frac{1}{2}\rho U_0^2} = \left(\left(\frac{\sqrt{3}}{3(1-2\bar{a}_2)} \right)^2 - 1 \right) = \frac{1}{3(1-2\bar{a}_2)^2} - 1 \\ \frac{f_2}{\frac{1}{2}\rho U_0^2} = - \left(4 \left(\frac{\sqrt{3}}{3(1-2\bar{a}_2)} \right)^2 \right) (a_2(1 - a_2)) = -4 \frac{\bar{a}_2(1-\bar{a}_2)}{3(1-2\bar{a}_2)^2} \end{cases}$$

The global total enthalpy jump experienced by the flow is written by summing the loading of the two actuators (expression A.7):

$$\frac{h_e^t - h_0^t}{\frac{1}{2}U_0^2} = \frac{f_1 + f_2}{\frac{1}{2}\rho U_0^2} = \frac{1}{3(1-2\bar{a}_2)^2} - 1 - 4 \frac{\bar{a}_2(1-\bar{a}_2)}{3(1-2\bar{a}_2)^2} \quad (\text{A.23})$$

Reworking expression A.7 leads to:

$$\begin{aligned}
 \frac{h_e^t - h_0^t}{\frac{1}{2}U_0^2} &= \frac{1}{3(1-2\tilde{a}_2)^2} - \frac{4\tilde{a}_2(1-\tilde{a}_2)}{3(1-2\tilde{a}_2)^2} - 1 \\
 &= \frac{1-4\tilde{a}_2(1-\tilde{a}_2)}{3(1-2\tilde{a}_2)^2} - 1 \\
 &= \frac{1-4\tilde{a}_2(1-\tilde{a}_2)}{3(1-2\tilde{a}_2)^2} - \frac{3(1-2\tilde{a}_2)^2}{3(1-2\tilde{a}_2)^2} \\
 &= \frac{1-4\tilde{a}_2(1-\tilde{a}_2)-3(1-2\tilde{a}_2)^2}{3(1-2\tilde{a}_2)^2}
 \end{aligned} \tag{A.24}$$

The numerator of expression A.24 can be simplified into a square:

$$\begin{aligned}
 &1-4\tilde{a}_2(1-\tilde{a}_2)-3(1-2\tilde{a}_2)^2 \\
 &= 1-(4\tilde{a}_2-4\tilde{a}_2^2)-3(1-4\tilde{a}_2+4\tilde{a}_2^2) \\
 &= 1-4\tilde{a}_2+4\tilde{a}_2^2-3+12\tilde{a}_2-12\tilde{a}_2^2 \\
 &= 1-3-4\tilde{a}_2+12\tilde{a}_2+4\tilde{a}_2^2-12\tilde{a}_2^2 \\
 &= -2+8\tilde{a}_2-8\tilde{a}_2^2 \\
 &= -2(1-4\tilde{a}_2+4\tilde{a}_2^2) \\
 &= -2(1-2\tilde{a}_2)^2
 \end{aligned} \tag{A.25}$$

Inserting expression A.25 back into expression A.24 leads to :

$$\frac{h_e^t - h_0^t}{\frac{1}{2}U_0^2} = -\frac{2(1-2\tilde{a}_2)^2}{3(1-2\tilde{a}_2)^2} = -\frac{2}{3} \tag{A.26}$$

Which shows that the optimality condition of expression 2.35 leads to a constant global total enthalpy jump on the flow, irrespective of the chosen \tilde{a}_2 value (provided expression 2.34 is fulfilled). It corresponds to extracting $2/3 \approx 66.6\%$ of the mechanical energy carried by each parcel of fluid in the free-stream. The figure is higher in the Betz limit situation, in which case $8/9 \approx 88.8\%$ of the mechanical energy carried by each parcel of fluid is extracted.

Expression A.26 can be reworked to find the velocity of the fully developed terminal wake ($u_e = U_e/U_0 > 0$ where $h_e = h_0$) in the considered optimality regime:

$$\begin{aligned}
 \frac{h_e^t - h_0^t}{\frac{1}{2}U_0^2} &= -\frac{2}{3} \\
 \Leftrightarrow \frac{(\frac{1}{2}U_e^2 + h_e) - (\frac{1}{2}U_0^2 + h_0)}{\frac{1}{2}U_0^2} &= -\frac{2}{3} \\
 \Leftrightarrow \frac{(\frac{1}{2}U_e^2 + h_0) - (\frac{1}{2}U_0^2 + h_0)}{\frac{1}{2}U_0^2} &= -\frac{2}{3} \\
 \Leftrightarrow \frac{\frac{1}{2}(U_e^2 - U_0^2)}{\frac{1}{2}U_0^2} &= -\frac{2}{3} \\
 \Leftrightarrow \left(\frac{U_e}{U_0}\right)^2 - 1 &= -\frac{2}{3} \\
 \Leftrightarrow \left(\frac{U_e}{U_0}\right)^2 &= \frac{1}{3} \\
 \Rightarrow \frac{U_e}{U_0} &= \frac{1}{\sqrt{3}} = \frac{\sqrt{3}}{3} > U_{turb}
 \end{aligned} \tag{A.27}$$

Expression A.24 shows that the terminal wake velocity is equal to U_e/U_0 independent of the selected \tilde{a}_2 , provided that it fulfills conditions 2.34 and that b is chosen according to expression 2.35.

Now, consider that the prescribed induction factor (\tilde{a}_2) is chosen infinitely close (that is $\tilde{a}_2 \rightarrow 0.5^-$) but below its maximum permissible value ($\tilde{a}_2 < 0.5^-$). The conditions of expression 2.34 will be fulfilled () and expression .. will be applicable.. Expression .. describes the power coefficient of a matched-actuator setup with infinite separation between actuator disks operating in steady inviscid flow. And, for the conditions considered here, it predicts that the power coefficient will tend to infinity (expression ..., restated below):

$$C_P^{(\tilde{a}_2)} = -\frac{2\sqrt{3}}{9} \frac{(1 - \tilde{a}_2)}{(1 - 2\tilde{a}_2)} \quad , \quad \forall \tilde{a}_2 < \frac{1}{2}$$

The optimal power coefficient tends to infinity as the prescribed induction factor approaches its maximum permissible value:

$$\lim_{\tilde{a}_2 \rightarrow \frac{1}{2}} C_P^{(\tilde{a}_2)} = -\frac{2\sqrt{3}}{9} \frac{(1 - \tilde{a}_2)}{(1 - 2\tilde{a}_2)} = -\infty$$

So does the mass-flux of flow that crosses the machine:

$$\lim_{a_2 \rightarrow \frac{1}{2}} (\dot{m})|_{(a_2, b(a_2))} = \lim_{a_2 \rightarrow \frac{1}{2}} \rho S_2 U_0 \left(\frac{\sqrt{3}}{3(1 - 2a_2)} \right) (1 - a_2) = \infty$$

The setup then extracts energy from an unbounded amount of fluid, harnessed from a streamtube whose area in the unperturbed free-stream (S_0) tends to infinity:

$$\lim_{a_2 \rightarrow \frac{1}{2}} \left(\frac{S_0}{S_2} \right) |_{(a_2, b(a_2))} = \lim_{a_2 \rightarrow \frac{1}{2}} \left(\frac{\sqrt{3}}{3(1 - 2a_2)} \right) (1 - a_2) = \infty$$

The key difference between matched-actuator setups and isolated actuator-disks lies in the ability of the former to extract energy from an unbounded amount of fluid. But, even in that extreme case, they continue to extract a modest share of energy from each parcel of fluid that crosses them.

B

INFINITESIMAL STREAMTUBE LEMMAS

B.1. CONSERVATION OF MASS

Proof of Lemma 1, regarding conservation of mass over infinitesimal streamtubes. The key step is the integration of the incompressible continuity equation over infinitesimal streamtubes with the divergence theorem. Consider an open subset $p_a \subset P_a$ and its image through the M^σ map, denoted as p_b :

$$p_b = \{ \mathbf{x}_b \in \mathbb{R}^3 : \mathbf{x}_b = M_{(\mathbf{x}_a)}^\sigma, \forall \mathbf{x}_a \in p_a \}$$

Construct a streamtube $\psi \subset \mathbb{R}^3$ that connects p_a to p_b along the flow streamlines. The streamtube forms a 3-manifold whose boundary $\partial\psi$ can be partitioned into a closed side p_s and two open caps:

$$\partial\psi = p_a \cup p_s \cup p_b$$

Integrate the continuity equation over the ψ volume:

$$\int (\nabla \cdot \mathbf{U}) d\psi = 0$$

Recast the integral with the divergence theorem, and apply the boundary partition with inward pointing normal unit vectors:

$$\begin{aligned} \int (\nabla \cdot \mathbf{U}) d\psi &= \int (\mathbf{U} \cdot \mathbf{n}^{in}) d(\partial\psi) \\ &= \int (\mathbf{U} \cdot \mathbf{n}_a^{in}) d(p_a) + \int (\mathbf{U} \cdot \mathbf{n}_s^{in}) d(p_s) + \int (\mathbf{U} \cdot \mathbf{n}_b^{in}) d(p_b) \end{aligned}$$

The sides of the streamtube p_s follow streamlines, meaning that the flow direction is aligned with the boundary, and hence:

$$\mathbf{x} \in p_s \Rightarrow (\mathbf{U}_{(\mathbf{x})} \cdot \mathbf{n}^{in}) = 0 \quad \Rightarrow \quad \int (\mathbf{U} \cdot \mathbf{n}) d(p_s) = 0$$

The integral of the continuity equation over the streamtube volume can therefore be rewritten as:

$$\int (\mathbf{U} \cdot \mathbf{n}_a^{in}) d(p_a) = - \int (\mathbf{U} \cdot \mathbf{n}_b^{in}) d(p_b)$$

Because it holds for any arbitrary subset of $p_a \subset P_a$, the above equation establishes a relation between differential elements:

$$\left(\mathbf{U}_{(x_a)} \cdot \mathbf{n}_a^{in} \right) dP_a = - \left(\mathbf{U}_{(x_b)} \cdot \mathbf{n}_b^{in} \right) dP_b \quad \text{with } \mathbf{x}_b = M_{(x_a)}^\sigma$$

Switching the orientation of the normal unit vectors to be consistent in terms of flow direction leads to the desired result:

$$\left(\mathbf{U}_{(x_a)} \cdot \mathbf{n}_a \right) dP_a = \left(\mathbf{U}_{(x_b)} \cdot \mathbf{n}_b \right) dP_b$$

B.2. CONSERVATION OF MOMENTUM

Proof of Lemma 2: Rework the convective derivative into the product of the velocity field $\mathbf{U} : \mathbb{R}^3 \rightarrow \mathbb{R}^3$ with its jacobian $J_{\mathbf{U}} : \mathbb{R}^{3 \times 3} \rightarrow \mathbb{R}^3$:

$$(\mathbf{U} \cdot \nabla) \mathbf{U} = \begin{bmatrix} U \frac{\partial U}{\partial x} + V \frac{\partial U}{\partial y} + W \frac{\partial U}{\partial z} \\ U \frac{\partial V}{\partial x} + V \frac{\partial V}{\partial y} + W \frac{\partial V}{\partial z} \\ U \frac{\partial W}{\partial x} + V \frac{\partial W}{\partial y} + W \frac{\partial W}{\partial z} \end{bmatrix} = \begin{bmatrix} \frac{\partial U}{\partial x} & \frac{\partial U}{\partial y} & \frac{\partial U}{\partial z} \\ \frac{\partial V}{\partial x} & \frac{\partial V}{\partial y} & \frac{\partial V}{\partial z} \\ \frac{\partial W}{\partial x} & \frac{\partial W}{\partial y} & \frac{\partial W}{\partial z} \end{bmatrix} \begin{bmatrix} U \\ V \\ W \end{bmatrix} = [J^{\mathbf{U}}] \mathbf{U}$$

Place into the Euler equation, divide both sides by the magnitude of the velocity field $|\mathbf{U}| : \mathbb{R}^3 \rightarrow \mathbb{R}^3$, and integrate over σ :

$$\int [J^{\mathbf{U}}] \frac{\mathbf{U}}{|\mathbf{U}|} d\sigma = - \frac{1}{\rho} \int \frac{\nabla p}{|\mathbf{U}|} d\sigma S + \int \frac{1}{\rho} \frac{\mathbf{f}}{|\mathbf{U}|} d\sigma$$

Given that $\frac{\mathbf{U}}{|\mathbf{U}|}$ corresponds to the unit-vector of the streamline direction, the fundamental theorem of calculus implies that:

$$\int [J^{\mathbf{U}}] \frac{\mathbf{U}}{|\mathbf{U}|} d\sigma = \int [J^{\mathbf{U}}] \mathbf{r} d\sigma = \mathbf{U}_{(x_b)} - \mathbf{U}_{(x_a)}$$

Leading to the desired result:

$$\mathbf{U}_{(x_b)} - \mathbf{U}_{(x_a)} = - \frac{1}{\rho} \int \frac{\nabla p}{|\mathbf{U}|} d\sigma + \frac{1}{\rho} \int \frac{\mathbf{f}}{|\mathbf{U}|} d\sigma$$

Lemma 2 is concerned with conservation of momentum over infinitesimal streamtubes. The key step consists in restating the convective derivative in terms of the Jacobian to apply the fundamental theorem of multivariate calculus. An alternate, and narrower but extremely lengthy, proof is possible by integrating all terms explicitly over a tubular streamtube attached to some arbitrary streamline. The key to that route is to consider that velocity and pressure fields are harmonic and can be developed into convergent Taylor series over vanishingly small balls.

B.3. CONSERVATION OF ENERGY

Proof of Lemma 3: Rewrite fundamental thermodynamic relation into spatial gradients while implementing the isotropy assumption ($ds = 0$):

$$\begin{aligned} ds = 0 &\Rightarrow dh = \frac{1}{\rho} dp \Rightarrow \frac{1}{\rho} \nabla p = \nabla h \\ &\Rightarrow h = \frac{p}{\rho} + \epsilon, \quad \epsilon \in \mathbb{R} \end{aligned}$$

Feed the relation between the static enthalpy h and the static pressure p into the transport equation:

$$(\mathbf{U} \cdot \nabla) \mathbf{U} = -\nabla h + \frac{1}{\rho} \mathbf{f} + \frac{1}{\rho} \mathbf{f}_{visc}$$

Rework the convective derivative with an identity for the double cross-product to obtain a common form of Crocco's theorem:

$$\begin{aligned} (\mathbf{U} \cdot \nabla) \mathbf{U} &= \frac{1}{2} \nabla (\mathbf{U} \cdot \mathbf{U}) - \mathbf{U} \times (\nabla \times \mathbf{U}) = \frac{1}{2} \nabla (\mathbf{U} \cdot \mathbf{U}) - \mathbf{U} \times \boldsymbol{\omega} \\ \mathbf{U} \times \boldsymbol{\omega} &= \nabla \left(h + \frac{1}{2} \mathbf{U} \cdot \mathbf{U} \right) - \frac{1}{\rho} \mathbf{f} \end{aligned}$$

Integrate the streamwise component of Crocco's equation along the streamline segment σ :

$$\int (\mathbf{U} \times \boldsymbol{\omega}) \cdot \mathbf{r}^\sigma d\sigma = \int \nabla \left(h + \frac{1}{2} \mathbf{U} \cdot \mathbf{U} \right) \cdot \mathbf{r}^\sigma d\sigma - \int \left(\frac{1}{\rho} \mathbf{f} \right) \cdot \mathbf{r}^\sigma d\sigma \quad \text{with } \mathbf{r}^\sigma = \frac{\mathbf{U}}{|\mathbf{U}|} \in T_\sigma$$

The tangent unit vector \mathbf{r}^σ is aligned with the flow \mathbf{U} , whose direction is normal to the cross-product of the velocity vector with its curl, $\mathbf{U} \times \boldsymbol{\omega}$:

$$\mathbf{U} \times \boldsymbol{\omega} \perp \mathbf{U} \Rightarrow (\mathbf{U} \times \boldsymbol{\omega}) \cdot \frac{\mathbf{U}}{|\mathbf{U}|} = (\mathbf{U} \times \boldsymbol{\omega}) \cdot \mathbf{r} = 0$$

The integrand of the right hand side term vanishes, but the static enthalpy h and kinetic energy $\frac{1}{2} \mathbf{U} \cdot \mathbf{U}$ integrals stem directly from the fundamental theorem of multivariate calculus:

$$\int \nabla \left(h + \frac{1}{2} \mathbf{U} \cdot \mathbf{U} \right) \cdot \mathbf{r} d\sigma = \left(h + \frac{1}{2} \mathbf{U} \cdot \mathbf{U} \right) \Big|_{x_a}^{x_b}$$

Feed back into Crocco's equation to reach the desired result:

$$\left(h + \frac{1}{2} \mathbf{U} \cdot \mathbf{U} \right) \Big|_{x_a}^{x_b} = \frac{1}{\rho} \int \mathbf{f} \cdot \mathbf{r} d\sigma$$

Lemma 3 is concerned with conservation of energy over infinitesimal streamtubes and has narrower scope than Crocco's theorem. This proof was presented for completeness: it is based on the exposition of [Greitzer et al. \(2004\)](#) to which it adds no value.

B.4. CROSSING OF ACTUATION SURFACE

Proof of Lemma 4: The κ surface can be charted with a bijective map $\mathbf{s}^\kappa_{(\eta,\zeta)} : D^\kappa \subset \mathbb{R}^2 \rightarrow \kappa$, and its normal unit vector can be described as a vector field $\mathbf{n}^\kappa_{(\eta,\zeta)} : D^\kappa \subset \mathbb{R}^2 \rightarrow \mathbb{R}^3$:

$$\mathbf{n}^\kappa_{(\eta,\zeta)} = \frac{\frac{\partial \mathbf{s}^\kappa}{\partial \eta} \times \frac{\partial \mathbf{s}^\kappa}{\partial \zeta}}{\left| \frac{\partial \mathbf{s}^\kappa}{\partial \eta} \times \frac{\partial \mathbf{s}^\kappa}{\partial \zeta} \right|} = \left(\frac{\partial \mathbf{s}^\kappa}{\partial \eta} \times \frac{\partial \mathbf{s}^\kappa}{\partial \zeta} \right) \left(\left| \frac{\partial \mathbf{s}^\kappa}{\partial \eta} \times \frac{\partial \mathbf{s}^\kappa}{\partial \zeta} \right| \right)^{-1}$$

Let us generate a thin actuation volume $\psi \subset \mathbb{R}^3$ surrounding the actuation surface κ with a constant thickness $t \in \mathbb{R}_0^+$:

$$\psi = \left\{ \mathbf{x} \in \mathbb{R}^3 : \mathbf{x} = \mathbf{k} + \tau \mathbf{n}^\kappa, \quad \mathbf{k} \in \kappa, \quad 0 < \tau < t \right\}$$

The actuation volume ψ can be charted with a map $\mathbf{s}^\psi_{(\eta,\zeta,\tau)} : D^\psi \rightarrow \psi$ such that $D^\psi = \{D^{\kappa^j} \times D^\tau\} \subset \mathbb{R}^3$:

$$\mathbf{s}^\psi_{(\eta,\zeta,\tau)} = \mathbf{s}^\kappa_{(\eta,\zeta)} + \tau \mathbf{n}^\kappa_{(\eta,\zeta)} \quad \text{with } D^\tau = [0, t] \subset \mathbb{R}$$

It can be shown that the $\mathbf{s}^\psi_{(\eta,\zeta,\tau)}$ map will be bijective if κ is smooth and t is sufficiently small. Let us now define a surjective map \mathbf{p}^{ψ^κ} projecting D^ψ into its bidimensional counterpart D^κ :

$$\mathbf{p}^{\psi^\kappa} : D^\psi \rightarrow D^\kappa, \quad \mathbf{p}^{\psi^\kappa}_{(\eta,\zeta,\tau)} = (\eta, \zeta)$$

Each point belonging to ψ can be projected into κ by composing \mathbf{s}^κ with \mathbf{p}^{ψ^κ} together with the inverse of \mathbf{s}^ψ , prompting the definition of an additional surjective map $\mathbf{q} : \psi \rightarrow \kappa$:

$$\mathbf{q} = \mathbf{s}^\kappa \circ \left(\mathbf{p}^{\psi^\kappa} \circ \mathbf{s}^{\psi^{-1}} \right) \Rightarrow \mathbf{q}_{(\mathbf{x})} = \mathbf{s}^\kappa \left(\mathbf{p}^{\psi^\kappa} \left(\mathbf{s}^{\psi^{-1}}_{(\mathbf{x})} \right) \right) \in \kappa$$

The body force surface density field $\boldsymbol{\phi} : \kappa \rightarrow \mathbb{R}^3$ can be spread into the thin surrounding volume ψ to define the volume body force vector field $\mathbf{f} : \mathbb{R}^3 \rightarrow \mathbb{R}^3$:

$$\mathbf{f}_{(\mathbf{x})} = \begin{cases} \frac{1}{t} \boldsymbol{\phi}_{(\mathbf{q}_{(\mathbf{x})})} & \mathbf{x} \in \psi \\ 0 & \mathbf{x} \notin \psi \end{cases}$$

In this setup, the $\mathbf{g}_{(\mathbf{x})} \mathbf{f}_{(\mathbf{x})}$ product will be null everywhere but over the intersection between the streamline and the actuation volume $\sigma_\psi = \sigma \cap \psi$, and the integral can be simplified into:

$$\int \mathbf{g}_{(\mathbf{x})} \mathbf{f}_{(\mathbf{x})} d\sigma = \int \mathbf{g}_{(\mathbf{x})} \mathbf{f}_{(\mathbf{x})} d\sigma_\psi \quad \text{with } \sigma_\psi = \sigma \cap \psi$$

When the streamline σ only crosses the actuation surface once, the intersection set $\sigma \cap \psi$ is a simply connected 1-manifold and the volume entry points can be defined as:

$$\mathbf{x}^\kappa \in \partial(\sigma \cap \psi) \cap \kappa, \quad \mathbf{x}^t \in \partial(\sigma \cap \psi) \setminus \kappa$$

The streamline intersection with the actuation volume σ_ψ is a one manifold immersed in \mathbb{R}^n , and it can be charted with an homeomorphism $\mathbf{s}_{(\gamma)}^\sigma : D^\sigma \rightarrow \sigma_\psi \subset \psi$:

$$\mathbf{s}_{(\gamma)}^\sigma = \mathbf{x}^\kappa + \int_0^\gamma \frac{\mathbf{U}(\mathbf{s}_{(\gamma)}^\sigma)}{\left| \mathbf{U}(\mathbf{s}_{(\gamma)}^\sigma) \right|} d\gamma_t \quad , \quad D^\sigma = [0, \gamma_t] \quad \text{with} \quad \gamma_t : \mathbf{s}_{(\gamma_t)}^\sigma = \mathbf{x}^t$$

$$J_{(\gamma)}^{\mathbf{s}^\sigma} = \frac{d\mathbf{s}^\sigma}{d\gamma} = \frac{\mathbf{U}(\mathbf{s}_{(\gamma)}^\sigma)}{\left| \mathbf{U}(\mathbf{s}_{(\gamma)}^\sigma) \right|} = \frac{1}{|\mathbf{U}|} \begin{bmatrix} U \\ V \\ W \end{bmatrix} \in \mathbb{R}^3 \quad \Rightarrow \quad \left| J_{(\gamma)}^{\mathbf{s}^\sigma} \right| = \left| \frac{d\mathbf{s}^\sigma}{d\gamma} \right| = 1 \perp \gamma$$

Alone, the \mathbf{s}^σ homeomorphism is not a very convenient to conduct the integration. We will complement it with an additional set of maps, and start by defining a surjective map $p^{\psi\tau} : D^\psi \rightarrow D^\tau$:

$$p_{(\eta, \zeta, \tau)}^{\psi\tau} = \tau \quad , \quad J^{p^{\psi\tau}} = \nabla p^{\psi\tau} = \begin{bmatrix} 0 & 0 & 1 \end{bmatrix}$$

And use $p^{\psi\tau}$ we can define a map h from $D^\sigma \subset \mathbb{R}$ to $D^\tau \subset \mathbb{R}$ via ψ and D^ψ :

$$\mathbf{h}_{(\gamma)} = p^{\psi\tau} \circ (\mathbf{s}^{\psi^{-1}} \circ \mathbf{s}^\sigma) = p^{\psi\tau} \left(\begin{matrix} \mathbf{s}^{\psi^{-1}} \\ \mathbf{s}_{(\gamma)}^\sigma \end{matrix} \right)$$

In	Transformation	Out
γ	$\mathbf{s}^\sigma : D^\sigma \rightarrow \sigma_\psi \subset \psi$	\mathbf{x}
\mathbf{x}	$\mathbf{s}^{\psi^{-1}} : \psi \rightarrow D^\psi$	(η, ζ, τ)
(η, ζ, τ)	$p^{\psi\tau} : D^\psi \rightarrow D^\tau$	τ

Because h is a composition, its derivative can be written with the chain rule:

$$\begin{aligned} \frac{dh}{d\gamma} &= J \left(p^{\psi\tau} \circ (\mathbf{s}^{\psi^{-1}} \circ \mathbf{s}^\sigma) \right) = J^{p^{\psi\tau}} \left(\begin{matrix} \mathbf{s}^{\psi^{-1}} \\ \mathbf{s}_{(\gamma)}^\sigma \end{matrix} \right) J(\mathbf{s}^{\psi^{-1}} \circ \mathbf{s}^\sigma) \\ &= J^{p^{\psi\tau}} \left(\begin{matrix} \mathbf{s}^{\psi^{-1}} \\ \mathbf{s}_{(\gamma)}^\sigma \end{matrix} \right) \begin{pmatrix} J^{\mathbf{s}^{\psi^{-1}}} J^{\mathbf{s}^\sigma} \end{pmatrix} \in \mathbb{R} \end{aligned}$$

For sufficiently small t , \mathbf{s}^ψ is invertible, and the Jacobian of $\mathbf{s}^{\psi^{-1}}$ can be obtained from the Jacobian of \mathbf{s}^ψ through the inverse function theorem:

$$\left[J^{\mathbf{s}^{\psi^{-1}}} \right] = \left[J^{\mathbf{s}^\psi} \right]^{-1}$$

The Jacobian of $\mathbf{s}_{(\eta, \zeta, \tau)}^\psi$ is a 3×3 matrix whose columns correspond to the map's partial derivatives:

$$\left[J^{\mathbf{s}^\psi} \right] = \left[\begin{array}{ccc} \frac{\partial \mathbf{s}^\psi}{\partial \eta} & | & \frac{\partial \mathbf{s}^\psi}{\partial \zeta} & | & \frac{\partial \mathbf{s}^\psi}{\partial \tau} \end{array} \right] \in \mathbb{R}^{3 \times 3}$$

$$\frac{\partial \mathbf{s}^\psi}{\partial \eta} = \frac{\partial \mathbf{s}^\kappa}{\partial \eta} + \tau \frac{\partial \mathbf{n}}{\partial \eta} \quad , \quad \frac{\partial \mathbf{s}^\psi}{\partial \zeta} = \frac{\partial \mathbf{s}^\kappa}{\partial \zeta} + \tau \frac{\partial \mathbf{n}}{\partial \zeta} \quad , \quad \frac{\partial \mathbf{s}^\psi}{\partial \tau} = \mathbf{n}_{(\eta, \zeta)}^\kappa$$

For any 3×3 matrix, the rows of the inverse correspond to the cross-product of the columns scaled by the inverse of the determinant. The Jacobian of \mathbf{s}^ψ^{-1} can then be written as:

$$\left[J^{\mathbf{s}^\psi} \right]^{-1} = \frac{1}{\det(J^{\mathbf{s}^\psi})} \begin{bmatrix} \frac{\partial \mathbf{s}^\psi}{\partial \zeta} \times \frac{\partial \mathbf{s}^\psi}{\partial \tau} \\ - \\ \frac{\partial \mathbf{s}^\psi}{\partial \tau} \times \frac{\partial \mathbf{s}^\psi}{\partial \eta} \\ - \\ \frac{\partial \mathbf{s}^\psi}{\partial \eta} \times \frac{\partial \mathbf{s}^\psi}{\partial \zeta} \end{bmatrix} \quad \text{with} \quad \det(J^{\mathbf{s}^\psi}) = \left(\frac{\partial \mathbf{s}^\psi}{\partial \eta} \times \frac{\partial \mathbf{s}^\psi}{\partial \zeta} \right) \cdot \frac{\partial \mathbf{s}^\psi}{\partial \tau}$$

So that the derivative of h can be stated explicitly:

$$\frac{dh}{d\gamma} = \begin{bmatrix} 0 & 0 & 1 \end{bmatrix} \left(\frac{1}{\det(J^{\mathbf{s}^\psi})} \begin{bmatrix} \frac{\partial \mathbf{s}^\psi}{\partial \zeta} \times \frac{\partial \mathbf{s}^\psi}{\partial \tau} \\ \frac{\partial \mathbf{s}^\psi}{\partial \tau} \times \frac{\partial \mathbf{s}^\psi}{\partial \eta} \\ \frac{\partial \mathbf{s}^\psi}{\partial \eta} \times \frac{\partial \mathbf{s}^\psi}{\partial \zeta} \end{bmatrix} \frac{d\mathbf{s}^\sigma}{d\gamma} \right) = \frac{\left(\frac{\partial \mathbf{s}^\psi}{\partial \eta} \times \frac{\partial \mathbf{s}^\psi}{\partial \zeta} \right) \cdot \frac{d\mathbf{s}^\sigma}{d\gamma}}{\left(\frac{\partial \mathbf{s}^\psi}{\partial \eta} \times \frac{\partial \mathbf{s}^\psi}{\partial \zeta} \right) \cdot \frac{\partial \mathbf{s}^\psi}{\partial \tau}}$$

If the streamline does not revert inside the actuation volume, $\mathbf{h} : D^\sigma \rightarrow D^\tau$ will be an homeomorphism and its inverse exists $\mathbf{h}^{-1} : D^\tau \rightarrow D^\sigma$. In these conditions the streamline can be charted with a function composition $\mathbf{s}^{\tau\sigma} : D^\tau \rightarrow \sigma_\psi$ defined as:

$$\mathbf{s}^{\tau\sigma} = \mathbf{s}^\sigma \circ \mathbf{h}_{(\tau)}^{-1} \quad . \quad \mathbf{s}_{(\tau)}^{\tau\sigma} = \mathbf{s}^\sigma_{(\mathbf{h}_{(\tau)}^{-1})}$$

Using the inverse function theorem to obtain a Jacobian for $\mathbf{h}_{(\tau)}^{-1}$:

$$\frac{d\mathbf{s}^{\tau\sigma}}{d\tau} = \frac{d\mathbf{s}^\sigma}{d\gamma} \Big|_{\gamma=\mathbf{h}_{(\tau)}^{-1}} \frac{d\mathbf{h}^{-1}}{d\tau} \Big|_{\tau} = \frac{d\mathbf{s}^\sigma}{d\gamma} \Big|_{\gamma=\mathbf{h}_{(\tau)}^{-1}} \left(\frac{d\mathbf{h}}{d\gamma} \Big|_{\gamma=\mathbf{h}_{(\tau)}^{-1}} \right)^{-1}$$

And recalling that the original streamline chart \mathbf{s}^σ was normalized leads to:

$$\Rightarrow \quad \left| \frac{d\mathbf{s}^{\tau\sigma}}{d\tau} \right| = \frac{\left| \frac{d\mathbf{s}^\sigma}{d\gamma} \Big|_{\gamma=\mathbf{h}_{(\tau)}^{-1}} \right|}{\frac{d\mathbf{h}}{d\gamma} \Big|_{\gamma=\mathbf{h}_{(\tau)}^{-1}}} = \frac{1}{\frac{d\mathbf{h}}{d\gamma} \Big|_{\gamma=\mathbf{h}_{(\tau)}^{-1}}}$$

So that the integral can be restated with the variable change theorem:

$$\begin{aligned} \int \mathbf{g}_{(x)} \mathbf{f}_{(x)} d\sigma_\psi &= \int_0^t \mathbf{g}_{(\mathbf{s}_{(\tau)}^{\tau\sigma})} \mathbf{f}_{(\mathbf{s}_{(\tau)}^{\tau\sigma})} \left| \frac{d\mathbf{s}^{\tau\sigma}}{d\tau} \right| d\tau \\ &= \frac{1}{t} \int_0^t \left(\frac{\mathbf{g}_{(\mathbf{s}_{(\tau)}^{\tau\sigma})} \Phi(\mathbf{q}_{(\mathbf{s}_{(\tau)}^{\tau\sigma}))}}{\frac{d\mathbf{h}}{d\gamma} \Big|_{\gamma=\mathbf{h}_{(\tau)}^{-1}}} \right) d\tau \end{aligned}$$

Expand the integrand into a Taylor series in around $\tau = 0$, in which case $\mathbf{s}_{(\tau=0)}^{\tau\sigma} = \mathbf{x}^k$ and $\gamma = \mathbf{h}_{(\tau=0)}^{-1} = 0$:

$$\frac{\mathbf{g}\left(\mathbf{s}_{(\tau)}^{\tau\sigma}\right)\boldsymbol{\phi}\left(\mathbf{q}\left(\mathbf{s}_{(\tau)}^{\tau\sigma}\right)\right)}{\left.\frac{dh}{d\gamma}\right|_{\gamma=\mathbf{h}_{(\tau)}^{-1}}} = \frac{\mathbf{g}\left(\mathbf{x}^k\right)\boldsymbol{\phi}\left(\mathbf{x}^k\right)}{\left.\frac{dh}{d\gamma}\right|_0} + O(\tau)$$

Feed the Taylor series expansion into the integral:

$$\int \mathbf{g}\left(\mathbf{x}\right)\mathbf{f}\left(\mathbf{x}\right)d\sigma_{\psi} = \frac{1}{t} \int_0^t \left(\frac{\mathbf{g}\left(\mathbf{x}^k\right)\boldsymbol{\phi}\left(\mathbf{x}^k\right)}{\left.\frac{dh}{d\gamma}\right|_0} + O(\tau) \right) d\tau = \frac{\mathbf{g}\left(\mathbf{x}^k\right)\boldsymbol{\phi}\left(\mathbf{x}^k\right)}{\left.\frac{dh}{d\gamma}\right|_0} + O(t)$$

And have the thickness of the actuation volume tend to zero:

$$\lim_{t \rightarrow 0} \int \mathbf{g}\left(\mathbf{x}\right)\mathbf{f}\left(\mathbf{x}\right)d\sigma_{\psi} = \frac{\mathbf{g}\left(\mathbf{x}^k\right)\boldsymbol{\phi}\left(\mathbf{x}^k\right)}{\left.\frac{dh}{d\gamma}\right|_0}$$

The derivative of the h map at the surface intersection point is stated as:

$$\left.\frac{dh}{d\gamma}\right|_0 = \frac{\left(\left.\frac{\partial \mathbf{s}^{\psi}}{\partial \eta}\right|_{(\eta,\zeta,0)} \times \left.\frac{\partial \mathbf{s}^{\psi}}{\partial \zeta}\right|_{(\eta,\zeta,0)} \right) \cdot \left.\frac{d\mathbf{s}^{\sigma}}{d\gamma}\right|_{\gamma=0}}{\left(\left.\frac{\partial \mathbf{s}^{\psi}}{\partial \eta}\right|_{(\eta,\zeta,0)} \times \left.\frac{\partial \mathbf{s}^{\psi}}{\partial \zeta}\right|_{(\eta,\zeta,0)} \right) \cdot \left.\frac{\partial \mathbf{s}^{\psi}}{\partial \tau}\right|_{(\eta,\zeta,0)}}$$

To rework it into a convenient format, observe that:

$$\begin{aligned} \left.\frac{d\mathbf{s}^{\sigma}}{d\gamma}\right|_{\gamma=0} &= \frac{\mathbf{U}\left(\mathbf{x}^k\right)}{\left|\mathbf{U}\left(\mathbf{x}^k\right)\right|} \quad , \quad \left.\frac{\partial \mathbf{s}^{\psi}}{\partial \tau}\right|_{(\eta,\zeta,0)} = \mathbf{n}_{(\eta,\zeta)}^k \\ \left.\frac{\partial \mathbf{s}^{\psi}}{\partial \eta}\right|_{(\eta,\zeta,0)} &= \frac{\partial \mathbf{s}^k}{\partial \eta} \quad , \quad \left.\frac{\partial \mathbf{s}^{\psi}}{\partial \zeta}\right|_{(\eta,\zeta,0)} = \frac{\partial \mathbf{s}^k}{\partial \zeta} \end{aligned}$$

Feed back into the expression for the derivative of the h map, together with the definition of the surface normal unit vector $\mathbf{n}_{(\eta,\zeta)}^k$:

$$\left.\frac{dh}{d\gamma}\right|_0 = \frac{\left(\frac{\partial \mathbf{s}^k}{\partial \eta} \times \frac{\partial \mathbf{s}^k}{\partial \zeta} \right) \cdot \left(\frac{\mathbf{U}\left(\mathbf{x}^k\right)}{\left|\mathbf{U}\left(\mathbf{x}^k\right)\right|} \right)}{\left(\frac{\partial \mathbf{s}^k}{\partial \eta} \times \frac{\partial \mathbf{s}^k}{\partial \zeta} \right) \cdot \left(\frac{\frac{\partial \mathbf{s}^k}{\partial \eta} \times \frac{\partial \mathbf{s}^k}{\partial \zeta}}{\left| \frac{\partial \mathbf{s}^k}{\partial \eta} \times \frac{\partial \mathbf{s}^k}{\partial \zeta} \right|} \right)} = \mathbf{n}_{(\eta,\zeta)}^k \cdot \left(\frac{\mathbf{U}\left(\mathbf{x}^k\right)}{\left|\mathbf{U}\left(\mathbf{x}^k\right)\right|} \right)$$

Insert into the limit of the integral to obtain the desired result:

$$\lim_{t \rightarrow 0} \int \mathbf{g}\left(\mathbf{x}\right)\mathbf{f}\left(\mathbf{x}\right)d\sigma_{\psi} = \frac{\mathbf{g}\left(\mathbf{x}^k\right)\boldsymbol{\phi}\left(\mathbf{x}^k\right)}{\mathbf{n}_{(\eta,\zeta)}^k \cdot \mathbf{U}\left(\mathbf{x}^k\right)} \left|\mathbf{U}\left(\mathbf{x}^k\right)\right|$$

Lemma 4 is applicable to arbitrary actuation surfaces, which can be curved and exert both normal or tangential forces. A much simpler line of proof based on geometric arguments exists for planar actuator disks that only axial forces. The added value of lemma 4 is that it enables consideration of complex geometries like convex or concave actuator disks representing the effect rotor coning and blade deformation.

B.5. CONSISTENCY WITH MACROSCOPIC MODELS

B.5.1. POWER COEFFICIENT OF ENTIRE ACTUATOR-DISK

The total force (F_a) that the actuator-disk exerts on the flow corresponds to the integral its loading density (ϕ_a) over its surface $\Omega_a \subset \mathbb{R}^3$:

$$F_a = \int \phi_a d\Omega_a = \frac{1}{2} \rho U_o^2 \int C_{\phi_a} d\Omega_a \quad , \quad C_{F_a} = \frac{F_a}{\frac{1}{2} \rho U_o^2 S_a} = \frac{\int C_{\phi_a} d\Omega_a}{\int d\Omega_a}$$

Total power transfer between the actuator and the flow (P) consists in the sum of infinitesimal power exchanges dP across all infinitesimal streamtubes crossing the actuation surface Ω_a . It is obtained by integrating expression 4.19 over the actuation surface $\Omega_a \subset \mathbb{R}^3$:

$$\begin{aligned} P &= \int dP = \int \phi_a(\eta, \zeta) U_a(\eta, \zeta) d\Omega_a \\ &= \frac{1}{2} \rho U_o^3 \int \left(\frac{\phi_a(\eta, \zeta)}{\frac{1}{2} \rho U_o^2} \right) \left(\frac{U_a(\eta, \zeta)}{U_o} \right) d\Omega_a \end{aligned} \quad (\text{B.1})$$

A global power coefficient C_P is now defined with the area of the complete actuator S_a as a reference:

$$C_P = \frac{P}{\frac{1}{2} \rho U_o^3 S_a} \quad , \quad S_a = \int d\Omega_a$$

Rework with expression B.1 and identify the relation with the power coefficient at the local level, expressions 4.19 and :

$$\begin{aligned} C_P &= \frac{\int \left(\frac{\phi_a}{\frac{1}{2} \rho U_o^2} \right) \left(\frac{U_a}{U_o} \right) d\Omega_a}{\int d\Omega_a} = \frac{\int C_{\phi_a} u_a d\Omega_a}{\int d\Omega_a} = \frac{\int C^{dP} d\Omega_a}{\int d\Omega_a} \\ &= \frac{1}{\int d\Omega_a} \int \left(\frac{1}{2} \left(1 + \sqrt{C_{\phi_a} + 1} \right) (C_{\phi_a} - C_{\phi_b}) \right) d\Omega_a \end{aligned} \quad (\text{B.2})$$

PARTICULAR CASE FOR HOMOGENEOUSLY LOADED ACTUATOR

For the particular case of constant loading distribution actuators, $C_{\phi_a \perp}(\eta, \zeta)$, the wake has constant terminal speed:

$$\phi_a \perp \mathbf{x} \in \Omega_a \quad \Rightarrow \quad u_e \perp \mathbf{x} \in \Omega_a \quad \Rightarrow \quad C_{F_a} = C_{\phi_a} = u_e^2 - 1$$

The integral of expression B.2 is then simplified:

$$C_{\bar{P}} = \frac{1}{2} \left(1 + \sqrt{C_{\phi_a} + 1} \right) \left(C_{\phi_a} - \frac{\int C_{\phi_b} d\Omega_a}{\int d\Omega_a} \right)$$

Prompting the identification of the interaction coefficient C_{F_b} and its dimensional version F_b , whose units correspond to those of a force:

$$C_{F_b} = \frac{\int C_{\phi_b} d\Omega_a}{\int d\Omega_a} = \frac{\int \phi_b d\Omega_a}{\frac{1}{2} \rho U_o^2 S_a} = \frac{F_b}{\frac{1}{2} \rho U_o^2 S_a} \quad , \quad F_b = \int \phi_b d\Omega_a \quad (\text{B.3})$$

Through which the global power coefficient of a constant loading actuator with a nearby body is written exactly:

$$\begin{aligned}
 C_{\bar{p}} &= \frac{1}{2} \left(1 + \sqrt{C_{F_a} + 1} \right) (C_{F_a} - C_{F_b}) \\
 &= \frac{1}{2} (1 + u_e) ((u_e^2 - 1) - C_{F_b})
 \end{aligned} \tag{B.4}$$

Quite expectably, equation B.4 is identical the power coefficient law of de Vries, deduced with a more conventional procedure in section 3.1. It serves as an incomplete verification for the consistency of the infinitesimal streamtube formulation against well established analytical approaches.

C

DISCRETIZATION OF VORTEX-MIXING EQUATION

The finite-difference approximation of equation 10.17 is stated in terms of discrete gradient (∇_{ij}^{yz}) and laplacian (Δ_{ij}^{yz}) operators over regular crossflow meshes $\{(Y_{ij}, Z_{ij})\}$:

$$\frac{D\tilde{U}_{ij}}{DT_x} + \left((\tilde{V}_{ij}, \tilde{W}_{ij}) \cdot \nabla_{ij}^{yz} \right) \tilde{U}_{ij} = (v + v_t) \Delta_{ij}^{yz} \tilde{U}_{ij} - \left((\tilde{V}_{ij}, \tilde{W}_{ij}) \cdot \nabla_{ij}^{yz} \right) \tilde{U}_{ij}$$
$$with \quad \begin{cases} \tilde{V}_{ij} = \tilde{V}_{(X, Y_{ij}, Z_{ij})} \\ \tilde{W}_{ij} = \tilde{W}_{(X, Y_{ij}, Z_{ij})} \end{cases} \quad (C.1)$$

First-order central difference operators were chosen for their robustness [Kuzmin \(2010\)](#). Domain boundaries were handled with single-sided differences and Neumann flow periodicity conditions were explicitly enforced. A lagrangian perspective is adopted for the streamwise coordinate which is then treated like a time [Kunik \(1986\)](#). Expression 10.10 establishes a first-order accurate correspondence between forward steps in time (ΔT_x) and space (ΔX):

$$\left(\tilde{U}_{ij}^n + \tilde{U}_{ij}^n \right) \Delta T_x = \Delta X \quad (C.2)$$

Superscript (n) denotes the current time step within the framework of a first-order explicit Euler scheme (C.3):

$$\begin{cases} \tilde{U}_{ij}^{n+1} = \tilde{U}_{ij}^n + \frac{D\tilde{U}_{ij}^n}{DT_x} \Delta T_x \\ \frac{D\tilde{U}_{ij}^n}{DT_x} = (v + v_t) \Delta_{ij}^{yz} \tilde{U}_{ij}^n - \left((\tilde{V}_{ij}^n, \tilde{W}_{ij}^n) \cdot \nabla_{ij}^{yz} \right) \tilde{U}_{ij}^n - \left((\tilde{V}_{ij}^n, \tilde{W}_{ij}^n) \cdot \nabla_{ij}^{yz} \right) \tilde{U}_{ij}^n \end{cases} \quad (C.3)$$

Streamwise time steps ΔT_x were capped to respect a Courant-Friedrichs-Lewy condition [Courant et al. \(1967\)](#) based on crossflow mesh spacing and vortical velocities. Artificial diffusion can be added to maintain modest Peclet mesh numbers [Kuzmin \(2010\)](#)

but has negligible impact on obtained solutions. A domain spanning the $Y \in [0, 4\delta_{ref}]$ by $Z \in [-2S, 2S]$ range with 101×101 points was found to provide sufficient mesh independence. Coarse meshes are acceptable because the finite-difference method only applies to the interaction field (\hat{U}) and induces no diffusion of vortex cores or of the shear layer.

REFERENCES

- Wind in power - 2009 European Statistics*. EWEA, 2010. [1](#)
- Ira H. Abbott, Albert E. von Doenhoff, and Louis Stivers. Summary of airfoil data. Technical report, NACA TR 824, January 1945. [9.2.1](#)
- Imad Abdallah, Anand Natarajan, and John Dalsgaard Sorensen. Impact of uncertainty in airfoil characteristics on wind turbine extreme loads. *Renewable Energy*, 75:283–300, 2015. [9](#)
- J.F.H. Acero, O. Probst, and P.E. Rethore. A review of methodological approaches for the design and optimization of wind farms. *Energies*, 7:6930–7016, 2014. [2](#)
- U. Ahrens, M. Diehl, and R. Schmehl, editors. *Airborne Wind Energy*. Springer, 2013. [1.1](#)
- P.H. Alfredsson and A. Segalini. Wind farms in complex terrains: an introduction. *Philosophical Transactions of the Royal Society A*, 375(2091), 2017. [3](#)
- D. Althaus. The influence of dissipation laws on the calculation of turbulent boundary layers with pressure rise. *Zeitschrift Flugwissenschaften und Weltraumforschung*, 17: 253–256, 1993. [9](#), [9.1.1](#), [9.2](#)
- P. Argyle, S. Watson, C. Montavon, I. Jones, and M. Smith. Turbulence intensity within large offshore wind farms. In *EWEA 2015 Conference Proceedings*, 2015. [7](#)
- J. Arnqvist. *Mean Wind and Turbulence Conditions over Forests*. PhD thesis, Uppsala Universitet, 2013. [7](#)
- VESTAS AS. *Vestas 2 MW platform reaches 20,000 installed turbines globally*. Vestas AS News Release, 2017. [1](#)
- T. Ashuri. *Beyond Classical Upscaling: Integrated Aeroservoelastic Design and Optimization of Large Offshore Wind Turbines*. PhD thesis, Delft University of Technology, 2012. [8.3](#)
- D. Astolfi, F. Castellani, and L. Terzi. A study of wind turbine wakes in complex terrain through rans simulations and scada. *Journal of Solar Energy Engineering*, 140(031001), 2018. [2](#)
- C. Bak, P.B. Andersen, H.A. Madsen, M. Gaunaa, P. Fuglsang, and S. Bove. Design and verification of airfoils resistant to surface contamination and turbulence intensity. *26th AIAA Applied Aerodynamics Conference, Honolulu, USA*, 2008. [7](#), [7.2.5](#)

- C. Bak, W. Skrzypiński, A. Fischer, M. Gaunaa, N. F. Brønnum, and E. K. Kruse. Wind tunnel tests of an airfoil with 18pc relative thickness equipped with vortex generators. *Journal of Physics: Conference Series*, 1037(022044), 2018. [10](#)
- D. Baldacchino, D. Ragni, C.S. Ferreira, and G.J.W. Van Bussel. Towards integral boundary layer modelling of vane-type vortex generators. In *45th AIAA Fluid Dynamics Conference*, volume AIAA 2015-3345, 2015. [10.4](#), [10.5](#), [10.7](#), [10.1](#), [10.3](#), [10.3.1](#), [10.4.2](#)
- B. Baldwin and H. Lomax. Thin-layer approximation and algebraic model for separated turbulent flows. In *16th Aerospace Sciences Meeting, AIAA1978-0257*, 1978. [10.2.3](#)
- World Bank/OECD/IEA. World bank data portal. Technical report, World Bank, 2018. [8.4](#)
- M.F. Barone, J.A. Fike, K.S. Chowdhary, J. Ling, and S. Martin. Machine learning models of errors in large eddy simulation predictions of surface pressure fluctuations. In *47th AIAA Fluid Dynamics Conference*, 2017. [9](#)
- M. Bastankhah and F. Porte-Agel. Experimental and theoretical study of wind turbine wakes in yawed conditions. *Journal of Fluid Mechanics*, 806:506–541, 2017. [2](#)
- G. K. Batchelor. *An Introduction to Fluid Dynamics*. Cambridge University Press, 1967. [2.1.1](#), [2.2.3.2](#), [5.3.2](#)
- J. T. Beale, T. Kato, and A. Majda. Remarks on the breakdown of smooth solutions for the 3-d euler equations. *Communications in Mathematical Physics*, 94:61–66, 1984. [2.2.3.2](#), [2.2.4.2](#)
- E.E. Bender, B.H. Anderson, and P.J. Yagle. Vortex generator modelling for navier-stokes codes. In *3rd ASME/JSM E Joint Fluids Engineering Conference*, volume FEDSM99-6919, 1999. [10](#)
- S. Bernardy. Investigation into the effects of turbulence in thermals on sailplane airfoil performance. Master's thesis, Delft University of Technology, 2002. [6](#), [6.3](#)
- F. P. Bertolotti. Effect of atmospheric turbulence on a laminar boundary-layer. *XXVI OSTIV Congress, Bayreuth, Germany*, 1999. [6.3](#)
- A. Betz. Schraubenpropeller mit geringstem energieverlust. *Nachrichten von der Gesellschaft der Wissenschaften zu Göttingen, Mathematisch-Physikalische Klasse*, 2, 1919. [II](#), [2](#), [4](#)
- A. Betz. Das maximum der theoretisch ausnuetzung de windes durch windmotoren. *Zeitschrift fuer das gesamte Turbinenwesen*, 26:307–309, 1920. [2](#), [2.2](#), [2.2.2.1](#), [2.3.1](#), [4](#)
- A. Betz. Propellers questions. *NACA*, 1929a. [2.4](#), [3](#)
- A. Betz. Energieumsetzungen in venturidusen. *Die Naturwissenschaften*, 10:160–164, 1929b. [II](#)
- G. Birkhoff. *Hydrodynamics: a study in logic, fact and similitude*. Princeton University Press, 1960. [2.2.3.2](#), [2.2.4.2](#), [3.2](#)

- Anders Bjorck. Coordinates and calculations for the ffa-w1-xxx, ffa-w2-xxx and ffa-w3-xxx series of airfoils for horizontal axis wind turbines. Technical report, Flygtekniska Forsöksanstalten, FFA TN 1990-15, 1990. [7.3](#)
- H. Blasius. The boundary layer in fluids with little friction. Technical report, NACA TM 1256, 1950. [9.1.1](#)
- M. Blaug. The fundamental theorems of modern welfare economics, historically contemplated. *History of Political Economy*, 39(2), 2007. [1.3](#)
- L. L. M. Boermans. Improvement of sailplane climb performance by airfoil design. *XXIX Ostiv Congress, Lusse-Berlin, Germany*, 2008. [6](#), [6.3](#), [8.1.2](#)
- R. Bontempo. *The Nonlinear Actuator Disk Method as Applied to Open and Ducted Rotors*. PhD thesis, University of Naples Federico II, 2014. [3](#)
- R. Bontempo and M. Manna. A nonlinear and semi-analytical actuator disk method accounting for general hub shapes. part 1. open rotor. *Journal of Fluid Mechanics*, 792:910–935, 2016. [2](#), [4](#), [4.3.3](#)
- K. Boorsma, A. Muñoz, B. Méndez, S Gómez, A Irisarri, X Munduate, MG Sieros, P Chaviaropoulos, S Voutsinas, J Prospathopoulos, M Manolesos, WZ Shen, WJ Zhu, and H.A. Madsen. *New airfoils for high rotational speed wind turbines*. InnWind.EU Deliverable 2.12, 2015. [7](#)
- S.T. Bose and G.I. Park. Wall-modeled large-eddy simulation for complex turbulent flows. *Annual Review of Fluid Mechanics*, 50:535–561, 2018. [9](#)
- C.L. Bottasso and M. Muskulus. Design methods. In *Long-term research challenges in wind energy - A research agenda by the EAWE*, edited by G. van Kuik and J. Peinke, 2017. [IV](#)
- P. Bradshaw. The response of a constant-pressure turbulent boundary layer to the sudden application of an adverse pressure gradient. Technical report, British ARC RM 3575, 1969. [9.1.1](#)
- P. Bradshaw. Turbulent secondary flows. *Ann. Rev. Fluid Mechanics*, 19:53–74, 1987a. [10](#), [10.3](#)
- V. Brederode. *Aerodinamica Incompressivel: Fundamentos*. Lisboa: IST Press, 2014. [5](#)
- M. L. Buhl. A new empirical relationship between thrust coefficient and induction factor for the turbulent windmill state. Technical Report TP-500-36834, NREL, 2005. [2.2.3.2](#), [8.1.4](#)
- T. Burton, D. Sharpe, N. Jenkins, and E. Bossanyi. *Wind Energy Handbook*. Wiley, New York, 2002. [2](#), [2.2.3.2](#), [2.3.1](#), [4](#)
- R.H. Byrd, M. E. Hribar, and J. Nocedal. An interior algorithm for large scale nonlinear programming. *ACM*, 1997. [8.1.4](#), [9.2.4](#)

- J.S. Carlton. *Marine Propellers and Propulsion*. Butterworth-Heinemann, 2007. 3
- Ralph Carmichael. Algorithm for calculating coordinates of cambered naca airfoils at specified chord locations. In *1st AIAA, Aircraft, Technology Integration, and Operations Forum*, 2011. 9.2.1
- L. Castillo and X. Wang. Similarity analysis for nonequilibrium turbulent boundary layers. *Journal of Fluids Engineering*, 2004. 9.1.1
- G.T. Chapman and M. Tobak. Observations, theoretical ideas and modeling of turbulent flows - past, present and future. Technical Memorandum 86679, Nasa, 1985. 9
- P. Chaviaropoulos, N. Sørensen, M. Hansen, I. Nikolaou, K. Aggelis, J. Johansen, and M. Gaunaa. Viscous and aeroelastic effects on wind turbine blades. the viscel project. part ii: aeroelastic stability investigations. *Wind Energy*, 6(4):387–403, 2003. 8.3
- A. J. Chorin. New perspectives in turbulence. *Quarterly of applied mathematics*, 1998. 9.1.1
- F. Clauser. Turbulent boundary layers in adverse pressure gradients. *Journal of Aeronautical Sciences*, 21, 1954. 9.1.1, 9.2, 9.3.2
- H. Coanda, 1910. 3
- R. P. Coleman, A. M. Feingold, and C. W. Stempin. Evaluation of the induced-velocity field of an idealized helicopter rotor. Technical Report ARR L5E10, NACA, 1945. 2, 4
- D. Coles. The law of the wake in the turbulent boundary layer. *Journal of Fluid Mechanics*, 1956. 9.1.1, 9.3.2, 10.3.1
- J. T. Conway. Analytical solutions for the actuator disk with variable radial distribution of load. *Journal of Fluid Mechanics*, 297:327–355, 1995. 4, 4.3.3
- G. P. Corten and P. Schaak. Heat and flux : Increase of wind farm production by reduction of the axial induction. In *European Wind Energy Conference, Madrid*, 2003. 2
- G. P. Corten, K. Lindenburg, and P. Schaak. Assembly of energy flow collectors, such as windpark, and method of operation, 2004. 2
- G. H. Cottet and P. Koumoutsakos. *Vortex Methods - Theory and Practice*. Cambridge University Press, 2000. 2.3.2.1, 10.1.4, 10.2.2.2
- R. Courant, K. Friedrichs, and H. Lewy. On the partial difference equations of mathematical physics. *IBM J. of Res. and Dev.*, 11(2):215–234, 1967. C
- J. Cousteix and J. Mauss. *Asymptotic Analysis and Boundary Layers*. Springer, 2007. 5, 10.1.1
- J.A.C. Falcao de Campos. *On the calculation of ducted propeller performance in axisymmetric flows*. PhD thesis, Delft University of Technology, 1983. 2.3.2.1

- M de Lellis, R Reginatto, R Saraiva, and A Trofino. The betz limit applied to airborne wind energy. *Renewable Energy*, 128:32–40, 2018. [5.2](#)
- G. de Oliveira. Wind turbine airfoils with boundary layer suction, a novel design approach. *Msc Thesis, Delft University of Technology*, 2011. [7](#), [7.1](#), [7.1.1](#)
- G. de Oliveira, R. B. Pereira, D. Ragni, and F. Avallone. How does the presence of a body affect the performance of an actuator disk ? *J. of Physics: Conf. Series*, 753(022005), 2016. [2.2.1.1](#), [2.3.2.1](#)
- G. de Oliveira, M. Kotsonis, and B. Van Oudheusden. Laminar boundary layer flow with dbd plasma actuation: a similarity equation. In *Boundary and Interior Layers BAIL 2016*, number 120 in Springer Lecture Notes in Computational Science and Engineering, 2017. [9.1.1](#), [10.2.1](#)
- G. de Oliveira, V. Dighe, D. Ragni, F. Avallone, and G. J. W. Van Bussel. Numerical solution of complex actuator disk flows in vorticity formulation. *Wind Energy Science (submitted)*, 2018a. [2.3.2.1](#)
- O. De Vries. *Fluid Dynamic Aspects of Wind Energy Conversion*. AGARD, Brussels, 1979. [2](#), [3](#), [3.1](#), [3.1](#), [3.1.2](#), [3.2.1](#), [3.4](#), [4](#)
- G. Di Cicca, G. Iuso, P. Spazzini, and M. Onorato. Piv study of the influence of large-scale streamwise vortices on a turbulent boundary layer. *Experiments in Fluids*, 33(5): 663–669, 2002. [10.3](#)
- V. Dighe, G. de Oliveira, F. Avallone, and G. J. W. Van Bussel. On the effects of the shape of the duct for ducted wind turbines. In *AIAA Scitech 2018 conference, Kissimee, FL*, number 2018-0997, 2018a. [2.3.2.1](#), [3.2.1](#), [3.3.2](#)
- V.V. Dighe, G. de Oliveira, F. Avallone, and G. J. W. Van Bussel. Towards improving the aerodynamic performance of a ducted wind turbine: A numerical study. *Journal of Physics: Conference Series*, 2018b. [2.3.2.1](#), [3.3.2](#)
- V.V. Dighe, G. de Oliveira, F. Avallone, and G.J.W. van Bussel. Characterization of aerodynamic performance of ducted wind turbines: A numerical study. *Wind Energy (submitted)*, 2018c. [3.3.2](#)
- E. Dobbinga. Grondslagen voor het ontwerp van een grenslaagtunnel. Technical report, TH-Delft Vliegtuigbouwkunde 126, 1968. [10.3](#)
- G. Dragomir, A. Serban, G. Nastase, and A. I. Brezeanu. Wind energy in romania: A review from 2009 to 2016. *Renewable and Sustainable Energy Reviews*, 2016. [7](#)
- C. Draxl and G. J. Mayr. Meteorological wind energy potential in the alps using era40 and wind measurement sites in the tyrolean alps. *Wind Energy*, 2010. [7](#)
- M. Drela. Xfoil: An analysis and design system for low reynolds number airfoils. In *Low Reynolds Number Aerodynamics*, number 54 in Lecture Notes in Engineering. Springer-Verlag, 1989b. [9](#)

- M. Drela and M. B. Giles. Viscous-inviscid analysis of transonic and low reynolds number airfoils. *AIAA Journal*, 25(10):1347–1355, 1987. [9.1.1](#), [9.1.1](#), [10](#), [10.2.1](#)
- D.Tavernier, D.Baldacchino, and C.Ferreira. An integral boundary layer engineering model for vortex generators implemented in xfoil. *Wind Energy*, 2018. [10](#)
- J.C. Dudek. Modeling vortex generators in the wind-us code. In *48th AIAA Aerospace Sciences Meeting*, volume AIAA-2010-32, 2010. [10](#)
- K. Durasaimy, A.P. Singh, and S. Pan. Augmentation of turbulence models using field inversion and machine learning. In *55th AIAA Aerospace Sciences Meeting*, 2017. [9](#)
- P.A. Durbin. Some recent developments in turbulence closure modeling. *Annual Review of Fluid Mechanics*, 50:77–103, 2018. [9](#)
- ECORYS. *Study on challenges in the commercialisation of airborne wind energy*. DG Research and Innovation (European Union), 2018. [1.1](#)
- A. H. El-din and A. Diab. A preliminary study of the blade erosion of a wind turbine operating in a dusty environment. In *ASME Turbo Expo 2016, Seoul*, 2016. [7](#)
- G. Emanuel. *Analytical fluid dynamics*. CRC Press, Boca Raton, 2001. [9.1.1](#)
- R. Eppler. Some new airfoils. *Universitat Stuttgart*, 1979. [7](#), [7.2.5](#)
- Richard Eppler and Dan M. Somers. A computer program for the design and analysis of low-speed airfoils. Technical report, NASA TM-80210, 1980. [9.3.2](#)
- ETIP. *Strategic research and innovation agenda 2016*. ETIP Wind, 2016. [1.1](#)
- L. Euler. Principes généraux du mouvement des fluides. *Mémoires de l'Académie des Sciences de Berlin*, 11:274–315, 1757. [2.1.1](#)
- EWEA. *Wind energy - the facts : a guide to the technology, economics and future of wind power*. European Wind Energy Association, 2009. [1](#)
- V.M. Falkner and S.W. Skan. Solutions of the boundary layer equations. *Philosophical Magazine*, 12(80):865–896, 1931. [9.1.1](#), [10.2.1](#)
- P.A. Farrell, A.F. Hegarty, J.J.H. Miller, E. O’riordan, and G.I. Shishkin. *Robust computational techniques for boundary layers*. Chapman Hall/CRC Press, Boca Raton, 2000. [9.1.1](#)
- A. M. Feldman and R. Serrano. *Welfare economics and social choice theory*. Springer, 2006. [1.3](#)
- U. Fernandez-Gamiz, G. Zamorano, and E. Zulueta. Computational study of the vortex path variation with vg heigh. *J. Phys. Conf. Ser.*, 524:012024, 2014. [10](#)
- U. Fernandez-Gamiz, C.M. Velte, P.E. Rethore, N.N. Sorensen, and E. Egusquiza. Testing of self-similarity and helical symmetry in vortex generator flow simulations. *Wind Energy*, 19:1043–1052, 2016. [10](#), [10.2.2.4](#)

- U. Fernandez-Gamiz, I. Errasti, R. Gutierrez-Amo, and O. Barambones. Computational modelling of rectangular sub-boundary layer vortex generators. *Applied Sciences*, 8 (138), 2018. [10](#)
- D.H. Ferriss, P. Bradshaw, and N.P. Atwell. Calculation of boundary layer development using the turbulent energy equation. *Journal of Fluid Mechanics*, 28:593–616, 1967. [9.1.1](#)
- R. Fletcher. *Multi-Objective Optimization using Evolutionary Algorithms*. John Wiley Sons, 2001. [8.1.4](#)
- L. Florentie, A.H. Van Zuijlen, and H. Bijl. Towards a multi-fidelity approach for cfd simulations of vortex generator arrays. In *6th European Conference on Computational Fluid Dynamics (ECFD VI)*, volume 1879, 2014. [10](#)
- L. Florentie, A.H. Van Zuijlen, S.J. Hulshoff, and H. Bijl. Effectiveness of side force models for flow simulations downstream of vortex generators. *AIAA Journal*, 2016. [10](#)
- R. E. Froude. On the part played in propulsion by difference of fluid pressure. *Transaction of the Institution of Naval Architects*, 30:390, 1889. [2.2](#), [4.2](#)
- P. Fuglsang, C. Bak, M. Gaunaa, and I. Antoniou. Design and verification of the riso-b1 airfoil family for wind turbines. *Journal of Solar Energy Engineering*, 126:1002–1010, 2004. [7](#), [7.2.4](#)
- Siemens Gamesa. *SG2.1-122 Product Brochure*. Siemens Gamesa, 2018. [I](#)
- S. Gamme, G. de Oliveira, D. Ragni, and F. Lau. A fast panel code for complex actuator disk flows. In *AIAA-2017-0752*, 2017. [2.3.2.1](#), [3.2.1](#), [4.3.3](#)
- Robert Gardon and John Cobonpue. Heat transfer between a flat plate and jets of air impinging on it. In *International Developments in Heat Transfer. ASME.*, pages 454–460, 1963. [5.3.5](#)
- J.W. Gauntner, J.N.B. Livingood, and P. Hrycak. Survey of literature on flow characteristics of a single turbulent jet impinging on a flat plate. Technical report, NASA TN D-5652, 1970. [5.3.5](#)
- P. Gebraad, J. Thomas, A. Ning, P. Fleming, and K. Dykes. Maximization of the annual energy production of wind power plants by optimization of layout and yaw-based wake control. *Wind Energy*, 20(1):97–107, 2016. [2](#)
- H. Glauert. The analysis of experimental results in the windmill brake and vortex ring states of an airscrew. Technical Report RM No. 1026, 1926a. [2.2.3.2](#)
- H. Glauert. General theory of the autogyro. Technical Report 1111, British ARC, Reports and Memoranda, 1926b. [2](#)
- H. Glauert. *Aerodynamic Theory*, volume 4, chapter Airplane Propellers. Springer, Berlin, 1935. [2](#), [4](#)

- H. Glauert. *The elements of airfoil and airscrew theory*. Cambridge University Press, 2nd edition, 1948. [2](#), [2.2.2.1](#)
- T. Gocmen, P. Van Der Laan, P.E. Rethore, A. Pena Diaz, G.C. Larsen, and S. Ott. Wind turbine wake models developed at the technical university of denmark: A review. *Renewable and Sustainable Energy Reviews*, 60:752–769, 2016. [5.3.1](#)
- G. Godard and M. Stanislas. Control of a decelerating boundary layer. part 1: Optimization of passive vortex generators. *Aerospace Science and Technology*, 10(3):181–191, 2006. [10.3](#)
- J. P. Goit and J. Meyers. Optimal control of energy extraction in wind-farm boundary layers. *Journal of Fluid Mechanics*, 768:5–50, 2015. [2](#)
- S. Goldstein. On the vortex theory of screw propellers. Technical report, St. John's College, Cambridge, 1929. [2](#), [4](#)
- J. S. Gonzalez and R. Lacal-Arantequi. A review of regulatory framework for wind energy in european union countries: Current state and expected developments. *Renewable and Sustainable Energy Reviews*, 56:588–602, 2016. [1](#)
- I. Goodfellow, Y. Bengio, and A. Courville. *Deep Learning*. MIT Press, 2016. [9.2](#), [9.3.3](#)
- F. Grasso, D. Coiro, N. Bizzarini, and G. Calise. Design of advanced airfoil for stall-regulated wind turbines. *Wind Energy Science*, 2:403–413, 2017. [6](#), [7](#)
- J.E. Green. Application of head's entrainment method to the prediction of turbulent boundary layers and wakes in compressible flow. Technical report, British ARC RM-3788, 1976. [10](#), [10.3.1](#)
- J.E. Green, D.J. Weeks, and J.W.F. Brooman. Prediction of turbulent boundary layers and wakes in compressible flow by a lag-entrainment method. Technical report, British ARC RM 3791, 1977. [9.1.1](#)
- E.M. Greitzer, C.S. Tan, and M.B. Graf. *Internal Flow: Concepts and Applications*. Cambridge University Press, 2004. [2.1.1](#), [2.1.1](#), [2.2.3.1](#), [2.2.4.2](#), [4.1.3](#), [B.3](#)
- D.A. Griffin. Investigation of vortex generator for augmentation of wind turbine power performance. Technical report, NREL/SR-440-21399, 1996. [10](#)
- GWEC. Top 10 new installed capacity jan-dec 2017. Technical report, GWEC Datasets. [8.4](#)
- M.O.L. Hansen, N.N. Sorensen, and R.G.J. Flay. Effect of placing a diffuser around a wind turbine. *Wind Energy*, 3:207–213, 2000. [3](#)
- G. Hinton, N. Srivastava, and K. Swersky. Rmsprop in neural networks for machine learning. Technical report, University of Toronto, 2016. [9.3.3](#)
- S. Hjort and H. Larsen. Rotor design for diffuser augmented wind turbines. *Energies*, 2015. [3](#)

- A. Hyvarinnen and A. Segalini. Effects from complex terrain on wind-turbine performance. *Journal of Energy Resources Technology*, 139(5), 2017. 3
- IEA. *IEA Task 26: The past and future cost of wind energy*. IEA, 2012. 1
- IEA. *Technology Roadmap for Wind Energy 2013-2050*. IEA/OECD, 2013. 1.1
- IEC. *IEC 61400-1 Ed3: Wind turbines - Part 1: Design Requirements*. International Electrotechnical Commission, 2005. 6.1.3, 6.1.3, 6.1.4, 7, 8.1.2
- O. Igra. Design and performance of a turbine suitable for an aerogenerator. *Energy Conversion*, 15:143–151, 1976. 3
- L. Ingber. Adaptive simulated annealing (asa) : Lessons learned. *Polish Journal Control and Cybernetics*, 1995. 9.3.3
- IRENA. *Innovation outlook: offshore wind*. International Renewable Energy Agency, Abu Dhabi, 2016. 1.1
- IRENA. *Renewable Power Generation Costs in 2017*. International Renewable Energy Agency, Abu Dhabi, 2017. 1, 8.4
- P. Jamieson. Beating betz - energy extraction limits in a uniform flow field. In *Proceedings of the European Wind Energy Conference*, 2008a. 3, 3.2.1, 3.2.2
- P. Jamieson. Generalized limits for energy extraction in a linear constant velocity flow field. *Wind Energy*, 11:445–457, 2008b. 3, 3.2.1, 3.4
- P. Jamieson and M. Branney. Multi-rotors; a solution to 20mw and beyond? *Energy Procedia*, 2012. 1.1
- P. Jamieson, J.M.R. Graham, E. Hart, and A. Giles. Formulation of the general momentum equations. *Journal of Physics: Conference Series*, 1037, 2018. II, 3.1, 4, 4.3.1.2, 4.3.3
- N. O. Jensen. A note on wind generator interaction. Technical report, Risoe, DTU National Laboratory for Sustainable Energy, 1983. 2, 5, 5.3.1
- A. Jirasek. A vortex generator model and its application to flow control. In *22nd AIAA Applied Aerodynamics Conference*, volume AIAA-2004-4975, 2004. 10
- E.N. Johnson and M.A. Turbe. Modeling, control, and flight testing of a small-ducted fan aircraft. *Journal of Guidance, Control, and Dynamics*, 29(4):767–779, 2006. 3
- J.P. Jones. The calculation of the paths of vortices from a system of vortex generators, and a comparison with experiment. Technical report, British ARC CP-361, 1957. 10, 10.1.1, 10.2.2.3
- N. I. Joukowski. *Theorie tourbillonnaire de l'helice propulsive*. Gauthier-Villars, Paris, 1929. 2.3.1, 4, 4.2
- N.E. Joukovsky. Windmill of the nej type. *Transactions of the Central Institute for Aero-Hydrodynamics of Moscow*, 1920. 2

- P. Kapitza. Viscosity of liquid helium below the lambda-point. *Nature*, 141, 1938. [2.2.4.2](#)
- J. Katz and A. Plotkin. *Low Speed Aerodynamics*. Cambridge University Press, 2006. [2.3.2.1](#), [6.3](#)
- M. Kehro and B. Kramer. Enhanced airfoil design incorporating boundary layer mixing devices. *41st AIAA Aerospace Sciences Meeting and Exhibit*, AIAA 2003-0211, 2003. [10](#)
- M. Kelly, G. Larsen, N. K. Dimitrov, and A. Natarajan. Probabilistic meteorological characterization for turbine loads. *Journal of Physics: Conference Series*, 524(012076), 2014. [6](#)
- J. Kevorkian and J. D. Cole. *Multiple scale and singular perturbation methods*. Number 114 in Applied mathematical sciences. Springer, New York, 1996. [5.2.1](#), [9.1](#)
- R.N. King, K. Dykes, P. Graf, and P.E. Hamilton. Optimization of wind plant layouts using an adjoint approach. *Wind Energy Science*, 2:115–131, 2017. [2](#)
- L. Kort. Combined device of a ship's propeller enclosed by a nozzle. *US Patent*, 2.030.375, 1936. [3](#)
- I. Kroo and S. Smith. The computation of induced drag with nonplanar and deformed wakes. *Journal of Aerospace*, 99(1):1880–1888, 1990. [10.3.2](#)
- Brenda M. Kulfan. A universal parametric geometry representation method - "cst". In *45th AIAA Aerospace Sciences Meeting and Exhibit*, 2007. [7.1.1](#), [8.1.3](#), [9.2.3](#), [9.2.3](#)
- Brenda M. Kulfan and John E. Bussoletti. Fundamental" parametric geometry representations for aircraft component shapes. In *11th AIAA/ISSMO Multidisciplinary Analysis and Optimization Conference*, number 2006-6948, 2006b. [7.1.1](#), [8.1.3](#)
- W.G. Kunik. Application of a computational model for vortex generators in subsonic internal flows. In *AIAA/ASME/SAE/ASEE 22nd Joint Propulsion Conference*, volume AIAA-86-1458, 1986. [10](#), [C](#)
- J. N. Kutz. Deep learning in fluid dynamics. *Journal of Fluid Mechanics*, 2017. [9](#)
- D. Kuzmin. A guide to numerical methods for transport equations. Technical report, Friedrich-Alexander Universitat, Erlangen-Nuernberg, 2010. [C](#), [C](#)
- P.Y. Lagree. *Multiscale Hydrodynamic Phenomena: Matched Asymptotic Expansions*. Course Notes, Paris Jussieu, 2016. [10.1.1](#)
- B.E. Launder and D.B. Spalding. *Mathematical Models of Turbulence*. Academic Press, 1972. [10.2.3](#)
- S. Lee, P. Vorobieff, and S. Poroseva. Interaction of wind turbine wakes under various atmospheric conditions. *Energies*, 11(1442), 2018. [2](#)
- Marcel Lesieur. *Turbulence in Fluids*. Springer Netherlands, 2008. [9](#)

- X. Li, K. Yang, C. Liao, J. Bai, L. Zhang, and J. Xu. Overall design optimization of dedicated outboard airfoils for horizontal axis wind turbine blades. *Wind Energy*, (2164), 2017. [6](#), [7](#), [7.2.5](#)
- R. Liebeck. On the design of subsonic airfoils for high lift. In *AIAA 9th Fluid and Plasma Dynamics Conference*, 1976. [6](#), [7](#), [7.2.4](#), [7.2.5](#)
- M.J. Lighthill. On displacement thickness. *Journal of Fluid Mechanics*, 4:383–392, 1958. [5](#)
- L.E.M. Lignarolo, D. Mehta, RJAM Stevens, AE Yilmaz, G.A.M. Van Kuik, S. Andersen, C. Meneveau, C.J. Ferreira, D. Ragni, J. Meyers, G.J.W. Van Bussel, and J. Holierhoek. Validation of four les and a vortex model against stereo-piv measurements in the near wake of an actuator disc and a wind turbine. *Renewable energy*, 94:510–523, 2016. [5.3.6](#)
- G.M. Lilley and W.J. Rainbird. A preliminary report on the design and performance of a ducted windmill. Technical Report 102, College of Aeronautics, Cranfield U.K., 1956. [3](#)
- J. Ling and J. Templeton. Evaluation of machine learning algorithms for prediction of regions of high reynolds average navier stokes uncertainty. *Physics of Fluids*, 27(8): 085103, 2015. [9](#)
- J. Ling, A. Kurzawski, and J. Templeton. Reynolds average turbulence modelling using deep neural networks with embedded invariance. *Journal of Fluid Mechanics*, 807: 155–166, November 2016a. [9](#)
- P. B. S. Lissaman. Energy effectiveness of arbitrary arrays of wind turbines. *J. of Energy*, 3 (6):323–328, 1979. [2](#)
- C. N. H. Lock. Note on the characteristic curve for an airscrew or helicopter. Technical Report RM 2673, British ARC, 1947. [2.2.3.2](#)
- C. N. H. Lock, H. Bateman, and H. C. H. Townend. An extension of the vortex theory of airscrews with applications to airscrews of small pitch, including experimental results. Technical report, British ARC, 1926. [2.2.3.2](#)
- O. Logdberg, K. Angele, and P. Henrik Alfredsson. On the scaling of turbulent separating boundary layers. *Physics of Fluids*, 20(075104), 2008. [10.4.2](#)
- O. Logdberg, J.H.M. Fransson, and P.H. Alfredsson. Streamwise evolution of longitudinal vortices in a turbulent boundary layer. *Journal of Fluid Mechanics*, 623:27–58, 2009. [10.2.2.3](#), [10.2.2.3](#), [10.2.2.4](#), [10.3](#)
- E.N. Lorenz. Deterministic non-periodic flow. *Journal of the atmospheric sciences*, 1963. [9](#)
- Hao Lu and Christopher J. Rutland. Structural subgrid-scale modeling for large-eddy simulation: a review. *Acta Mechanica Sinica*, 2016. [9](#)

- J.L. Lumley. Coherent structures in turbulence. In R.E. Meyer, editor, *Transition and Turbulence*, pages 215–242. Academic Press, 1981. [9](#)
- L. A. H. Machiels, S. Barth, E. T. G. Bot, and Hendriks H. B. Optimization of wind turbine positioning in large windfarms. Technical Report ECN-E-07-105, ECN, 2007. [2](#)
- H. A. Madsen, G. C. Larsen, and K. Thomsen. Wake flow characteristics in low ambient turbulence conditions. In *Copenhagen Offshore Wind Conference*, 2005. [2](#)
- H.A. Madsen, L. Bergami, and F. Rasmussen, editors. *New aerodynamic rotor concepts specifically for very large offshore wind turbines*. InnWind.EU Deliverable 2.11, 2013. [1.1](#)
- Helge Aagaard Madsen. The actuator cylinder - a flow model for vertical axis wind turbines. Technical report, Institute of Industrial Constructions and Energy Technology, Aalborg University Centre, 1982. [5.2](#)
- M. Manolesos and S.G. Voutsinas. Experimental investigation of the flow past passive vortex generators on an airfoil experiencing three-dimensional separation. *J. Wind. Eng. Ing. Aerodyn.*, 142:130–148, 2015. [10.3](#)
- M. Manolesos, N.N. Sorensen, N. Troldborg, G. Papadakis, and S. Voutsinas. Computing the flow past vortex generators: Comparison between rans simulations and experiments. *J. Phys.: Conf. Ser.*, 753:022014, 2016. [10](#)
- J. Manwell, J. McGowan, and A. Rogers. *Wind Energy Explained-Theory, Design and Application*. John Wiley and Sons, 2002. [6.1.2](#)
- H. R. Marden, S. D. Ruben, and L. Y. Pao. Surveying game theoretic approaches for wind farm optimization. In *50th AIAA Aerospace Sciences Meeting*, number AIAA 2012-1154, 2012. [2](#)
- I. Marusic and A.E. Perry. A wall-wake model for the turbulence structure of boundary layers. part 2. further experimental support. *Journal of Fluid Mechanics*, 298:389–407, 1995. [9.1.1](#), [9.1.1](#), [9.3.2](#)
- R. Maulik and O. San. A neural network approach for the blind deconvolution of turbulent flows. *Journal of Fluid Mechanics*, 831:151–181, November 2017. [9](#)
- N.E. May. A new vortex generator model for use in complex configuration cfd solvers. In *19th Applied Aerodynamics Conference*, volume AIAA-2001-2434, 2001. [10](#)
- J. M. McDonough. Introductory lectures on turbulence. Technical report, University of Kentucky, Dept. of Mech. Eng. and Math., 2007. [9](#)
- S. McLaren-Gow, P. Jamieson, and J.M.R. Graham. An inviscid approach to ducted turbine analysis. In *Proceedings of the European Wind Energy Conference (Vienna)*, volume 1, pages 931–938, 2013. [3](#)
- K.J. McNaughton and C.J. Sinclair. Submerged jets in short cylindrical flow vessels. *Journal of Fluid Mechanics*, 25(2):367–375, 1966. [5.3.5](#)

- R.D. Metha and P. Bradshaw. Longitudinal vortices imbedded in turbulent boundary layers. part 1. vortex pair with 'common flow' upwards. *Journal of Fluid Mechanics*, 188:529–546, 1988. [10](#), [10.3](#), [10.4.2](#)
- J. Meyers and C. Meneveau. Optimal turbine spacing in fully developed wind-farm boundary layers. *Wind Energy*, 15(305-317), 2012. [2](#)
- J. Meyers and C. Meneveau. Flow visualization using momentum and energy transport tubes and applications to turbulent flow in wind farms. *Journal of Fluid Mechanics*, 715:335–358, 2013. [2](#)
- P.G. Migliore, W.P. Wolfe, and J.B. Fanucci. Flow curvature effects on darrieus turbine blade aerodynamics. *Journal of Energy*, 4(2):49–55, 1980. [3.3.1](#)
- R. F. Mikkelsen, S. Sarmast, D. Hennigson, and J. N. Sorensen. Rotor aerodynamic power limits at low tip speed ratio using cfd. *J. of Physics: Conf. Series*, 524(012099), 2014. [2](#), [A.4](#)
- T.M. Mitchell. *Machine Learning*. McGraw-Hill, New York, 1997. [9.1.3](#)
- C. Mone, T. Stehly, B. Maples, and E. Settle. *2014 Cost of Wind Energy Review*. NREL, 2014. [1](#)
- L. Morino, M. Gennaretti, and S.F. Shen. Lighthill transpiration velocity revisited: an exact formulation. *Meccanica*, 30(2):122–137, 1995. [9.1](#)
- G. Mosetti, C. Poloni, and D. Diviacco. Optimization of wind turbine positioning in large windfarms by means of a genetic algorithm. *J. Wind Eng. Ind. Aero.*, 51:105–111, 1994. [2](#)
- OECD, IEA, and IRENA. *Perspectives for the Energy Transition*. International Renewable Energy Agency, Abu Dhabi, 2017. [1](#)
- S. Oerlemans. Wind turbine noise: primary noise sources. Technical report, National Aerospace Laboratory (NLR), 2011. [7](#)
- S. Oerlemans and P. Fuglsang. Low-noise wind turbine design. In *EWEA Noise Workshop, Oxford*, 2012. [7](#)
- V. L. Okulov and G. A. M. Van Kuik. The betz-joukowsky limit: on the contribution to rotor aerodynamics by the british, german and russian scientific schools. *Wind Energy*, 15 (2):335–344, 2012. [2](#)
- O.A. Oleinik and V.N. Samokhin. *Mathematical Models in Boundary Layer Turbulence*. Chapman Hall/CRC Press, Boca Raton, 1999. [9.1.1](#)
- R.A. Oman, K.M. Forema, and B.L. Gilbert. Proc. 3rd biennial conf. and workshop on wind energy conversion systems washington dc. In *A Progress Report on the Diffuser Augmented Wind Turbine*, pages 826–829, 1975. [3](#)
- E.H. Oon. Decay of trailing vortices. Technical report, British ARC CP-1238, 1973. [10.2.2.2](#)

- M.W.C. Oosterveld. *Wake Adapted Ducted Propellers*. PhD thesis, Delft University of Technology, 1970. [3](#)
- P. Overbeek. Propelled wind on a wind turbine, a new optimum. In *Researchgate post 2.1.4321.8405*, 2015. [2.1](#)
- A. S. Padron, J. Thomas, A. P. J. Stanley, J. J. Alonso, and A. Ning. Polynomial chaos to efficiently compute the annual energy production in wind farm layout optimization. *Wind Energy Science*, 2018. [2](#)
- H.H. Pearcey. Introduction to shock-induced separation and its prevention by design and boundary layer control. In *Boundary Layer and Flow Control*, volume 2, pages 1167–1344, 1961. [10.2.2.3](#)
- Alfredo Peña, Pierre-Elouan Réthoré, and Paul Van Der Laan. On the application of the jensen wake model using a turbulence-dependent wake decay coefficient: the sexbierum case. *Wind Energy*, 2015. [5.3.1](#)
- R. Pereira, W.A. Timmer, G. de Oliveira, and G. J. W. Van Bussel. Design of hawt airfoils tailored for active flow control. *Wind Energy*, 20(9), 2017. [6.1.3](#), [7.1](#), [7.1.1](#), [7.3](#)
- A.E. Perry. Turbulent boundary layers in decreasing adverse pressure gradients. *Journal of Fluid Mechanics*, 26:481–506, 1966. [9.1.1](#)
- A.E. Perry and W.H. Schofield. Mean velocity and shear stress distributions in turbulent boundary layers. *Physics of Fluids*, 16(2068), 1973. [9.3.2](#)
- A.E. Perry, I. Marusic, and M.B. Jones. New evolution equations for turbulent boundary layers in arbitrary pressure gradients. *Surveys in Fluid Mechanics IV*, 23(5-6):443–457, 1998. [9.1.1](#), [9.1.1](#), [9.3.2](#)
- E. L. Petersen. In search of the wind energy potential. *Journal of Renewable and Sustainable Energy*, 2017. [1](#)
- D.G. Philips. *An investigation on diffuser augmented wind turbine design*. PhD thesis, University of Auckland, 2003. [3](#)
- L P Pitaevskii and S Stringari. *Bose-Einstein condensation and superfluidity*. Oxford University Press, 2016. [2.2.4.2](#)
- D. M. Pitt and D. A. Peters. Theoretical prediction of dynamic inflow derivatives. *Vertica*, 5:21–34, 1981. [6.1.1](#)
- D. Chortis PK, Chaviaropoulos and D. Lekou. Definition of the reference wind turbine - analysis of rotor design parameters. Technical report, Innwind Deliverable 1.2.1, 2013. [8.3](#), [8.3](#)
- H. Polinder and A. Abrahamsen. Electromechanical conversion. In *Long-term research challenges in wind energy - A research agenda by the EAWE*, edited by G. van Kuik and J. Peinke, 2017. [1.1](#)

- A.R Porro, W.R. Hingst, C.A. Wasserbauer, and T.B. Andrews. The nasa lewis research center internal fluid mechanics facility. Technical report, NASA TM-105187, 1991. [10.2.2.1](#)
- L. Prandtl. Über untersuchungen zur ausgebildeten turbulenz. *Zeitschrift für angewandte Mathematik und Mechanik*, 5:136–139, 1925. [9](#)
- M. Putti and C. Paniconi. Picard and newton linearization for the coupled model for salt-water intrusion in aquifers. *Advances in Water Resources*, 18(3):159–170, 1995. [2.3.2.1](#)
- J. Quick, K. Dykes, P. Graf, and F. Zahle. Optimization under uncertainty of site-specific turbine configurations. *Journal of Physics: Conference Series*, 753(6), 2016. [2](#)
- J. Quick, J. Annoni, R. King, K. Dykes, P. Fleming, and A. Ning. Optimization under uncertainty for wake steering strategies. In *Wakes Conference 2017, Visby, Sweden*, 2017. [2](#)
- Giridhar Ramanujam, Huseyin Ozdemir, and H.W.M. Hoeijmakers. Improving airfoil drag prediction. In *34th AIAA/ASME Wind Energy Symposium*, number 2016-0748, 2016. [9.1.1](#)
- W. J. M. Rankine. On the mechanical principles of the action of propellers. *Transactions of the Institution of Naval Architects*, 6:13–39, 1865. [2.2](#)
- F. Rasmussen, J. Petersen, and H. Madsen. Dynamic stall and aerodynamic damping. *Transactions of the ASME*, 121:150–155, 1999. [6.3](#), [7](#)
- A. Reeh, M. Weismuller, and C. Tropea. In-flight investigation of transition under turbulent conditions on a laminar wing glove. *AIAA Journal*, 52(10), 2014. [6.3](#)
- A. D. Reeh and C. Tropea. Behaviour of a natural laminar flow aerofoil in flight through atmospheric turbulence. *Journal of Fluid Mechanics*, 767, 2015. [6.3](#), [7.2.4](#)
- P.E. Rethore, P. Fuglsang, G.C. Larsen, T. Buhl, and T.J. Larsen. Topfarm: Multifidelity optimization of wind farms. *Wind Energy*, 17(12):1797–1816, 2013. [2](#)
- P.E. Rethore, P. van der Laan, N. Troldborg, F. Zahle, and N.N. Sorensen. Verification and validation of an actuator disk model. *Wind Energy*, 17, 2014. [4.3.3](#)
- O. Reynolds. On the dynamical theory of turbulent incompressible fluids and the determination of the criterion. *Philosophical Transactions of the Royal Society London A*, 186, 1894. [9](#)
- A. Rezaeihaa, R. Pereira, and M. Kotsonis. Fluctuations of angle of attack and lift coefficient and the resultant fatigue loads for a large horizontal axis wind turbine. *Renewable Energy*, 114:904–916, 2017. [6](#), [6.2](#), [6.1](#), [6.2.1](#), [8.1.2](#)
- J. M. Rinker. Calculating the sensitivity of wind turbine loads to wind inputs using response surfaces. *Journal of Physics: Conference Series*, 753(032057), 2016. [6](#)
- K. Rokenes. *Investigation of terrain effects with respect to wind farm siting*. PhD thesis, NTNU, 2009. [3](#)

- L. Rosenhead. The formation of vortices from a surface of discontinuity. *Proc. R. Soc. Lond. A*, 134, 1931. [2.2.3.2](#), [2.2.4.2](#)
- Harold Rosenstein and Ross Clark. Aerodynamic development of the v-22 tilt rotor. In *12th European Rotorcraft Forum*, number 14, 1986. [5](#)
- David Ruelle. Differentiable dynamical systems and the problem of turbulence. *Bulletin of the American Mathematical Society*, 1981. [9](#)
- P. Sagaut. Towards advanced subgrid models for lattice-boltzmann-based large-eddy simulation: Theoretical formulations. *Computers and mathematics with applications*, 59, 2010. [9](#)
- H. Sarlak. Large eddy simulation of an sd7003 airfoil: Effects of reynolds number and subgrid-scale modeling. In *Journal of physics: conference series*, number 854, 2017. [9](#)
- H. Sarlak, F. Pierella, R. Mikkelsen, and J.N. Sorensen. Comparison of two les codes for wind turbine wake studies. *Journal of Physics: Conference Series*, 524, 2014. [5.3.6](#)
- J. G. Schepers. *Engineering models in wind energy aerodynamics - Development, implementation and analysis using dedicated aerodynamic measurements*. PhD thesis, Delft University of Technology, 2012. [6.1.1](#)
- H. Schlichting. *Boundary Layer Theory*. McGraw-Hill, 1979, 7th Ed. [10](#), [10.2.1](#), [10.2.1](#)
- Hermann Schlichting and Klaus Gersten. *Boundary Layer Theory*. Springer-Verlag Berlin Heidelberg, 2017. [9.1](#), [9.1](#), [9.2](#), [9.3.2](#), [10.1.3](#)
- J. Schluntz and R.H.J. Willden. The effect of blockage on tidal turbine rotor design and performance. *Renewable Energy*, 81:432–441, 2015. [3](#)
- M. Schramm, H. Rahimi, B. Stoevesand, and K. Tangager. The influence of eroded blades on wind turbine performance using numerical simulations. *Energies*, 10(1420), 2017. [7](#)
- G.B. Schubauer and H.K. Skramstad. Laminar boundary-layer oscillations and transition on a flat plate. Technical report, NACA Report 909, 1948. [9](#)
- G.B. Schubauer and W.G. Spangenberg. Forced mixing in boundary layers. *Journal of Fluid Mechanics*, 8(5):10–32, 1960. [10](#), [10.3](#)
- I.M.M.A. Shabaka, R.D. Metha, and P. Bradshaw. Longitudinal vortices imbedded in turbulent boundary layers. part 1. single vortex. *Journal of Fluid Mechanics*, 155:37–57, 1985. [10](#), [10.3](#)
- D. J. Sharpe. A general momentum theory applied to an energy extracting actuator disk. *Wind Energy*, 13, 2010. [4](#)
- H. Shim, Y.H. Jo, K. Chang, and K.J. Kwon. Wake characteristics of vane-type vortex generators in a flat plate laminar boundary layer. *Intl J. of Aeronautical Space Sci.*, 16:3, 2015. [10.3](#)

- Gregory P.D. Siemens. Naca report tr-824 - digitized. 1994. [9.2.1](#)
- A.P. Singh and K. Durasaimy. Characterizing and improving predictive accuracy in shock-turbulent boundary layer interactions using data-driven models. In *55th AIAA Aerospace Sciences Meeting*, 2017. [9](#)
- A.P. Singh, R. Matai, K. Durasaimy, and P. Durbin. Data-drive augmentation of turbulence models for adverse pressure gradient flows. In *23rd AIAA Computational Fluid Dynamics Conference*, 2017. [9](#)
- J. Slotnick, A. Khodadoust, J. Alonso, D. Darmofal, W. Gropp, E. Lurie, and D. Mavriplis. Cfd vision 2030: A path to revolutionary computational aerosciences. Technical report, NASA CR-2014-218178, 2014. [IV](#), [9](#)
- F.T. Smith. Theoretical prediction and desing for vortex generators in turbulent boundary layers. *Journal of Fluid Mechanics*, 270:91–131, 1994. [10](#), [10.1.1](#)
- H. Snel and T. Van Holten. Review of recent aerodynamic research on wind turbines with relevance to rotorcraft. Technical Report CP-552, AGARD, 1995. [2](#)
- D. M. Somers. Design and experimental results for the s809 airfoil. Technical report, NREL/SR-440-6918, 1997. [7](#)
- J. N. Sorensen. *General Momentum Theory for Horizontal Axis Wind Turbines*, volume 4 of *Research Topics in Wind Energy*. Springer, 2016. [II](#), [2](#), [2.2.2.1](#), [3](#), [3.1](#), [3.2.1](#), [3.2.2](#), [4](#)
- J. N. Sorensen and A. Myken. Unsteady actuator disk model for horizontal axis wind turbines. *J. Wind Eng. Ind. Aero.*, 39:139–149, 1992. [2](#)
- J. N. Sorensen, W. Z. Shen, and X. Munduate. Analysis of wake states by a full-field actuator disk model. *Wind Energy*, 1, 1998. [4.3.3](#)
- N. N. Sorensen, B. Mendez, A. Munoz, G. Sieros, E. Jost, T. Lutz, G. Papadakis, S. Voutsinas, G.N. Barakos, S. Colonia, D. Baldacchino, C. Baptista, and C. Ferreira. Cfd code comparison for 2d airfoil flows. In *Journal of physics and conference series*, volume 753, 2016. [9](#)
- R. Speck. Generalized algebraic kernels and multipole expansions for massively parallel vortex particle methods. Technical Report IAS Series Vol. 7, Forschungszentrums Juelich, 2011. [2.3.2.1](#), [10.1.4](#)
- H.H. Squire. The growth of a vortex in turbulent flow. *Aeronautical Quarterly*, 16:302–306, 1965. [10](#), [10.2.2.1](#), [10.2.2.2](#)
- A.P.J. Stanley, J. Thomas, A. Ning, J. Annoni, K. Dykes, and P. Fleming. Gradient-based optimization of wind farms with different turbine heights. In *35th Wind Energy Symposium, AIAA SciTech Forum*, number 2017-1619, 2017. [2](#)
- F. Stilffried, S. Wallin, and A.V. Johansson. An improved passive vortex generator model for flow separation control. In *5th Flow Control Conference*, volume AIAA-2010-5091, 2010. [10](#)

- F. Stilffried, S. Wallin, and A.V. Johansson. Statistical vortex-generator-jet model for turbulent flow separation control. *AIAA Journal*, 51 (5):1119–1129, 2013. [10](#)
- L. Stipa. Stipa monoplane with venturi fuselage. *Rivista Aeronautica*, 9(7), 1933. [3](#)
- T.W. Swafford. Analytical approximation of two dimensional separated turbulent boundary layer velocity profiles. *AIAA Journal*, 21(6):923–926, 1982. [10.2.1](#), [10.3.1](#)
- V.V. Sychev, A.I. Ruban, V.V. Sychev, and G.L. Korolev. *Asymptotic Theory of Separated Flows*. Cambridge University Press, 1998. [5](#)
- J. L. Tangler and D. M. Somers. Status of the special- purpose airfoil families. In *Proceedings of the Windpower 87 Conference, San Francisco*, 1987. [7](#)
- D. Taylor. Application of vortex generator mixing principle to diffusers. Technical report, UAC Rep R-15064-5, 1948. [10](#)
- G.I. Taylor. Statistical theory of turbulence. *Proceedings of the Royal Society London A*, 151:421–478, 1935. [9](#)
- H. Tennekes and J.L. Lumley. *A first course in turbulence*. MIT Press, 1972. [9](#)
- T. Theodorsen. *Theory of Propellers*. McGraw-Hill Book Company, New York, 1948. [2](#), [4](#)
- K. Thomsen and P. Sorensen. Fatigue loads for wind turbines operating in wakes. *Journal of Wind Engineering and Industrial Aerodynamics*, 80(1-2):121–136, 1999. [2](#)
- W. A. Timmer and R.P.J.O.M. Van Rooij. Summary of the delft university wind turbine dedicated airfoils. *41st AIAA Aerospace Sciences Meeting and Exhibit*, 2003-0352, 2003. [6](#), [7.3](#)
- W.A. Timmer. An overview of naca 6-digit airfoil series characteristics with reference to airfoils for large wind turbine blades. In *47th AIAA Aerospace Sciences Meeting and Exhibit*, number 2009-268, 2009a. [6](#), [9.1.2](#), [9.1.2](#), [9.3.1](#)
- W.A. Timmer and R.P.J.O.M. Van Rooij. De invloed van een klepuitslag op de prestaties van profiel du 95-w-180. Technical Report IW-98003R, TU-Delft, 1998. [9.3.1](#)
- N. Tobin and L. P. Chamorro. Windbreak effects within infinite wind farms. *Energies*, 10 (1140), 2017. [2](#)
- O. Tornblom and A.V. Johansson. A reynolds stress closure description of separation control with vortex generators in a plane asymmetric diffuser. *Physics of Fluids*, 19: 115108, 2007. [10](#)
- B. Tracey, K. Durasaimy, and J.J. Alonso. Application of supervised learning to quantify uncertainties in turbulence and combustion modelling. In *AIAA Aerospace Sciences Meeting*, 2013. [9](#)
- B. Tracey, K. Durasaimy, and J.J. Alonso. A machine learning strategy to assist turbulence model development. In *53rd AIAA Aerospace Sciences Meeting, Machine Learning, Turbulence*, Major 2015. [9](#), [9.2](#)

- N. Troldborg, N.N. Sørensen, F. Zahle, and P.E. Rethore. Simulation of a mw rotor equipped with vortex generators using cfd and an actuator shape model. In *53rd AIAA Aerospace Sciences Meeting*, volume AIAA 2015-1035, 2015. [10](#)
- H.S. Tsien. Two-dimensional subsonic flows of compressible fluids. *Journal of Aeronautical Sciences*, 6(399-407), 1939. [5](#)
- E.F. Valentine and R.B. Carrol. Effects of several arrangements of rectangular vortex generators on the static pressure rise through a short 2:1 diffuser. Technical report, NACA RM L40L04, 1951. [10](#)
- G. J. W. Van Bussel. An assessment of the performance of diffuser augmented wind turbines (dawts). In *FEDSM99-7830, Proceedings of the 3d ASME/JSM E Joint Fluids Conference San Francisco CA*, 1999. [3](#), [3.2.1](#)
- G. J. W. Van Bussel. The science of making more torque from wind: Diffuser experiments and theory revisited. *Journal of Physics: Conference Series*, 2007. [2](#), [3](#), [3.2.1](#), [3.2.2](#)
- G.J.W. Van Bussel. The use of the asymptotic acceleration potential method for horizontal axis windturbine rotor aerodynamics. *J. Wind Eng. Ind. Aero.*, 39:161–172, 1992. [2](#)
- L.M.M. van den Boz and B. Sanderse. Uncertainty quantification for wind energy applications - literature review. Technical Report SC-1701, Centrum Wiskunde Informatica, 2017. [2](#), [6.1.3](#), [8.1.2](#)
- A. Van Garrel. *Multilevel panel method for wind turbine rotor flow simulations*. PhD thesis, University of Twente, 2016. [5](#)
- J. Van Ingen and M. Kotsonis. A two-parameter method for en transition prediction. In *6th AIAA Theoretical Fluid Mechanics Conference*, number AIAA 2011-3928, 2011. [9](#), [9.1.1](#)
- G.A.M Van Kuik. Joukowsky actuator disk momentum theory. *Wind Energy Science*, 2017. [2](#)
- G.A.M Van Kuik and L.E.M. Lignarolo. Potential flow solutions for energy extracting actuator disk flows. *Wind Energy*, 2015. [4.2](#), [4.3.3](#), [5.3.6](#)
- G.A.M. Van Kuik, D. Micallef, I. Herraез, A.H. Van Zuijlen, and D. Ragni. The role of conservative forces in rotor aerodynamics. *Journal of Fluid Mechanics*, 750:284–315, 2014. [II](#), [2.3.2.3](#), [4.2](#), [4.3.3](#)
- R.P.J.O.M. van Rooij. Modification of the boundary layer calculation in rfoil for improved airfoil stall prediction. Technical Report IVW Report IW-96087R, Delft University of Technology, 1996a. [7.1.2](#)
- R.P.J.O.M. van Rooij. Modification of the boundary layer calculation in rfoil for improved airfoil stall prediction. Technical report, Delft University of Technology, Report IW-96087R, 1996b. [9](#), [9.1.1](#), [9.2](#)

- R.P.J.O.M. Van Rooij and W. A. Timmer. Roughness sensitivity considerations for thick rotor blade airfoils. *ASME Journal of Solar Energy Engineering*, 125, 2003. [7](#)
- A.E.P. Veldman. Boundary layers. Technical report, University of Groningen, Lecture Notes, 2008. [9.1](#), [9.1](#)
- C.M. Velte. Vortex generator flow model based on self-similarity. *AIAA Journal*, 51 (2): 526–529, 2013. [10.2.2.4](#)
- C.M. Velte, M.O.L. Hansen, K.E. Meyer, and P. Fuglsang. Evaluation of the performance of vortex generators on the du 91-w2-250 profile using stereoscopic piv. In *WM-SCI 2008:12th World Multi-Conference on Systemics, Cybernetics and Informatics*, volume 2, 2008. [10.3](#)
- M.C. Vila and M. Alfaro. New airfoil family design for large wind turbine blades. In *33rd Wind Energy Symposium, AIAA 2015-0996*, 2015. [6](#), [7](#), [7.2.6](#), [7.3](#)
- Ricardo Vinuesa, Seyed M. Hosseini, Ardeshir Hanifi, Dan S. Henningson, and Philipp Schlatter. Pressure-gradient turbulent boundary layers developing around a wing section,. *Flow, Turbulence and Combustion*, 99(3-4):613–641, 2017. [9.3.2](#), [9.6](#)
- A. Volland, G. Balarac, and C. Corre. Subgrid-scale scalar flux modelling based on optimal estimation theory and machine-learning procedures. *Journal of Turbulence*, 18(9): 854–878, 2017. [9](#)
- L. Vollmer, G. Steinfeld, D. Heinemann, and M. Kuhn. Estimating the wake deflection downstream of a wind turbine in different atmospheric stabilities: an les study. *Wind Energy Science*, 1:129–141, 2016. [2](#)
- Per Volund. Loads on a horizontal axis wind turbine operating in wake. *Journal of Wind Engineering and Industrial Aerodynamics*, 39(1-3):317–328, 1992. [2](#)
- T. von Karman. Compressibility effects in aerodynamics. *Journal of Aeronautical Sciences*, 8:337–356, 1941. [5](#)
- A. Vuillet and F Morelli. New aerodynamic design of the fenestron. In *Proc. 12th Eur. Rot. Forum*, 1986. [3](#)
- J.W. Wagenaar and P.J. Eecen. 3d turbulence at the offshore wind farm egmond aan zee. Technical report, Energy Center of the Netherlands ECN-E-10-075, 2010. [1](#)
- S. Wahono. Development of virtual blade model for modelling helicopter rotor downwash in openfoam. Technical report, DSTO Defence Science and Technology Organisation (Australia) DSTO-TR-2931, 2014. [5.3.4](#)
- K.A. Waithe. Source term model for an array of vortex generator vanes. Technical report, NASA CR-2003-21215, 2003. [10](#)
- F Wallin and L.E. Eriksson. A tuning-free body-force vortex generator model. In *44th AIAA Aerospace Sciences Meeting*, volume AIAA-2006-873, 2006. [10](#)

- R.A. Waltz, J.L. Morales, J. Nocedal, and D. Orban. An interior algorithm for nonlinear optimization that combines line search and trust region steps. *ACM*, 2006. [5.1.1](#), [8.1.4](#), [9.2.4](#)
- J.X. Wang, J.L. Wu, and H. Xiao. Physics-informed machine learning approach for reconstructing reynolds stress modeling discrepancies based on dns data. *Physical Review Fluids*, 2(3):034603, 2017. [9](#)
- J. Weatheritt and R.D. Sandberg. The development of algebraic stress models using a novel evolutionary algorithm. *International Journal of Heat and Fluid Flow*, 68:298–318, 2017. [9](#)
- Michael Weismuller. *A new approach to aerodynamic performance of aircraft under turbulent atmospheric conditions*. PhD thesis, Technische Universitaet Darmstadt, 2011. [6](#), [6.3](#), [8.1.2](#)
- B.J. Wendt. Initial peak vorticity behavior for vortices shed from airfoil vortex generators. In *36th AIAA Aerospace Sciences Meeting and Exhibit*, 1997. [10.1.1](#), [10.2.2.1](#), [10.4.2](#)
- B.J. Wendt. Initial circulation and peak vorticity of vortices shed from airfoil vortex generators. Technical report, NASA CR-2001-211144, 2001. [10](#), [10.1.1](#), [10.2.2.1](#)
- B.J. Wendt, B.A. Reicher, and J.D. Foster. The decay of longitudinal vortices shed from airfoil vortex generators. Technical report, NASA CR-198356, 1995. [10.2.2.2](#), [10.2.2.3](#)
- J.J. Wendt. Parametric study of vortices shed from airfoil vortex generators. *AIAA Journal*, 42 (11):2185–2195, 1965. [10.2.2.1](#)
- M.J. Werle and W.M. Presz. Ducted wind/water turbines and propellers revisited. *Journal of Propulsion and Power*, 24(5):1146–1150, 2008. [3](#), [3.2.1](#), [3.2.2](#), [3.3](#), [3.4](#)
- R.V Westphal, Pauley W.R., and J.K. Eaton. Interaction between a vortex and turbulent boundary. Technical report, NASA TM-88361, 1987. [10.1.4](#), [10.2.2](#), [10.3](#)
- J.I. Whelan, J.M.R. Graham, and J. Peiro. A free-surface and blockage correction for tidal turbines. *Journal of Fluid Mechanics*, 624(281-291), 2009. [3](#)
- D.C. Wilcox. *Turbulence modelling for CFD*. DCW Industries, 2006. [9](#)
- R. E. Wilson and P. B. S. Lissaman. Applied aerodynamics of wind power machines. Technical report, Oregon State University, May 1974. [2](#), [4](#)
- WindEurope. *Wind in power 2017*. Wind Europe, 2018. [1](#)
- D. H. Wood. Maximum wind turbine performance at low tip speed ratio. *Journal of Renewable and Sustainable Energy*, 7(053126), 2015. [2](#)
- Y. T. Wu and F. Porte-Agel. Simulations of turbulent flow inside and above wind farms: model validation and layout effects. *Boundary Layer Meteorology*, 146:181–205, 2013. [2](#)

- O. Ceyhan Yilmaz and et al. Summary of the blind test campaign to predict the high reynolds number performance of du00-w210 airfoil. In *35th AIAA/ASME Wind Energy Symposium*, number AIAA 2017-0915, 2017. [9](#)
- M. V. Zagarola and A. J. Smits. Mean-flow scaling of turbulent pipe flow. *Journal of Fluid Mechanics*, 373, October 1998. [9.1.1](#)
- F. Zahle, C. Bak, N. Sorensen, T. Vronsky, and N. Gaudern. Design of the lrp airfoil series using 2d cfd. *J. Phys. Conf. Ser.*, 524:012020, 2014. [6](#), [7](#)
- Z.J. Zhang and K. Durasaimy. Machine learning methods for data-driven turbulence modeling. In *AIAA Computational Fluid Dynamics Conf. 2015-2460*. [9](#)

LIST OF PUBLICATIONS

Double peer-reviewed contributions:

1. **G. de Oliveira**, R. Pereira, D. Ragni, B.W. van Oudheusden. *Mechanisms of boundary-layer mixing by streamwise vortices*. (ready for submission)
2. **G. de Oliveira**, R. Pereira, W.A. Timmer, G.J.W. van Bussel. *Role of wake interactions in optimal conversion of wind energy*. (ready for submission)
3. V.V. Dighe, **G. de Oliveira**, F. Avallone and G.J.W. van Bussel. *Characterization of aerodynamic performance of ducted wind turbines: A numerical study*. Wind Energy (submitted)
4. P. Thedens, **G. de Oliveira** and R. Schmehl. *Ram-air kite airfoil and reinforcements optimization for airborne wind energy applications*. Wind Energy, 2019.
5. **G. de Oliveira**, R. Pereira, W.A. Timmer and R.P.J.M. van Rooij. *Improved airfoil polar predictions with data-driven boundary-layer closure relations*. Journal of Physics Conference Series 1037(2):022009 , 2018.
6. V. Dighe, **G. de Oliveira**, F. Avallone and G. van Bussel. *Towards improving the aerodynamic performance of a ducted wind turbine: A numerical study*. Journal of Physics Conference Series 1037(2):022016, 2018.
7. R. Pereira, **G. de Oliveira**, W. A. Timmer and E. Quaeghebeur. *Probabilistic Design of Airfoils for Horizontal Axis Wind Turbines*. Journal of Physics Conference Series 1037(2):022042, 2018.
8. R. Pereira, W.A. Timmer, **G. de Oliveira** and G.J.W. van Bussel. *Design of HAWT airfoils tailored for Active Flow Control*. Wind Energy, 2017.
9. S. Vedamanickam, D. Ragni, **G. de Oliveira** and L. Veldhuis. *Aerodynamics of an Aircraft Propeller Model with Passive Tip Jet*. Journal of Aircraft 55(4), 1-11, 2018.
10. **G. de Oliveira**, M. Kotsonis and B.W. Van Oudheusden. *Laminar Boundary Layer Flow with DBD Plasma Actuation: A Similarity Equation*. Springer Lecture Notes in Computational Science (120), 2017.
11. **G. de Oliveira**, R. Pereira, D. Ragni, F. Avallone and G. van Bussel. *How does the presence of a body affect the performance of an actuator disk?* Journal of Physics Conference Series 753(2):022005, 2016.
12. R. Pereira, M. Kotsonis, **G. de Oliveira** and D. Ragni. *Analysis of local frequency response of flow to actuation: Application to the dielectric barrier discharge plasma actuator*. Journal of Applied Physics 118(15):153501, 2015.

Single or non peer-reviewed contributions:

1. F. Espenica, R. Pereira, **G. de Oliveira**, J. Baltazar and J. Campos. *Design and optimization of hydrofoils tailored for marine current turbines*. EWTEC 2019 Conference. (accepted)
2. M. Zaikin, R. Pereira, **G. de Oliveira** and M. Kotsonis. *DBD Plasma Actuator Substrate Tailoring: Design, Construction and Experimental Testing*. AIAA Aviation 2019 Conference. (accepted)
3. V. Dighe, **G. de Oliveira**, F. Avallone and G. van Bussel. *On the effects of the shape of the duct for ducted wind turbines*. Proceedings of 56th AIAA Aerospace Sciences Meeting, 2018.
4. **G. de Oliveira**, W. A. Timmer and B.W. van Oudheusden. *Integral Equations for Boundary Layers with Streamwise Vortices*. Proceedings of the 52nd 3AF International Conference on Applied Aerodynamics, Lyon, 2017.
5. E.C. Battle, R. Pereira, M. Kotsonis and **G. de Oliveira**. *Airfoil Optimisation for DBD Plasma Actuator in a Wind Energy Environment: Design and Experimental Study*. Proceedings of 55th AIAA Aerospace Sciences Meeting, 2017.
6. S. Gamme, **G. de Oliveira**, D. Ragni and F. Lau. *A Fast Panel Code for Complex Actuator Disk Flows*. Proceedings of 55th AIAA Aerospace Sciences Meeting, AIAA2017-0752, 2017.
7. S. Bal, R. Pereira, **G. de Oliveira** and D. Ragni. *Investigating the Influence of DBD Plasma Actuators on the Skin Friction in Integral Boundary Layer Formulation*. Proceedings of 54th AIAA Aerospace Sciences Meeting, AIAA2016-2162, 2016.
8. **G. de Oliveira**, R. Pereira, D. Ragni and M. Kotsonis. *Modeling DBD Plasma Actuators in Integral Boundary Layer Formulation for Application in Panel Methods*. Proceedings of the 46th AIAA Plasmadynamics and Lasers Conference, AIAA2015-3367, 2015.

Poster-only or presentation-only contributions:

1. **G. de Oliveira**, R. Pereira, W.A. Timmer, D. Ragni, F. Lau and G. van Bussel. *Gazing at clouds to understand turbulence on wind turbine airfoils*. 8th EO School of the European Space Agency, 2016. (Award from European Meteorological Society)
2. **G. de Oliveira**, R. Pereira, G. van Bussel, F. Avallone and D. Ragni, *Passive and active flow augmentation: from diffusers to multi-rotor machines*, Wind Energy Science Conference (WESC), Copenhagen, 2017.
3. **G. de Oliveira**, U. Fechner, R. Pereira. *Multiobjective airfoil design for wind energy*. AWEC Conference, Freiburg, 2017.
4. U. Fechner, **G. de Oliveira**. *On the way to small-scale drones – a networked approach*. AWEC Conference, Freiburg, 2017.

AUTHORSHIP NOTICE

This thesis is primarily the work of its author, Gael de Oliveira. Even so, several images, text and ideas received contributions from other authors. In particular:

1. Chapters 6 and 8 re-use text from an article of which Ricardo pereira is the first author. Contributions from the other co-authors (Erik Quagebeur and Nando Timmer) to the text were also substantial.
2. Figure 6.2 was produced by Ricardo Pereira and uses data that was generated by Abdolrahim Rezaeiha and re-processed by Ricardo Pereira
3. Figure 6.1 was produced by Erik Quagebeur and Ricardo Pereira
4. Figures 3.8, 3.9 and 3.10 were produced by Vinit Dighe using data generated by Vinit Dighe and Gael de Oliveira.

Several parts of this work result from endless scientific emulation with colleagues. Ricardo Pereira deserves an extraordinary mention in that respect. Creative sessions with Daniele Ragni, Francesco Avallone, Vinit Dighe and Nando Timmer were also remarkable. Furthermore, many of the ideas presented here benefitted from conversations with Simon Gamme, Erik Quagebeur, Paul Thedens, Lorenzo Lignarolo and Rene Bos. Also, I must acknowledge that I “stole” the turquoise color idea from the thesis of Rene Bos; no endorsement implied, the graphism of his thesis was far above anything I can produce.

CURRICULUM VITAE

Gaël de Oliveira was born on March 17th 1985 in Chateauroux, France. His education was the result of a nurturing family that supported engagement with people of diverse background, culture and opinion. He attended the following institutions:

- 1995 - 2^o Jardim Escola João de Deus, Figueira da Foz, Portugal
- 2002 - Escola Secundaria Dr. Joaquim de Carvalho, Figueira da Foz, Portugal
- 2008 - BSc Aerospace Engineering, Instituto Superior Técnico, Lisbon, Portugal
- 2011 - MSc Aerospace Engineering, Delft University of Technology
- 2017 - Pg. Cert Poverty Reduction: Policy and Practice, School of Oriental and African Studies, University of London International Programmes

His career involved several positions, amongst which:

- 2009/11 - Actiflow, Breda, Netherlands - Wind turbine blade design engineer
- 2011/12 - Eol Mali, Mopti, Mali - Co-founder (international development)
- 2012/13 - ENGIM, Mali/Italy - Chargé de Mission (international development)
- 2017/18 - Nsira, Delft, Netherlands - Founder, Aerodynamicist
- 2018/19 - Jacobs Engineering, The Hague, Netherlands - System Specialist
- 2014/19 - TU Delft, Delft, Netherlands - Researcher and PhD candidate